INVESTIGATION OF BOUNDARY LAYER PARAMETERS IN APG NOZZLE AND THE FLOW INTERFERENCE CAUSED BY SECONDARY INJECTION

FINAL REPORT

nes co

CONTRACT NO. NAS7-166

MAY 1963

NATIONAL ENGINEERING SCIENCE CO.

PREPARED FOR

NATIONAL AERONAUTICS AND SPACE ADMINISTRATION
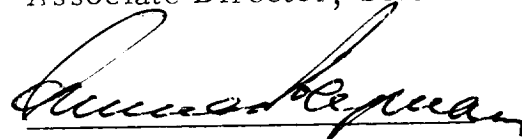
WASHINGTON, D.C.

FINAL REPORT

INVESTIGATION OF BOUNDARY LAYER PARAMETERS IN APG NOZZLE AND THE FLOW INTERFERENCE CAUSED BY SECONDARY INJECTION

Prepared for: National Aeronautics and Space Administration
Washington 25, D. C.
Attention: Mr. Henry Burlage, Jr.
Chief, Liquid Propulsion Systems, RPL
Contract No. NAS7-166

Prepared by: S. Hozaki
R. Gagnon
E. Mayer
J. Tromblay
J. Wu

Approved by:

G. V. R. Rao, Sc. D.
Associate Director, Science

Gunnar B. Bergman, Ph. D.
Vice President, Science

ABSTRACT

Secondary gas injection through multiport injector for thrust vector control of rocket engines is examined. Utilizing multiradial ports and opposed-tangential ports, the influence of injection port spacing is examined as to the effect on flow interference and the resultant side force. Theoretical analysis of injection port spacing requirement for mutual flow interference is presented. A conical nozzle and a nozzle contoured to exhibit adverse pressure gradient on the wall were tested employing cold air for the injectant as well as for the main nozzle flow. The results of the investigation show that the flow interference pattern is affected by the injection port spacing. Considerable improvement in the injectant performance is observed with multiradial port injection compared to single port injection. The test data also show the definite gain in injectant performance obtained in the adverse pressure gradient nozzle compared to that in the conical nozzle.

TABLE OF CONTENTS

LIST OF FIGURES

LIST OF TABLES

LIST OF SYMBOLS

a	- Speed of sound	ft/sec
A	- Area	in.^{2}
AR	- Area ratio	
b	- Width of jet	in.
c	- Distance between injection port centers	in.
C	- Constant	
C_D	- Drag coefficient	
C_f	- Friction coefficient	
d	- Diameter	in.
D	- Drag force	lb
F_{AV}°	- Vacuum axial thrust with vectoring	lb
F_r°	- Vacuum thrust of a sonic jet	lb
F_s	- Side force	lb
f(s, n)	- Defined in Equation D(9)	
h	- Specific enthalpy	ft-lb/lb
k	- Number of dimension, k = 0 two-dimensional and k = 1 axisymmetric	
K	- Karman constant	
L	- Length of diverging portion of nozzle	in.
m	- Power for velocity distribution	
M	- Mach number	
n	- Distance normal to and measured from wall	
N	- Transformed coordinate of n	

p	-	Static pressure	psia
P	-	Stagnation pressure	psia
P_c	-	Chamber stagnation pressure	psia
p	-	Static pressure	psia
P	-	Stagnation pressure	psia
Pr	-	Prandtl number	
q	-	Velocity	ft/sec
r	-	Radial coordinate	
R	-	Radius	in.
RF	-	Recovery factor	
s	-	Distance measured along surface	
S	-	Transformed coordinate of s	
T	-	Temperature	°R
u	-	s component of velocity	ft/sec
U	-	S component of velocity	ft/sec
v	-	n component of velocity	ft/sec
V	-	N component of velocity	ft/sec
w	-	Temperature exponent of viscosity	
$\dot{w}$	-	Weight flow rate	lb/sec
x	-	Coordinate	
y	-	Coordinate	
α	-	Shock angle	degrees
β	-	Angular measurement	degrees
β_M	-	$\sqrt{M^2 - 1}$	
γ	-	Specific heat ratio	
Γ	-	$(1 - \overline{U}_e^2 / \overline{U}_e^{*2})$	
δ	-	Boundary layer thickness	in.
δ^*	-	Displacement thickness	in.

δ_M	-	Momentum thickness	in.
Δ_o	-	Standoff distance	in.
ϵ	-	Density ratio	
ζ, η, ξ	-	Coordinate system	
θ	-	Circumferential angle	degrees
λ_p	-	Primary pressure ratio	
λ_s	-	Secondary pressure ratio	
$\lambda_1 \ldots \lambda_6$	-	Defined in equation D(29) through D(34)	
Λ (m)	-	Defined in equation E(19)	
μ	-	Viscosity	lb/sec-ft
ν	-	Kinematic viscosity	ft-in/sec
ρ	-	Density	lb/ft^3
σ	-	Flow deflection angle	degrees
Σ	-	$(\overline{h}_w/\overline{h}_o - 1)$	
τ	-	Shear stress	psi
ϕ	-	Jet trajectory angle	degrees
ϕ_w	-	Wall angle	degrees
ψ	-	Stream function	
ω_1, ω_2	-	Compressibility scaling parameters	
Ω	-	$\delta_{M_i} (\overline{U}_e \delta_{M_i}/\overline{\nu}_o)^{2/(m+1)}$	

Subscript

b	-	Body
c	-	Chord
cr	-	Critical
d	-	Disturbed
e	-	External
eff	-	Effective

i	-	Incompressible
in	-	Initial
inj	-	Injection station
j	-	Injector
jc	-	Junction
p	-	Primary
r	-	Recovery
ref	-	Reference
s	-	Secondary
sh	-	Shock wave
w	-	Wall
o	-	Stagnation
∞	-	Free stream
, ( )	-	$\partial/\partial(\ )$ Partial differentiation

Superscript

- (bar)	-	Temporal mean value
' (prima)	-	Instantaneous fluctuations from the mean
*	-	Point of zero pressure gradient

I. INTRODUCTION

The use of secondary gas injection into the divergent portion of a rocket nozzle for thrust vector control has recently received considerable attention. The elimination of moving mechanical parts in contact with the hot propellant gases constitutes the main advantage of secondary injection over present methods of thrust vector control. The total side force experienced by the rocket due to secondary gas injection can be conceptually divided into two parts: that portion due to momentum reaction of the injectant and that portion due to excess pressures on the nozzle wall caused by the flow interference. It can be generally said that improvements in injectant performance are related to improvements in that portion of the force due to flow interference for a given momentum reaction force of the injectant.

Improvements in the side force due to flow interference can be obtained by contouring the rocket nozzle to exhibit adverse pressure gradient along the nozzle wall and thereby, increasing the wall pressures in the nozzle flow. In a previous program, Ref. 1, it was shown that properly designed nozzle contour can produce adverse pressure gradient on the wall without undue loss in axial thrust. It is also shown that such adverse pressure gradient nozzles provide considerable improvement in secondary injectant performance, compared to conical nozzles having the same area ratio and length.

Besides adverse pressure gradient on the nozzle wall, the flow interference can also be increased by injecting the secondary fluid through multiple ports instead of a single port. The main objective of the present

investigation is to explore the effect of multiple port injection and the influence of injection port spacing on the injectant performance. Two injector configurations are investigated, one with three radial ports and the other with two opposed-tangential ports. The intersection of the adjacent injectant flow is analyzed and appropriate injection port spacings are selected for the test program. The purpose of examining the two injector configurations is not to compare the performance of one against the other, but rather to evaluate the influence of injection port spacings in the two configurations.

The shock pattern caused by secondary injection through a single port and the basic concept of flow separation are analyzed with the aid of schlieren photographs obtained from the Jet Propulsion Laboratory of the California Institute of Technology, (JPL).

The experimental program of the present investigation consisted of cold-air flow tests on a conical nozzle and an adverse pressure gradient nozzle, to evaluate the two-injector configurations at different weight flow ratios and different injection port spacing ratios. The nozzle parameters and the contour details are given in Ref. 1. In the conical nozzle the injectors were located at a distance from the nozzle throat of 70% of the nozzle length, whereas in the adverse pressure gradient nozzle the location was at 95% of the nozzle length. For each injection port spacing and weight flow ratio, measurements were taken for the nozzle axial thrust, side force, primary flow through the nozzle, and the total injectant flow. Wall pressure measurements are taken at different axial and circumferential locations during each test run. The influence of injection port spacing on the wall pressure distributions is discussed in this report.

Because of the interest in the nozzle contours incorporating adverse pressure gradient, theoretical computation of boundary layer parameters in such nozzles are presented. The possibility of deducing flow separation criteria as influenced by boundary layer conditions is also investigated.

II.   THEORETICAL STUDIES

The theoretical studies are divided into three subsections consisting of, the selection of spacing between injection ports, analysis of single port flow interference, and boundary layer analysis. The general analyses are discussed in the subsections with detailed information given in the appendices.

A.   Selection of Spacing Between Injection Ports

An important parameter in a multiport configuration, distributed circumferentially, is the ratio of the distance between the injection port centers to the injection port diameter. To determine the magnitude of the injection port spacing for consideration in the present test program, two analytic models are postulated and analyzed.

1.   Model for Multiradial Port Configuration

The postulated model consists of two parallel jets expanding supersonically and forming two plumes of diameter d_{eff}. A hypothesis is made that when the plumes are at a critical injection port spacing the primary flow will not pass between them, forcing the primary flow over the plumes as if a step-like obstacle is placed in the primary stream. It is further hypothesized that the critical injection port spacing exists when the expanded plumes of diameter d_{eff} intersect. The detailed analysis for determining the critical injection port spacing as a function of primary and secondary stream conditions is presented in Appendix A. The main parameters are the primary stream Mach number and the ratio of the injectant static pressure to the local primary stream static pressure, p_j/p_∞.

For the present investigation, the primary stream Mach number at the point of injection is approximately 4.0 for both the APG-1 and conical nozzles. The ratio of p_j/p_∞ is varied from 50 to 150 consistent with the desired injectant flow rates. From Table III in Appendix A, the value of the critical injection port spacing ratio, c_{cr}/d_j, varies from 1.46 to about 2.0 for the present test conditions. Based on these considerations, the injection port spacing ratios, c/d_j, are selected at 1.8, 2.5, and 3.5 for the test program.

2.   Model for Opposed-Tangential Port Configuration

In the preceding model, for parallel jets, the penetration of the jets into the supersonic stream is not considered in calculating the critical injection port spacing. In the present model for opposed-tangential jets, the penetration depth is considered to be of primary importance in determining whether or not strong mutual flow interference between adjacent injection ports occurs. In order to assure strong interaction, it is postulated that the impingement should occur sufficiently close to the injection ports where the jets behave essentially as "rigid" obstacles to the primary flow. The detailed analysis is presented in Appendix B.

For the opposed-tangential port configuration used in the previous investigation (Ref. 1), the analysis indicated that the given injection port spacing ratio is critical at a weight flow ratio $\dot{w}_s/\dot{w}_p$ of 0.042 in the APG-1 nozzle. The test results presented in Ref. 1 seem to indicate that mutual flow interference occurred at $\dot{w}_s/\dot{w}_p$ of 0.06 and above.

For the present investigation, it is intended to have the critical injection port spacing ratio occur at a lower $\dot{w}_s/\dot{w}_p$ than obtained in the previous investigation (Ref. 1). The injection port spacing ratios,

therefore, are selected at 2. 1, 2. 6, and 3. 2, compared with the injection port spacing ratio of 3. 7 used in Ref. 1.

B. Analysis of Single Port Flow Interference

Analysis of flow interference in the case of multiport injection depend to a large extent on the validity of the "basic model" representing the flow interference for single port injection. Effort in this subsection is confined to checking the validity of the "basic model" representing injection through a single port.

Due to injection of a secondary fluid, an obstruction is formed in the supersonic flow in the nozzle and for single port injection, the obstruction can be assumed to exhibit axial symmetry about the undisturbed nozzle flow streamline passing through the injection port. If our attention is limited to the flow region upstream of the injection port, it is sufficient to consider the nose shape of the obstruction, ignoring the downstream behavior of the injectant. For the present purpose, it is immaterial whether the obstruction is caused by gas injection or volatile liquid injection, since the obstruction is treated as a solid body. The present analysis is limited to the possibility of predicting the shock configuration and flow separated region if the body shape is known. In the case of volatile liquid injection, it has been possible to define a representative body shape for the obstruction from schlieren photographs, whereas it has not been possible for gas injection. Recently the Jet Propulsion Laboratory, California Institute of Technology, obtained schlieren and spark shadowgraph pictures of Freon being injected from a flat plate into a supersonic stream. The details of these tests are reported in Ref. 2. Based on the obstruction, as seen from the schlieren photographs, a method of

predicting the shock configuration is formulated. The results of such predictions are verified against the shock patterns observed in the schlieren photographs.

1.   Formulation of Flow Interference Model

A study of the shock wave structure produced by the secondary injection revealed two types of pattern as shown in figures 1 and 2. In both cases, the interference pattern consists of a bow-shock wave detached from the obstruction. The difference between the two types of pattern consists of the magnitude of the separation-shock wave and its point of intersection with the bow-shock wave. The formulation of the interference model for predicting the shock wave structure consists of predicting the separation-shock wave, the bow-shock wave, and the intersection point of the separation-shock wave with the bow-shock wave.

Separation-Shock Wave - A method for predicting the shock angle consistent with boundary layer separation has been presented by Mager in Ref. 3. The analysis gave the shock angle as a function of the free stream Mach number and the specific heat ratio γ. The predicted values of shock angles of the separation-shock wave are in close agreement with the observed schlieren photographs shown in figures 1 and 2.

Bow-Shock Wave - The bow-shock wave formed by the obstruction is obtained by approximating the obstruction with a hemisphere capping a cylinder. The bow-shock wave shape is obtained using the standoff distance equation from Ref. 4 for a sphere and requiring the shock wave shape to be hyperbolic. The detailed derivations are given in Appendix C.

Intersection of Two Shock Waves - At the intersection of the
separation-shock wave with the bow-shock wave, these shock waves can
be treated locally as plane oblique shock waves. A schematic of the
shock wave intersection is shown in figure 3. Assuming the shock waves
are free to adjust themselves to satisfy the boundary conditions, namely,
they do not create a reflection wave and yet satisfy both the pressure
and flow direction across the slip stream, two solutions are found. In
the limiting case, the wave C-B in figure 3 degenerated and became a
Mach line. In the general case, the angles α_3 and α_4 are found to be

$$\alpha_3 = \sin^{-1}\left[\frac{1}{2\gamma M_2^2}\; \frac{2(\gamma+1)M_1^2 \sin^2\alpha_4 - (\gamma-1)(\gamma+1)}{2\gamma\, M_1^2 \sin^2\alpha_2 - (\gamma-1)} + (\gamma-1)\right]^{1/2}$$

$$\alpha_4 = \sin^{-1}\; \frac{1}{M_2^2} + \sigma_2$$

The detailed derivation of the above is given in Appendix C. The inter-
section point on the bow-shock wave is determined by locating a point
where the slope of the bow-shock wave is equal to the average of α_3 plus
σ_2 and α_4.

2.   Comparison of Analysis with Schlieren Photographs

        The two flow interference models, limiting and general cases,
are compared with the schlieren photographs obtained during the tests
conducted at JPL where Freon-12 was injected from a flat plate into a
uniform supersonic air stream. The comparisons are shown in figures
4 and 5. In the figures, the outline of the obstruction and the shock waves,
obtained from the schlieren photographs, are represented by dash lines.

The simplified obstruction and the shock waves predicted from theory are represented by solid lines. The obstruction and shock configuration are shown nondimensionalized by setting R_b equal to unity. The comparisons presented in figures 4 and 5 indicate that the postulated models for shock wave intersection predict the results with a fair amount of accuracy.

3. Limitations to the Analysis

The assumptions used in postulating the present flow interference model limit its usefulness at the present time. For example, the formation of a hemispherical obstruction may not always occur. Also, certain minor changes in the shape of the obstruction, not discernable in the schlieren photographs, appear to determine the nature of shock wave intersection pattern.

Criteria for Model Selection - At present there exist no criteria for selecting the proper case (limiting or general) without the help of a schlieren photograph. Indications do exist, however, that the criteria of selection should include the bluntness of the obstruction near the injection port. The two schlieren photographs presented in figures 1 and 2 were obtained for two different initial temperatures of the injectant, Freon-12. The photograph shown in figure 1 is for the case with higher initial injectant temperature of $67^{\circ}F$ illustrating a condition where the Freon-12 appears to undergo flash vaporization upon injection. The case shown in figure 2 is for Freon-12 at $-75^{\circ}F$ with flash vaporization not expected to occur upon injection. Since the volume formed by the flash vaporized Freon-12 would be larger than the second case, it appears that the limiting case should be used with the blunter obstructions.

Symmetrical Obstruction - Aside from the influence of the obstruction in determining the location of shock wave intersection, the shape of the obstruction defines the formation of the bow-shock wave pattern. It is conceivable that the injectant penetrates sufficiently into the nozzle to present an ellipsoidal obstruction to the supersonic flow. The shock wave analysis then becomes quite difficult and beyond the scope of the present postulated model.

The trend of the asymmetric bow-shock wave has been noted in Ref. 5. For gas injection from an orifice in a flat plate, information was obtained as to the location of the shock wave on the flat plate and schlieren photographs indicated the shock wave pattern in the plane of injection. This information is plotted and shown in figure 6. In this figure, the traces of the bow-shock waves in plane normal to plate (obtained from schlieren photographs) are superimposed on the locus of maximum pressure coefficient (in plane of plate, representing bow-shock wave on plate). The figure shows that as the injection rate is increased, the jet does not spread appreciably on the plate, even though the trace of the bow-shock wave (in plane normal to plate) changes appreciably, indicating jet penetration and consequent asymmetric obstruction. However, at small injection rates, the assumption of a hemispherical obstruction appears to be reasonable.

Formation of Obstruction - For the present analysis the assumption is made that the obstruction is known and can be approximated by a hemisphere of radius R_b. However, a method of predicting the shape of the obstruction as a function of injection parameters remains to be formulated. Also, the influence of the shape of the obstruction downstream

of the injector upon the bow-shock shape remains to be investigated.

C.   Boundary Layer Analysis

The effect of an adverse pressure gradient on the boundary layer parameters is investigated.   Also, a provisional separation criterion for compressible turbulent flow with no mass addition is formulated.

1.   Boundary Layer Parameters

A method for predicting the compressible turbulent boundary layer parameters was presented previously in Ref. 1.   The method consisted of solving two integral equations, one equation being the momentum integral equation and the other being an auxiliary equation which accounts for the variation of boundary layer shape factor.   This is an acceptable method when solving the turbulent boundary layer parameters for incompressible flow.   When extending this method to compressible flow by use of Stewartson's (6) and Mager's (7) transformation, however, the calculated values of shape factor are not in agreement with experimental results as shown by McLafferty and Barber (8).   The calculated values predict the shape factor increasing monotonically in the presence of an adverse pressure gradient; while the experimental results show that the shape factor first increases and then decreases.

Because of this difference between calculated and experimental values, the two-integral equation technique is discarded in favor of a single quadrature technique.   The advantage of the single quadrature technique lies in predicting the shape factor which is in agreement with experimental data in the presence of an adverse pressure gradient.   This method predicts the shape factor increasing at first and then decreasing in the

presence of an adverse pressure gradient. The detailed analysis of

the single quadrature technique is presented in Appendix D.

Using the single quadrature technique, the displacement

thickness is computed for the APG-1 nozzle and is shown in figure 7.

Also presented in figure 7 is the displacement thickness computed by

the method consisting of solving two integral equations. As pointed out

before, the displacement thickness computed by the single quadrature

method does decrease in the presence of an adverse pressure gradient.

2. Boundary Layer Separation Criterion

The provisional separation criterion for compressible turbu-

lent flow with no mass addition is formulated and programmed on the

CDC 1604 computer. The detailed derivation of the criterion is given

in Appendix E. The point of separation is found by solving the following

equation, E(18)

$$
(1 - \frac{M_e^2}{M_e^{*2}})^{\frac{m-2}{m}} \frac{d}{ds} (1 - \frac{M_e^2}{M_e^{*2}}) = \frac{\Lambda(m) (\frac{a_o R_T}{\bar{\nu}_o})^{\frac{2}{m+3}} (M_e^*)^{\frac{2}{m+3}} \omega_2}{\left[\int_0^s \omega_2 \, ds \right]^{\frac{m+1}{m+3}}} \qquad E(18)
$$

Separation should occur in the flow when the equality represented in the

above equation is satisfied.

The APG-1 nozzle used in this test program is analyzed using

the separation criterion. The wall pressure distribution computed from

inviscid flow analysis is shown in the upper half of figure 8. The results

of the left and right side of equation E(18) are shown in the lower half of

figure 8. The crossover point is found to occur at a distance of x/R_T of 10.2,

measured from the nozzle throat, indicating that separation will occur

even without secondary injection. The nozzle wall pressures measured

on the APG-1 nozzle at different operation pressure ratios λ_p, are

reproduced and presented in figure 9. Due to fabrication difficulties no

pressure taps were placed beyond x/R_T of 11.0. Even at very low ex-

haust pressure, i.e., $\lambda_p = 390$, the data scatter at x/R_T of 11.0 indicates

a local separation condition.

III. EXPERIMENTAL PROGRAM

The test program was conducted in the aerodynamic facilities (Elk River) of FluiDyne Corporation. The test models, test setup, and instrumentation were identical to that used in Ref. 1 with the exceptions described in the following subsections.

A. Test Models and Test Parameters

The APG-1 and conical nozzles, which were fabricated under the previous program, Ref. 1, are utilized for the present test program. Modification to these test nozzles are made to allow for changes in the injection port configuration. The modifications to the nozzles are shown in figures 10 and 11. The nozzles are modified to include a ring which contains the injection ports. Two sets of rings are made for each nozzle with three injection port configurations per ring, with different values of spacing between the injection ports. A photograph of the models and injection port rings are shown in figure 12.

The injection port angle in the meridional plane is set at 45° up-stream, measured from the local wall, as shown in figure 13, for both the APG-1 and conical nozzles. For the opposed-tangential port configuration the injection ports are inclined toward each other by 60°, measured from the normal to the wall as shown in figure 13. The injection port orientation is the same as used in Ref. 1. For the multiradial port configuration three ports, each with a diameter of 0.188 inches, are used. For the opposed-tangential port configuration two ports, each with a diameter of 0.188 inches, are used. The multiradial ports are oriented

with the port centerlines intersecting at the nozzle axis. The detailed orientation and spacings of the injection ports are presented in figures 14 through 17.

The injection port locations are selected at the optimum for each test nozzle based on the results of Ref. 1. The injection port location is set at $(x/L)_{inj}$ of 0.95 for the APG-1 nozzle and at $(x/L)_{inj}$ of 0.69 for the conical nozzle. The injection port location is not a parameter in the present test program.

The test parameters for the present program are shown in Tables I and II. Three injection port spacings are used for each injection port configuration. For each test condition measurements are taken at three values of injectant flow rate. In addition, at an injection port spacing the injectant flow rate is varied in small increments for investigating whether the mutual flow interference causes the side force to vary smoothly or abruptly with variation of injectant flow rate.

B.   Description of Test Facility

The test program was conducted at FluiDyne's Elk River Aero-dynamics Laboratory. This facility is equipped with an axisymmetric free-jet nozzle test stand designed for obtaining nozzle performance over a wide range of pressure ratios. The test cell is similar to the one used in Ref. 1 except it is equipped with a two-stage ejector system which allows operation over a greater range of nozzle pressure ratios. The first stage is composed of an air ejector followed by a steam ejector system for the second stage. A layout of the nozzle test facility is shown in figure 18. A photograph of the test facility during a typical run is shown in figure 19. The system is composed of a high pressure air

storage system which is throttled to 100 psia and discharged through the test nozzle into the test cell connected to a diffuser and a two-stage ejector system. The test nozzle is mounted in an assembly as shown in figure 20. The secondary air is supplied to the test nozzle assembly which forms a plenum chamber around the test nozzle. The secondary air lines are connected to both sides of the test nozzle assembly to minimize the restraining loads on the nozzle and the force balance due to the secondary air supply.

C. Instrumentation

The instrumentation used for measuring forces, flow rates, and static pressures are identical to the ones used in Ref. 1.

In addition to the locations of wall static pressure taps used in Ref. 1, ten new locations are added to the models as shown in figures 21 and 22. These new locations served to provide additional information in the separated region. Accurate values of the pressure tap locations, obtained from inspection, are shown in figures 23 through 26.

The primary and secondary flow rates are measured using metering orifices. However, in the present test program the size of the metering orifice is changed to keep the metering orifice choked at all test conditions. This is to alleviate the problem encountered in the previous test program (Ref. 1), in which the metering orifice became unchoked for certain test conditions.

The calibration and data reduction procedure are similar to the method used in Ref. 1 and are not repeated in this report.

D.   Discussion of Test Results

The analysis of the test results is presented by evaluating the influence of the injection port configuration and geometry on the secondary injectant performance. Use is also made of the wall pressure information to qualitatively substantiate the trends found in the experiment. Wherever possible, the present test data are compared with the data obtained in Ref. 1 to check for repeatability and additional comparison of the various test parameters. When data from Ref. 1 are used the notation (Ref. 1) is placed next to the symbol for identification.

The tests for the present program were all conducted at a nominal nozzle pressure ratio of 500. The effect of nozzle operating pressure ratio was not a parameter in the present test program as in the test data presented in Ref. 1. The secondary flow rates were varied in three increments for most injection port configurations which were nominally 3%, 6%, and 9% of the primary nozzle flow rate. In a few of the cases the flow rates were varied in eight increments. The compilation of the test data is presented in Appendix F.

The secondary injectant performance in this report is evaluated in terms of the amplification factor which is defined as:

$$\text{Amplification Factor} = \frac{\text{side force/vacuum axial thrust with vectoring}}{\text{injectant flow rate/primary flow rate}}$$

The magnification factor defined as:

$$\text{Magnification Factor} = \frac{\text{side force}}{\text{vacuum thrust of a sonic jet}}$$

is not used as the performance parameter since secondary pressure

measurement is not accurate. It appears that the strip-a-tubes used to connect the wall pressure taps to the manometer board have provided sufficient obstruction in the secondary manifold as to interfere with the secondary pressure measurements.

The investigation is limited to evaluating the effect of mutual flow interference in a given type of injection configuration and not the secondary injectant performance between the opposed-tangential and multiradial port injection. The comparison of the secondary injectant performance between the opposed-tangential and multiradial port injection is meaningless since the optimum injection station for the opposed-tangential port configuration is not used.

1.   Nozzle Performance with No Secondary Injection

Axial thrust data were obtained in both the conical and APG-1 nozzles with no secondary injection. For these test runs the injection ports were plugged externally and filled with wax to permit a smooth finish internally. However, one set of three injection ports machined in the interchangeable ring was not filled with wax, causing a slight asymmetry in the nozzle flow. The axial thrust data obtained in the tests were affected somewhat by the local disturbances at the unwaxed injection port.

The vacuum thrust coefficient with no secondary injection is computed from the measured thrust with the necessary correction for the ambient pressure. For the conical nozzle, the vacuum thrust coefficient is found to be 1.64 based on two test runs (4 and 36). For the APG-1 nozzle the vacuum thrust coefficient is also found to be 1.64, based on runs 18 and 54. The values obtained from Ref. 1 are 1.62 for the conical

nozzle and 1.63 for the APG-1 nozzle. The discrepancy is small and is considered to be within the experimental accuracy.

2. Single Port Injection

Single port injection performance is obtained for both the conical and APG-1 nozzles by using one port of the multiradial port configuration. The injection angle in the meridional plane is, therefore, equal to 45° measured from the local nozzle wall, similar to the value used in Ref. 1 for the meridional port injection configuration. The injection port area used in the present test program, however, is equal to one-half the injection port area used in Ref. 1.

Effect of Injection Port Diameter (Conical Nozzle) - Using the present test data and the data from Ref. 1, the effect of injection port diameter on the secondary injectant performance is presented in figure 27. Due to the low pressure ratio across the nozzle used in the tests reported in Ref. 1, no definite conclusion can be drawn as to the effect of injection port diameter.

A comparison of the wall pressure data is made in both the meridional plane of injection and at various circumferential planes, as shown in figures 28 and 29, for a nominal weight flow ratio of 3%. The nozzle wall pressure in the meridional plane (figure 28) indicates that the separation distance upstream of the injection port is greater for the smaller injection port. The greater separation distance contributes to higher interference force, which is consistent with the side force measurement. However, all of the difference in side force shown in figure 27 may not be due to interference force alone. The reaction force between the two cases may be different since the pressure ratio across the

injection port differs by a factor of two. Although the injection port has constant area, it is oriented at 45° with the local wall, which can cause the injectant to expand within the port, thereby making the reaction force a function of the pressure ratio across the injection port.

Effect of Injection Port Diameter (APG-1 Nozzle) - A comparison of the injectant performance is presented in figure 30 for the two injection port diameters obtained with the APG-1 nozzle. The results indicate that at a weight flow ratio of 3% there exists about 8% difference in amplification factor, whereas the difference is negligible at 5% weight flow ratio. Higher weight flow ratios were not employed in the present tests due to limitation on secondary pressure. A look at the nozzle wall pressures (figures 31 and 32) in the region of the injection port indicate the separated regions are the same for the two injection port diameters for the 3% weight flow ratio condition. The difference in the observed injectant performance at the 3% weight flow ratio condition must be due to the differences in the reaction force of the jet, due to changes in pressure ratio across the injection port.

Effect of Nozzle Contour - The effect of the nozzle wall pressure gradient on the injectant performance as obtained for the conical and APG-1 nozzles is shown in figure 33. At a weight flow ratio of 3% the amplification factor is about 20% higher for APG-1 nozzle with injection at $(x/L)_{inj} = 0.95$ as compared to the conical nozzle with injection at $(x/L)_{inj} = 0.69$. This is in agreement with results reported earlier in Ref. 1. For the sake of comparison, the injectant performance reported in Ref. 1 for a conical nozzle with injection at $(x/L)_{inj} = 0.95$, is also shown in the figure.

In order to make a comparison of the wall pressure distributions the pressure data from Ref. 1 is used for the conical nozzle with the same injection station, $(x/L)_{inj} = 0.95$, as is used for the APG-1 nozzle. The value of the excess pressures is plotted in figures 34 and 35. As noted in figure 34, the separated area is larger for the APG-1 nozzle, giving rise to higher interference forces and consequent increase in performance, as indicated in figure 33.

3.   Multiport Injection

Two types of multiport injection configuration are tested. The first type is called the multiradial port configuration, which consists of three ports oriented so that their centerlines intersect at the nozzle axis. The second type is called the opposed-tangential port configuration, which consists of two ports oriented so that they are opposing each other. The two types of multiport injection configuration are tested in both the conical and APG-1 nozzles.

The opposed-tangential port configuration was tested with a c/d_j of 3.7 and reported in Ref. 1. This information can, therefore, be used to supplement the present test data. The multiradial port configuration, however, was not tested in Ref. 1.

Multiradial Port Injection (Conical Nozzle) - The injectant performance for the multiradial port configuration in the conical nozzle is shown in figure 36. The results indicate that a change in injection port spacing by a factor of two does not change the amplification factor by an appreciable amount. The injectant performance is plotted in figure 37 as a function of the injection port spacing ratio. The hypothesis that a critical spacing ratio exists, giving rise to improved injectant performance,

-22-

does not appear to be borne out by the test data. However, examination of the nozzle wall pressures in the region of the injection port reveals some interesting information.

The wall pressure distribution for the case of 3% weight flow ratio indicates that as the injection ports are brought closer together, the separation distance upstream of the injection port increases, as shown in figure 38. In the circumferential plane, close to the injection port, the separated area decreases as the injection ports are brought closer together, as shown in figure 39. The wall pressure data indicate that the injectant penetrates deeper into the primary stream as the injection ports are brought closer together, which would account for the increased separation distance. Also, the curves shown in figure 39 indicate that the pressure distribution for the close injection port spacing should be similar to the data for a single port injecting the same flow rate. A comparison of the wall pressure distribution in the meridional plane for single and multiradial port injection is shown in figure 40. The curve shows the separation distance to be approximately the same in the meridional plane for the two injection port configurations. The pressure distribution in the circumferential plane far upstream is also similar, as can be seen in figure 41. However, there are some differences in wall pressure distribution close to the injection port, as can be expected. It is also interesting to note that as the separation distance is increased by decreasing the injection port spacing, the excess pressures in the region downstream of the injection port diminish and even become negative, as shown in figure 38. Since the injectant performance appears to be relatively unaffected as the injection port spacing is changed by a factor

of two, it is reasonable to conclude that the total interference force
due to the upstream and downstream disturbance is constant. However,
the pressure distribution is altered appreciably, indicating that contri-
butions due to the upstream and downstream regions change. Hence,
the optimum injection port location would be dependent upon the injection
port spacing.

As the weight flow ratio is increased to 6%, the separation
distance in the meridional plane does not change appreciably as the in-
jection port spacing ratio is decreased below 2.5, as shown in figure
42. Also, the spreading of the separated area in the circumferential
direction far from the injection port does not change as the injection port
spacing ratio is decreased below 2.5, as shown in figure 43. At 9%
weight flow ratio, the separation distance is insensitive to the injection
port spacing, which can be seen in figure 44. Also, the spreading of the
separated area in the circumferential direction becomes insensitive to
spacing at this high value of injectant flow rate, as illustrated in figure 45.

The comparison of the injectant performance for single port
and multiradial port injection, as shown in figure 36, indicates that it
is more efficient to use a multiradial port configuration than a single
port for the same total weight flow ratio. However, if the injectant per-
formance is compared on a weight flow rate per port, then the single port
has the higher efficiency. The performance of the multiradial port con-
figuration with three ports is less than three times the single port con-
figuration at one third the injectant flow rate. The wall pressure distri-
butions in the meridional plane are presented in figure 46 for the single
port configuration, with $\dot{w}_s/\dot{w}_p$ of 0.02, as compared to the multiradial

port configuration with total $\dot{w}_s/\dot{w}_p = .06$ or $\dot{w}_s/\dot{w}_p = 0.02$ on a per port basis. Although the separation distance is shorter for the single port configuration if the comparison is made on a weight flow rate per port, the total affected area for three ports would be about the same as superposing the pressure field three times. If the same injection port spacings are used in the superposition as for the multiradial port configuration, then it is clearly seen that a large portion of the disturbed pressure region is counted twice and in some regions three times. Such superposition of pressures is shown in figures 47 and 48 for two locations of the circumferential plane. If the sum of the superposed wall pressures are compared to the wall pressures for the multiradial port configuration, the former is much higher on the average. Therefore, it appears that the excess pressures and the affected area for a multiradial port configuration would always be lower than that expected from superposition of data obtainable on a weight flow rate per port basis. The side force data also shows that superposition to obtain multiport injectant performance is not applicable and leads to overestimation of its performance. In the preceding discussion no account is taken of the component loss which is incurred by the fact that the side force developed by the outer ports is not in the direction of the measured side force. This minor loss can be ignored since the maximum included angle between adjacent ports is only 20°.

Multiradial Port Injection (APG-1 Nozzle) - The injectant performance for the multiradial port configuration in the APG-1 nozzle is presented in figure 49. The injectant performance is also plotted as a function of injection port spacing ratio for weight flow ratio of 3%, 6%, and

9% and is shown in figure 50. The results indicate that the optimum injection port spacing ratio is equal to 2.9 for 3% weight flow ratio. However, an optimum injection port spacing is not found in the range used in the test for weight flow ratios greater than 6%. Although an optimum injection port spacing is found for the 3% weight flow ratio condition, the improvement in injectant performance is not appreciable. These results, along with data for the multiradial port injection in the conical nozzle, indicate that the injectant performance at a given injection port location is not a strong function of injection port spacing, although optimum location may exist which would be a function of injection port spacing.

Examination of the wall pressure distribution in the meridional plane for 3% weight flow ratio as shown in figure 51, indicates the separation distance upstream of the injection port to increase and then decrease as the injection port spacing is increased. The wall pressure distribution in the circumferential plane presented in figure 52 shows the lateral spread of separation area for different injection port spacing. The wall pressure data, therefore, show the total separated area to increase and then decrease with increasing injection port spacing. This is consistent with the side force measurements at 3% weight flow ratio presented in figure 49.

At 6% weight flow ratio, the wall pressure distribution in the meridional plane is unaffected by the change in injection port spacing, see figure 53. The wall pressure data in the circumferential plane is also similar for the three injection port spacing, see figure 54.

The wall pressure distributions for the 9% weight flow ratio are shown in figures 55 and 56. Although the separation distance for the

case with an injection port spacing ratio of 1.8 is larger, the pressures close to the injection port are much lower than the cases with increased injection port spacing. Since the side force data show negligible variation with injection port spacing, the variation in the wall pressure distribution must give the same interference force.

A comparison of the injectant performance for the single and multiradial port configuration is shown in figure 49. At a weight flow ratio of 3%, the injectant performance for the single port configuration appears as good as the multiradial port configuration. However, the injectant performance drops off more rapidly for the single port configuration as compared to the multiradial port configuration. A comparison of the wall pressure data for the single and multiradial port configuration is shown in figures 57 and 58, for 3% weight flow ratio. The wall pressure data indicate the separated area upstream of the injection port are the same for the single and multiradial port configuration.

Opposed-Tangential Port Injection (Conical Nozzle) - The injectant performance for the opposed-tangential port configuration in the conical nozzle is shown in figure 59. The results indicate no appreciable effect of injection port spacing ratio variation from 2.1 to 3.2 on the injectant performance. However, the data from Ref. 1, taken at an injection port spacing ratio of 3.7, show an appreciable performance loss as shown in figure 59. Figure 60 is presented to show the effect of injection port spacing on the amplification factor at different injectant flow rates. An increase in injection port spacing ratio beyond 3.2 causes a decrease in injectant performance.

Examination of the wall pressure distribution presented in figures 61 and 62 shows that the separated area upstream of the injection port is essentially unaffected as the injection port spacing ratio is changed from 2.1 to 3.2 for 3% weight flow ratio. Similar conclusion can be made for the 6% weight flow ratio from the pressure distributions presented in figures 63 and 64. The interference force, therefore, can be expected to be insensitive to changes in the injection port spacing ratio from 2.1 to 3.2. This deduction from the wall pressure data is consistent with the amplification factors presented in figure 59.

To investigate the reason for the injectant performance drop-off reported in Ref. 1 for the injection port spacing ratio of 3.7, the wall pressure distributions are compared for the case with 3% weight flow ratio in figures 61 and 62. The wall pressure distribution in the meridional plane is found to be similar. Therefore, the lateral spread of the affected area appears to shrink suddenly at an injection port spacing ratio of 3.7, although a definite conclusion cannot be drawn from figure 62. The drop in injectant performance may be attributed to the abrupt changes in the affected area as the injection port spacing ratio is increased from 3.2 to 3.7. Thus, it may be concluded that the critical spacing ratio for the opposed-tangential ports is between 3.2 and 3.7 at 3% weight flow ratio.

Opposed-Tangential Port Injection (APG-1 Nozzle) - The injectant performance for the opposed-tangential port configuration in the APG-1 nozzle is shown in figure 65. No appreciable change in injectant performance is noted as the injection port spacing ratio is changed from 2.1 to 3.2. However, the injectant performance data from Ref. 1

at an injection port spacing ratio of 3.7 varies appreciably from the present test results. The injectant performance from present tests is also plotted in figure 66 as a function of injection port spacing ratio for weight flow ratio of 3%, 6%, and 9%. Due to the unusual behavior found in the data from Ref. 1 no definite conclusion can be reached as to the optimum injection port spacing.

In order to understand the trends found in Ref. 1, the wall pressure distributions at 9% weight flow ratio are plotted in figures 67 and 68 for the injection port spacing ratios of 2.1 and 3.7. The wall pressure data appear quite similar for the two case. The difference in the side force, as shown in figure 65, for the two cases is probably due to the affected area downstream of the injection port. Since the test reported in Ref. 1 was conducted at low nozzle pressure ratios, a possibility exists that the region downstream of the injection port, which is usually at very low pressure, was fed with high ambient pressure. This condition could account for the injectant performance at the 9% weight flow ratio condition reported in Ref. 1.

Examination of the wall pressure distribution presented in figures 69 and 70 for 3% weight flow ratio show that the separated area upstream of the injection port is essentially unaffected as the injection port spacing ratio is changed from 2.1 to 3.2. Similar conclusions can be made for the 6% weight flow ratio condition from the pressure distributions presented in figures 71 and 72. The wall pressure data is, therefore, consistent with the amplification factors presented in figure 65.

A close examination of the injectant performance shown in figure 65 at an injection port spacing ratio of 2.1 indicates abrupt performance loss beyond a weight flow ratio of 6%. Examination of the wall

pressure distributions in the meridional plane shown in figure 73 for 5%, 6%, and 7% weight flow ratios do not indicate any appreciable changes in the separated area and pressures upstream of the injection port. The amplification factor variation observed for the injection port spacing of 2. 1 cannot be explained with the present wall pressure data. At the other values of injection port spacing ratios, the weight flow ratio increments are not close enough to indicate such phenomena.

IV.   CONCLUDING REMARKS

A.   The following conclusions can be drawn from the results
of the investigation presented here.

1.   The injectant performance for the multiradial port
configuration is significantly better than for the single port
configuration in both the conical and adverse pressure grad-
ient nozzles.

2.   The amplification factor at any fixed weight flow
ratio is found to increase with increasing injection port spacing
for the multiradial port configuration in the conical nozzle,
within the injection port spacing ratios investigated.

3.   For 3% weight flow ratio through the multiradial
port configuration located in the APG-1 nozzle, optimum inject-
ant performance is obtained at an injection port spacing ratio
of 2.9.   At 6% and 9% weight flow ratios the injectant perform-
ance increased with injection port spacing, within the injection
port spacing ratios investigated.

4.   The relative contribution to the side force by the
excess pressure regions upstream and downstream of the injec-
tion port appear to be greatly affected by the injection port
spacing.

5.   As indicated by wall pressure measurements, the
flow interference pattern is altered considerably by varying
the injection port spacing without discernable effect on the total
side force.

6.   Considerable improvement in the injectant performance is realized in the adverse pressure gradient nozzle compared to the conical nozzle. This result, observed for multiradial port injection, is in agreement with the data previously reported in Ref. 1 for single port injection.

7.   Both in the APG-1 nozzle and the conical nozzle, injection through opposed-tangential ports did not show the influence of injection port spacing within the range of injection port spacing ratios investigated.

8.   With increasing weight flow ratios the amplification factor decreased both in the case of opposed-tangential injection and multiradial port injection. Both in the APG nozzle and the conical nozzle, amplification factors obtained with multiradial port injection are higher than those obtained with opposed-tangential injection located at the same station. Comparison with the data presented in Ref. 1, for different axial locations, showed that opposed-tangential injection performance can be improved to approach that of multiradial ports by appropriate selection of injection stations.

B.   The desirability of multiport injection is evident from the consideration of structural design problems and possible thrust performance losses associated with a single large injection port required for thrust vector control by gaseous injection. Furthermore, the results presented here have established the injectant performance gain obtained by utilizing multiport injection. Due to the considerable shift in the wall pressure distributions, dependent upon the injection port spacing, the

optimum axial location for the multiport injection is expected to be up-stream of the location employed in the present investigation.

To fully realize the advantage of multiport injection, it is recommended that the optimum location for the multiport injection be investigated. Such an investigation should also take into account the dependence of the optimum location on the number of ports and the spacing between the ports.

APPENDIX A

MULTIPORT INTERFERENCE EFFECTS WITH
GASEOUS INJECTION INTO A SUPERSONIC STREAM

The following study presents a preliminary model of multi-port jet interference effects for the semi-empirical description of critical injection port spacing whereby the performance of secondary gaseous injectant in TVC can be improved.

The model employed envisages that the supersonic expansion of the injectants leads to impingement of the expanding jets resulting in a step-like obstacle to the main flow. The critical injection port spacing c_{cr} for the occurrence of impingement is determined in terms of fluid data pertaining to the primary and secondary flows. An order-of-magnitude check is obtained with experimental data on multiport interference resulting in enhancement of TVC side force.

A.   Model of Multiple-Jet-Interaction in Supersonic Primary Stream

If interaction occurs, the flow field obtained is that due to a two-shock system as described in Ref. 9. The injected jets expand into the effective pressure field, p_{eff}, just downstream of the shock system. If the jet pressure is p_j at the injection port of diameter d_j, the supersonic expansion of an individual jet into the pressure p_{eff} would result in a change of jet diameter from d_j at p_j to d_{eff} at p_{eff} where $(d_{eff}/d_j)^2$ can be estimated from one-dimensional compressible flow formulas.

In the model under consideration it is assumed that interference between jets occurs if the expanded jets of diameter d_{eff} intersect. Thus, if the injection ports are distributed along a line normal to the flow direction, interference occurs if the injection port spacing, c, is less than a critical distance

$$c_{cr} = d_{eff} \qquad\qquad A(1)$$

Under these conditions, the linear distribution of jets constitutes a "forward-facing step" at the wall boundary of the primary flow. The p_{eff} resulting from the two-shock system associated with the "step" is readily estimated in terms of the primary free stream data, p_{∞}, M_{∞}, γ. As noted above, the calculation of d_{eff} or c_{cr} in terms of p_{eff} and the secondary injectant gas parameters d_j, p_j, γ_j, is readily accomplished by one-dimensional compressible flow formulas.

For a finite number of interacting jets, the critical injection port spacing is anticipated to be somewhat smaller than c_{cr} based on the model of the forward facing step. Thus, the c_{cr} estimated in this analysis is an upper limit of the critical injection port spacing for the design of interacting injectant ports.

B.   Effective Pressure Relation

The calculation of p_{eff} in a two-shock system is conveniently discussed with the aid of figure 74. It is well known that the jet issuing from the wall into the supersonic flow stream obstructs the flow in a manner resembling that due to a solid insert. In such a case the main stream is deflected through an angle σ_2 by means of

an oblique shock, across which the pressure ratio can be estimated
by the empirical relation

$$\frac{P_2}{P_\infty} = 1 + \frac{\gamma}{2} M_\infty^2 \left[\frac{3.2}{8 + (M_\infty - 1)^2} \right] \qquad A(2)$$

based on the results of Ref. 10. This result is valid only for $\gamma = 1.4$
(i. e. , for diatomic gases such as air), but more general semi-
empirical results of this type can be obtained for arbitrary γ on the
basis of calculations in Ref. 3.

If under the deflection σ_2 the flow reattaches itself to the body
so that the flow direction is tangent to the radius of curvature of the
body at reattachment, then the flow is not deflected a second time.
However, if the body projects sufficiently far into the mainstream,
a second flow deflection occurs under a second oblique shock as
shown in various experimental observations (e. g. Ref. 5, 9). We
postulate that the injected jet in thrust vectoring application gener-
ally results in such a two-shock system, as sketched in figure 74.
Thus, the P_2 and M_2 obtained after the first shock is assumed to
undergo a second oblique shock leading to the effective pressure,
P_{eff}, given by appropriate application of equation A(2):

$$\frac{P_{eff}}{P_2} = 1 + \frac{\gamma}{2} (M_2)^2 \left[\frac{3.2}{8 + (M_2 - 1)^2} \right] \qquad A(3)$$

The pressure, P_{eff}, calculated by means of equations A(2) and A(3),
is therefore the local pressure into which the secondary jet expands.

The data p_2/p_∞, and M_2 vs. M_∞ required in the calculations for p_{eff} based on equations A(2), A(3) and oblique-shock charts in Ref. 11 are shown here in figure 75 for $\gamma = 1.4$. The corresponding data for $\gamma = 1.2$, based on Ref. 3 and 11 are shown here in figure 76.

C. Expansion of the Secondary Jet

The expansion of the secondary jet is calculated from the well known formula (Ref. 12) for isentropic flow relating the cross section A to the sonic cross section A_T in one-dimensional flow:

$$\frac{A_T}{A} = \left[\frac{2}{\gamma_j - 1} \left(\frac{\gamma_j + 1}{2} \right)^{\frac{\gamma_j + 1}{\gamma_j - 1}} \right]^{\frac{1}{2}} \left(\frac{p}{P_j} \right)^{\frac{1}{\gamma_j}} \left[1 - \left(\frac{p}{P_j} \right)^{\frac{\gamma_j - 1}{\gamma_j}} \right]^{\frac{1}{2}} \qquad A(4)$$

where P_j is the total pressure of the secondary jet.

With sonic injection, therefore, equations A(2), A(3) and A(4) lead to

$$\frac{d_{eff}}{d_j} = \left[\frac{\dfrac{\gamma_j - 1}{\gamma_j + 1} \left(\dfrac{P_\infty}{P_{eff}} \right)^{\frac{2}{\gamma_j}} \left(\dfrac{P_j}{P_\infty} \right)^{\frac{2}{\gamma_j}}}{1 - \dfrac{2}{\gamma_j + 1} \left(\dfrac{P_{eff}}{P_\infty} \right)^{\frac{\gamma_j - 1}{\gamma_j}} \left(\dfrac{P_\infty}{P_j} \right)^{\frac{\gamma_j - 1}{\gamma_j}}} \right]^{\frac{1}{4}} \qquad A(5)$$

where p_j is the static pressure at the sonic injection port, i.e., from the compressible flow relations Ref. 12, p_j is related to the total pres-

-38-

sure P_j by

$$P_j = P_j \left(\frac{\gamma_j + 1}{2}\right)^{-\frac{\gamma_j}{\gamma_j - 1}}$$ A(6)

D.   Critical Injection Port Spacing Ratio

The results calculated for $c_{cr} = d_{eff}$ by means of equation A(5) are obtained as follows. The required ratio

$$\frac{P_{eff}}{P_\infty} = \left(\frac{P_{eff}}{P_2}\right) \cdot \left(\frac{P_2}{P_\infty}\right)$$ A(7)

is determined by calculation of the right hand term involving the factors given by equations A(2) and A(3) which can readily be obtained from figures 75 and 76 for $\gamma = 1.4$ and $\gamma = 1.2$, respectively, over a range of free stream Mach number $M_\infty = 2, 3, 4$. Next, we calculate $\frac{d_{eff}}{d_j}$ for a range of p_j/p_∞, with M_∞ as a parameter implicit in P_{eff}/P_∞. Thus, in view of equation A(1) the results obtained for the critical injection port spacing are expressed over the range $5 \leq p_j/p_\infty \leq 100$, $2 \leq M_\infty \leq 4$ with $\gamma = 1.2$ and 1.4 as shown in table III. The blank spaces correspond to subcritical pressures P_j relative to P_{eff}.

E.   Comparison With Experimental Data

The principal published data which provides evidence of multiport interference effects is that reported by Rodriguez in Ref. 13. Air-to-air injection through a twenty-port sonic injection system $(d_j = .094$ in.$)$, extending over a circumferential arc of 3.54 in.

yielded a side-force enhancement of about 50 percent (figures 20 and 21 of Ref. 13) corresponding to an 80 percent enhancement of the induced side force (figure 26 of Ref. 13). These results are obtained in a 16:1 bell nozzle at an expansion ratio of AR = 14.9.

From the port configuration data the injection port spacing ratio is

$$\frac{c}{d_j} = \frac{3.54/20}{.094} = 1.88$$

Inasmuch as no details are given as to the local Mach number of free stream pressure, we estimate these from data for conical nozzle at AR = 14.9:

$$M_\infty = 4.4; \ \frac{P_\infty}{P_c} = .004$$

It is further indicated in Ref. 13 that both primary and secondary injection are obtained from the same supply tank; therefore, we assume $P_c \stackrel{\sim}{=} P_j$; and since $p_j/P_j = .528$, we estimate

$$p_j/p_\infty \stackrel{\sim}{=} \frac{.528}{.004} = 132$$

It is clear that the extrapolation of the calculated data for $\gamma = 1.4$ to $M_\infty = 4.4$ and $p_j/p_\infty = 132$ leads to a slightly higher value of c_{cr}/d_j than c/d_j employed in the experiment which yielded strong interference effects. The close agreement obtained here must be qualified by noting that a) the model employed is greatly simplified, and b) the use of conical nozzle flow data and assumption regarding $P_c \stackrel{\sim}{=} P_j$ are not strictly accurate. However, the order of magnitude

agreement indicates that the model employed is plausible for predicting

trends of the multiport interference effect with variation of fluid and

injection parameters.

APPENDIX B

MULTIPORT INTERFERENCE EFFECTS WITH GASEOUS INJECTION INTO A SUPERSONIC STREAM FOR ARBITRARY INJECTOR ANGLES

In Appendix A a semiempirical formula is given for the critical injection port spacing required to achieve multiport interference effects with gaseous injection normal to the wall. The following analysis is a generalization of the critical injection port spacing formula applicable to pairs of impinging gaseous injectant jets.

A. Model

For the previously considered parallel jets (Appendix A) it is postulated that the critical injection port spacing c_{cr} which produces interference is determined by the following requirement: the jets which enter (with sonic speed at pressure p_j) through the ports of diameter d_j expand to diameter d_{eff} by one-dimensional isentropic expansion process across the pressure ratio p_j/p_{eff}, where p_{eff} is the ambient local pressure resulting from a two-step shock deflection of the main flow by the jets. The injection port spacing $c = c_{cr} = d_{eff}$, which assures contact between the expanding jets is the critical value which causes interference. The penetration of the jets into the supersonic stream did not enter into consideration in calculation of c_{cr}.

In the present model for impinging jets the penetration depth is of primary importance in determining whether or not strong interference between adjacent injection ports occurs. To be sure, opposed jets,

although more or less deflected by the main flow, will to some extent impinge sufficiently far downstream from the injection port sites. In order to assure strong interaction, it is necessary that the impingement shall occur sufficiently close to the injection ports where the jets behave essentially as "rigid" obstacles to the main flow. A criterion for characterizing the portion of the injected jet as "rigid" can be formulated on the basis of the jet configuration analyzed in Ref. 14. In particular, the latter reference describes the trajectory of the median element in the deflected jet; and the coordinates x_c, y_c of the median element which define the termination of the "rigid" portion of the jet can be estimated on the basis of concepts relevant to the model of Ref. 14. The coordinate y_c in effect defines the penetration distance of the jet injected into the main stream.

In order to utilize the developments of Ref. 14 in application to impinging jets we consider, with the aid of figure 77, the kinematics of a jet injected with arbitrary velocity vector $\vec{q}_j$ into the supersonic stream of velocity $\vec{q}_\infty$. The orthogonal coordinate system, ξ, η, ζ shown in figure 77 is oriented so that ζ is along $\vec{q}_\infty$, and the ξ, ζ plane coincides with the wall. The components of $\vec{q}_j$ are in general, $q_{j,\xi}$, $q_{j,\eta}$, $q_{j,\zeta}$. The trajectory of the deflected-jet median lies in a plane, the x-y plane containing the vectors $\vec{q}_\infty$, $\vec{q}_j$. The x-y plane, therefore, forms a dihedral angle β_ξ with the wall

$$\beta_\xi = \tan^{-1} \frac{q_{j,\eta}}{q_{j,\xi}} \qquad\qquad B(1)$$

The contrastream direction of q_j is specified by the angle

$$\beta_y = \tan^{-1} \frac{-q_{j,\zeta}}{q_{j,\eta}} \qquad\qquad B(2)$$

which, together with β_ξ completely define the direction of q_j.

The trajectory of the median in the x-y plane is described by orienting the y axis along the stream direction and taking the origin x = 0 to coincide with the injection port center, as sketched in figure 78. The following features of the expanding jet are further illustrated in this figure. Immediately upon injection the jet expands from diameter d_j to diameter $d_{eff} = 2b$, corresponding to a pressure ratio of p_j/p_{eff}, according to Appendix A. Subsequently, the jet median, shown in figure 78 by the dotted curve, deflects under the aerodynamic forces as described in Ref. 14. However, the jet boundary remains coaxial with the median at the constant value of the jet diameter 2b. This assumption implies that the pressure in the neighborhood of the jet does not differ greatly from p_{eff} in case of strong multiport interaction. (For the single-jet analysis of Ref. 14, the decreasing strength of the bow shock around the entry jet resulted in an elliptical rather than a circular cross section of the deflected jet.) Another special assumption relates to the determination of the penetration depth or of the boundary which divides the jet into the upstream "rigid" portion and the downstream strongly deflected portion. The "rigid" jet is assumed to terminate at the median coordinates x_c, y_c shown in figure 78 which, as indicated in the figure, is obtained by the intersection of the median trajectory

$$y = y (x, M_\infty, p_\infty, p_j \cdots \beta_y) \qquad\qquad B(3)$$

and the dashed line C C

$$y = (x = b) \cot \beta_y \qquad\qquad B(4)$$

The latter is parallel to velocity vector $\vec{q}_j$ and is displaced an amount

$x = b$, downstream of the injection port center. The coordinate y_c ob-

tained by simultaneous solution of equations B(3), B(4) is thus, by definition,

an effective penetration depth.

Finally, we note the relation between β_η in equation B(2) and β_y

in equations B(3) and B(4). The angle β_η refers to the ξ, η, ζ coordinate

system introduced in this analysis. The angle β_y refers to the x-y plane

employed in the analysis of the median trajectory (Ref. 14). With the

aid of figure 77 it is readily shown that

$$\tan \beta_y = \tan \beta_\eta \cdot \sin \beta_\xi \qquad\qquad B(5)$$

The injection port interference criterion for impinging jets can now be

formulated with the aid of the sketch in figure 79 as follows. Figure 79

shows the aspect of the single jets seen by viewing along the primary

stream direction. Impingement occurs at point P. The separation param-

eter c is defined, in this case, as the chord between port centers. It is

then postulated that if the intersection point P is in the "rigid" portion

of the jet, injection port interference effects will be produced and, con-

versely, figure 79 shows impinging jets at the threshold of interference

with $c = c_{cr}$. Thus, we infer with the aid of figure 79

$$c_{cr} = 2y_c \cos \beta_c + 2b \sin \beta_c \qquad\qquad B(6)$$

where β_c is the angle between the injection vector and the chord. Since,

in practical cases, the local nozzle radius is far greater than the chord

length c, the angle β_c is practically equal to the angle β_ξ contained between the injection vector and the local nozzle-wall tangent plane.

B. Critical Port Spacing Ratio

The coordinates of any point traced by the jet median in the x-y plane are given by the parametric equations of Ref. 14 as

$$\frac{x_c}{d_j} = \frac{2b}{d_j} \left[\frac{9\pi}{64} + \left(\frac{\gamma+1}{\gamma-1}\right) \frac{3\pi}{8\left(\frac{P_{eff}}{P_\infty}-1\right)} \left(\frac{2\gamma}{\gamma+1} \left\langle\frac{P_j}{P_\infty}\right\rangle^{\frac{\gamma-1}{\gamma}} - 1 \right)\left(\frac{1}{\sin\phi \cos\beta_y}\right) \right] \left(\cos\beta_y - \sin\phi\right)$$

B(7)

$$\frac{y_c}{d_j} = \frac{2b}{d_j} \left[\left(\frac{\gamma+1}{\gamma-1}\right) \frac{3\pi}{16\left(\frac{P_{eff}}{P_\infty}-1\right)} \left(\frac{2\gamma}{\gamma+1} \left\langle\frac{P_j}{P_\infty}\right\rangle^{\frac{\gamma-1}{\gamma}} - 1 \right)\ln\frac{1+\cos\phi}{1-\cos\phi}\cdot\frac{1+\sin\beta_y}{1-\sin\beta_y} + \frac{9\pi}{64}(\cos\phi+\sin\beta_y) \right]$$

B(8)

In these expressions,

$$\frac{2b}{dj} = \left[\frac{\left(\frac{2}{\gamma+1}\right)^{\frac{\gamma+1}{\gamma-1}} \left(\frac{P_j}{P_{eff}}\right)^{\frac{\gamma+1}{\gamma}}}{\frac{2}{\gamma-1}\left(\left\langle\frac{P_j}{P_{eff}}\right\rangle^{\frac{\gamma-1}{\gamma}}-1\right)} \right]^{1/4}$$

is the ratio of the expanded jet diameter $d_{eff} = 2b$ to the port diameter d_j and ϕ is the angle between a tangent line to the median and q_∞. Solution of these equations, in conjunction with the previously established relation

$$y_c = (x_c - b) \cot \beta y$$

enable us to calculate the penetratration distance, y_c/d_j, as a function of the variable parameters M_∞, P_j/p_∞ and βy.

Figure 80 shows the dependence of penetration distance on free stream Mach number. It can be seen that the secondary jet penetrates further into the primary stream at the higher Mach numbers if the stagnation pressure ratio, P_j/p_∞, is maintained invariant. Figure 81 shows that the penetration distance at a constant Mach number increases with pressure ratio P_j/p_∞. Figure 82 shows that the penetration distance is maximized when injection is normal to the primary flow direction.

The critical injection port spacing ratio is shown in figure 83 as a function of port inclination angle β_ξ for various stagnation pressure ratios. Presumably, the widest spacing is desirable to provide the maximum blockage of the main stream flow. The widest spacing is given by the relation

$$\tan \beta_\xi = \frac{b}{y_c} \tag{B(9)}$$

which results from differentiation of the equation for the injection port spacing ratio previously given. This maximum is shown as a dashed line in figure 83.

As seen in figure 83 the variation of the injection port spacing ratio with β_ξ is relatively weak. Therefore, by use of equation B(9) in equation B(6) one obtains the following approximate formula in which β_ξ does not appear explicitly:

$$c \simeq 2b \sqrt{1 + \left(\frac{y_c}{b}\right)^2} \tag{B(10)}$$

In order to compare the latter with the criterion $c \stackrel{\sim}{=} d_{eff}$ reported

earlier, we put equation B(8) in the form

$$c = d_{eff} \sqrt{1 + \left(\frac{2y_c}{d_{eff}}\right)^2} \qquad\qquad B(11)$$

and note that since the penetration depth y_{eff} is generally of the order

of d_{eff}, the impinging jet spacing for strong port interaction is typically

twice as large as that for parallel injectant jets.

The results of tests of a configuration such as is considered here

are reported in Ref. 1. The two sonic ports had a spacing ratio of

3.9 and were inclined 30° toward each other and 45° upstream. This

point is spotted on figure 83. According to the present analysis, the

critical spacing ratio would occur at a mass flow ratio, $\dot{w}_s/\dot{w}_p$, of

.0425. In other words, at lower secondary flow rates, impingement

of the jets would not occur with the given injection port spacing ratio.

The tests were conducted at mass flow ratios of .03, .06, and .09.

The results of the tests are reproduced in figure 84. Note that for

meridional injection, the trend is for the side force to decrease con-

tinuously as the mass flow ratio is increased. On the other hand, the

side force produced by tangential opposed jets decreases at low mass

flow rates when the secondary flow is increased, reaches a minimum,

and subsequently increases. It can be postulated that the increase in

side force begins when the secondary flow rate is great enough to cause

impingement of the two jets. This critical mass flow ratio is seen to be

.06 from the test results, although intermediate data at points between

.03 and .06 were not taken. Based upon these meager results, we can conclude that the present analysis may be used to calculate injection port spacings for test models and to estimate optimum injectant parameters.

APPENDIX C

ANALYSIS OF SINGLE PORT FLOW INTERFERENCE
WITH SECONDARY INJECTION

The analysis of single port flow interference with secondary injection has received considerable attention in recent years. However, many of the models formulated for the flow interference analysis do not appear to agree with the shock wave structures visualized from schlieren photographs and spark shadowgraphs.

The analysis in this study is confined to predicting the shock wave structure produced by the secondary injectant if the shape of the obstruction made by the injectant is known. For the present purpose, is is immaterial whether the obstruction is formed by gas injection or volatile liquid injection and it can be treated as a solid body obstruction. In the case of gas injection, it has not been possible to define a representative body shape for the obstruction from schlieren photographs. Therefore, the injection of volatile liquid is used to formulate the model since the obstruction can be seen on a schlieren photograph. The following model is based on schlieren and spark shadowgraph pictures obtained during freon injection tests conducted at Jet Propulsion Laboratory, California Institute of Technology. The details of these tests are given in Ref. 2.

A.   Formulation of Single Port Flow Interference Model

A study of the shock wave structure produced by the secondary injection revealed two types of pattern as shown in figures 1 and 2. In both cases, the interference pattern consisted of a bow-shock wave detached from the obstruction with an attendant shock wave formed by the boundary layer separation ahead of the obstruction. The difference between the two types consisted of the magnitude of the separation-shock wave and its point of intersection with the bow-shock wave. The formulation of the interference model for predicting the shock wave structure consisted of predicting the separation-shock wave, the bow-shock wave, and the intersection point of the separation-shock wave with the bow-shock wave.

1.   Separation-Shock Wave

A method for predicting the shock angle formed by boundary layer separation has been presented by Mager in Ref. 3. The analysis gave the shock angle as a function of the free stream Mach number and γ. The analysis predicts the shock angle of the separation-shock wave of figures 1 and 2 very well.

2.   Bow-Shock Wave

The bow-shock wave formed by the obstruction is obtained by approximating the obstruction with a hemisphere capping a cylinder.

Since the obstruction is a blunt-nosed shape, the detached bow-shock wave can be located with good accuracy by replacing the obstruction by a corresponding sphere of the same radius (see

figure 85). Let R_b be the radius of this sphere. At $y = 0$ the standoff distance Δ_o is approximately the difference between the shock wave curvature R_{sh} at the nose and the body radius R_b, i.e.,

$$R_{sh} - R_b = \Delta_o \text{ at } y = 0 \qquad\qquad C(1)$$

R_{sh} and Δ_o can be expressed in terms of R_b and the density ratio ϵ by the above relation and the constant density approximation theory (Ref. 4). The constant density approximation theory is used to obtain Δ_o since the value of Δ_o can be obtained analytically. Also, the value of Δ_o agrees very well with the experimental data down to a free stream Mach number of 2. 0. The relationships can be written as

$$R_{sh} = \left[\frac{1 + \sqrt{\frac{8\epsilon}{3}}}{1 + \sqrt{\frac{8\epsilon}{3}} - \epsilon} \right] R_b \qquad\qquad C(2)$$

and

$$\Delta_o = \frac{\epsilon R_b}{1 + \sqrt{\frac{8\epsilon}{3}} - \epsilon} \qquad\qquad C(3)$$

where

$$\epsilon = \frac{(\gamma - 1) M_1^2 + 2}{(\gamma + 1) M_1^2} \qquad\qquad C(4)$$

γ is the specific heat ratio, and M_1 is the free stream Mach number.

In the usual supersonic flow region, it is a good approximation to use the hyperbolic equation to represent the bow-shock wave. The asymptotes of the hyperbola are equal to the free

stream Mach wave. Therefore, by knowing the free stream condition and the radius of curvature of the shock wave at its nose, one can uniquely determine this hyperbola.

Let the hyperbolic equation be

$$y^2 = C_1 x^2 - C_2 \qquad\qquad C(5)$$

then its asymptotes are

$$y = \pm C_1 x.$$

Now, let the Mach wave angle be α, then

$$\sin^2 \alpha = \frac{1}{M^2}$$

and

$$\tan^2 \alpha = \frac{1}{M^2 - 1} = \frac{1}{\beta_M^2}$$

where $\beta_M = \sqrt{M^2 - 1}$. The constant C_1 is, therefore, equal to $1/\beta_M^2$. The radius of curvature of an arbitrary curve is given by

$$R = \frac{\left[1 + (\frac{dy}{dx})^2 \right]^{\frac{3}{2}}}{\frac{d^2 y}{dx^2}} \qquad\qquad C(6)$$

Now, $y^2 = \frac{1}{\beta_M^2} x^2 - C_2$; differentiating twice, one obtains

$$(\frac{dy}{dx})^2 + y \frac{d^2 y}{dx^2} = \frac{1}{\beta_M^2}$$

A further manipulation gives

$$\frac{d^2 y}{dx^2} = \frac{-C_2}{\beta_M^2 y^3}$$

By equation C(6) and substituting negative R_{sh} for R due to the fact that they are in the other side of the curve, one obtains

$$R_{sh} = \frac{1}{C_2} \left[\beta_M^{\frac{4}{3}} y^2 + \beta_M^{-\frac{8}{3}} x^2 \right]^{\frac{3}{2}}$$

The value of R_{sh} which is of interest is at y = 0, so that

$$R_{sh} = \frac{1}{C_2} \left[\beta_M^{-\frac{8}{3}} x^2 \right]^{\frac{3}{2}}$$

Therefore, C_2 can be determined. The final equation for the hyperbola is

$$y^2 = \frac{1}{\beta_M^2} x^2 - \beta_M^2 R_{sh}^2 \qquad\qquad C(7)$$

Hence one can determine the origin of the coordinates and the shock wave position as shown in figure 86.

The shock wave caused by the boundary layer separation has been assumed in our previous analysis to be a function of free stream Mach number only (Ref. 3 and 15). This shock wave is either a conical or a plane oblique shock wave, depending on whether the injection port is a circular shape or a long slot. This shock wave will hit the bow-shock wave ahead of the blunt-nosed body. The bow-shock wave actually will change its shape and shift

its location by the boundary layer separation and the separation-shock wave. If the separation region is small, the change of the bow-shock wave is relatively small, because the local shape of the nose is not a critical factor in determining the shock shape and location. Furthermore, in the Mach number range of interest the shift of the bow-shock wave by using the free stream condition or the condition after an oblique shock wave is quite small. Therefore, within the accuracy of our approximation this shift can be neglected.

3. Intersection of Two Shocks

The intersection of the separation-shock wave with the bow-shock wave is treated locally as a plane oblique shock wave. A schematic of the intersection of the shock wave is shown in figure 3. Assuming the shock waves are free to adjust themselves to satisfy the boundary conditions, namely, it does not create a reflection wave and yet satisfies both the pressure and flow direction, the following analysis can be made.

As shown in figure 3, the flow field can be divided into four regions. Locally, these shock waves can all be treated as plane oblique shock waves. Employing the conditions of Ref. 3 and 15, the first shock wave angle α_2 is fixed along with the flow direction σ_2. The boundary conditions are

$$P_4 = P_3$$

$$\sigma_4 = \sigma_2 + \sigma_3$$

C(8)

Using the oblique-shock wave relation

$$\frac{P_2}{P_1} = \frac{2\gamma \ M_1^2 \sin^2 \ \alpha_2 - (\gamma - 1)}{\gamma + 1}$$

<div align="right">C(9)</div>

$$\cot \ \sigma_2 = \tan \ \alpha_2 \left[\frac{(\gamma + 1) \ M_1^2}{2 \ (M_1^2 \sin^2 \ \alpha_2 - 1)} - 1 \right]$$

and equations C(8) and C(9), one obtains

$$2\gamma \ (\gamma + 1) \ M_1^2 \sin^2 \ \alpha_4 - (\gamma - 1) (\gamma + 1) =$$

<div align="right">C(10)</div>

$$\left[2\gamma \ M_1^2 \sin^2 \ \alpha_2 - (\gamma - 1) \right] \left[2\gamma \ M_2^2 \sin^2 \ \alpha_3 - (\gamma - 1) \right]$$

and

$$\cot^{-1} \left[\tan \ \alpha_4 \left(\frac{(\gamma + 1) \ M_1^2}{2 \ (M_1^2 \sin^2 \ \alpha_4 - 1)} - 1 \right) \right] =$$

$$\cot^{-1} \left[\tan \ \alpha_3 \left(\frac{(\gamma + 1) \ M_2^2}{2 \ (M_2^2 \sin^2 \ \alpha_3 - 1)} - 1 \right) \right] +$$

<div align="right">C(11)</div>

$$\cot^{-1} \left[\tan \ \alpha_2 \left(\frac{(\gamma + 1) \ M_1^2}{2 \ (M_1^2 \sin^2 \ \alpha_2 - 1)} - 1 \right) \right]$$

where

$$M_2^2 = \frac{(\gamma + 1)^2 \ M_1^4 \sin^2 \ \alpha_2 - 4 \ (M_1^2 \sin^2 \ \alpha_2 - 1) \ (\gamma \ M_1^2 \sin^2 \ \alpha_2 + 1)}{\left[2\gamma \ M_1^2 \sin^2 \ \alpha_2 - (\gamma - 1) \right] \left[(\gamma - 1) \ M_1^2 \sin^2 \ \alpha_2 + 2 \right]}$$

<div align="right">C(12)</div>

Hence, one can solve for α_3 and α_4.

Usually α_4 is very close to $\alpha_3 + \sigma_2$. For our purposes, to locate this intersection point on the bow-shock wave, an average value of α_4 and $\alpha_3 + \sigma_2$ is used and is denoted as α_{3-4}. The tangent point on the hyperbola can be obtained by differentiating equation C(7); it is

$$\frac{dy}{dx} = \frac{1}{\beta_M^2} \frac{x}{y} = \tan \alpha_{3-4}$$

Now, eliminating x by the original equation, one obtains the y coordinate in terms of its tangent, i.e.,

$$y = \frac{\beta_M R_{sh}}{\left[\beta_M^2 \frac{dy^2}{dx} - 1\right]^{1/2}} \qquad\qquad C(13)$$

Once the angle α_{3-4} is known its tangent is known and, therefore, the intersection point is located. Furthermore, since the separation-shock wave angle α_2 is known the starting separation point can be located.

In solving for α_3 and α_4 explicitly, the following results are obtained. It is found from the analysis, that two solutions exist. The first solution is obtained where wave B-C in figure 3 degenerated and became a Mach line and is called the limiting case. Then

$$\alpha_4 = \alpha_2 \qquad\qquad C(14)$$

$$\alpha_3 = \sin^{-1} \frac{1}{M_2^2} \quad \text{(Mach wave)} \qquad\qquad C(15)$$

In the more general case, the value of α_3 and α_4 is equal to the following

$$\alpha_4 = \sin^{-1} \frac{1}{M_2^2} + \sigma_2 \qquad \qquad \text{C(16)}$$

$$\alpha_3 = \sin^{-1} \left[\frac{1}{2\gamma \ M_2^2} \left(\frac{2(\gamma + 1) \ M_1^2 \sin^2 \alpha_4 - (\gamma - 1)(\gamma + 1)}{2\gamma \ M_1^2 \sin^2 \alpha_2 - (\gamma - 1)} + (\gamma - 1) \right) \right]^{\frac{1}{2}} \qquad \text{C(17)}$$

APPENDIX D

TURBULENT BOUNDARY LAYER CALCULATION PROCEDURE

A procedure for calculating turbulent boundary parameters in compressible flows with arbitrary pressure gradient is presented. The method uses a modification of the techniques proposed in Refs. 6 and 7 to transform the compressible boundary layer equations to approximately an incompressible form. For the case of an insulated surface and Prandtl number of unity the transformation becomes exact.

A.   Flow Geometry and Boundary Layer Equations

The flow under consideration may be either two-dimensional or axisymmetric with the following geometry.
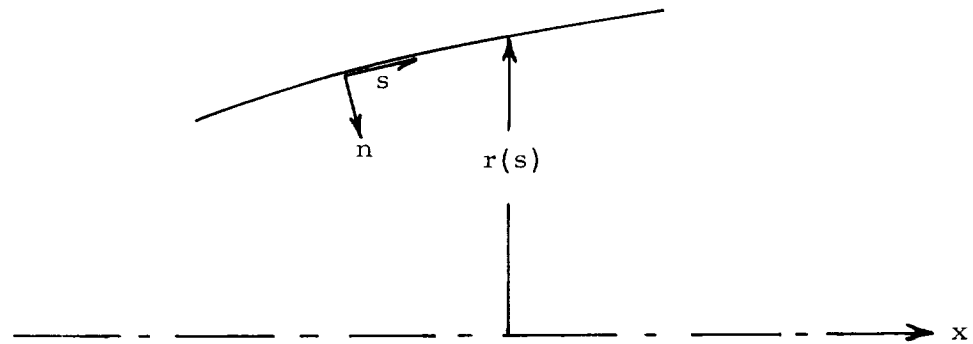
x	-	direction of main flow
r(s)	-	distance from line of symmetry to solid surface
s	-	distance measured along surface
n	-	distance normal to and measured from wall

The boundary layer equations are:

Continuity:

$$(\bar{\rho}\,\bar{u}\,r^k)_{,s} + (\overline{\rho\,v}\,r^k)_{,n} = 0 \qquad\qquad D(1)$$

$k = 0$ for two-dimensional flow, and $k = 1$ for

axisymmetric flow.

Momentum:

$$\bar{\rho}\,\bar{u}\,\bar{u}_{,s} + \overline{\rho\,v}\,\bar{u}_{,n} = -\frac{d\bar{p}}{ds} + (\bar{\mu}\,\bar{u}_{,n} - \overline{(\rho v)'\,u'})_{,n} \qquad D(2)$$

Energy:

$$\bar{\rho}\,\bar{u}\,\bar{h}_{,s} + \overline{\rho\,v}\,\bar{h}_{,n} = \bar{u}\frac{d\bar{p}}{ds} + (\frac{\bar{\mu}}{Pr}\,\bar{h}_{,n} - \overline{(\rho v)'\,h'})_{,n} + \overline{\tau\bar{u}}_{,n} \quad D(3)$$

In the above equations all bar values are understood to be temporal mean values. The bar (——) over two terms indicates the temporal mean of the product, and the primes indicate the instantaneous fluctuations from the mean. The commas before the subscripted variables s and n indicate partial differentiation, for example,

$$u_{,s} = \frac{\partial u}{\partial s}$$

Transformation of Equations

Define a new coordinate system by

$$N = \omega_1(s) \int_0^n \frac{\bar{\rho}}{\bar{\rho}_o}\,dn; \qquad\qquad S = \int_0^s \omega_2(s)\,ds$$

$$\frac{\partial}{\partial n} = \omega_1\frac{\bar{\rho}}{\bar{\rho}_o}\frac{\partial}{\partial N}; \qquad \frac{\partial}{\partial s} = \omega_2\frac{\partial}{\partial S} + N_{,s}\frac{\partial}{\partial N} \qquad\qquad D(4)$$

where $\bar{\rho}_o$ is constant and arbitrary for the present.

Introducing the stream function defined by

$$r^k \bar{\rho} \bar{u} = \psi_{,n} \quad ; \qquad r^k \overline{\rho v} = - \psi_{,s} \qquad\qquad D(5)$$

and using equation D(4) gives the continuity equation and velocities $\bar{u}$ and $\overline{\rho v}$ as

$$(\bar{U} r^k)_{,S} + (\bar{V} r^k)_{,N} = 0$$

$$\qquad\qquad\qquad\qquad\qquad\qquad\qquad\qquad\qquad D(6)$$

$$\bar{u} = \omega_1 \bar{U} \quad ; \qquad \overline{\rho v} = \bar{\rho}_o (\omega_2 \bar{V} - N_{,s} \bar{U})$$

where

$$r^k \bar{U} = \frac{1}{\bar{\rho}_o} \psi_{,N} \quad ; \qquad r^k \bar{V} = - \frac{1}{\bar{\rho}_o} \psi_{,S}$$

In order to transform the momentum equation, it is necessary to make an assumption regarding the transformation of the turbulent shear term $- \overline{(\rho v)' u'}$. Following the suggestion of Ref. 7, it is assumed that the turbulent shear associated with an elemental mass of fluid is invariant, which requires that

$$\bar{\rho} \left(\overline{(\rho v)' u'} \right) ds\ dn = \bar{\rho}_o^2\ \overline{(V' U')}\ d S\ d N$$

or

$$\overline{(\rho v)' u'} = \frac{\bar{\rho}_o^2}{\bar{\rho}} \overline{(V' U')} \frac{\partial (S,\ N)}{\partial (s,\ n)} = \omega_1 \omega_2 \bar{\rho}_o \overline{(V' U')} \qquad D(7)$$

Using equations D(4) and D(7) gives the momentum equation as

$$\bar{U} \bar{U}_{,S} + \bar{V} \bar{U}_{,N} = f(s, n) \bar{U}_e \frac{d\bar{U}_e}{dS} + \frac{1}{\bar{\rho}_o \omega_1 \omega_2} (\frac{\overline{\rho \mu}}{\bar{\rho}_o} \omega_1 \bar{U}_{,N} - \omega_1^2 \omega_2 \bar{\rho}_o \overline{V' U'})_{,N}$$

$$\qquad\qquad\qquad\qquad\qquad\qquad\qquad\qquad\qquad\qquad D(8)$$

where

$$f(s,n) = \frac{\dfrac{1}{\bar{\rho}} + \dfrac{1}{\omega_1}\dfrac{d\omega_1}{d\bar{p}}\bar{u}^2}{\dfrac{1}{\bar{\rho}_e} + \dfrac{1}{\omega_1}\dfrac{d\omega_1}{d\bar{p}}\bar{u}_e^2}$$

D(9)

The subscript (e) refers to external flow conditions outside the boundary layer. By choosing the product $\bar{\rho}\,\bar{\mu}$ to be evaluated at a reference temperature (or enthalpy), that is, $\bar{\rho}\,\bar{\mu} = \bar{\rho}_{ref}\,\bar{\mu}_{ref}$ (s), equation D(8) gives the following relationship between ω_1 and ω_2.

$$\omega_1 = \omega_2\,(\bar{\rho}_o\,\bar{\mu}_o/\bar{\rho}_{ref}\,\bar{\mu}_{ref})$$

D(10)

The condition that $\bar{\rho}\,\bar{\mu} = \bar{\rho}_{ref}\bar{\mu}_{ref}$ transforms the laminar shear stress as

$$\bar{\mu}\,\bar{u}_{,n} = \omega_1\,\omega_2\,\bar{\mu}_o\,\bar{U}_{,N}$$

D(11)

which is identical to saying that the laminar shear associated with an elemental mass of fluid is invariant. The assumption made regarding the turbulent shear transformation is then in agreement with the laminar shear transformation.

In order to find the functional form of $f(s,n)$, it is necessary to know the density variation in the boundary layer. Since it is desired to uncouple the momentum and energy equations, the density variation must be known in terms of the velocity distribution. It is well known that for flows with zero pressure gradient and both laminar and turbulent Prandtl numbers of unity (Ref. 16) that the enthalpy distribution is given by

$$\overline{h} = \overline{h}_w + (\overline{h}_o - \overline{h}_w)(\overline{u}/\overline{u}_e) - (\overline{h}_o - \overline{h}_e)(\overline{u}/\overline{u}_e)^2 \qquad \text{D(12)}$$

where $\overline{h}_w$, $\overline{h}_o$ and $\overline{h}_e$ are the wall, stagnation and external static enthalpies respectively. For Prandtl numbers other than unity, it is acceptable to replace the stagnation enthalpy by the recovery enthalpy $\overline{h}_r$. The density variation through the boundary layer may then be approximated by

$$\frac{\overline{\rho}}{\overline{\rho}_e} \cong \frac{\overline{h}_e}{\overline{h}} \qquad \text{D(13)}$$

Due to lack of knowledge regarding the enthalpy distribution with pressure gradients, it will be assumed here that the density variation is given by the quadratic form of equation D(12), namely,

$$\frac{\overline{\rho}_e}{\overline{\rho}} = \frac{\overline{h}_w}{\overline{h}_e} + \left(\frac{\overline{h}_r}{\overline{h}_e} - \frac{\overline{h}_w}{\overline{h}_e}\right)\left(\frac{\overline{u}}{\overline{u}_e}\right) - \left(\frac{\overline{h}_r}{\overline{h}_e} - 1\right)\left(\frac{\overline{u}}{\overline{u}_e}\right)^2 \qquad \text{D(14)}$$

where the recovery enthalpy is defined by

$$\frac{\overline{h}_r - \overline{h}_e}{\overline{h}_o - \overline{h}_e} = RF = \text{(Recovery Factor)}$$

Rearranging equation D(9) and using equation D(14) gives

$$\left[1 + \frac{\overline{p}}{\omega_1}\frac{d\omega_1}{d\overline{p}}\gamma M_e^2\right]\left[f(s,n) - \left(\frac{\overline{u}}{\overline{u}_e}\right)^2\right] = \frac{\overline{h}_w}{\overline{h}_e}\left(1 - \frac{\overline{u}}{\overline{u}_e}\right) + \frac{\overline{h}_r}{\overline{h}_e}\frac{\overline{u}}{\overline{u}_e}\left(1 - \frac{\overline{u}}{\overline{u}_e}\right) \quad \text{D(15)}$$

and choosing

$$1 + \frac{\overline{p}}{\omega_1}\frac{d\omega_2}{d\overline{p}}\gamma M_e^2 = \frac{\overline{h}_o}{\overline{h}_e} = 1 + \frac{\gamma-1}{2}M_e^2 \qquad ,$$

the following relations for $f(s, n)$ and ω_1 are obtained

$$f(s, n) = \frac{\overline{h}_w}{\overline{h}_o} (1 - \frac{\overline{u}}{\overline{u}_e}) + \frac{\overline{h}_r}{\overline{h}_o} \frac{\overline{u}}{\overline{u}_e} (1 - \frac{\overline{u}}{\overline{u}_e}) + (\frac{\overline{u}}{\overline{u}_e})^2 \qquad D(16)$$

and

$$\omega_1 = (\overline{p}/\overline{p}_o)^{\frac{\gamma-1}{2\gamma}} \qquad D(17)$$

If the viscosity variation with enthalpy is given by $\overline{\mu} = \overline{\mu}_o (\overline{h}/\overline{h}_o)^w$, the product $\overline{\rho}\,\overline{\mu} = \overline{\rho}_{ref}\overline{\mu}_{ref}$ is then

$$\overline{\rho}_{ref}\overline{\mu}_{ref} = \overline{\rho}_o \overline{\mu}_o (\overline{p}/\overline{p}_o) (\overline{h}_{ref}/\overline{h}_o)^{w-1} \qquad D(18)$$

and ω_2 is given by

$$\omega_2 = (\overline{h}_{ref}/\overline{h}_o)^{(w-1)} (\overline{p}/\overline{p}_o)^{(\frac{3\gamma-1}{2\gamma})} \qquad D(19)$$

The reference enthalpy taken from Ref. 17 is given by

$$\overline{h}_{ref} = \overline{h}_e + \frac{1}{2} (\overline{h}_w - \overline{h}_e) + 0.22 (\overline{h}_r - \overline{h}_e) \qquad D(20)$$

The momentum equation D(8) becomes

$$\overline{U}\,\overline{U}_{,S} + \overline{V}\,\overline{U}_{,N} = f(s, n)\,\overline{U}_e \frac{d\overline{U}_e}{dS} + (\overline{\nu}_o \overline{U}_{,N} - \overline{v'U'})_{,N} \qquad D(21)$$

The transformation becomes identical with Ref. 7 when $RF = w = 1.0$ and $\overline{h}_r = \overline{h}_w$. This is the particular case when the total enthalpy distribution through the boundary layer is a constant, e.g., $h + \frac{1}{2} u^2 = $ constant.

Momentum Integral Equation

Using equation D(6) and integrating equation D(21) across the boundary layer, the momentum integral equation is then

$$\frac{d \, \delta_{M_i}}{dS} + \left[2 + \frac{(RF-1) \frac{\gamma-1}{2} M_e^2}{1 + \frac{\gamma-1}{2} M_e^2} + \frac{\bar{h}_w}{\bar{h}_o} \frac{\delta^*_i}{\delta_{M_i}} \right] \frac{\delta_{M_i}}{\bar{U}_e} \frac{d \bar{U}_e}{dS} + k \frac{\delta_{M_i}}{r} \frac{dr}{dS} = \frac{C_{f_i}}{2}$$

$$D(22)$$

where δ_{M_i} and δ^*_i are given by

$$\delta_{M_i} = \int_0^{\delta_i} \frac{\bar{U}}{\bar{U}_e} (1 - \frac{\bar{U}}{\bar{U}_e}) \, dN$$

$$\delta^*_i = \int_0^{\delta_i} (1 - \frac{\bar{U}}{\bar{U}_e}) \, dN$$

Using a power law for the velocity distribution through the boundary layer $\bar{U}/\bar{U}_e = (N/\delta_i)^{1/m}$ gives δ_{M_i} and δ^*_i as

$$\delta_{M_i} = \delta_i m/(m+1)(m+2); \qquad \delta^*_i = \delta_i/(m+1) \qquad D(23)$$

In Ref. 18 it is shown that the coefficient of friction $C_{f_i}/2$ may be represented by

$$C_{f_i}/2 = (\frac{C_3}{m})^{\frac{m-1}{m+1}} (\frac{\bar{\nu}_o}{\bar{U}_e \delta_i})^{\frac{2}{m+1}} \qquad D(24)$$

Using the definition of δ_{M_i} from equation D(23), equation D(24) becomes

$$\frac{C_{f_i}}{2} = \left(\frac{C_3}{m}\right)^{\frac{m-1}{m+1}} \left(\frac{m}{(m+1)(m+2)}\right)^{\frac{2}{m+1}} \left(\frac{\bar{v}_o}{\bar{U}_e \delta_{M_i}}\right)^{\frac{2}{m+1}} \qquad D(25)$$

In Ref. 18, C_3 was found by choosing $m = 7$ and requiring that the coefficient $(C_3/m)^{\frac{m-1}{m+1}}$ became identical with the Blasius coefficient 0.0225. The value is $C_3 = 0.0444$. If the value of C_3 is taken as 0.04528, it is noteworthy to mention that equation D(25) for values of m of 7, 9 and 11 are extremely close to the experimental values of Prandtl, Young and Falkner.

m	Calculated $\dfrac{C_3}{2}$	Experimental	Source	Per Cent Diff.
7	$0.01273 \left(\dfrac{\bar{v}_o}{\delta_{M_i} \bar{U}_e}\right)^{1/4}$	$0.0128 \left(\dfrac{\bar{v}_o}{\delta_{M_i} \bar{U}_e}\right)^{1/4}$	Prandtl	0.547
9	$0.00879 \left(\dfrac{\bar{v}_o}{\delta_{M_i} \bar{U}_e}\right)^{1/5}$	$0.00885 \left(\dfrac{\bar{v}_o}{\delta_{M_i} \bar{U}_e}\right)^{1/5}$	Young	1.81
11	$0.00654 \left(\dfrac{\bar{v}_o}{\delta_{M_i} \bar{U}_e}\right)^{1/6}$	$0.00653 \left(\dfrac{\bar{v}_o}{\delta_{M_i} \bar{U}_e}\right)^{1/6}$	Falkner	-0.153

Although m varies with pressure gradient and Reynolds number, it is well known for incompressible flows that when m is assumed to be constant, the calculated values of momentum thickness δ_{M_i} are within the range of experimental error.

Using equation D(25) for $C_{f_i}/2$ and defining a new variable Ω by

$$\Omega = \delta_{M_i} (\bar{U}_e \, \delta_{M_i}/\bar{v}_o)^{2/(m+1)}, \text{ assuming the recovery factor RF to be}$$

constant, using the condition that $\bar{U}_e = a_o M_e$ (from equations D(6) and

D(17), and neglecting any heat conduction along the wall, i.e., $d\bar{h}_w/dS = 0$

the momentum integral equation may be integrated over S to give

$$\tilde{\Omega} = \tilde{\Omega}_{in} \left(\frac{M_{in}}{M_e}\right)^{\lambda_6} \left[\frac{1 + \frac{\gamma-1}{2} M^2}{1 + \frac{\gamma-1}{2} M_{in}^2}\right]^{\lambda_2} \left(\frac{\tilde{r}_{in}}{\tilde{r}}\right)^{\lambda_3}$$

$$+ \frac{\lambda_4 (1 + \frac{\gamma-1}{2} M_e^2)^{\lambda_2}}{M_e^{\lambda_1} \tilde{r}^{\lambda_3}} \int_{s_{in}}^{s} \frac{M_e^{\lambda_1} \tilde{r}^{\lambda_3} (\bar{h}_{ref}/\bar{h}_o)^{(w-1)} d\tilde{s}}{(1 + \frac{\gamma-1}{2} M_e^2)^{\lambda_5}} \qquad \text{D(26)}$$

where all dimensional lengths s, r and Ω have been made nondimensional

by a reference length R_T, i.e., $\tilde{\Omega} = \Omega/R_T$, $\tilde{r} = r/R_T$ and $\tilde{s} = s/R_T$. The

subscript (in) indicates initial conditions and Ω_{in}, $(\bar{h}_{ref}/\bar{h}_o)$ and the λ's

are given by

$$\tilde{\Omega}_{in} = \frac{(160)^{(m+3)/(m+1)}}{M_{in} (a_o R_T/\bar{\nu}_o)} \qquad \text{D(27)}$$

$$\frac{\bar{h}_{ref}}{\bar{h}_o} = \frac{1 + (0.5 + 0.22RF)^{\frac{\gamma-1}{2}} M_e^2}{1 + \frac{\gamma-1}{2} M_e^2} + \frac{1}{2} \Sigma_w \qquad \text{D(28)}$$

$$\lambda_1 = \left(\frac{m+2}{m+1}\right) \left[3 \left(\frac{m+1}{m}\right) + \frac{m+3}{m} \Sigma_w\right] \qquad \text{D(29)}$$

$$\lambda_2 = \left(\frac{1-RF}{2}\right) \left(\frac{m+3}{m+1}\right) \qquad \text{D(30)}$$

$$\lambda_3 = k \left(\frac{m+3}{m+1}\right) \qquad \text{D(31)}$$

$$\lambda_4 = (\frac{m+3}{m+1}) \left[\frac{m}{(m+1)(m+2)} \right]^{2/(m+1)} \bigg/ (22.1\ m)^{(m-1)/(m+1)} \qquad \text{D(32)}$$

$$\lambda_5 = \frac{3\gamma-1}{2(\gamma-1)} + (\frac{1-RF}{2}) \frac{m+3}{m+1} \qquad \text{D(33)}$$

$$\lambda_6 = \frac{(m+3)}{m} \left[2+(\frac{m+2}{m+1})\ \Sigma_w \right] \qquad \text{D(34)}$$

where

$$\Sigma_w = \frac{\bar{h}_w}{\bar{h}_o} - 1$$

From the calculated values of $\tilde{\Omega}$, the actual boundary layer parameters are found as follows:

Momentum thickness:

$$\tilde{\delta}_M = \frac{\tilde{\Omega}^{(m+1)/(m+3)}\ (1 + \frac{\gamma-1}{2} M_e^2)^{(\gamma+1)/2(\gamma-1)}}{M_e^{2\ (m+3)}\ (a_o\ R_T/\bar{\nu}_o)^{2(m+3)}} \qquad \text{D(35)}$$

Displacement thickness:

$$\tilde{\delta}* = \tilde{\delta}_M \left[(\Sigma_w + 1)\ (\frac{m+2}{m})\ (1 + \frac{\gamma-1}{2}M_e^2) + RF\ \frac{\gamma-1}{2} M_e^2 \right] \qquad \text{D(36)}$$

Boundary layer thickness:

$$\tilde{\delta} = \tilde{\delta}_M \left[(\Sigma_w + 1)\ (\frac{m+2}{m})\ (1 + \frac{\gamma-1}{2}M_e^2) + RF\ \frac{\gamma-1}{2}M_e^2 + m + 2 \right] \qquad \text{D(37)}$$

Friction coefficient:

$$\frac{C_f}{2} = \lambda_4\ (\frac{m+1}{m+3})\ \frac{\tilde{\delta}_M}{\tilde{\Omega}}\ \frac{(\bar{h}_{ref}/\bar{h}_o)^{(w-1)}}{(1 + \frac{\gamma-1}{2}\ M_e^2)^{(3\gamma-1)/2(\gamma-1)}} \qquad \text{D(38)}$$

Skin Friction Drag:

The component of skin friction drag in the direction of main flow (x direction) is found as follows:
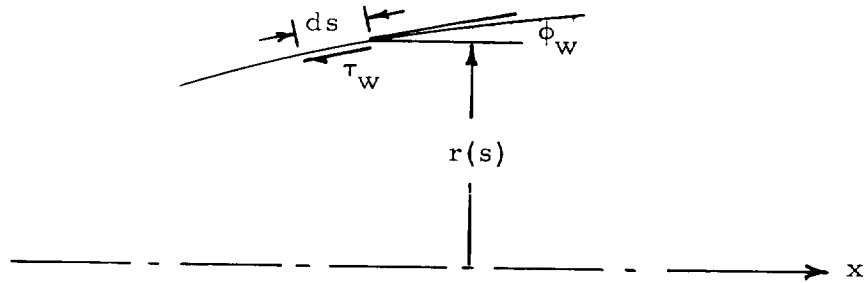
The elemental component of drag force in the x direction is

$$d\,D_x = \tau_w\,\cos\phi_w\,d\,A \qquad\qquad\qquad D(39)$$

where dA is the elemental surface area and is given by

$$dA = (2\pi)^k\,r^k\,ds.$$

Since $\cos\phi_w\,ds = dx$, the integrated drag force is then

$$D_x = (2\pi)^k \int_{x_i}^{x} \tau_w\,r^k\,dx \qquad\qquad\qquad D(40)$$

Now divide by the stagnation pressure P_o and an 'area' defined by

$A_T = \bar{\tau}^{-k}\,(R_T)^{1+k}$ and equation D(40) becomes

$$\frac{D}{P_o A_T} = 2^k \int_{x_i}^{x} \frac{\bar{\tau}_w}{P_o}\,\tilde{r}^k\,d\tilde{x} \qquad\qquad\qquad D(41)$$

-71-

Noting that $C_f/2 = \bar{\tau}_w / \bar{\rho}_e \bar{u}_e^2$ and $\bar{\rho}_e \bar{u}_e^2 / \bar{P}_o = \gamma M_e^2 / (1 + \frac{\gamma-1}{2} M_e^2)^{\gamma/(\gamma-1)}$

the drag coefficient is then

$$C_D = \frac{D}{P_o A_T} = 2^k \gamma \int_{\tilde{x}_i}^{\tilde{x}} \frac{C_f}{2} \frac{M_e^2 \, \tilde{r}^k \, d\tilde{x}}{(1 + \frac{\gamma-1}{2} M_e^2)^{\gamma/(\gamma-1)}} \qquad D(42)$$

APPENDIX E

SEPARATION CRITERION FOR COMPRESSIBLE FLOW

A method for predicting the separation point for a compressible turbulent boundary layer is presented based on an extension of the incompressible separation criterion of Ref. 19. In the following analysis the following assumptions are made:

(1)   The surface is adiabatic.

(2)   The recovery factor is unity.

Under these assumptions the momentum equation D(21) reduces to

$$\bar{\rho}_o \, \bar{U}\bar{U}_{,S} + \bar{\rho}_o \, \bar{V}\bar{U}_{,N} = \bar{\rho}_o \, \bar{U}_e \, \frac{d\bar{U}_e}{dS} + \frac{\partial \bar{T}}{\partial N} \qquad\qquad E(1)$$

Following the approach of Ref. 19, it is proposed that the boundary layer may be divided into two distinct regions, an outer region and an inner region. In the outer region it is assumed that the shear losses along a streamline are the same as for a flow without a pressure gradient. Changing the variables on the left hand side of equation E(1) from S and N to S and ψ gives

$$\bar{\rho}_o \, \bar{U} \, \left(\frac{\partial \bar{U}}{\partial S} \right)_\psi = \bar{\rho}_o \, \bar{U}_e \, \frac{d\bar{U}_e}{dS} + \left(\frac{\partial \bar{T}}{\partial N} \right)_{S, \, \psi} \qquad\qquad E(2)$$

For zero pressure gradient

$$\bar{\rho}_o \, \bar{U}^* \, \left(\frac{\partial \bar{U}^*}{\partial S} \right)_\psi = \left(\frac{\partial \bar{T}^*}{\partial N} \right)_{S, \, \psi} \qquad\qquad E(3)$$

-73-

where the asterisk denotes the point where the pressure gradient is zero, immediately preceding the adverse pressure gradient region.

Under the assumption that $(\partial \overline{T}/\partial N)_{S, \psi} = (\partial \overline{T*}/\partial \overline{N*})_{S, \psi}$ the velocity distribution along a streamline is then

$$\overline{U}^2(S, \psi) = \overline{U*}^2(S, \psi) + \overline{U}_e^2 - \overline{U*}_e^2; \ (\psi > \psi_{jc}) \qquad \text{E(4)}$$

Equation E(4) states the difference between the dynamic head $\overline{U}^2$ at any point in the boundary layer and the dynamic head of the external flow $\overline{U}_e^2$ is the same as for a flow without a pressure gradient. Differentiating equation E(4) with respect to ψ and noting that $r^k \overline{U}(\partial/\partial \psi)_S$ equals $(\partial/\partial N)_S$ gives

$$\frac{\partial \overline{U}}{\partial N} = \frac{\partial \overline{U*}}{\partial N*} \quad ; \ (\psi \geq \psi_{jc}) \qquad \text{E(5)}$$

The stream function ψ is

$$\psi = \psi* = r^k \int_0^{N*} \overline{U*} \ dN* \qquad \text{E(6)}$$

Choosing the velocity distribution $\overline{U*} = \overline{U*}_e \ (\frac{N*}{\delta*})^{\frac{1}{m}}$ gives

$$\frac{\partial \overline{U}}{\partial N} = \frac{1}{m} \frac{\overline{U*}_e}{\delta*} \ (\frac{N*}{\delta*})^{(1-m)/m} \quad ; \ (\psi > \psi_{jc}) \qquad \text{E(7)}$$

and

$$\psi = r^k \frac{m}{m+1} \ \overline{U*}_e \ \delta* \ (\frac{N*}{\delta*})^{\frac{m+1}{m}} \qquad \text{E(8)}$$

Neglecting the effects of inertia forces with respect to pressure and shear forces in the inner layer gives a direct balance between the

pressure and shear forces as

$$\frac{\partial \bar{T}}{\partial N} = -\bar{\rho}_o \, \bar{U}_e \, \frac{d\bar{U}_e}{dS} \; ; \quad (\psi < \psi_{jc}) \qquad\qquad E(9)$$

Integrating equation E(9) for the case of zero shear stress at the surface, and introducing Prandtl's mixing length theory for the shear stress gives

$$\frac{\partial \bar{U}}{\partial N} = \frac{1}{K} \left[-\bar{\rho}_o \, \bar{U}_e \, \frac{d\bar{U}_e}{dS} \right]^{\frac{1}{2}} \left[\frac{1}{N} \right]^{\frac{1}{2}} \; ; \quad (\psi < \psi_{jc}) \qquad\qquad E(10)$$

where K is the Karman constant. The velocity distribution and stream function are then

$$\bar{U} = \frac{2}{K} \left[-\bar{\rho}_o \, \bar{U}_e \, \frac{d\bar{U}_e}{dS} \right]^{\frac{1}{2}} N^{\frac{1}{2}} \; ; \quad (\psi < \psi_{jc}) \qquad\qquad E(11)$$

$$\psi = r^k \, \frac{4}{3K} \left[-\bar{\rho}_o \, \bar{U}_e \, \frac{d\bar{U}_e}{dS} \right]^{\frac{1}{2}} N^{\frac{3}{2}} \; ; \quad (\psi < \psi_{jc}) \qquad\qquad E(12)$$

The junction of the two regions is determined from the following conditions:

(1)   The velocity of the two regions must be equal

$$\bar{U} (\psi < \psi_{jc}) = \bar{U} (\psi > \psi_{jc}) \; ; \quad (\psi = \psi_{jc})$$

(2)   Continuity of mass flow must be satisfied, which requires that

$$\psi (\psi < \psi_{jc}) = \psi (\psi > \psi_{jc}) \; ; \quad (\psi = \psi_{jc})$$

(3)   The shear stress must be the same for the two regions. This requires that the velocity gradients be matched.

$$\frac{\partial \bar{U}}{\partial N} (\psi < \psi_{jc}) = \frac{\partial \bar{U}}{\partial N} (\psi > \psi_{jc}) \; ; \; (\psi = \psi_{jc})$$

Equating $\psi \left(\frac{\partial \bar{U}}{\partial N}\right)^3$ for the outer and inner regions gives the reference flat plate position as

$$\frac{N*}{\delta*}^{(2m-4)/m} = \frac{3 K^4}{4(m+1) \left(-m \frac{\rho_o \bar{U}_e}{\bar{U}_e^{*2}} \frac{d\bar{U}_e}{dS} \delta* \right)^2} \qquad E(13)$$

Comparing $\bar{U}^2/(\psi \, \partial \bar{U}/\partial N)$ for the flat plate flow and actual flow gives

$$(\bar{U}/\bar{U}*)^2 = 3/(m+1) \qquad E(14)$$

Substituting equation E(14) into E(4) gives

$$\left(1 - \frac{\bar{U}_e^2}{\bar{U}_e^{*2}}\right) = \left(\frac{m-2}{m+1}\right) \left(\frac{N*}{\delta*}\right)^{\frac{2}{m}} \qquad E(15)$$

Eliminating $(N*/\delta*)$ between equations E(13) and E(15) and defining
$\Gamma = (1 - \bar{U}_e^2/\bar{U}_e^{*2})$ gives

$$\Gamma^{\frac{m-2}{2}} \left(\delta* \frac{d\Gamma}{dS}\right) = \left[\frac{3K^4}{m^2(m+1)}\right]^{\frac{1}{2}} \left(\frac{m-2}{m+1}\right)^{\frac{m-2}{2}} \qquad E(16)$$

The reference flat plate boundary layer thickness is given by

$$\delta* = \frac{C_3}{m}^{\frac{m-1}{m+3}} \frac{(m+2)(m+3)}{m}^{\frac{m+1}{m+3}} \frac{\bar{\nu}_o}{\bar{U}_e^*}^{\frac{2}{m+3}} S^{\frac{m+1}{m+3}} \qquad E(17)$$

Making all lengths nondimensional by dividing by the the reference length R_T and using the transformation relations

$$\bar{U}_e = a_o M_e$$

-76-

and

$$S = \int_0^s \omega_2 \, ds$$

the separation criterion is then

$$\left(1 - \frac{M_e^2}{M_e^{*2}}\right)^{\frac{m-2}{m}} \frac{d}{ds} \left(1 - \frac{M_e^2}{M_e^{*2}}\right) = \frac{\Lambda(m) \left(\frac{a_o R_T}{\nu_o}\right)^{\frac{2}{m+3}} (M_e^*)^{\frac{2}{m+3}} \omega_2}{\left[\int_0^s \omega_2 \, ds\right]^{\frac{m+1}{m+3}}} \qquad E(18)$$

where

$$\Lambda(m) = \left[\frac{3K^4}{m^2(m+1)}\right]^{\frac{1}{2}} (22.1m)^{\frac{m-1}{m+3}} \left[\frac{m}{(m+2)\,(m+3)}\right]^{\frac{m+1}{m+3}} \left(\frac{m-2}{m+1}\right)^{\frac{m-2}{2}} \qquad E(19)$$

and

$$\omega_2 = (\bar{h}_{ref}/\bar{h}_o)^{(w-1)} \Big/ \left[1 + \frac{\gamma-1}{2} M_e^2\right]^{\frac{3\gamma-1}{2(\gamma-1)}} \qquad E(20)$$

Equation E(18) is a provisional separation criterion for compressible turbulent flow, the accuracy of which must be determined from experimental data.

APPENDIX F

EXPERIMENTAL DATA AND RUN SCHEDULE

Port Configuration	Nominal $\dot{w}_s/\dot{w}_p$, %	Conical Nozzle Run No's.	APG-1 Nozzle Run No's.
CT13	3	1	15
	6	2	16
	9	3	17
AT13	0	4	18
	3	5	19
	4	6	20
	5	7	21
	6	8	22
	7	9	23
	8	10	24
	9	11	25
BT13	3	12	26
	6	13	27
	9	14	28
AR2	2	29	47
	3	30	48
	4	31	49
	5	32	50
CR123	3	33	51
	6	34	52
	9	35	53

EXPERIMENTAL DATA AND RUN SCHEDULE (cont'd.)

Port Configuration	Nominal $\dot{w}_s/\dot{w}_p$, %	Conical Nozzle Run No's.	APG-1 Nozzle Run No's.
AR123	0	36	54
	3	37	55
	4	38	56
	5	39	57
	6	40	58
	7	41	59
	8	42	60
	9	43	61
BR123	3	44	62
	6	45	63
	9	46	64

DATA SHEET

NOZZLE TYPE __Conical (CT 1, 3)__   RUN NO. __1__

PRESSURE RATIO, PRIMARY, λ_p __526.40__   PRESSURE RATIO, SECONDARY, λ_s __228.37__

CHAMBER PRESSURE __99.81__ psia   SECONDARY PRESSURE __43.39__ psia

WEIGHT FLOW RATIO, $\dot{w}_s / \dot{w}_p$ __0.0301__   AMBIENT PRESSURE __0.190__ psia

TOTAL SIDE FORCE __6.14__ LB   AMPLIFICATION FACTOR __1.581__

TOTAL AXIAL FORCE __125.35__ LB   VACUUM THRUST COEFFICIENT __1.647__

PRESSURE DISTRIBUTION

TAP LOCATION	PRESSURE RATIO p/P_c	TAP LOCATION	PRESSURE RATIO p/P_c
1	.0032	18	.0039
2	.0032	35	.0152
3	.0032	19	.0147
4	.0032	36	.0125
5	.0049	37	.0211
6	.0228	20	.0278
7	.0194	21	.0059
31	.0297	22	.0054
8	.0199	23	.0094
9	.0319	38	.0090
10	.0270	39	.0164
11	.0140	24	.0206
12	.0044	40	.0236
13	.0046	25	
30	.0036	26	.0029
14	.0157	27	.0036
32	.0184	28	.0093
33	.0152	29	.0036
15	.0196	CAN	.0022
34	.0315	90	.0022
16	.0246	91	.0022
17	.0044		

DATA SHEET

NOZZLE TYPE ___Conical (CT 1, 3)___   RUN NO. ___2___

PRESSURE RATIO, PRIMARY, λ_p ___518.72___   PRESSURE RATIO, SECONDARY, λ_s ___452.28___

CHAMBER PRESSURE ___99.88___ psia   SECONDARY PRESSURE ___87.29___ psia

WEIGHT FLOW RATIO, $\dot{W}_s / \dot{W}_p$ ___0.0606___   AMBIENT PRESSURE ___0.193___ psia

TOTAL SIDE FORCE ___10.60___ LB   AMPLIFICATION FACTOR ___1.345___

TOTAL AXIAL FORCE ___126.30___ LB   VACUUM THRUST COEFFICIENT ___1.658___

PRESSURE DISTRIBUTION

TAP LOCATION	PRESSURE RATIO p/P_c	TAP LOCATION	PRESSURE RATIO p/P_c
1	.0030	18	.0039
2	.0030	35	.0189
3	.0030	19	.0184
4	.0030	36	.0189
5	.0064	37	.0172
6	.0309	20	.0266
7	.0226	21	.0059
31	.0226	22	.0074
8	.0320	23	.0103
9	.0256	38	.0088
10	.0388	39	.0177
11	.0359	24	.0172
12	.0044	40	.0261
13	.0049	25	
30	.0039	26	.0027
14	.0157	27	.0034
32	.0155	28	.0088
33	.0246	29	.0049
15	.0280	CAN	.0020
34	.0261	90	.0020
16	.0334	91	.0020
17	.0044		

DATA SHEET

NOZZLE TYPE Conical (CT 1, 3)   RUN NO. ___3___

PRESSURE RATIO, PRIMARY, λ_p _523.94_   PRESSURE RATIO, SECONDARY, λ_s _677.43_

CHAMBER PRESSURE _99.86_ psia   SECONDARY PRESSURE _127.39_ psia

WEIGHT FLOW RATIO, $\dot{W}_s/\dot{W}_p$ _0.0907_   AMBIENT PRESSURE _0.191_ psia

TOTAL SIDE FORCE _14.88_ LB   AMPLIFICATION FACTOR _1.258_

TOTAL AXIAL FORCE _126.65_ LB   VACUUM THRUST COEFFICIENT _1.663_

PRESSURE DISTRIBUTION

TAP LOCATION	PRESSURE RATIO p/P_c	TAP LOCATION	PRESSURE RATIO p/P_c
1	.0027	18	.0044
2	.0027	35	.0177
3	.0027	19	.0172
4	.0034	36	.0216
5	.0084	37	.0206
6	.0403	20	.0224
7	.0295	21	.0059
31	.0123	22	.0069
8	.0369	23	.0123
9	.0288	38	.0101
10	.0366	39	.0216
11	.0460	24	.0148
12	.0044	40	.0231
13	.0044	25	
30	.0034	26	.0030
14	.0143	27	.0037
32	.0128	28	.0093
33	.0192	29	.0054
15	.0334	CAN	.0025
34	.0270	90	.0025
16	.0364	91	.0025
17	.0042		

DATA SHEET

NOZZLE TYPE __Conical (AT 1, 3)__   RUN NO. ___4___

PRESSURE RATIO, PRIMARY, λ_p __502.75__   PRESSURE RATIO, SECONDARY, λ_s ___--___

CHAMBER PRESSURE __99.77__ psia   SECONDARY PRESSURE ___--___ psia

WEIGHT FLOW RATIO, $\dot{W}_s / \dot{W}_p$ ___0___   AMBIENT PRESSURE __0.198__ psia

TOTAL SIDE FORCE __0.28*__ LB   AMPLIFICATION FACTOR ___--___

TOTAL AXIAL FORCE __124.19__ LB   VACUUM THRUST COEFFICIENT __1.635__

PRESSURE DISTRIBUTION

TAP LOCATION	PRESSURE RATIO p/P_c	TAP LOCATION	PRESSURE RATIO p/P_c
1	.0040	18	.0057
2	.0042	35	.0062
3	.0045	19	.0064
4	.0045	36	.0072
5	.0055	37	.0084
6	.0062	20	.0094
7	.0062	21	.0055
31	.0069	22	.0050
8	.0079	23	.0062
9	.0097	38	.0055
10	.0116	39	.0069
11	.0141	24	.0082
12	.0057	40	.0097
13	.0062	25	
30	.0052	26	.0030
14	.0064	27	.0037
32	.0067	28	.0094
33	.0079	29	.0045
15	.0084	CAN	.0025
34	.0099	90	
16	.0119	91	
17	.0055		

* Ports plugged but not filled to form smooth contour.

DATA SHEET

NOZZLE TYPE Conical (AT 1, 3)   RUN NO. 5

PRESSURE RATIO, PRIMARY, λ_p 508.85   PRESSURE RATIO, SECONDARY, λ_s 238.52

CHAMBER PRESSURE 99.94 psia   SECONDARY PRESSURE 46.75 psia

WEIGHT FLOW RATIO, $\dot{W}_s / \dot{W}_p$ 0.0298   AMBIENT PRESSURE 0.196 psia

TOTAL SIDE FORCE 5.91 LB   AMPLIFICATION FACTOR 1.540

TOTAL AXIAL FORCE 124.90 LB   VACUUM THRUST COEFFICIENT 1.640

PRESSURE DISTRIBUTION

TAP LOCATION	PRESSURE RATIO p/P_c	TAP LOCATION	PRESSURE RATIO p/P_c
1	.0037	18	.0059
2	.0037	35	.0086
3	.0037	19	.0089
4	.0032	36	.0116
5	.0037	37	.0197
6	.0155	20	.0261
7	.0126	21	.0062
31	.0276	22	.0045
8	.0182	23	.0087
9	.0310	38	.0084
10	.0246	39	.0133
11	.0138	24	.0182
12	.0050	40	.0207
13	.0052	25	
30	.0042	26	.0025
14	.0165	27	.0037
32	.0155	28	.0091
33	.0177	29	.0047
15	.0182	CAN	.0025
34	.0300	90	.0028
16	.0219	91	.0028
17	.0062		

DATA SHEET

NOZZLE TYPE __Conical (AT 1, 3)__   RUN NO. __6__

PRESSURE RATIO, PRIMARY, λ_p __503.56__   PRESSURE RATIO, SECONDARY, λ_s __314.65__

CHAMBER PRESSURE __99.89__ psia   SECONDARY PRESSURE __62.30__ psia

WEIGHT FLOW RATIO, $\dot{W}_s / \dot{W}_p$ __0.0400__   AMBIENT PRESSURE __0.198__ psia

TOTAL SIDE FORCE __7.47__ LB   AMPLIFICATION FACTOR __1.458__

TOTAL AXIAL FORCE __124.31__ LB   VACUUM THRUST COEFFICIENT __1.634__

PRESSURE DISTRIBUTION

TAP LOCATION	PRESSURE RATIO p/P_c	TAP LOCATION	PRESSURE RATIO p/P_c
1	.0035	18	.0060
2	.0035	35	.0104
3	.0033	19	.0107
4	.0043	36	.0107
5	.0040	37	.0173
6	.0185	20	.0276
7	.0129	21	.0060
31	.0259	22	.0043
8	.0198	23	.0080
9	.0303	38	.0075
10	.0338	39	.0117
11	.0144	24	.0178
12	.0050	40	.0239
13	.0050	25	
30	.0040	26	.0028
14	.0179	27	.0038
32	.0141	28	.0092
33	.0227	29	.0053
15	.0158	CAN	.0026
34	.0296	90	.0028
16	.0335	91	.0028
17	.0060		

DATA SHEET

NOZZLE TYPE Conical (AT 1, 3)   RUN NO. ___7___

PRESSURE RATIO, PRIMARY, λ_p __509.12__   PRESSURE RATIO, SECONDARY, λ_s __403.38__

CHAMBER PRESSURE __100.03__ psia   SECONDARY PRESSURE __79.06__ psia

WEIGHT FLOW RATIO, $\dot{w}_s / \dot{w}_p$ __0.0505__   AMBIENT PRESSURE __0.196__ psia

TOTAL SIDE FORCE __8.97__ LB   AMPLIFICATION FACTOR __1.372__

TOTAL AXIAL FORCE __125.57__ LB   VACUUM THRUST COEFFICIENT __1.647__

PRESSURE DISTRIBUTION

TAP LOCATION	PRESSURE RATIO p/P_c	TAP LOCATION	PRESSURE RATIO p/P_c
1	.0038	18	.0058
2	.0036	35	.0119
3	.0036	19	.0122
4	.0033	36	.0109
5	.0046	37	.0159
6	.0225	20	.0254
7	.0144	21	.0060
31	.0173	22	.0046
8	.0291	23	.0075
9	.0252	38	.0070
10	.0377	39	.0105
11	.0314	24	.0161
12	.0053	40	.0242
13	.0053	25	
30	.0043	26	.0024
14	.0141	27	.0033
32	.0129	28	.0087
33	.0240	29	.0053
15	.0195	CAN	.0019
34	.0257	90	.0021
16	.0372	91	.0024
17	.0060		

DATA SHEET

NOZZLE TYPE __Conical (AT 1, 3)__   RUN NO. ___8___

PRESSURE RATIO, PRIMARY, λ_p __506.04__   PRESSURE RATIO, SECONDARY, λ_s __480.00__

CHAMBER PRESSURE __99.92__ psia   SECONDARY PRESSURE __94.56__ psia

WEIGHT FLOW RATIO, W_s/W_p __0.0606__   AMBIENT PRESSURE __0.197__ psia

TOTAL SIDE FORCE __10.30__ LB   AMPLIFICATION FACTOR __1.309__

TOTAL AXIAL FORCE __125.97__ LB   VACUUM THRUST COEFFICIENT __1.655__

PRESSURE DISTRIBUTION

TAP LOCATION	PRESSURE RATIO p/P_c	TAP LOCATION	PRESSURE RATIO p/P_c
1	.0036	18	.0058
2	.0033	35	.0139
3	.0033	19	.0144
4	.0033	36	.0124
5	.0051	37	.0149
6	.0267	20	.0240
7	.0164	21	.0063
31	.0134	22	.0051
8	.0338	23	.0078
9	.0223	38	.0070
10	.0387	39	.0102
11	.0400	24	.0154
12	.0056	40	.0240
13	.0056	25	
30	.0046	26	.0026
14	.0124	27	.0036
32	.0117	28	.0090
33	.0235	29	.0060
15	.0248	CAN	.0024
34	.0235	90	.0024
16	.0385	91	.0026
17	.0060		

DATA SHEET

NOZZLE TYPE Conical (AT 1, 3)   RUN NO. 9

PRESSURE RATIO, PRIMARY, λ_p 513.7   PRESSURE RATIO, SECONDARY, λ_s 565.69

CHAMBER PRESSURE 99.92 psia   SECONDARY PRESSURE 110.31 psia

WEIGHT FLOW RATIO, $\dot{W}_s / \dot{W}_p$ 0.0706   AMBIENT PRESSURE 0.195 psia

TOTAL SIDE FORCE 11.77 LB   AMPLIFICATION FACTOR 1.280

TOTAL AXIAL FORCE 126.40 LB   VACUUM THRUST COEFFICIENT 1.659

PRESSURE DISTRIBUTION

TAP LOCATION	PRESSURE RATIO p/P_c	TAP LOCATION	PRESSURE RATIO p/P_c
1	.0088	18	.0058
2	.0086	35	.0154
3	.0086	19	.0159
4	.0086	36	.0152
5	.0061	37	.0157
6	.0312	20	.0228
7	.0184	21	.0063
31	.0113	22	.0056
8	.0351	23	.0086
9	.0231	38	.0073
10	.0373	39	.0103
11	.0420	24	.0147
12	.0056	40	.0233
13	.0058	25	
30	.0046	26	.0027
14	.0117	27	.0036
32	.0105	28	.0090
33	.0213	29	.0061
15	.0290	CAN	.0024
34	.0223	90	.0027
16	.0373	91	.0027
17	.0061		

-89-

DATA SHEET

NOZZLE TYPE Conical (AT 1, 3) RUN NO. 10

PRESSURE RATIO, PRIMARY, λ_p 503.44 PRESSURE RATIO, SECONDARY, λ_s 631.87

CHAMBER PRESSURE 99.91 psia SECONDARY PRESSURE 125.11 psia

WEIGHT FLOW RATIO, $\dot{W}_s / \dot{W}_p$ 0.0807 AMBIENT PRESSURE 0.198 psia

TOTAL SIDE FORCE 13.26 LB AMPLIFICATION FACTOR 1.261

TOTAL AXIAL FORCE 126.40 LB VACUUM THRUST COEFFICIENT 1.660

PRESSURE DISTRIBUTION

TAP LOCATION	PRESSURE RATIO p/P_c	TAP LOCATION	PRESSURE RATIO p/P_c
1	.0034	18	.0051
2	.0034	35	.0152
3	.0034	19	.0164
4	.0034	36	.0174
5	.0061	37	.0174
6	.0351	20	.0216
7	.0204	21	.0059
31	.0090	22	.0054
8	.0326	23	.0090
9	.0282	38	.0073
10	.0346	39	.0098
11	.0464	24	.0140
12	.0051	40	.0125
13	.0054	25	
30	.0041	26	.0027
14	.0110	27	.0036
32	.0095	28	.0090
33	.0186	29	.0063
15	.0301	CAN	.0027
34	.0238	90	.0027
16	.0354	91	.0027
17	.0056		

DATA SHEET

NOZZLE TYPE __Conical (AT 1, 3)__   RUN NO. __11__

PRESSURE RATIO, PRIMARY, λ_p __520.92__   PRESSURE RATIO, SECONDARY, λ_s __656.09__

CHAMBER PRESSURE __99.74__ psia   SECONDARY PRESSURE __125.97__ psia

WEIGHT FLOW RATIO, $\dot{w}_s / \dot{w}_p$ __0.0819__   AMBIENT PRESSURE __0.192__ psia

TOTAL SIDE FORCE __13.28__ LB   AMPLIFICATION FACTOR __1.193__

TOTAL AXIAL FORCE __126.70__ LB   VACUUM THRUST COEFFICIENT __1.666__

PRESSURE DISTRIBUTION

TAP LOCATION	PRESSURE RATIO p/P_c	TAP LOCATION	PRESSURE RATIO p/P_c
1	.0030	18	.0047
2	.0028	35	.0148
3	.0028	19	.0163
4	.0032	36	.0185
5	.0060	37	.0190
6	.0343	20	.0212
7	.0202	21	.0057
31	.0089	22	.0055
8	.0332	23	.0096
9	.0284	38	.0077
10	.0343	39	.0101
11	.0466	24	.0138
12	.0047	40	.0222
13	.0050	25	
30	.0040	26	.0030
14	.0106	27	.0035
32	.0089	28	.0092
33	.0175	29	.0064
15	.0309	CAN	.0025
34	.0242	90	.0025
16	.0345	91	.0025
17	.0052		

DATA SHEET

NOZZLE TYPE Conical (BT 1, 3)   RUN NO.   12

PRESSURE RATIO, PRIMARY, λ_p 512.78   PRESSURE RATIO, SECONDARY, λ_s 225.49

CHAMBER PRESSURE 99.74 psia   SECONDARY PRESSURE 43.97 psia

WEIGHT FLOW RATIO, $\dot{W}_s / \dot{W}_p$ 0.0300   AMBIENT PRESSURE 0.195 psia

TOTAL SIDE FORCE 5.93 LB   AMPLIFICATION FACTOR 1.533

TOTAL AXIAL FORCE 125.19 LB   VACUUM THRUST COEFFICIENT 1.647

PRESSURE DISTRIBUTION

TAP LOCATION	PRESSURE RATIO p/P_c	TAP LOCATION	PRESSURE RATIO p/P_c
1	.0032	18	.0053
2	.0032	35	.0107
3	.0032	19	.0102
4	.0028	36	.0131
5	.0035	37	.0205
6	.0191	20	.0220
7	.0151	21	.0063
31	.0299	22	.0053
8	.0191	23	.0107
9	.0299	38	.0097
10	.0166	39	.0163
11	.0141	24	.0176
12	.0048	40	.0127
13	.0048	25	
30	.0038	26	.0028
14	.0191	27	.0038
32	.0210	28	.0092
33	.0195	29	.0043
15	.0200	CAN	.0021
34	.0279	90	.0023
16	.0136	91	.0023
17	.0053		

DATA SHEET

NOZZLE TYPE <u>Conical (BT 1, 3)</u>   RUN NO. <u>13</u>

PRESSURE RATIO, PRIMARY, λ_p <u>516.04</u>   PRESSURE RATIO, SECONDARY, λ_s <u>457.63</u>

CHAMBER PRESSURE <u>99.87</u> psia   SECONDARY PRESSURE <u>88.78</u> psia

WEIGHT FLOW RATIO, $\dot{W}_s / \dot{W}_p$ <u>0.0604</u>   AMBIENT PRESSURE <u>0.194</u> psia

TOTAL SIDE FORCE <u>10.47</u> LB   AMPLIFICATION FACTOR <u>1.331</u>

TOTAL AXIAL FORCE <u>126.43</u> LB   VACUUM THRUST COEFFICIENT <u>1.660</u>

PRESSURE DISTRIBUTION

TAP LOCATION	PRESSURE RATIO p/P_c	TAP LOCATION	PRESSURE RATIO p/P_c
1	.0029	18	.0053
2	.0029	35	.0156
3	.0029	19	.0151
4	.0029	36	.0117
5	.0048	37	.0161
6	.0294	20	.0252
7	.0201	21	.0065
31	.0208	22	.0070
8	.0329	23	.0095
9	.0245	38	.0075
10	.0368	39	.0166
11	.0292	24	.0174
12	.0043	40	.0228
13	.0046	25	
30	.0038	26	.0033
14	.0181	27	.0041
32	.0169	28	.0095
33	.0270	29	.0053
15	.0223	CAN	.0029
34	.0257	90	.0029
16	.0343	91	.0029
17	.0053		

DATA SHEET

NOZZLE TYPE Conical (BT 1, 3)   RUN NO. 14

PRESSURE RATIO, PRIMARY, λ_p 513.26   PRESSURE RATIO, SECONDARY, λ_s 672.97

CHAMBER PRESSURE 99.84 psia   SECONDARY PRESSURE 131.23 psia

WEIGHT FLOW RATIO, $\dot{W}_s / \dot{W}_p$ 0.0902   AMBIENT PRESSURE 0.195 psia

TOTAL SIDE FORCE 14.44 LB   AMPLIFICATION FACTOR 1.225

TOTAL AXIAL FORCE 126.86 LB   VACUUM THRUST COEFFICIENT 1.667

PRESSURE DISTRIBUTION

TAP LOCATION	PRESSURE RATIO p/P_c	TAP LOCATION	PRESSURE RATIO p/P_c
1	.0029	18	.0053
2	.0029	35	.0196
3	.0029	19	.0206
4	.0033	36	.0201
5	.0070	37	.0164
6	.0171	20	.0225
7	.0265	21	.0065
31	.0107	22	.0078
8	.0397	23	.0107
9	.0245	38	.0078
10	.0358	39	.0186
11	.0437	24	.0156
12	.0048	40	.0035
13	.0051	25	
30	.0041	26	.0024
14	.0161	27	.0033
32	.0129	28	.0088
33	.0196	29	.0048
15	.0331	CAN	.0021
34	.0225	90	.0024
16	.0358	91	.0024
17	.0053		

DATA SHEET

NOZZLE TYPE __APG-1 (CT 1, 3)__   RUN NO. __15__

PRESSURE RATIO, PRIMARY, λ_p __517.23__   PRESSURE RATIO, SECONDARY, λ_s __239.12__

CHAMBER PRESSURE __100.10__ psia   SECONDARY PRESSURE __46.39__ psia

WEIGHT FLOW RATIO, $\dot{W}_s / \dot{W}_p$ __0.0299__   AMBIENT PRESSURE __0.194__ psia

TOTAL SIDE FORCE __6.76__ LB   AMPLIFICATION FACTOR __1.759__

TOTAL AXIAL FORCE __124.60__ LB   VACUUM THRUST COEFFICIENT __1.633__

PRESSURE DISTRIBUTION

TAP LOCATION	PRESSURE RATIO p/P_c	TAP LOCATION	PRESSURE RATIO p/P_c
1	.0445	36	.0080
2	.0110	37	.0068
3	.0125	17	
31	.0179	38	.0071
4	.0150	39	.0083
5	.0105	18	.0112
6	.0150	19	.0157
7	.0194	20	.0083
8	.0145	21	.0063
9	.0088	40	.0063
10	.0103	22	.0098
32	.0122	23	.0132
11	.0112	24	.0078
12	.0107	26	.0044
33	.0127	27	.0044
34	.0147	28	.0078
13	.0093	29	.0044
30	.0093	25	.0044
35	.0120	CAN	.0019
14	.0156	90	.0024
15	.0132	91	.0019
16	.0098		

DATA SHEET

NOZZLE TYPE __APG-1 (CT 1, 3)__   RUN NO. ___16___

PRESSURE RATIO, PRIMARY, λ_p _513.86_   PRESSURE RATIO, SECONDARY, λ_s _477.90_

CHAMBER PRESSURE _99.95_ psia   SECONDARY PRESSURE _93.19_ psia

WEIGHT FLOW RATIO, $\dot{W}_s / \dot{W}_p$ ___0.0600___   AMBIENT PRESSURE _0.195_ psia

TOTAL SIDE FORCE _11.88_ LB   AMPLIFICATION FACTOR ___1.542___

TOTAL AXIAL FORCE _124.62_ LB   VACUUM THRUST COEFFICIENT _1.636_

PRESSURE DISTRIBUTION

TAP LOCATION	PRESSURE RATIO p/P_c	TAP LOCATION	PRESSURE RATIO p/P_c
1	.0884	36	.0088
2	.0191	37	.0088
3	.0073	17	
31	.0058	38	.0122
4	.0122	39	.0127
5	.0216	18	.0103
6	.0167	19	.0147
7	.0137	20	.0226
8	.0211	21	.0068
9	.0265	40	.0054
10	.0132	22	.0063
32	.0087	23	.0113
11	.0113	24	.0196
12	.0058	26	.0044
33	.0068	27	.0044
34	.0103	28	.0078
13	.0152	29	.0046
30	.0142	25	.0049
35	.0191	CAN	.0019
14	.0132	90	.0024
15	.0211	91	.0014
16	.0117		

DATA SHEET

NOZZLE TYPE APG-1 (CT 1, 3)   RUN NO. 17

PRESSURE RATIO, PRIMARY, λ_p 506.44   PRESSURE RATIO, SECONDARY, λ_s 679.39

CHAMBER PRESSURE 100.00 psia   SECONDARY PRESSURE 133.84 psia

WEIGHT FLOW RATIO, $\dot{W}_s/\dot{W}_p$ 0.0872   AMBIENT PRESSURE 0.197 psia

TOTAL SIDE FORCE 16.17 LB   AMPLIFICATION FACTOR 1.425

TOTAL AXIAL FORCE 126.20 LB   VACUUM THRUST COEFFICIENT 1.656

PRESSURE DISTRIBUTION

TAP LOCATION	PRESSURE RATIO p/P_c	TAP LOCATION	PRESSURE RATIO p/P_c
1	.1279	36	.0061
2	.0265	37	.0061
3	.0097	17	
31	.0044	38	.0105
4	.0085	39	.0189
5	.0162	18	.0164
6	.0255	19	.0132
7	.0191	20	.0284
8	.0181	21	.0093
9	.0309	40	.0088
10	.0314	22	.0093
32	.0068	23	.0093
11	.0206	24	.0181
12	.0049	26	.0044
33	.0049	27	.0044
34	.0068	28	.0078
13	.0117	29	.0044
30	.0117	25	.0044
35	.0211	CAN	.0019
14	.0216	90	.0024
15	.0184	91	.0014
16	.0302		

DATA SHEET

NOZZLE TYPE __APG-1 (AT 1, 3)__   RUN NO. __18__

PRESSURE RATIO, PRIMARY, λ_p __562.10__   PRESSURE RATIO, SECONDARY, λ_s ____--____

CHAMBER PRESSURE __99.95__ psia   SECONDARY PRESSURE ____--____ psia

WEIGHT FLOW RATIO, $\dot{W}_s / \dot{W}_p$ ____0____   AMBIENT PRESSURE __0.178__ psia

TOTAL SIDE FORCE __0.32*__ LB   AMPLIFICATION FACTOR ____--____

TOTAL AXIAL FORCE __125.43__ LB   VACUUM THRUST COEFFICIENT __1.642__

PRESSURE DISTRIBUTION

TAP LOCATION	PRESSURE RATIO p/P_c	TAP LOCATION	PRESSURE RATIO p/P_c
1	.0058	36	.0058
2	.0048	37	.0048
3	.0048	17	
31	.0046	38	.0048
4	.0043	39	.0048
5	.0048	18	.0048
6	.0048	19	.0063
7	.0053	20	.0078
8	.0053	21	.0058
9	.0087	40	.0048
10	.0102	22	.0048
32	.0073	23	.0051
11	.0117	24	.0058
12	.0063	26	.0043
33	.0058	27	.0043
34	.0058	28	.0082
13	.0063	29	.0043
30	.0068	25	.0043
35	.0048	CAN	.0019
14	.0051	90	.0019
15	.0063	91	.0014
16	.0092		

* Ports plugged but not filled to form smooth contour.

DATA SHEET

NOZZLE TYPE <u>APG-1 (AT 1, 3)</u>   RUN NO. <u>19</u>

PRESSURE RATIO, PRIMARY, λ_p <u>500.54</u>   PRESSURE RATIO, SECONDARY, λ_s <u>241.38</u>

CHAMBER PRESSURE <u>100.07</u> psia   SECONDARY PRESSURE <u>47.07</u> psia

WEIGHT FLOW RATIO, $\dot{W}_s / \dot{W}_p$ <u>0.0299</u>   AMBIENT PRESSURE <u>0.200</u> psia

TOTAL SIDE FORCE <u>6.86</u> LB   AMPLIFICATION FACTOR <u>1.783</u>

TOTAL AXIAL FORCE <u>124.73</u> LB   VACUUM THRUST COEFFICIENT <u>1.637</u>

PRESSURE DISTRIBUTION

TAP LOCATION	PRESSURE RATIO p/P_c	TAP LOCATION	PRESSURE RATIO p/P_c
1	.1240	36	.0077
2	.0042	37	.0067
3	.0062	17	
31	.0185	38	.0067
4	.0140	39	.0077
5	.0106	18	.0101
6	.0150	19	.0121
7	.0194	20	.0077
8	.0165	21	.0047
9	.0086	40	.0052
10	.0099	22	.0086
32	.0069	23	.0077
11	.0113	24	.0071
12	.0079	26	.0042
33	.0123	27	.0042
34	.0148	28	.0077
13	.0099	29	.0042
30	.0089	25	.0042
35	.0113	CAN	.0017
14	.0145	90	.0015
15	.0165	91	.0013
16	.0091		

DATA SHEET

NOZZLE TYPE __APG-1 (AT 1, 3)__   RUN NO. __20__

PRESSURE RATIO, PRIMARY, λ_p __500.42__   PRESSURE RATIO, SECONDARY, λ_s __323.25__

CHAMBER PRESSURE __100.04__ psia   SECONDARY PRESSURE __63.68__ psia

WEIGHT FLOW RATIO, $\dot{W}_s / \dot{W}_p$ __0.0405__   AMBIENT PRESSURE __0.200__ psia

TOTAL SIDE FORCE __8.70__ LB   AMPLIFICATION FACTOR __1.664__

TOTAL AXIAL FORCE __125.18__ LB   VACUUM THRUST COEFFICIENT __1.643__

PRESSURE DISTRIBUTION

TAP LOCATION	PRESSURE RATIO p/P_c	TAP LOCATION	PRESSURE RATIO p/P_c
1	.1771	36	.0092
2	.0053	37	.0097
3	.0057	17	
31	.0107	38	.0097
4	.0224	39	.0097
5	.0116	18	.0087
6	.0121	19	.0175
7	.0170	20	.0082
8	.0219	21	.0048
9	.0097	40	.0048
10	.0102	22	.0072
32	.0062	23	.0131
11	.0116	24	.0190
12	.0062	26	.0043
33	.0087	27	.0043
34	.0141	28	.0077
13	.0161	29	.0043
30	.0131	25	.0043
35	.0116	CAN	.0018
14	.0121	90	.0013
15	.0215	91	.0013
16	.0092		

DATA SHEET

NOZZLE TYPE <u>APG-1 (AT 1, 3)</u>   RUN NO. <u>21</u>

PRESSURE RATIO, PRIMARY, λ_p <u>504.65</u>   PRESSURE RATIO, SECONDARY, λ_s <u>402.93</u>

CHAMBER PRESSURE <u>100.15</u> psia   SECONDARY PRESSURE <u>79.78</u> psia

WEIGHT FLOW RATIO, $\dot{W}_s / \dot{W}_p$ <u>0.512</u>   AMBIENT PRESSURE <u>0.198</u> psia

TOTAL SIDE FORCE <u>10.58</u> LB   AMPLIFICATION FACTOR <u>1.602</u>

TOTAL AXIAL FORCE <u>125.12</u> LB   VACUUM THRUST COEFFICIENT <u>1.640</u>

PRESSURE DISTRIBUTION

TAP LOCATION	PRESSURE RATIO p/P_c	TAP LOCATION	PRESSURE RATIO p/P_c
1	.2204	36	.0090
2	.0065	37	.0092
3	.0055	17	
31	.0085	38	.0131
4	.0207	39	.0119
5	.0188	18	.0095
6	.0114	19	.0171
7	.0161	20	.0136
8	.0230	21	.0065
9	.0185	40	.0055
10	.0102	22	.0075
32	.0053	23	.0124
11	.0114	24	.0212
12	.0053	26	.0041
33	.0070	27	.0041
34	.0112	28	.0077
13	.0171	29	.0041
30	.0166	25	.0046
35	.0176	CAN	.0016
14	.0114	90	.0011
15	.0230	91	.0009
16	.0095		

DATA SHEET

NOZZLE TYPE __APG-1 (AT 1, 3)__   RUN NO. __22__

PRESSURE RATIO, PRIMARY, λ_p __504.08__   PRESSURE RATIO, SECONDARY, λ_s __474.09__

CHAMBER PRESSURE __100.03__ psia   SECONDARY PRESSURE __93.87__ psia

WEIGHT FLOW RATIO, $\dot{W}_s / \dot{W}_p$ __0.0600__   AMBIENT PRESSURE __0.198__ psia

TOTAL SIDE FORCE __12.30__ LB   AMPLIFICATION FACTOR __1.587__

TOTAL AXIAL FORCE __125.29__ LB   VACUUM THRUST COEFFICIENT __1.644__

PRESSURE DISTRIBUTION

TAP LOCATION	PRESSURE RATIO p/P_c	TAP LOCATION	PRESSURE RATIO p/P_c
1	.2644	36	.0072
2	.0072	37	.0076
3	.0042	17	
31	.0027	38	.0136
4	.0155	39	.0148
5	.0224	18	.0113
6	.0121	19	.0162
7	.0150	20	.0221
8	.0219	21	.0084
9	.0256	40	.0072
10	.0108	22	.0072
32	.0052	23	.0118
11	.0118	24	.0216
12	.0050	26	.0042
33	.0059	27	.0042
34	.0094	28	.0079
13	.0175	29	.0052
30	.0170	25	.0072
35	.0216	CAN	.0020
14	.0113	90	.0013
15	.0226	91	.0008
16	.0099		

DATA SHEET

NOZZLE TYPE __APG-1 (AT 1,3)__   RUN NO. __23__

PRESSURE RATIO, PRIMARY, λ_p __507.09__   PRESSURE RATIO, SECONDARY, λ_s __554.67__

CHAMBER PRESSURE __100.13__ psia   SECONDARY PRESSURE __109.27__ psia

WEIGHT FLOW RATIO, $\dot{W}_s / \dot{W}_p$ __0.0699__   AMBIENT PRESSURE __0.197__ psia

TOTAL SIDE FORCE __13.80__ LB   AMPLIFICATION FACTOR __1.516__

TOTAL AXIAL FORCE __126.31__ LB   VACUUM THRUST COEFFICIENT __1.655__

PRESSURE DISTRIBUTION

TAP LOCATION	PRESSURE RATIO p/P_c	TAP LOCATION	PRESSURE RATIO p/P_c
1	.3104	36	.0064
2	.0084	37	.0069
3	.0042	17	
31	.0076	38	.0123
4	.0108	39	.0155
5	.0253	18	.0138
6	.0170	19	.0157
7	.0140	20	.0258
8	.0211	21	.0099
9	.0270	40	.0096
10	.0172	22	.0084
32	.0054	23	.0116
11	.0113	24	.0211
12	.0052	26	.0042
33	.0050	27	.0042
34	.0081	28	.0079
13	.0150	29	.0072
30	.0143	25	.0081
35	.0251	CAN	.0020
14	.0140	90	.0018
15	.0216	91	.0012
16	.0157		

-103-

DATA SHEET

NOZZLE TYPE <u>APG-1 (AT 1, 3)</u>　　　　　　　　RUN NO. <u>24</u>

PRESSURE RATIO, PRIMARY, λ_p <u>509.05</u>　　PRESSURE RATIO, SECONDARY, λ_s <u>630.46</u>

CHAMBER PRESSURE <u>100.02</u> psia　　　　SECONDARY PRESSURE <u>123.57</u> psia

WEIGHT FLOW RATIO, $\dot{W}_s / \dot{W}_p$ <u>0.0798</u>　　AMBIENT PRESSURE <u>0.196</u> psia

TOTAL SIDE FORCE <u>15.02</u> LB　　　　AMPLIFICATION FACTOR <u>1.442</u>

TOTAL AXIAL FORCE <u>126.60</u> LB　　　VACUUM THRUST COEFFICIENT <u>1.661</u>

PRESSURE DISTRIBUTION

TAP LOCATION	PRESSURE RATIO p / Pc	TAP LOCATION	PRESSURE RATIO p / Pc
1	.3499	36	.0052
2	.0099	37	.0055
3	.0045	17	
31	.0067	38	.0113
4	.0094	39	.0158
5	.0251	18	.0165
6	.0202	19	.0155
7	.0138	20	.0280
8	.0204	21	.0101
9	.0278	40	.0108
10	.0266	22	.0108
32	.0050	23	.0113
11	.0116	24	.0209
12	.0050	26	.0042
33	.0047	27	.0042
34	.0079	28	.0079
13	.0138	29	.0082
30	.0128	25	.0089
35	.0271	CAN	.0018
14	.0167	90	.0023
15	.0212	91	.0023
16	.0251		

DATA SHEET

NOZZLE TYPE __APG-1 (AT 1, 3)__   RUN NO ___25___

PRESSURE RATIO, PRIMARY, λ_p __506.77__   PRESSURE RATIO, SECONDARY, λ_s __680.05__

CHAMBER PRESSURE __100.07__ psia   SECONDARY PRESSURE __133.97__ psia

WEIGHT FLOW RATIO, $\dot{W}_s / \dot{W}_p$ __0.0866__   AMBIENT PRESSURE __0.197__ psia

TOTAL SIDE FORCE __15.97__ LB   AMPLIFICATION FACTOR __1.424__

TOTAL AXIAL FORCE __125.70__ LB   VACUUM THRUST COEFFICIENT __1.649__

PRESSURE DISTRIBUTION

TAP LOCATION	PRESSURE RATIO p/P_c	TAP LOCATION	PRESSURE RATIO p/P_c
1	.3498	36	.0052
2	.0098	37	.0054
3	.0044	17	
31	.0066	38	.0113
4	.0093	39	.0157
5	.0250	18	.0167
6	.0201	19	.0155
7	.0137	20	.0280
8	.0201	21	.0101
9	.0300	40	.0108
10	.0268	22	.0108
32	.0052	23	.0113
11	.0118	24	.0209
12	.0052	26	.0042
33	.0049	27	.0042
34	.0081	28	.0078
13	.0140	29	.0081
30	.0130	25	.0088
35	.0270	CAN	.0020
14	.0167	90	.0012
15	.0211	91	.0010
16	.0250		

DATA SHEET

NOZZLE TYPE __APG-1 (BT 1, 3)__   RUN NO. __26__

PRESSURE RATIO, PRIMARY, λ_p __503.89__   PRESSURE RATIO, SECONDARY, λ_s __239.29__

CHAMBER PRESSURE __99.99__ psia   SECONDARY PRESSURE __47.38__ psia

WEIGHT FLOW RATIO, $\dot{W}_s / \dot{W}_p$ __0.0297__   AMBIENT PRESSURE __0.198__ psia

TOTAL SIDE FORCE __6.52__ LB   AMPLIFICATION FACTOR __1.710__

TOTAL AXIAL FORCE __124.39__ LB   VACUUM THRUST COEFFICIENT __1.633__

PRESSURE DISTRIBUTION

TAP LOCATION	PRESSURE RATIO p / P_c	TAP LOCATION	PRESSURE RATIO p / P_c
1	.0966	36	.0067
2	.0065	37	.0057
3	.0082	17	
31	.0183	38	.0067
4	.0148	39	.0053
5	.0134	18	.0121
6	.0163	19	.0121
7	.0183	20	.0077
8	.0116	21	.0057
9	.0082	40	.0065
10	.0094	22	.0097
32	.0097	23	.0109
11	.0112	24	.0057
12	.0116	26	.0043
33	.0158	27	.0043
34	.0141	28	.0080
13	.0082	29	.0043
30	.0077	25	.0043
35	.0119	CAN	.0018
14	.0156	90	.0023
15	.0082	91	.0013
16	.0092		

DATA SHEET

NOZZLE TYPE <u>APG-1 (BT 1, 3)</u>   RUN NO. <u>27</u>

PRESSURE RATIO, PRIMARY, λ_p <u>516.93</u>   PRESSURE RATIO, SECONDARY, λ_s <u>499.90</u>

CHAMBER PRESSURE <u>100.04</u> psia   SECONDARY PRESSURE <u>96.98</u> psia

WEIGHT FLOW RATIO, $\dot{w}_s / \dot{w}_p$ <u>0.0601</u>   AMBIENT PRESSURE <u>0.194</u> psia

TOTAL SIDE FORCE <u>11.97</u> LB   AMPLIFICATION FACTOR <u>1.532</u>

TOTAL AXIAL FORCE <u>126.12</u> LB   VACUUM THRUST COEFFICIENT <u>1.654</u>

PRESSURE DISTRIBUTION

TAP LOCATION	PRESSURE RATIO p/P_c	TAP LOCATION	PRESSURE RATIO p/P_c
1	.2017	36	.0094
2	.0109	37	.0102
3	.0053	17	
31	.0062	38	.0151
4	.0119	39	.0148
5	.0237	18	.0097
6	.0158	19	.0158
7	.0143	20	.0205
8	.0224	21	.0067
9	.0254	40	.0055
10	.0111	22	.0067
32	.0072	23	.0116
11	.0136	24	.0200
12	.0053	26	.0043
33	.0055	27	.0043
34	.0082	28	.0080
13	.0165	29	.0077
30	.0141	25	.0048
35	.0219	CAN	.0021
14	.0175	90	.0023
15	.0271	91	.0016
16	.0104		

DATA SHEET

NOZZLE TYPE __APG-1 (BT 1, 3)__   RUN NO. ___28___

PRESSURE RATIO, PRIMARY, λ_p ___514.57___   PRESSURE RATIO, SECONDARY, λ_s ___681.64___

CHAMBER PRESSURE ___100.09___ psia   SECONDARY PRESSURE ___132.98___ psia

WEIGHT FLOW RATIO, $\dot{W}_s / \dot{W}_p$ ___0.0835___   AMBIENT PRESSURE ___0.195___ psia

TOTAL SIDE FORCE ___15.64___ LB   AMPLIFICATION FACTOR ___1.434___

TOTAL AXIAL FORCE ___126.85___ LB   VACUUM THRUST COEFFICIENT ___1.662___

PRESSURE DISTRIBUTION

TAP LOCATION	PRESSURE RATIO p/P_c	TAP LOCATION	PRESSURE RATIO p/P_c
1	.2771	36	.0060
2	.0148	37	.0060
3	.0070	17	
31	.0043	38	.0111
4	.0077	39	.0170
5	.0187	18	.0187
6	.0259	19	.0136
7	.0160	20	.0281
8	.0185	21	.0097
9	.0308	40	.0099
10	.0305	22	.0092
32	.0065	23	.0099
11	.0160	24	.0192
12	.0048	26	.0043
33	.0048	27	.0043
34	.0072	28	.0080
13	.0102	29	.0087
30	.0097	25	.0082
35	.0234	CAN	.0023
14	.0222	90	.0023
15	.0197	91	.0016
16	.0293		

DATA SHEET

NOZZLE TYPE Conical (AR 2)   RUN NO. 29

PRESSURE RATIO, PRIMARY, λ_p 512.27   PRESSURE RATIO, SECONDARY, λ_s 314.62

CHAMBER PRESSURE 99.64 psia   SECONDARY PRESSURE 61.35 psia

WEIGHT FLOW RATIO, $\dot{W}_s / \dot{W}_p$ 0.0192   AMBIENT PRESSURE 0.195 psia

TOTAL SIDE FORCE 4.58 LB   AMPLIFICATION FACTOR 1.865

TOTAL AXIAL FORCE 124.14 LB   VACUUM THRUST COEFFICIENT 1.635

PRESSURE DISTRIBUTION

TAP LOCATION	PRESSURE RATIO p/P_c	TAP LOCATION	PRESSURE RATIO p/P_c
1	.0040	18	.0095
2	.0040	35	.0124
3	.0043	19	.0129
4	.0040	36	.0193
5	.0040	37	.0174
6	.0178	20	.0095
7	.0193	21	.0065
31	.0178	22	.0060
8	.0235	23	.0109
9	.0100	38	.0109
10	.0124	39	.0181
11	.0149	24	.0095
12	.0058	40	.0095
13	.0058	25	
30	.0050	26	.0030
14	.0178	27	.0035
32	.0354	28	.0095
33	.0183	29	.0040
15	.0223	CAN	.0026
34	.0100	90	.0030
16	.0124	91	.0030
17	.0058		

DATA SHEET

NOZZLE TYPE Conical (AR 2)   RUN NO.   30

PRESSURE RATIO, PRIMARY, λ_p 512.78   PRESSURE RATIO, SECONDARY, λ_s 487.44

CHAMBER PRESSURE 99.74 psia   SECONDARY PRESSURE 95.05 psia

WEIGHT FLOW RATIO, $\dot{W}_s / \dot{W}_p$ 0.0300   AMBIENT PRESSURE 0.195 psia

TOTAL SIDE FORCE 6.89 LB   AMPLIFICATION FACTOR 1.797

TOTAL AXIAL FORCE 123.96 LB   VACUUM THRUST COEFFICIENT 1.631

PRESSURE DISTRIBUTION

TAP LOCATION	PRESSURE RATIO p/P_c	TAP LOCATION	PRESSURE RATIO p/P_c
1	.0032	18	.0070
2	.0032	35	.0272
3	.0032	19	.0205
4	.0026	36	.0168
5	.0026	37	.0230
6	.0176	20	.0134
7	.0141	21	.0060
31	.0301	22	.0065
8	.0242	23	.0099
9	.0228	38	.0104
10	.0119	39	.0210
11	.0139	24	.0193
12	.0050	40	.0094
13	.0060	25	
30	.0040	26	.0028
14	.0117	27	.0038
32	.0274	28	.0070
33	.0188	29	.0043
15	.0245	CAN	.0026
34	.0203	90	.0026
16	.0117	91	.0028
17	.0050		

DATA SHEET

NOZZLE TYPE __Conical (AR 2)__   RUN NO. ___31___

PRESSURE RATIO, PRIMARY, λ_p __526.09__   PRESSURE RATIO, SECONDARY, λ_s __667.63__

CHAMBER PRESSURE __99.75__ psia   SECONDARY PRESSURE __126.85__ psia

WEIGHT FLOW RATIO, $\dot{W}_s / \dot{W}_p$ __0.0403__   AMBIENT PRESSURE __0.190__ psia

TOTAL SIDE FORCE __8.74__ LB   AMPLIFICATION FACTOR __1.695__

TOTAL AXIAL FORCE __124.16__ LB   VACUUM THRUST COEFFICIENT __1.632__

PRESSURE DISTRIBUTION

TAP LOCATION	PRESSURE RATIO p / P_c	TAP LOCATION	PRESSURE RATIO p / P_c
1	.0035	18	.0048
2	.0035	35	.0284
3	.0033	19	.0365
4	.0030	36	.0208
5	.0030	37	.0242
6	.0163	20	.0259
7	.0144	21	.0058
31	.0420	22	.0082
8	.0227	23	.0134
9	.0296	38	.0094
10	.0139	39	.0220
11	.0139	24	.0227
12	.0050	40	.0151
13	.0060	25	
30	.0040	26	.0028
14	.0114	27	.0038
32	.0136	28	.0092
33	.0328	29	.0058
15	.0235	CAN	.0023
34	.0272	90	.0023
16	.0129	91	.0026
17	.0045		

DATA SHEET

NOZZLE TYPE <u>Conical (AR 2)</u>   RUN NO. <u>32</u>

PRESSURE RATIO, PRIMARY, λ_p <u>512.73</u>   PRESSURE RATIO, SECONDARY, λ_s <u>704.82</u>

CHAMBER PRESSURE <u>99.73</u> psia   SECONDARY PRESSURE <u>137.44</u> psia

WEIGHT FLOW RATIO, $\dot{W}_s / \dot{W}_p$ <u>0.0436</u>   AMBIENT PRESSURE <u>0.195</u> psia

TOTAL SIDE FORCE <u>9.06</u> LB   AMPLIFICATION FACTOR <u>1.622</u>

TOTAL AXIAL FORCE <u>124.33</u> LB   VACUUM THRUST COEFFICIENT <u>1.636</u>

PRESSURE DISTRIBUTION

TAP LOCATION	PRESSURE RATIO p/P_c	TAP LOCATION	PRESSURE RATIO p/P_c
1	.0035	18	.0050
2	.0035	35	.0264
3	.0032	19	.0375
4	.0028	36	.0163
5	.0030	37	.0237
6	.0173	20	.0262
7	.0153	21	.0057
31	.0427	22	.0082
8	.0222	23	.0151
9	.0296	38	.0101
10	.0168	39	.0224
11	.0138	24	.0230
12	.0050	40	.0212
13	.0064	25	
30	.0040	26	.0028
14	.0131	27	.0037
32	.0136	28	.0092
33	.0355	29	.0057
15	.0230	CAN	.0023
34	.0294	90	.0023
16	.0148	91	.0025
17	.0045		

DATA SHEET

NOZZLE TYPE Conical (CR 1, 2, 3)　　　　　　　RUN NO. _____ 33 _____

PRESSURE RATIO, PRIMARY, λ_p _512.68_　　PRESSURE RATIO, SECONDARY, λ_s _165.54_

CHAMBER PRESSURE _99.72_ psia　　　　　　　SECONDARY PRESSURE _32.28_ psia

WEIGHT FLOW RATIO, $\dot{W}_s / \dot{W}_p$ _0.0303_　　　　AMBIENT PRESSURE _0.195_ psia

TOTAL SIDE FORCE _7.40_ LB　　　　　　　AMPLIFICATION FACTOR _1.898_

TOTAL AXIAL FORCE _124.78_ LB　　　　　　VACUUM THRUST COEFFICIENT _1.642_

PRESSURE DISTRIBUTION

TAP LOCATION	PRESSURE RATIO p/P_c	TAP LOCATION	PRESSURE RATIO p/P_c
1	.0036	18	.0048
2	.0041	35	.0277
3	.0053	19	.0270
4	.0073	36	.0221
5	.0068	37	.0144
6	.0317	20	.0093
7	.0309	21	.0056
31	.0231	22	.0051
8	.0147	23	.0263
9	.0096	38	.0149
10	.0117	39	.0194
11	.0142	24	.0093
12	.0061	40	.0095
13	.0063	25	
30	.0053	26	.0029
14	.0354	27	.0036
32	.0250	28	.0088
33	.0231	29	.0038
15	.0174	CAN	.0024
34	.0098	90	.0024
16	.0117	91	.0026
17	.0053		

DATA SHEET

NOZZLE TYPE _Conical (CR 1, 2, 3)_   RUN NO. ___34___

PRESSURE RATIO, PRIMARY, λ_p _513.18_   PRESSURE RATIO, SECONDARY, λ_s _327.08_

CHAMBER PRESSURE _99.82_ psia   SECONDARY PRESSURE _63.78_ psia

WEIGHT FLOW RATIO, $\dot{W}_s / \dot{W}_p$ _0.0604_   AMBIENT PRESSURE _0.195_ psia

TOTAL SIDE FORCE _13.07_ LB   AMPLIFICATION FACTOR _1.669_

TOTAL AXIAL FORCE _125.77_ LB   VACUUM THRUST COEFFICIENT _1.653_

PRESSURE DISTRIBUTION

TAP LOCATION	PRESSURE RATIO p/P_c	TAP LOCATION	PRESSURE RATIO p/P_c
1	.0033	18	.0038
2	.0041	35	.0348
3	.0046	19	.0358
4	.0041	36	.0250
5	.0041	37	.0280
6	.0375	20	.0250
7	.0375	21	.0056
31	.0277	22	.0041
8	.0297	23	.0193
9	.0272	38	.0265
10	.0117	39	.0233
11	.0139	24	.0255
12	.0053	40	.0225
13	.0051	25	
30	.0043	26	.0029
14	.0467	27	.0036
32	.0430	28	.0090
33	.0275	29	.0061
15	.0297	CAN	.0024
34	.0272	90	.0024
16	.0115	91	.0026
17	.0043		

DATA SHEET

NOZZLE TYPE Conical (CR 1, 2, 3)   RUN NO. 35

PRESSURE RATIO, PRIMARY, λ_p 512.88   PRESSURE RATIO, SECONDARY, λ_s 481.38

CHAMBER PRESSURE 99.76 psia   SECONDARY PRESSURE 93.87 psia

WEIGHT FLOW RATIO, $\dot{W}_s/\dot{W}_p$ 0.0897   AMBIENT PRESSURE 0.195 psia

TOTAL SIDE FORCE 17.57 LB   AMPLIFICATION FACTOR 1.493

TOTAL AXIAL FORCE 127.39 LB   VACUUM THRUST COEFFICIENT 1.675

PRESSURE DISTRIBUTION

TAP LOCATION	PRESSURE RATIO p/P_c	TAP LOCATION	PRESSURE RATIO p/P_c
1	.0036	18	.0038
2	.0036	35	.0358
3	.0036	19	.0356
4	.0031	36	.0356
5	.0033	37	.0280
6	.0383	20	.0331
7	.0356	21	.0053
31	.0437	22	.0038
8	.0326	23	.0203
9	.0358	38	.0255
10	.0368	39	.0299
11	.0233	24	.0265
12	.0051	40	.0314
13	.0051	25	
30	.0041	26	.0034
14	.0297	27	.0036
32	.0386	28	.0090
33	.0457	29	.0065
15	.0304	CAN	.0026
34	.0304	90	.0026
16	.0368	91	.0029
17	.0043		

DATA SHEET

NOZZLE TYPE Conical (AR 1, 2, 3)   RUN NO. __36__

PRESSURE RATIO, PRIMARY, λ_p __516.09__   PRESSURE RATIO, SECONDARY, λ_s ___--___

CHAMBER PRESSURE __99.88__ psia   SECONDARY PRESSURE ___--___ psia

WEIGHT FLOW RATIO, $\dot{W}_s / \dot{W}_p$ __0__   AMBIENT PRESSURE __0.194__ psia

TOTAL SIDE FORCE __-.09 *__ LB   AMPLIFICATION FACTOR ___--___

TOTAL AXIAL FORCE __124.77__ LB   VACUUM THRUST COEFFICIENT __1.639__

PRESSURE DISTRIBUTION

TAP LOCATION	PRESSURE RATIO p/P_c	TAP LOCATION	PRESSURE RATIO p/P_c
1	.0037	18	.0052
2	.0039	35	.0059
3	.0039	19	.0061
4	.0039	36	.0069
5	.0044	37	.0084
6	.0059	20	.0093
7	.0059	21	.0047
31	.0069	22	.0042
8	.0079	23	.0054
9	.0096	38	.0047
10	.0116	39	.0066
11	.0140	24	.0076
12	.0054	40	.0093
13	.0056	25	
30	.0047	26	.0030
14	.0061	27	.0034
32	.0064	28	.0091
33	.0074	29	.0037
15	.0084	CAN	.0022
34	.0098	90	.0024
16	.0116	91	.0024
17	.0047		

* Ports plugged but not filled to form smooth contour.

DATA SHEET

NOZZLE TYPE <u>Conical (AR 1, 2, 3)</u>   RUN NO. <u>37</u>

PRESSURE RATIO, PRIMARY, λ_p <u>513.03</u>   PRESSURE RATIO, SECONDARY, λ_s <u>164.87</u>

CHAMBER PRESSURE <u>99.79</u> psia   SECONDARY PRESSURE <u>32.15</u> psia

WEIGHT FLOW RATIO, $\dot{W}_s/\dot{W}_p$ <u>0.0301</u>   AMBIENT PRESSURE <u>0.195</u> psia

TOTAL SIDE FORCE <u>7.15</u> LB   AMPLIFICATION FACTOR <u>1.860</u>

TOTAL AXIAL FORCE <u>123.96</u> LB   VACUUM THRUST COEFFICIENT <u>1.632</u>

PRESSURE DISTRIBUTION

TAP LOCATION	PRESSURE RATIO p/P_c	TAP LOCATION	PRESSURE RATIO p/P_c
1	.0030	18	.0035
2	.0030	35	.0205
3	.0035	19	.0242
4	.0030	36	.0200
5	.0030	37	.0242
6	.0296	20	.0151
7	.0362	21	.0050
31	.0224	22	.0055
8	.0244	23	.0148
9	.0269	38	.0119
10	.0114	39	.0197
11	.0138	24	.0205
12	.0045	40	.0099
13	.0047	25	
30	.0040	26	.0030
14	.0261	27	.0035
32	.0335	28	.0092
33	.0212	29	.0040
15	.0261	CAN	.0023
34	.0222	90	.0023
16	.0114	91	.0025
17	.0040		

DATA SHEET

NOZZLE TYPE Conical (AR 1, 2, 3)   RUN NO. 38

PRESSURE RATIO, PRIMARY, λ_p 507.80   PRESSURE RATIO, SECONDARY, λ_s 218.77

CHAMBER PRESSURE 99.77 psia   SECONDARY PRESSURE 42.88 psia

WEIGHT FLOW RATIO, $\dot{W}_s / \dot{W}_p$ 0.0404   AMBIENT PRESSURE 0.196 psia

TOTAL SIDE FORCE 9.29 LB   AMPLIFICATION FACTOR 1.800

TOTAL AXIAL FORCE 124.00 LB   VACUUM THRUST COEFFICIENT 1.632

PRESSURE DISTRIBUTION

TAP LOCATION	PRESSURE RATIO p/P_c	TAP LOCATION	PRESSURE RATIO p/P_c
1	.0041	18	.0043
2	.0041	35	.0193
3	.0041	19	.0260
4	.0036	36	.0181
5	.0038	37	.0250
6	.0238	20	.0260
7	.0282	21	.0053
31	.0287	22	.0053
8	.0275	23	.0189
9	.0302	38	.0129
10	.0142	39	.0196
11	.0139	24	.0225
12	.0053	40	.0203
13	.0058	25	
30	.0043	26	.0031
14	.0238	27	.0038
32	.0304	28	.0090
33	.0260	29	.0051
15	.0260	CAN	.0026
34	.0297	90	.0026
16	.0132	91	.0029
17	.0046		

DATA SHEET

NOZZLE TYPE <u>Conical (AR 1, 2, 3)</u>　　　　　　　RUN NO. <u>39</u>

PRESSURE RATIO, PRIMARY, λ_p <u>531.34</u>　　PRESSURE RATIO, SECONDARY, λ_s <u>282.07</u>

CHAMBER PRESSURE <u>99.70</u> psia　　　　　　SECONDARY PRESSURE <u>53.03</u> psia

WEIGHT FLOW RATIO, $\dot{w}_s/\dot{w}_p$ <u>0.0500</u>　　　AMBIENT PRESSURE <u>0.188</u> psia

TOTAL SIDE FORCE <u>10.87</u> LB　　　　AMPLIFICATION FACTOR <u>1.702</u>

TOTAL AXIAL FORCE <u>124.07</u> LB　　　VACUUM THRUST COEFFICIENT <u>1.632</u>

PRESSURE DISTRIBUTION

TAP LOCATION	PRESSURE RATIO p/P_c	TAP LOCATION	PRESSURE RATIO p/P_c
1	.0031	18	.0033
2	.0031	35	.0191
3	.0031	19	.0272
4	.0026	36	.0196
5	.0023	37	.0250
6	.0242	20	.0284
7	.0267	21	.0048
31	.0338	22	.0045
8	.0272	23	.0213
9	.0314	38	.0161
10	.0240	39	.0198
11	.0139	24	.0230
12	.0040	40	.0245
13	.0043	25	
30	.0033	26	.0026
14	.0245	27	.0031
32	.0284	28	.0087
33	.0304	29	.0053
15	.0257	CAN	.0070
34	.0309	90	.0067
16	.0210	91	.0070
17	.0033		

DATA SHEET

NOZZLE TYPE __Conical (AR 1, 2, 3)__   RUN NO. __40__

PRESSURE RATIO, PRIMARY, λ_p __505.05__   PRESSURE RATIO, SECONDARY, λ_s __319.59__

CHAMBER PRESSURE __99.73__ psia   SECONDARY PRESSURE __62.96__ psia

WEIGHT FLOW RATIO, $\dot{W}_s / \dot{W}_p$ __0.0600__   AMBIENT PRESSURE __0.197__ psia

TOTAL SIDE FORCE __12.45__ LB   AMPLIFICATION FACTOR __1.620__

TOTAL AXIAL FORCE __124.18__ LB   VACUUM THRUST COEFFICIENT __1.635__

PRESSURE DISTRIBUTION

TAP LOCATION	PRESSURE RATIO p/P_c	TAP LOCATION	PRESSURE RATIO p/P_c
1	.0036	18	.0036
2	.0036	35	.0208
3	.0036	19	.0285
4	.0029	36	.0228
5	.0033	37	.0235
6	.0235	20	.0299
7	.0253	21	.0043
31	.0383	22	.0043
8	.0287	23	.0211
9	.0327	38	.0166
10	.0295	39	.0191
11	.0139	24	.0226
12	.0046	40	.0270
13	.0051	25	
30	.0038	26	.0029
14	.0238	27	.0036
32	.0258	28	.0093
33	.0346	29	.0058
15	.0265	CAN	.0026
34	.0327	90	.0026
16	.0287	91	.0029
17	.0038		

DATA SHEET

NOZZLE TYPE <u>Conical (AR 1, 2, 3)</u>   RUN NO. <u>41</u>

PRESSURE RATIO, PRIMARY, λ_p <u>507.88</u>   PRESSURE RATIO, SECONDARY, λ_s <u>375.35</u>

CHAMBER PRESSURE <u>99.79</u> psia   SECONDARY PRESSURE <u>73.57</u> psia

WEIGHT FLOW RATIO, $\dot{W}_s / \dot{W}_p$ <u>0.696</u>   AMBIENT PRESSURE <u>0.196</u> psia

TOTAL SIDE FORCE <u>14.42</u> LB   AMPLIFICATION FACTOR <u>1.603</u>

TOTAL AXIAL FORCE <u>125.38</u> LB   VACUUM THRUST COEFFICIENT <u>1.649</u>

PRESSURE DISTRIBUTION

TAP LOCATION	PRESSURE RATIO p/P_c	TAP LOCATION	PRESSURE RATIO p/P_c
1	.0032	18	.0032
2	.0032	35	.0209
3	.0030	19	.0278
4	.0027	36	.0293
5	.0030	37	.0229
6	.0226	20	.0308
7	.0229	21	.0047
31	.0921	22	.0047
8	.0315	23	.0219
9	.0347	38	.0185
10	.0342	39	.0194
11	.0140	24	.0214
12	.0042	40	.0283
13	.0047	25	
30	.0032	26	.0030
14	.0207	27	.0034
32	.0226	28	.0089
33	.0349	29	.0059
15	.0298	CAN	.0025
34	.0337	90	.0025
16	.0335	91	.0025
17	.0034		

DATA SHEET

NOZZLE TYPE <u>Conical (AR 1, 2, 3)</u>   RUN NO. <u>42</u>

PRESSURE RATIO, PRIMARY, λ_p <u>507.58</u>   PRESSURE RATIO, SECONDARY, λ_s <u>431.43</u>

CHAMBER PRESSURE <u>99.73</u> psia   SECONDARY PRESSURE <u>84.56</u> psia

WEIGHT FLOW RATIO, $\dot{W}_s / \dot{W}_p$ <u>0.0803</u>   AMBIENT PRESSURE <u>0.196</u> psia

TOTAL SIDE FORCE <u>15.80</u> LB   AMPLIFICATION FACTOR <u>1.518</u>

TOTAL AXIAL FORCE <u>125.73</u> LB   VACUUM THRUST COEFFICIENT <u>1.654</u>

PRESSURE DISTRIBUTION

TAP LOCATION	PRESSURE RATIO p/P_c	TAP LOCATION	PRESSURE RATIO p/P_c
1	.0036	18	.0041
2	.0036	35	.0199
3	.0036	19	.0273
4	.0034	36	.0379
5	.0036	37	.0248
6	.0233	20	.0302
7	.0241	21	.0044
31	.0453	22	.0044
8	.0332	23	.0221
9	.0357	38	.0214
10	.0366	39	.0219
11	.0162	24	.0211
12	.0054	40	.0285
13	.0061	25	
30	.0044	26	.0029
14	.0209	27	.0036
32	.0229	28	.0091
33	.0347	29	.0061
15	.0329	CAN	.0029
34	.0334	90	.0027
16	.0359	91	.0029
17	.0041		

DATA SHEET

NOZZLE TYPE Conical (AR 1, 2, 3)   RUN NO. 43

PRESSURE RATIO, PRIMARY, λ_p 507.52   PRESSURE RATIO, SECONDARY, λ_s 476.53

CHAMBER PRESSURE 99.72 psia   SECONDARY PRESSURE 93.40 psia

WEIGHT FLOW RATIO, $\dot{w}_s / \dot{w}_p$ 0.0893   AMBIENT PRESSURE 0.196 psia

TOTAL SIDE FORCE 16.98 LB   AMPLIFICATION FACTOR 1.455

TOTAL AXIAL FORCE 126.10 LB   VACUUM THRUST COEFFICIENT 1.659

PRESSURE DISTRIBUTION

TAP LOCATION	PRESSURE RATIO p/P_c	TAP LOCATION	PRESSURE RATIO p/P_c
1	.0035	18	.0040
2	.0035	35	.0188
3	.0035	19	.0265
4	.0033	36	.0326
5	.0035	37	.0277
6	.0258	20	.0306
7	.0265	21	.0050
31	.0476	22	.0045
8	.0348	23	.0218
9	.0348	38	.0242
10	.0373	39	.0252
11	.0228	24	.0223
12	.0053	40	.0289
13	.0060	25	
30	.0058	26	.0028
14	.0218	27	.0038
32	.0237	28	.0092
33	.0351	29	.0063
15	.0351	CAN	.0028
34	.0333	90	.0028
16	.0370	91	.0028
17	.0043		

DATA SHEET

NOZZLE TYPE Conical (BR 1, 2, 3)   RUN NO.   44

PRESSURE RATIO, PRIMARY, λ_p 507.90   PRESSURE RATIO, SECONDARY, λ_s 162.81

CHAMBER PRESSURE 99.75 psia   SECONDARY PRESSURE 31.91 psia

WEIGHT FLOW RATIO, $\dot{W}_s / \dot{W}_p$ 0.0305   AMBIENT PRESSURE 0.196 psia

TOTAL SIDE FORCE 7.36 LB   AMPLIFICATION FACTOR 1.848

TOTAL AXIAL FORCE 125.05 LB   VACUUM THRUST COEFFICIENT 1.645

PRESSURE DISTRIBUTION

TAP LOCATION	PRESSURE RATIO p/P_c	TAP LOCATION	PRESSURE RATIO p/P_c
1	.0033	18	.0043
2	.0033	35	.0228
3	.0038	19	.0258
4	.0041	36	.0218
5	.0038	37	.0221
6	.0322	20	.0090
7	.0314	21	.0053
31	.0250	22	.0046
8	.0248	23	.0166
9	.0100	38	.0122
10	.0117	39	.0191
11	.0142	24	.0149
12	.0053	40	.0093
13	.0051	25	
30	.0043	26	.0031
14	.0339	27	.0041
32	.0294	28	.0090
33	.0240	29	.0041
15	.0250	CAN	.0026
34	.0100	90	.0026
16	.0117	91	.0029
17	.0051		

DATA SHEET

NOZZLE TYPE Conical (BR 1, 2, 3)   RUN NO. 45

PRESSURE RATIO, PRIMARY, λ_p 523.63   PRESSURE RATIO, SECONDARY, λ_s 318.02

CHAMBER PRESSURE 99.69 psia   SECONDARY PRESSURE 62.65 psia

WEIGHT FLOW RATIO, $\dot{W}_s/\dot{W}_p$ 0.0604   AMBIENT PRESSURE 0.197 psia

TOTAL SIDE FORCE 12.77 LB   AMPLIFICATION FACTOR 1.639

TOTAL AXIAL FORCE 125.13 LB   VACUUM THRUST COEFFICIENT 1.648

PRESSURE DISTRIBUTION

TAP LOCATION	PRESSURE RATIO p/P_c	TAP LOCATION	PRESSURE RATIO p/P_c
1	.0034	18	.0038
2	.0034	35	.0216
3	.0031	19	.0287
4	.0029	36	.0231
5	.0031	37	.0255
6	.0302	20	.0290
7	.0307	21	.0046
31	.0393	22	.0036
8	.0275	23	.0221
9	.0332	38	.0211
10	.0319	39	.0211
11	.0142	24	.0238
12	.0051	40	.0238
13	.0051	25	
30	.0041	26	.0026
14	.0282	27	.0034
32	.0329	28	.0090
33	.0337	29	.0061
15	.0255	CAN	.0024
34	.0319	90	.0024
16	.0300	91	.0026
17	.0041		

DATA SHEET

NOZZLE TYPE Conical (BR 1, 2, 3) RUN NO. 46

PRESSURE RATIO, PRIMARY, λ_p 512.65   PRESSURE RATIO, SECONDARY, λ_s 475.90

CHAMBER PRESSURE 99.72 psia   SECONDARY PRESSURE 92.80 psia

WEIGHT FLOW RATIO, $\dot{W}_s / \dot{W}_p$ 0.0900   AMBIENT PRESSURE 0.195 psia

TOTAL SIDE FORCE 17.40 LB   AMPLIFICATION FACTOR 1.494

TOTAL AXIAL FORCE 125.55 LB   VACUUM THRUST COEFFICIENT 1.652

PRESSURE DISTRIBUTION

TAP LOCATION	PRESSURE RATIO p/P_c	TAP LOCATION	PRESSURE RATIO p/P_c
1	.0031	18	.0036
2	.0029	35	.0216
3	.0029	19	.0307
4	.0026	36	.0307
5	.0029	37	.0248
6	.0295	20	.0297
7	.0255	21	.0048
31	.0474	22	.0038
8	.0312	23	.0213
9	.0346	38	.0238
10	.0376	39	.0258
11	.0263	24	.0238
12	.0048	40	.0295
13	.0051	25	
30	.0038	26	.0026
14	.0287	27	.0026
32	.0292	28	.0088
33	.0381	29	.0063
15	.0297	CAN	.0021
34	.0332	90	.0021
16	.0368	91	.0026
17	.0041		

DATA SHEET

NOZZLE TYPE __APG-1 (AR 2)__   RUN NO. __47__

PRESSURE RATIO, PRIMARY, λ_p __519.18__   PRESSURE RATIO, SECONDARY, λ_s __364.53__

CHAMBER PRESSURE __99.71__ psia   SECONDARY PRESSURE __69.99__ psia

WEIGHT FLOW RATIO, $\dot{W}_s / \dot{W}_p$ __0.0200__   AMBIENT PRESSURE __0.192__ psia

TOTAL SIDE FORCE __5.74__ LB   AMPLIFICATION FACTOR __2.245__

TOTAL AXIAL FORCE __124.16__ LB   VACUUM THRUST COEFFICIENT __1.634__

PRESSURE DISTRIBUTION

TAP LOCATION	PRESSURE RATIO p / P_c	TAP LOCATION	PRESSURE RATIO p / P_c
1	.1237	36	.0129
2	.0082	37	.0085
3	.0208	17	
31	.0112	38	.0107
4	.0139	39	.0136
5	.0159	18	.0124
6	.0109	19	.0058
7	.0058	20	.0077
8	.0063	21	.0067
9	.0085	40	.0097
10	.0100	22	.0114
32	.0058	23	.0050
11	.0112	24	.0058
12	.0198	26	.0043
33	.0141	27	.0043
34	.0109	28	.0080
13	.0141	29	.0043
30	.0139	25	.0043
35	.0151	CAN	.0018
14	.0087	90	.0013
15	.0062	91	.0013
16	.0092		

DATA SHEET

NOZZLE TYPE APG-1 (AR 2)   RUN NO. 48

PRESSURE RATIO, PRIMARY, λ_p 523.87   PRESSURE RATIO, SECONDARY, λ_s 490.16

CHAMBER PRESSURE 99.84 psia   SECONDARY PRESSURE 93.62 psia

WEIGHT FLOW RATIO, $\dot{W}_s/\dot{W}_p$ 0.0301   AMBIENT PRESSURE 0.191 psia

TOTAL SIDE FORCE 8.38 LB   AMPLIFICATION FACTOR 2.169

TOTAL AXIAL FORCE 124.56 LB   VACUUM THRUST COEFFICIENT 1.636

PRESSURE DISTRIBUTION

TAP LOCATION	PRESSURE RATIO p/P_c	TAP LOCATION	PRESSURE RATIO p/P_c
1	.1858	36	.0126
2	.0079	37	.0180
3	.0089	17	
31	.0190	38	.0094
4	.0126	39	.0121
5	.0146	18	.0148
6	.0170	19	.0084
7	.0148	20	.0077
8	.0064	21	.0074
9	.0089	40	.0082
10	.0104	22	.0126
32	.0057	23	.0121
11	.0116	24	.0057
12	.0084	26	.0045
33	.0214	27	.0047
34	.0136	28	.0079
13	.0123	29	.0047
30	.0121	25	.0047
35	.0165	CAN	.0021
14	.0168	90	.0015
15	.0062	91	.0013
16	.0094		

DATA SHEET

NOZZLE TYPE __APG-1 (AR 2)__   RUN NO. __49__

PRESSURE RATIO, PRIMARY, λ_p __523.35__   PRESSURE RATIO, SECONDARY, λ_s __652.41__

CHAMBER PRESSURE __99.74__ psia   SECONDARY PRESSURE __124.61__ psia

WEIGHT FLOW RATIO, $\dot{W}_s / \dot{W}_p$ __0.0402__   AMBIENT PRESSURE __0.191__ psia

TOTAL SIDE FORCE __9.87__ LB   AMPLIFICATION FACTOR __1.925__

TOTAL AXIAL FORCE __123.78__ LB   VACUUM THRUST COEFFICIENT __1.628__

PRESSURE DISTRIBUTION

TAP LOCATION	PRESSURE RATIO p/P_c	TAP LOCATION	PRESSURE RATIO p/P_c
1	.2465	36	.0074
2	.0076	37	.0185
3	.0071	17	
31	.0236	38	.0118
4	.0145	39	.0118
5	.0140	18	.0145
6	.0177	19	.0155
7	.0185	20	.0076
8	.0106	21	.0130
9	.0089	40	.0079
10	.0103	22	.0116
32	.0054	23	.0150
11	.0116	24	.0066
12	.0069	26	.0042
33	.0153	27	.0044
34	.0209	28	.0079
13	.0123	29	.0047
30	.0118	25	.0047
35	.0170	CAN	.0020
14	.0177	90	.0012
15	.0096	91	.0012
16	.0091		

DATA SHEET

NOZZLE TYPE APG-1 (AR 2)   RUN NO. 50

PRESSURE RATIO, PRIMARY, λ_p 510.40   PRESSURE RATIO, SECONDARY, λ_s 703.90

CHAMBER PRESSURE 99.78 psia   SECONDARY PRESSURE 137.26 psia

WEIGHT FLOW RATIO, $\dot{W}_s/\dot{W}_p$ 0.0444   AMBIENT PRESSURE 0.195 psia

TOTAL SIDE FORCE 10.44 LB   AMPLIFICATION FACTOR 1.838

TOTAL AXIAL FORCE 124.08 LB   VACUUM THRUST COEFFICIENT 1.632

PRESSURE DISTRIBUTION

TAP LOCATION	PRESSURE RATIO p/P_c	TAP LOCATION	PRESSURE RATIO p/P_c
1	.2707	36	.0064
2	.0071	37	.0162
3	.0071	17	
31	.0233	38	.0145
4	.0164	39	.0113
5	.0140	18	.0145
6	.0180	19	.0174
7	.0194	20	.0078
8	.0135	21	.0150
9	.0091	40	.0086
10	.0103	22	.0113
32	.0056	23	.0157
11	.0175	24	.0088
12	.0076	26	.0041
33	.0108	27	.0041
34	.0231	28	.0078
13	.0130	29	.0041
30	.0125	25	.0046
35	.0174	CAN	.0021
14	.0177	90	.0017
15	.0130	91	.0012
16	.0093		

DATA SHEET

NOZZLE TYPE __APG-1 (CR 1, 2, 3)__   RUN NO. __51__

PRESSURE RATIO, PRIMARY, λ_p __500.54__   PRESSURE RATIO, SECONDARY, λ_s __167.39__

CHAMBER PRESSURE __99.82__ psia   SECONDARY PRESSURE __33.31__ psia

WEIGHT FLOW RATIO, $\dot{W}_s / \dot{W}_p$ __0.0302__   AMBIENT PRESSURE __0.199__ psia

TOTAL SIDE FORCE __8.64__ LB   AMPLIFICATION FACTOR __2.235__

TOTAL AXIAL FORCE __124.13__ LB   VACUUM THRUST COEFFICIENT __1.633__

PRESSURE DISTRIBUTION

TAP LOCATION	PRESSURE RATIO p/P_c	TAP LOCATION	PRESSURE RATIO p/P_c
1	.0617	36	.0036
2	.0209	37	.0177
3	.0125	17	
31	.0159	38	.0145
4	.0164	39	.0150
5	.0132	18	.0120
6	.0061	19	.0061
7	.0056	20	.0081
8	.0066	21	.0120
9	.0086	40	.0115
10	.0098	22	.0130
32	.0233	23	.0051
11	.0110	24	.0056
12	.0243	26	.0046
33	.0164	27	.0046
34	.0164	28	.0083
13	.0164	29	.0046
30	.0164	25	.0046
35	.0086	CAN	.0017
14	.0056	90	.0031
15	.0061	91	.0017
16	.0090		

DATA SHEET

NOZZLE TYPE __APG-1 (CR 1, 2, 3)__

RUN NO. ___52___

PRESSURE RATIO, PRIMARY, λ_p ___510.05___

PRESSURE RATIO, SECONDARY, λ_s ___336.77___

CHAMBER PRESSURE __99.71__ psia

SECONDARY PRESSURE __65.67__ psia

WEIGHT FLOW RATIO, $\dot{W}_s / \dot{W}_p$ ___0.0601___

AMBIENT PRESSURE __0.195__ psia

TOTAL SIDE FORCE ___14.81___ LB

AMPLIFICATION FACTOR ___1.910___

TOTAL AXIAL FORCE __125.21__ LB

VACUUM THRUST COEFFICIENT ___1.648___

PRESSURE DISTRIBUTION

TAP LOCATION	PRESSURE RATIO p/P_c	TAP LOCATION	PRESSURE RATIO p/P_c
1	.1214	36	.0032
2	.0116	37	.0091
3	.0185	17	
31	.0229	38	.0204
4	.0195	39	.0167
5	.0190	18	.0165
6	.0204	19	.0204
7	.0214	20	.0076
8	.0209	21	.0052
9	.0084	40	.0155
10	.0099	22	.0130
32	.0084	23	.0180
11	.0113	24	.0200
12	.0103	26	.0042
33	.0172	27	.0042
34	.0234	28	.0076
13	.0192	29	.0089
30	.0192	25	.0089
35	.0185	CAN	.0017
14	.0200	90	.0022
15	.0204	91	.0017
16	.0091		

DATA SHEET

NOZZLE TYPE <u>APG-1 (CR 1</u>, 2, 3)   RUN NO. <u>53</u>

PRESSURE RATIO, PRIMARY, λ_p <u>504.65</u> PRESSURE RATIO, SECONDARY, λ_s <u>488.88</u>

CHAMBER PRESSURE <u>99.65</u> psia   SECONDARY PRESSURE <u>96.31</u> psia

WEIGHT FLOW RATIO, $\dot{W}_s / \dot{W}_p$ <u>0.0896</u>   AMBIENT PRESSURE <u>0.197</u> psia

TOTAL SIDE FORCE <u>19.14</u> LB   AMPLIFICATION FACTOR <u>1.645</u>

TOTAL AXIAL FORCE <u>125.96</u> LB   VACUUM THRUST COEFFICIENT <u>1.659</u>

PRESSURE DISTRIBUTION

TAP LOCATION	PRESSURE RATIO p/P_c	TAP LOCATION	PRESSURE RATIO p/P_c
1	.1790	36	.0027
2	.0136	37	.0091
3	.0150	17	
31	.0279	38	.0200
4	.0239	39	.0229
5	.0210	18	.0195
6	.0219	19	.0219
7	.0229	20	.0111
8	.0234	21	.0047
9	.0121	40	.0121
10	.0096	22	.0170
32	.0081	23	.0180
11	.0111	24	.0229
12	.0111	26	.0042
33	.0126	27	.0042
34	.0237	28	.0076
13	.0239	29	.0116
30	.0234	25	.0121
35	.0219	CAN	.0027
14	.0210	90	.0027
15	.0234	91	.0017
16	.0091		

DATA SHEET

NOZZLE TYPE __APG-1 (AR 1, 2, 3)__

RUN NO. __54__

PRESSURE RATIO, PRIMARY, λ_p __513.84__

PRESSURE RATIO, SECONDARY, λ_s __--__

CHAMBER PRESSURE __99.59__ psia

SECONDARY PRESSURE __--__ psia

WEIGHT FLOW RATIO, $\dot{W}_s / \dot{W}_p$ __0__

AMBIENT PRESSURE __0.195__ psia

TOTAL SIDE FORCE __0.36 *__ LB

AMPLIFICATION FACTOR __--__

TOTAL AXIAL FORCE __124.85__ LB

VACUUM THRUST COEFFICIENT __1.639__

PRESSURE DISTRIBUTION

TAP LOCATION	PRESSURE RATIO p/P_c	TAP LOCATION	PRESSURE RATIO p/P_c
1	.0064	36	.0057
2	.0054	37	.0050
3	.0050	17	
31	.0047	38	.0047
4	.0045	39	.0047
5	.0052	18	.0050
6	.0054	19	.0059
7	.0059	20	.0076
8	.0064	21	.0052
9	.0088	40	.0045
10	.0100	22	.0047
32	.0071	23	.0050
11	.0111	24	.0057
12	.0062	26	.0040
33	.0057	27	.0040
34	.0057	28	.0076
13	.0059	29	.0043
30	.0062	25	.0045
35	.0047	CAN	.0017
14	.0052	90	.0017
15	.0062	91	.0012
16	.0090		

* Ports plugged but not filled to form smooth contour.

DATA SHEET

NOZZLE TYPE __APG-1 (AR 1, 2, 3)__   RUN NO. ___55___

PRESSURE RATIO, PRIMARY, λ_p __523.17__   PRESSURE RATIO, SECONDARY, λ_s __173.46__

CHAMBER PRESSURE __99.71__ psia   SECONDARY PRESSURE __33.13__ psia

WEIGHT FLOW RATIO, $\dot{W}_s / \dot{W}_p$ __0.0302__   AMBIENT PRESSURE __0.191__ psia

TOTAL SIDE FORCE __8.29__ LB   AMPLIFICATION FACTOR __2.139__

TOTAL AXIAL FORCE __124.64__ LB   VACUUM THRUST COEFFICIENT __1.639__

PRESSURE DISTRIBUTION

TAP LOCATION	PRESSURE RATIO p/P_c	TAP LOCATION	PRESSURE RATIO p/P_c
1	.0615	36	.0083
2	.0152	37	.0164
3	.0221	17	
31	.0164	38	.0105
4	.0166	39	.0132
5	.0169	18	.0152
6	.0166	19	.0073
7	.0102	20	.0078
8	.0063	21	.0085
9	.0083	40	.0083
10	.0098	22	.0125
32	.0068	23	.0115
11	.0107	24	.0056
12	.0122	26	.0043
33	.0196	27	.0046
34	.0157	28	.0078
13	.0144	29	.0043
30	.0149	25	.0046
35	.0166	CAN	.0019
14	.0159	90	.0019
15	.0066	91	.0009
16	.0095		

DATA SHEET

NOZZLE TYPE APG-1 (AR 1, 2, 3)

PRESSURE RATIO, PRIMARY, λ_p 507.58

PRESSURE RATIO, SECONDARY, λ_s 224.90

CHAMBER PRESSURE 99.73 psia

SECONDARY PRESSURE 44.08 psia

WEIGHT FLOW RATIO, $\dot{W}_s / \dot{W}_p$ 0.0405

AMBIENT PRESSURE 0.196 psia

TOTAL SIDE FORCE 10.42 LB

AMPLIFICATION FACTOR 2.012

TOTAL AXIAL FORCE 124.00 LB

VACUUM THRUST COEFFICIENT 1.632

PRESSURE DISTRIBUTION

TAP LOCATION	PRESSURE RATIO p/P_c	TAP LOCATION	PRESSURE RATIO p/P_c
1	.0824	36	.0046
2	.0102	37	.0125
3	.0262	17	
31	.0166	38	.0159
4	.0166	39	.0125
5	.0181	18	.0144
6	.0186	19	.0171
7	.0174	20	.0078
8	.0083	21	.0117
9	.0083	40	.0082
10	.0098	22	.0112
32	.0038	23	.0152
11	.0107	24	.0083
12	.0078	26	.0043
33	.0147	27	.0043
34	.0186	28	.0078
13	.0154	29	.0043
30	.0159	25	.0043
35	.0174	CAN	.0019
14	.0184	90	.0014
15	.0085	91	.0009
16	.0092		

DATA SHEET

NOZZLE TYPE __APG-1 (AR 1, 2, 3)__   RUN NO. ___57___

PRESSURE RATIO, PRIMARY, λ_p __502.60__   PRESSURE RATIO, SECONDARY, λ_s __275.35__

CHAMBER PRESSURE __99.74__ psia   SECONDARY PRESSURE __54.52__ psia

WEIGHT FLOW RATIO, $\dot{W}_s / \dot{W}_p$ __0.0504__   AMBIENT PRESSURE __0.198__ psia

TOTAL SIDE FORCE __12.37__ LB   AMPLIFICATION FACTOR __1.909__

TOTAL AXIAL FORCE __124.74__ LB   VACUUM THRUST COEFFICIENT __1.642__

PRESSURE DISTRIBUTION

TAP LOCATION	PRESSURE RATIO p / P_c	TAP LOCATION	PRESSURE RATIO p / P_c
1	.1001	36	.0040
2	.0107	37	.0094
3	.0282	17	
31	.0191	38	.0168
4	.0176	39	.0144
5	.0186	18	.0141
6	.0200	19	.0193
7	.0196	20	.0077
8	.0131	21	.0122
9	.0085	40	.0117
10	.0099	22	.0109
32	.0050	23	.0166
11	.0114	24	.0161
12	.0055	26	.0043
33	.0109	27	.0043
34	.0215	28	.0077
13	.0173	29	.0053
30	.0173	25	.0058
35	.0181	CAN	.0018
14	.0198	90	.0016
15	.0149	91	.0008
16	.0094		

DATA SHEET

NOZZLE TYPE __APG-1 (AR 1, 2, 3)__   RUN NO. __58__

PRESSURE RATIO, PRIMARY, λ_p __508.25__   PRESSURE RATIO, SECONDARY, λ_s __331.99__

CHAMBER PRESSURE __99.86__ psia   SECONDARY PRESSURE __65.07__ psia

WEIGHT FLOW RATIO, $\dot{W}_s / \dot{W}_p$ __0.0600__   AMBIENT PRESSURE __0.196__ psia

TOTAL SIDE FORCE __13.99__ LB   AMPLIFICATION FACTOR __1.805__

TOTAL AXIAL FORCE __125.32__ LB   VACUUM THRUST COEFFICIENT __1.647__

PRESSURE DISTRIBUTION

TAP LOCATION	PRESSURE RATIO p/P_c	TAP LOCATION	PRESSURE RATIO p/P_c
1	.1233	36	.0072
2	.0107	37	.0099
3	.0274	17	
31	.0205	38	.0205
4	.0183	39	.0200
5	.0180	18	.0178
6	.0198	19	.0232
7	.0203	20	.0109
8	.0185	21	.0139
9	.0090	40	.0180
10	.0099	22	.0151
32	.0055	23	.0193
11	.0116	24	.0232
12	.0060	26	.0072
33	.0090	27	.0072
34	.0205	28	.0107
13	.0190	29	.0102
30	.0188	25	.0121
35	.0210	CAN	.0048
14	.0225	90	.0045
15	.0225	91	.0038
16	.0124		

DATA SHEET

NOZZLE TYPE __APG-1 (AR 1, 2, 3)__   RUN NO. ___59___

PRESSURE RATIO, PRIMARY, λ_p __513.36__   PRESSURE RATIO, SECONDARY, λ_s __384.21__

CHAMBER PRESSURE __99.86__ psia   SECONDARY PRESSURE __74.92__ psia

WEIGHT FLOW RATIO, $\dot{W}_s / \dot{W}_p$ __0.0696__   AMBIENT PRESSURE __0.195__ psia

TOTAL SIDE FORCE __15.63__ LB   AMPLIFICATION FACTOR __1.737__

TOTAL AXIAL FORCE __125.50__ LB   VACUUM THRUST COEFFICIENT __1.649__

PRESSURE DISTRIBUTION

TAP LOCATION	PRESSURE RATIO p/P_c	TAP LOCATION	PRESSURE RATIO p/P_c
1	.1375	36	.0060
2	.0099	37	.0084
3	.0150	17	
31	.0155	38	.0173
4	.0197	39	.0173
5	.0192	18	.0146
6	.0192	19	.0197
7	.0197	20	.0101
8	.0210	21	.0114
9	.0116	40	.0150
10	.0094	22	.0123
32	.0067	23	.0156
11	.0109	24	.0207
12	.0082	26	.0040
33	.0089	27	.0045
34	.0170	28	.0074
13	.0205	29	.0077
30	.0207	25	.0084
35	.0192	CAN	.0015
14	.0178	90	.0013
15	.0210	91	.0013
16	.0094		

NOZZLE TYPE __APG-1 (AR 1, 2, 3)__   RUN NO. ___60___

PRESSURE RATIO, PRIMARY, λ_p __511.03__   PRESSURE RATIO, SECONDARY, λ_s __438.56__

CHAMBER PRESSURE __99.91__ psia   SECONDARY PRESSURE __85.52__ psia

WEIGHT FLOW RATIO, $\dot{W}_s / \dot{W}_p$ __0.0802__   AMBIENT PRESSURE __0.195__ psia

TOTAL SIDE FORCE __17.33__ LB   AMPLIFICATION FACTOR __1.676__

TOTAL AXIAL FORCE __125.14__ LB   VACUUM THRUST COEFFICIENT __1.644__

PRESSURE DISTRIBUTION

TAP LOCATION	PRESSURE RATIO p / P_c	TAP LOCATION	PRESSURE RATIO p / P_c
1	.1540	36	.0089
2	.0092	37	.0138
3	.0141	17	
31	.0172	38	.0172
4	.0200	39	.0153
5	.0209	18	.0133
6	.0195	19	.0175
7	.0131	20	.0146
8	.0209	21	.0141
9	.0187	40	.0131
10	.0106	22	.0106
32	.0106	23	.0141
11	.0111	24	.0195
12	.0136	26	.0042
33	.0136	27	.0042
34	.0170	28	.0077
13	.0202	29	.0067
30	.0209	25	.0067
35	.0212	CAN	.0023
14	.0168	90	.0018
15	.0212	91	.0008
16	.0099		

DATA SHEET

NOZZLE TYPE __APG-1 (AR 1, 2, 3)__   RUN NO. __61__

PRESSURE RATIO, PRIMARY, λ_p __503.91__   PRESSURE RATIO, SECONDARY, λ_s __479.34__

CHAMBER PRESSURE __100.00__ psia   SECONDARY PRESSURE __94.91__ psia

WEIGHT FLOW RATIO, $\dot{W}_s / \dot{W}_p$ __0.0895__   AMBIENT PRESSURE __0.198__ psia

TOTAL SIDE FORCE __18.60__ LB   AMPLIFICATION FACTOR __1.616__

TOTAL AXIAL FORCE __124.78__ LB   VACUUM THRUST COEFFICIENT __1.638__

PRESSURE DISTRIBUTION

TAP LOCATION	PRESSURE RATIO p/P_c	TAP LOCATION	PRESSURE RATIO p/P_c
1	.1729	36	.0096
2	.0088	37	.0155
3	.0133	17	
31	.0165	38	.0169
4	.0187	39	.0162
5	.0206	18	.0142
6	.0211	19	.0157
7	.0184	20	.0167
8	.0206	21	.0152
9	.0214	40	.0133
10	.0128	22	.0110
32	.0115	23	.0138
11	.0110	24	.0192
12	.0140	26	.0044
33	.0138	27	.0044
34	.0160	28	.0076
13	.0192	29	.0066
30	.0199	25	.0071
35	.0221	CAN	.0020
14	.0184	90	.0015
15	.0206	91	.0007
16	.0125		

DATA SHEET

NOZZLE TYPE __APG-1 (BR 1, 2, 3)__   RUN NO. ____62____

PRESSURE RATIO, PRIMARY, λ_p __503.22__   PRESSURE RATIO, SECONDARY, λ_s __170.30__

CHAMBER PRESSURE __99.86__ psia   SECONDARY PRESSURE __33.72__ psia

WEIGHT FLOW RATIO, $\dot{W}_s / \dot{W}_p$ __0.0302__   AMBIENT PRESSURE __0.198__ psia

TOTAL SIDE FORCE __8.90__ LB   AMPLIFICATION FACTOR __2.298__

TOTAL AXIAL FORCE __124.27__ LB   VACUUM THRUST COEFFICIENT __1.634__

PRESSURE DISTRIBUTION

TAP LOCATION	PRESSURE RATIO p/P_c	TAP LOCATION	PRESSURE RATIO p/P_c
1	.1392	36	.0042
2	.0146	37	.0126
3	.0227	17	
31	.0153	38	.0123
4	.0160	39	.0141
5	.0168	18	.0153
6	.0173	19	.0101
7	.0143	20	.0077
8	.0064	21	.0121
9	.0079	40	.0091
10	.0091	22	.0131
32	.1589	23	.0136
11	.0104	24	.0057
12	.0126	26	.0045
33	.0197	27	.0045
34	.0141	28	.0079
13	.0148	29	.0045
30	.0140	25	.0045
35	.0168	CAN	.0018
14	.0168	90	.0028
15	.0059	91	.0018
16	.0091		

DATA SHEET

NOZZLE TYPE **APG-1 (BR 1, 2, 3)**   RUN NO. **63**

PRESSURE RATIO, PRIMARY, λ_p **495.84**   PRESSURE RATIO, SECONDARY, λ_s **330.20**

CHAMBER PRESSURE **99.62** psia   SECONDARY PRESSURE **66.37** psia

WEIGHT FLOW RATIO, $\dot{W}_s / \dot{W}_p$ **0.0603**   AMBIENT PRESSURE **0.201** psia

TOTAL SIDE FORCE **14.30** LB   AMPLIFICATION FACTOR **1.847**

TOTAL AXIAL FORCE **124.47** LB   VACUUM THRUST COEFFICIENT **1.641**

PRESSURE DISTRIBUTION

TAP LOCATION	PRESSURE RATIO p/P_c	TAP LOCATION	PRESSURE RATIO p/P_c
1	.1440	36	.0036
2	.0107	37	.0072
3	.0272	17	
31	.0215	38	.0196
4	.0193	39	.0171
5	.0191	18	.0164
6	.0203	19	.0203
7	.0206	20	.0080
8	.0193	21	.0082
9	.0077	40	.0171
10	.0092	22	.0124
32	.1793	23	.0181
11	.0105	24	.0186
12	.0065	26	.0043
33	.0112	27	.0043
34	.0211	28	.0077
13	.0186	29	.0085
30	.0196	25	.0087
35	.0191	CAN	.0018
14	.0201	90	.0023
15	.0186	91	.0016
16	.0095		

DATA SHEET

NOZZLE TYPE APG-1 (BR 1, 2, 3)

PRESSURE RATIO, PRIMARY, λ_p ___505.50___

CHAMBER PRESSURE ___99.82___ psia

WEIGHT FLOW RATIO, $\dot{W}_s / \dot{W}_p$ ___0.0892___

TOTAL SIDE FORCE ___18.71___ LB

TOTAL AXIAL FORCE ___126.55___ LB

RUN NO. ___64___

PRESSURE RATIO, SECONDARY, λ_s ___492.13___

SECONDARY PRESSURE ___96.95___ psia

AMBIENT PRESSURE ___0.197___ psia

AMPLIFICATION FACTOR ___1.609___

VACUUM THRUST COEFFICIENT ___1.664___

PRESSURE DISTRIBUTION

TAP LOCATION	PRESSURE RATIO p/P_c	TAP LOCATION	PRESSURE RATIO p/P_c
1	.1544	36	.0036
2	.0127	37	.0058
3	.0201	17	
31	.0287	38	.0186
4	.0235	39	.0222
5	.0198	18	.0201
6	.0216	19	.0222
7	.0230	20	.0090
8	.0235	21	.0046
9	.0095	40	.0166
10	.0093	22	.0176
32	.1259	23	.0181
11	.0100	24	.0223
12	.0056	26	.0041
33	.0053	27	.0043
34	.0201	28	.0078
13	.0223	29	.0107
30	.0218	25	.0107
35	.0216	CAN	.0024
14	.0213	90	.0021
15	.0233	91	.0016
16	.0093		

REFERENCES

1. Hozaki, S., et al, "Thrust Vector Control System Utilizing an Adverse Pressure Gradient in the Nozzle," National Engineering Science Co., Pasadena, Calif., Final Report Contract No. NASw-249, NASA N62-11727, April (1962).

2. Dowdy, M. W., and Newton, J. F., "Wind Tunnel Experiments on Freon-12 Secondary Injection," JPL Report SPS 37-17, Vol. 4, (1962).

3. Mager, A., "On the Model of Free, Shock-Separated, Turbulent Boundary Layer," J. Aero. Sci., Feb. (1956).

4. Hays, W. D. and Probstein, R. F., "Hypersonic Flow Theory," Academic Press, N. Y., (1959).

5. Cubbison, R. W., Anderson, B. H., and Ward, J. J., "Surface Pressure Distributions with a Sonic Jet Normal to Adjacent Flat Surfaces at Mach 2.92 to 6.4," (NASA TND-580), Lewis Research Center, Cleveland, Ohio, February (1961).

6. Stewartson, K., "Correlated Incompressible and Compressible Boundary Layers," Proc. Roy. Soc. (London), Ser. A., Vol. 200, No. A1060, Pec. 22, pp. 84-100, (1949).

7. Mager, A., "Transformation of the Compressible Turbulent Boundary Layer," Jour. Aero. Sci., Vol. 25, No. 5, pp. 305-311, May (1958).

8. McLafferty, G. H., and Barber, R. E., "The Effect of Adverse Pressure Gradients on the Characteristics of Turbulent Boundary Layers in Supersonic Streams," Journal Aero. Sci., Vol. 29, No. 1, pp. 1-10, January (1962).

9. Romeo, D. J. and Sterrett, J. R., "Aerodynamic Interaction Effects Ahead of a Sonic Jet Exhausting Perpendicularly from a Flat Plate into a Mach Number 6 Free Stream," NASA TN D-743 April (1961).

10. Sterrett, J. R. and Emery, J. C., "Extension of Boundary-Layer-Separation Criteria to a Mach Number of 6.5 by Utilizing Flat Plates with Forward-Facing Steps," NASA TN D-618, Dec. (1960).

11. "Equations, Tables, and Charts for Compressible Flow," Ames Research Staff, NACA Report 1135 (1953).

12. Shapiro, A. H., "The Dynamics and Thermodynamics of Compressible Fluid Flow," The Ronald Press Company, New York, (1953).

13. Rodriguez, C. J., "An Experimental Investigation of Jet-Induced Thrust Vector Control Methods," presented at the Seventeenth Annual JANAF-ARPA-NASA Solid Propellant Meeting, Denver, Colorado, May 23-25 (1961).

14. Gagnon, R., "Thrust Vector Control of Plug Nozzles," Final Report Contract No. 61-125, January (1962). (Confidential Rept.)

15. Wu, J. M., Chapkis, R. L., and Mager, A., "Approximate Analysis of Thrust Vector Control by Fluid Injection," J. of ARS, Dec. (1961).

16. Van Driest, J. Aeronaut. Sci., 18, p. 145 (1951).

17. Jakob, M., "Heat Transfer," Vol. II, John Wiley and Sons, Inc., New York (1957).

18. Donaldson, C. duP., "On the Form of the Turbulent Skin-Friction Law and its Extension to Compressible Flows," NACA TN 2692, (1952).

19. Stratford, B. S., "The Prediction of Separation of the Turbulent Boundary Layer," J. Fluid Mech., Vol. 5, Part 1 (1959).

TABLE I

Test parameters for opposed-tangential port configuration.

Nozzle Type	Port Config.	Port Dia. d_j	Port Spacing Ratio c/d_j	Spacing Between Port C_L c	Weight Flow Ratio $\dot{w}_s/\dot{w}_p$	Total Cases
Conical	Opp. -Tan.	.188	2.1	.395	0, 3, 4, 5, 6, 7, 8, 9%	8
↓	↓	↓	2.6	.489	3, 6, 9%	3
			3.2	.602	3, 6, 9%	3
APG - 1			2.1	.395	3, 6, 9%	3
↓			2.6	.489	0, 3, 4, 5, 6, 7, 8, 9%	8
	↓	↓	3.2	.602	3, 6, 9%	3

Total Cases for Phase I =   28

Sketch of Port Spacing Notation
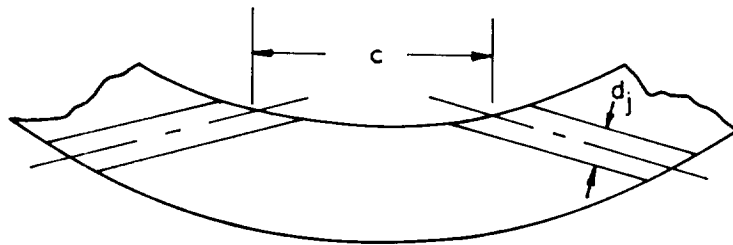
TABLE II

Test parameters for multiradial port configuration.

Nozzle Type	Port Config.	Port Dia. d_j	Port Spacing Ratio c/d_j	Spacing Between Port C_L c	Weight Flow Ratio $\dot{w}_s/\dot{w}_p$	Total Cases
Conical	1-Rad.	.188	-	-	2, 3, 4, 5%	4
	3-Rad.		1.8	.336	0, 3, 4, 5, 6, 7, 8, 9%	8
			2.5	.470	3, 6, 9%	3
			3.5	.658	3, 6, 9%	3
APG - 1	1-Rad.		-	-	2, 3, 4, 5%	4
	3-Rad		1.8	.336	3, 6, 9%	3
			2.5	.470	0, 3, 4, 5, 6, 7, 8, 9%	8
			3.5	.658	3, 6, 9%	3

Total Cases for Phase II = $\underline{36}$

Sketch of Port Spacing Notation

-148-
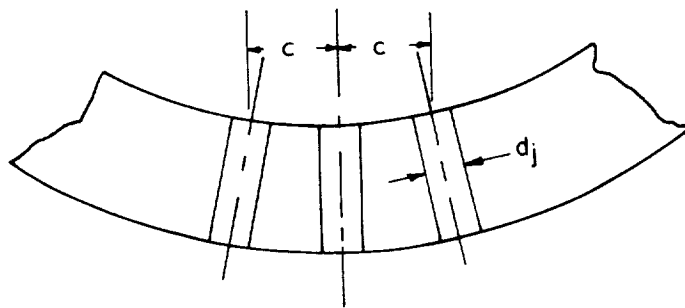
TABLE III

VALUES OF CRITICAL INJECTION PORT SPACING RATIOS, c_{cr}/d_j

		P_j/P_∞				
	M_∞	5	10	25	50	100
$\gamma = 1.2$	2	1.04	1.23	1.65	2.10	2.84
	3	——	1.03	1.29	1.60	2.03
	4	——	1.04	1.10	1.32	1.66
$\gamma = 1.4$	2	1.04	1.20	1.63	1.92	2.44
	3	——	1.06	1.41	1.61	2.00
	4	——	1.00	1.31	1.46	1.79
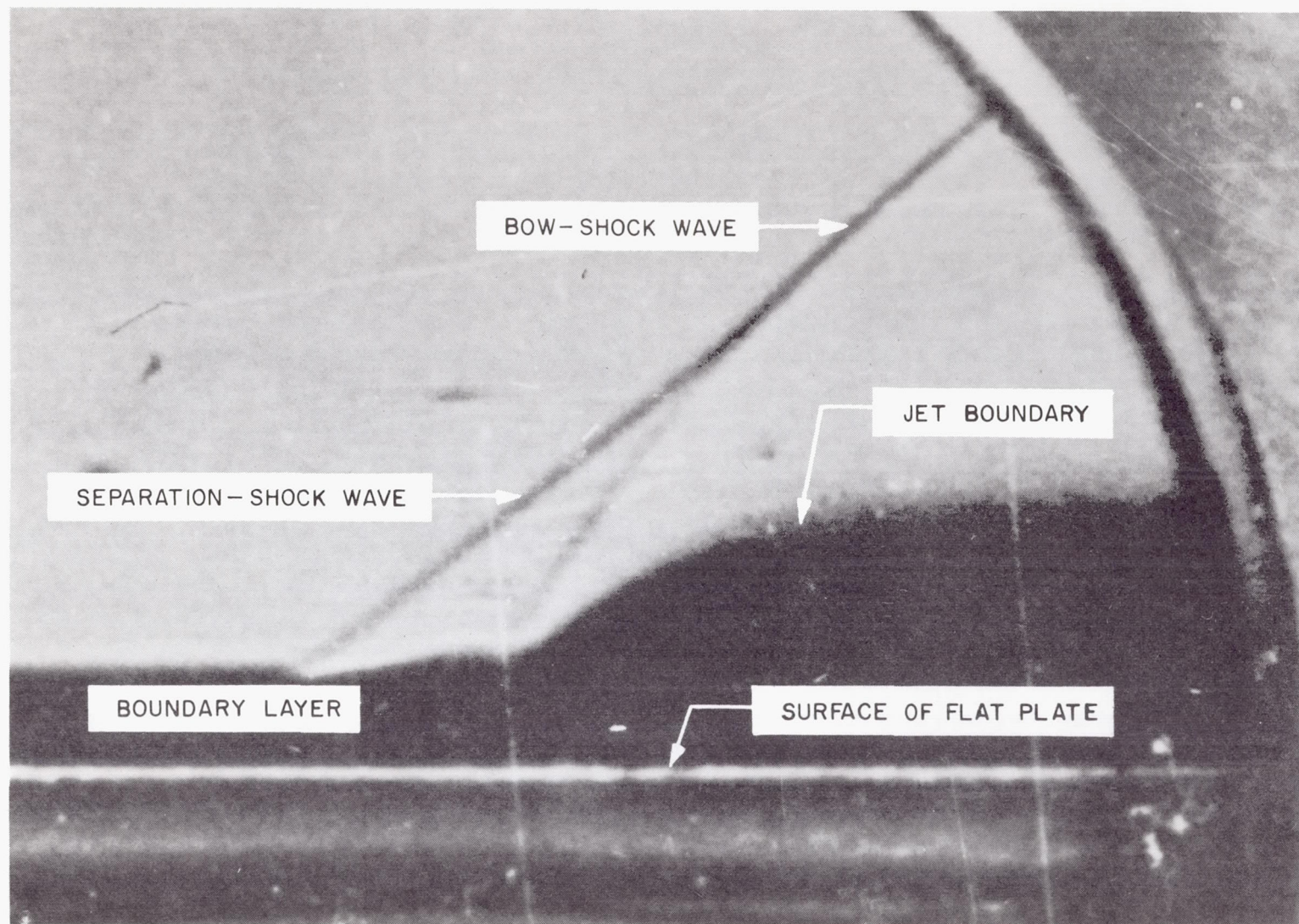
FIGURE 1

SCHLIEREN PHOTOGRAPH, WITH FREON-12 AS INJECTANT,

ENLARGED FROM REF. 2 (INJECTION TEMPERATURE = 67°F)
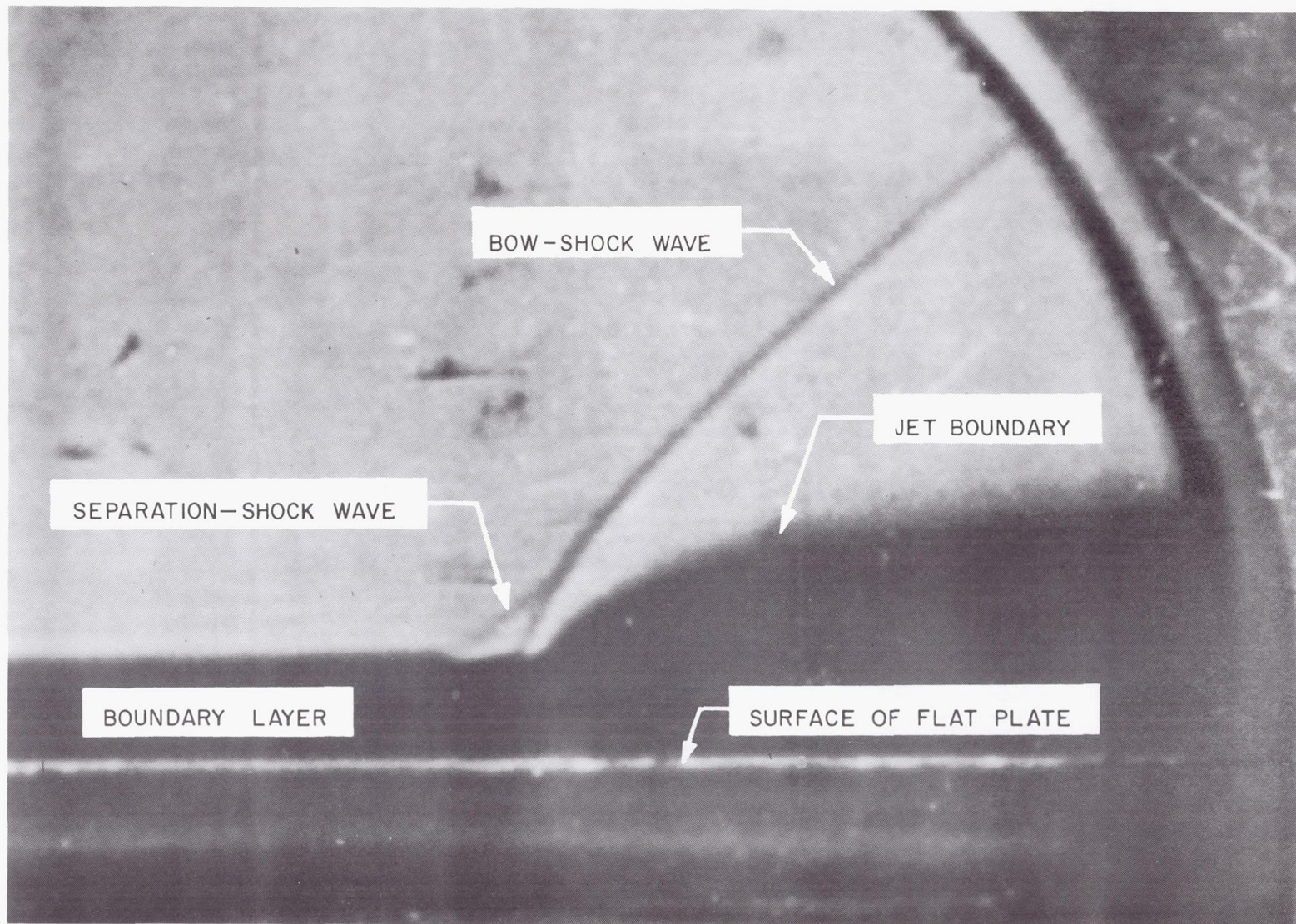
FIGURE 2

SCHLIEREN PHOTOGRAPH, WITH FREON-12 AS INJECTANT,

ENLARGED FROM REF. 2 (INJECTION TEMPERATURE = -75°F)
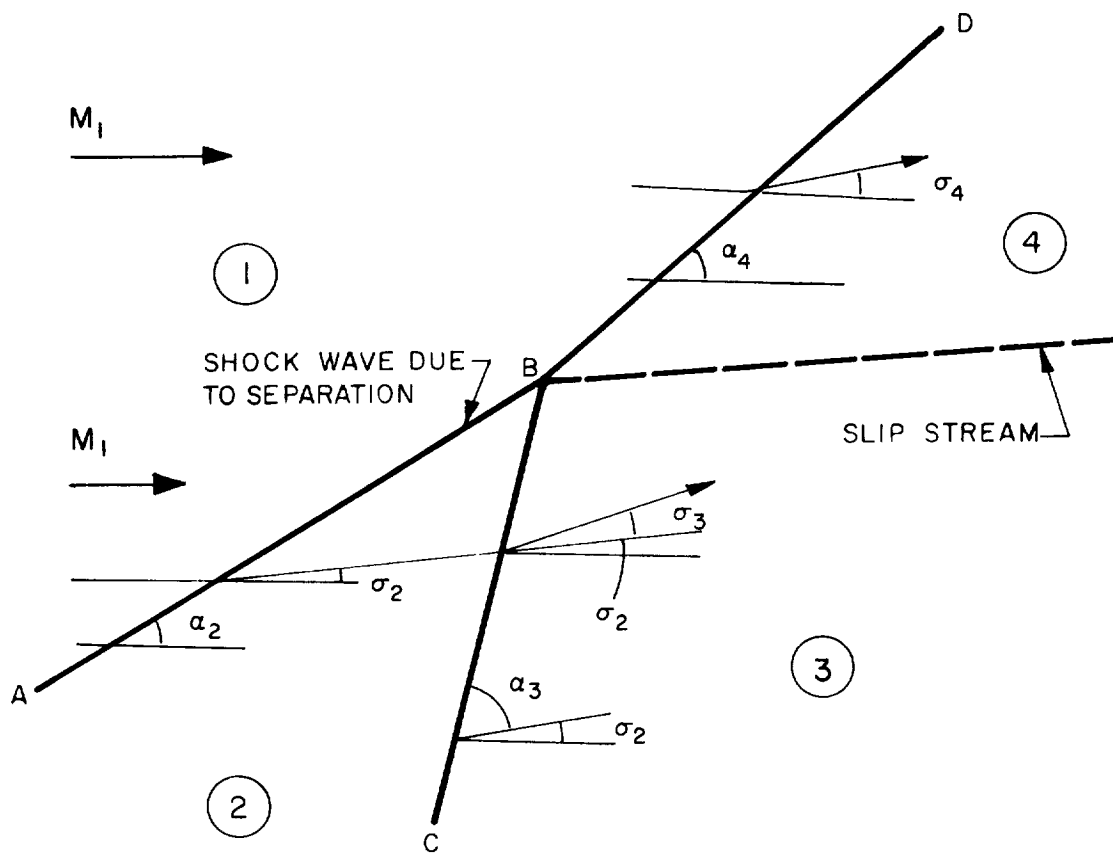
FIGURE 3

NOTATION FOR INTERSECTION OF SHOCK WAVE AND ITS FLOW
FIELD
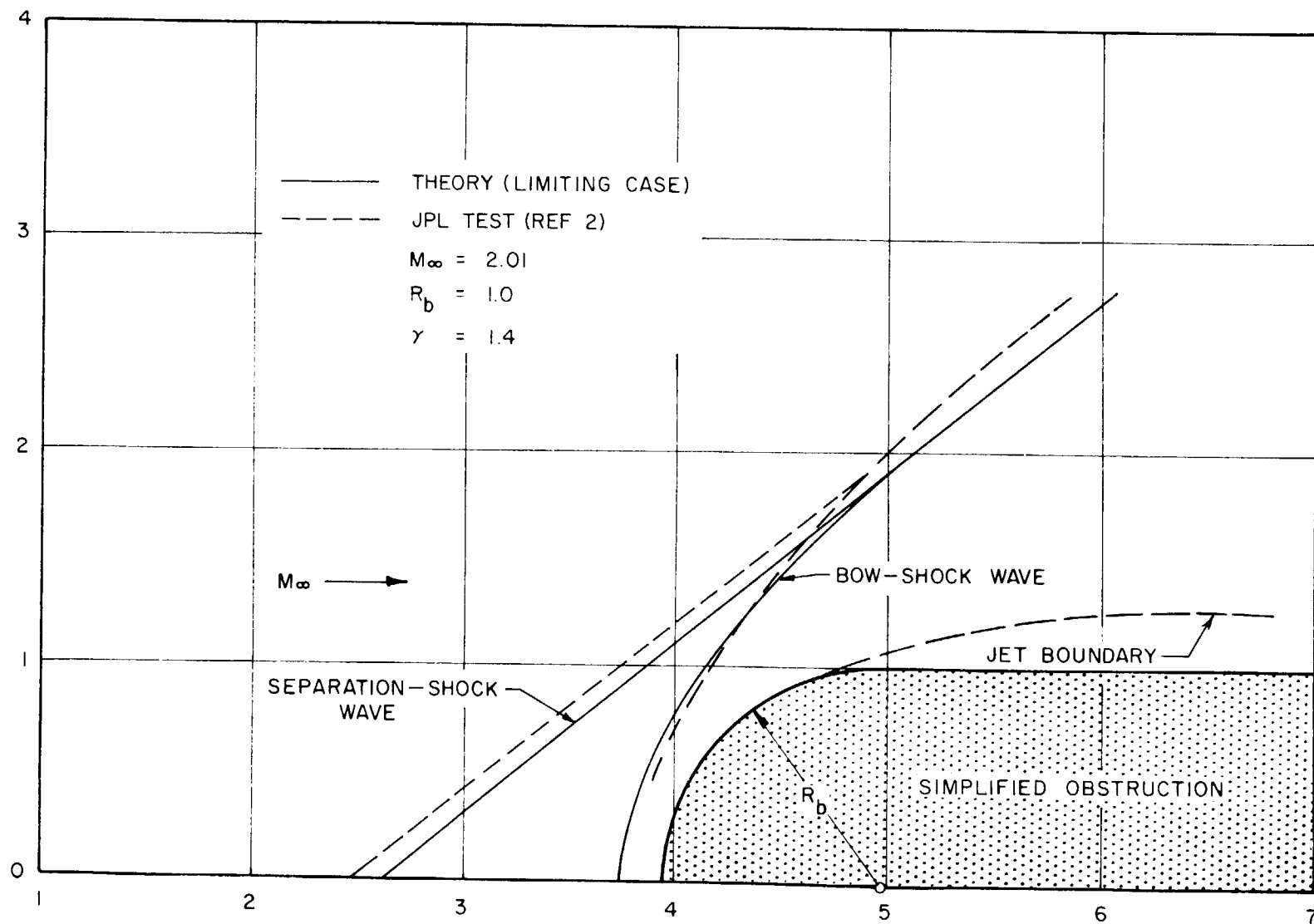
FIGURE 4

SHOCK WAVE STRUCTURE CONSTRUCTED FROM THEORY (LIMITING CASE)
COMPARED TO VISUAL OBSERVATION FROM SCHLIEREN PHOTOGRAPH (REF. 2)
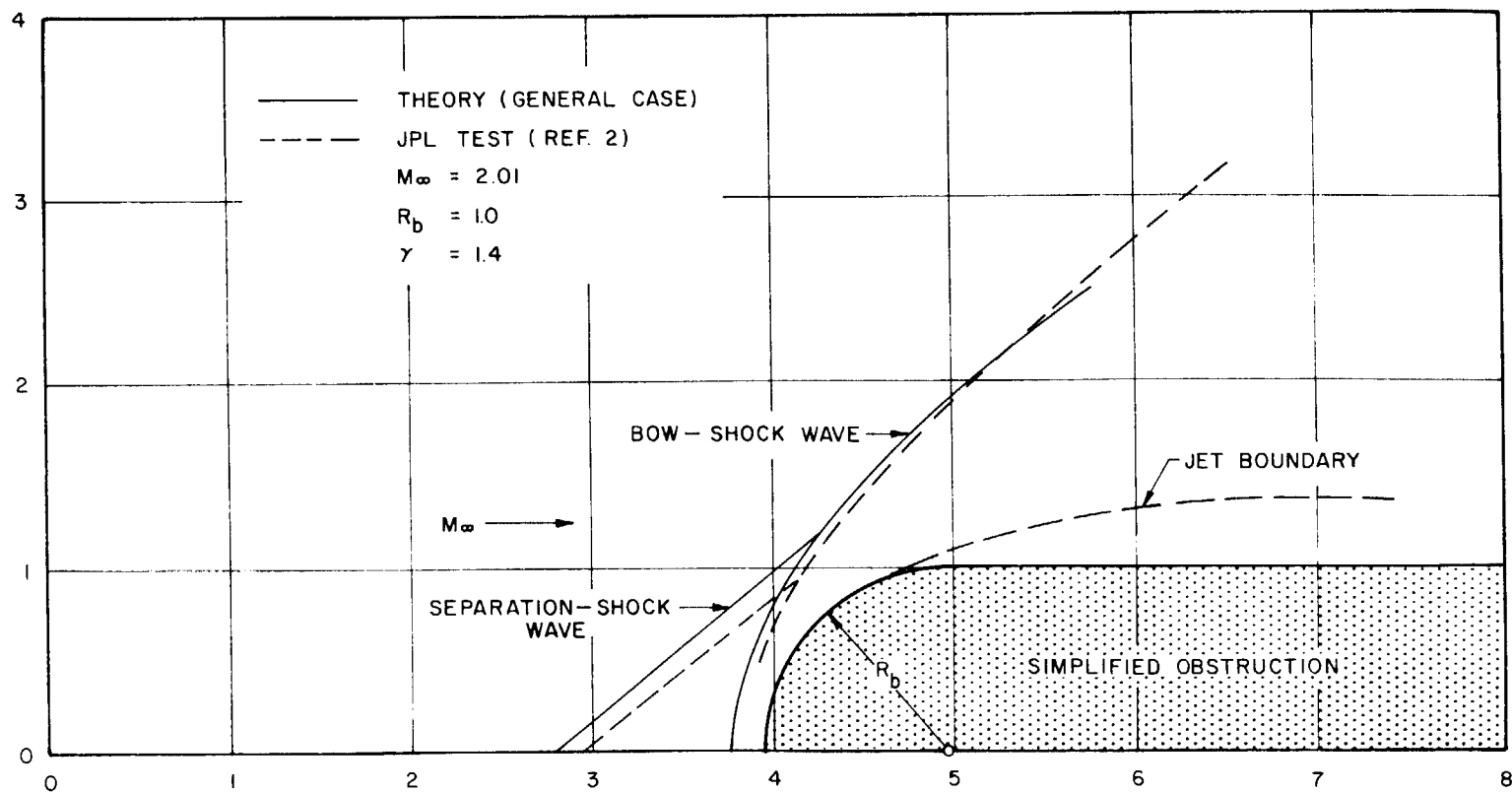
FIGURE 5

SHOCK WAVE STRUCTURE CONSTRUCTED FROM THEORY (GENERAL CASE)
COMPARED TO VISUAL OBSERVATION FROM SCHLIEREN PHOTOGRAPH (REF. 2)
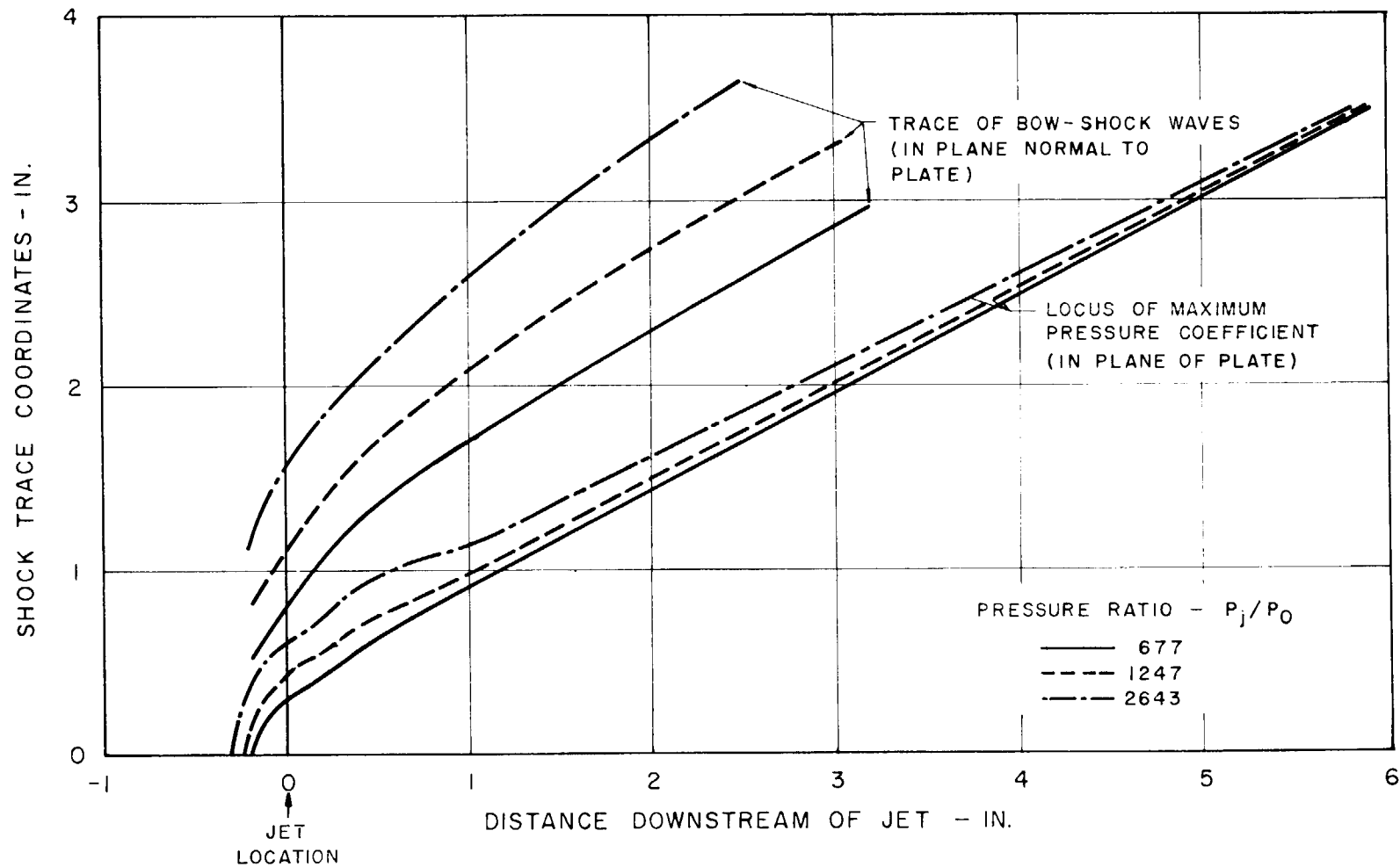
FIGURE 6

DEPENDENCE OF SHOCK WAVE CONFIGURATION ON GASEOUS INJECTANT
FLOW RATE THROUGH A CIRCULAR PORT IN FLAT PLATE (REF. 5)
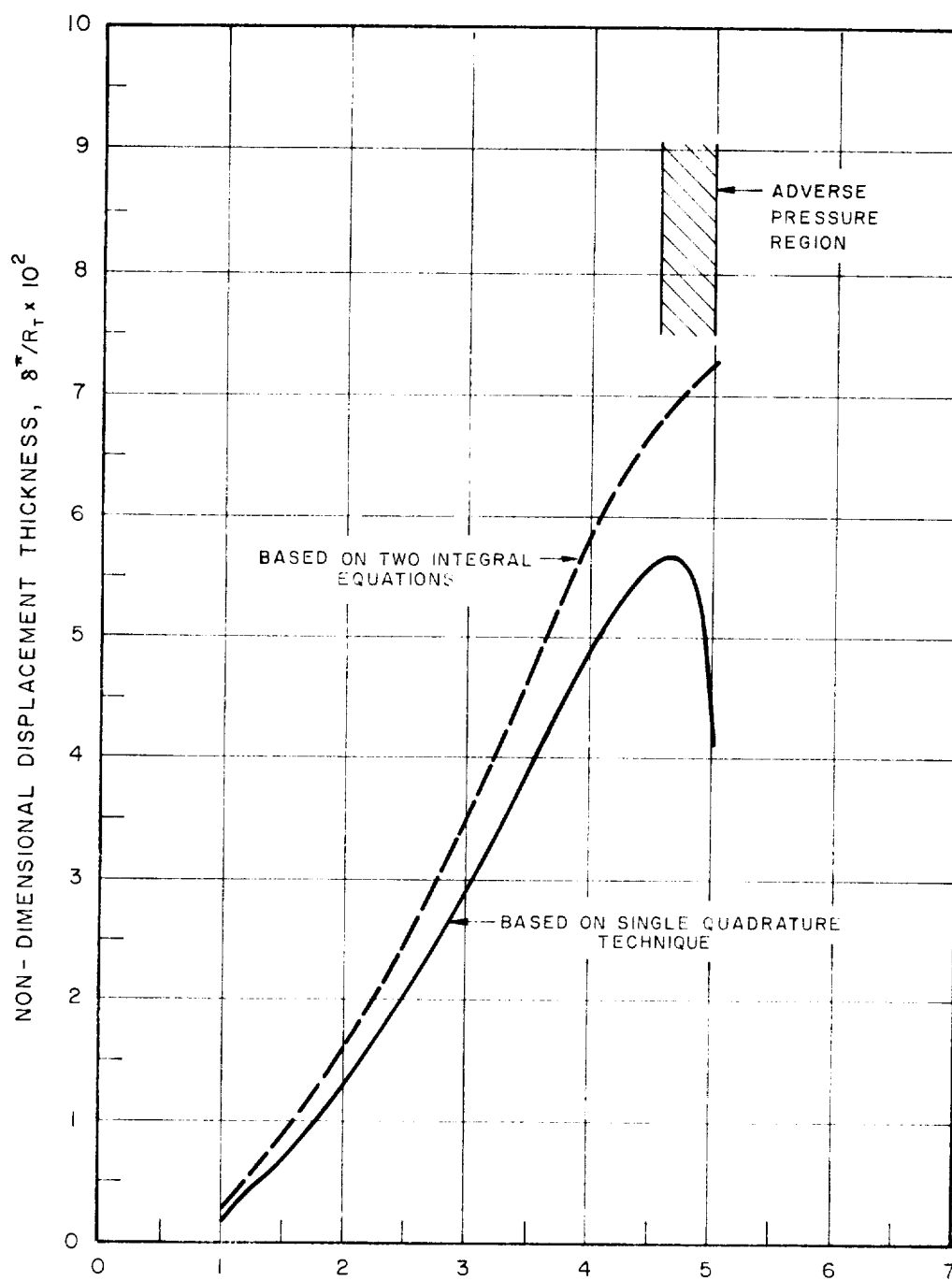
FIGURE 7

DISPLACEMENT THICKNESS FOR APG-1 NOZZLE
(TEST NOZZLE SIZE)
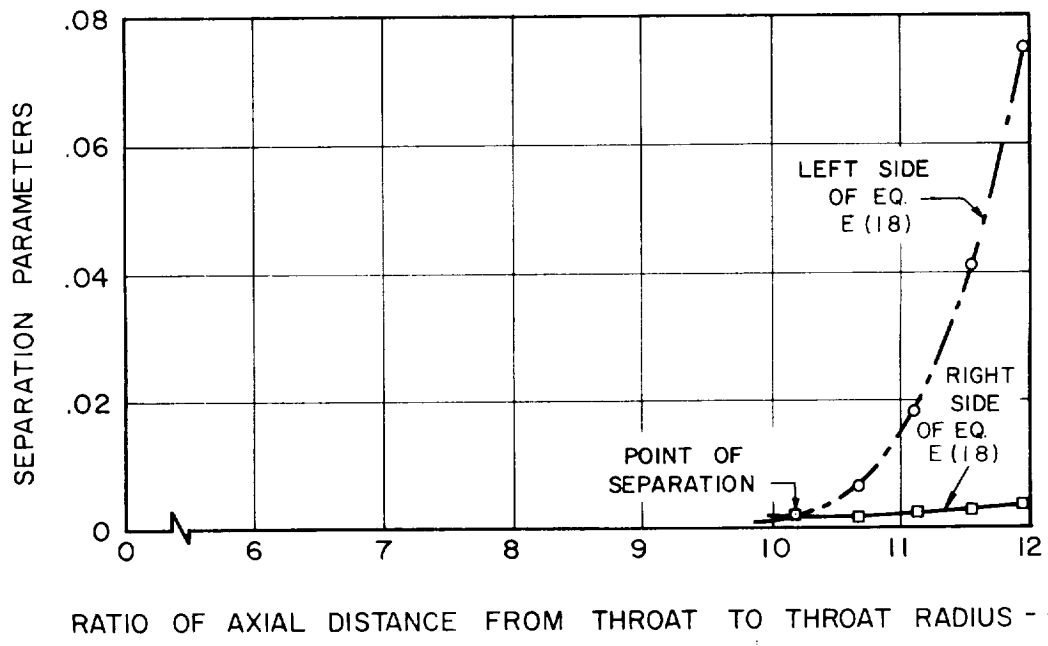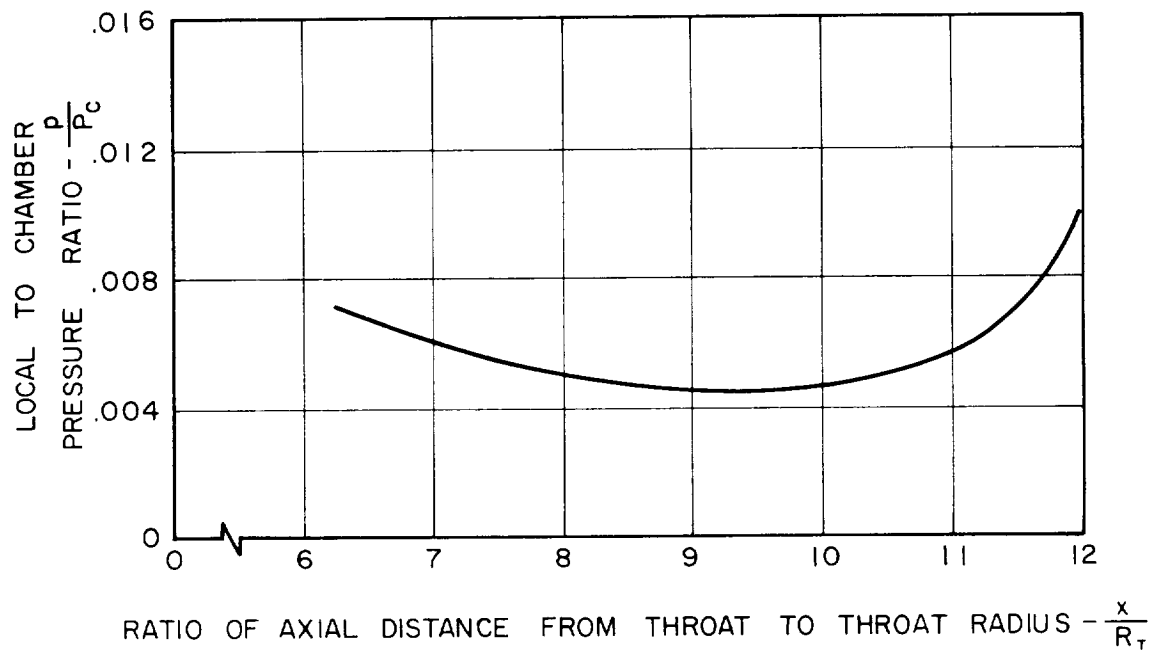
FIGURE 8

SEPARATION POINT AND PRESSURE DISTRIBUTION IN
APG-1 NOZZLE WITH NO SECONDARY INJECTION
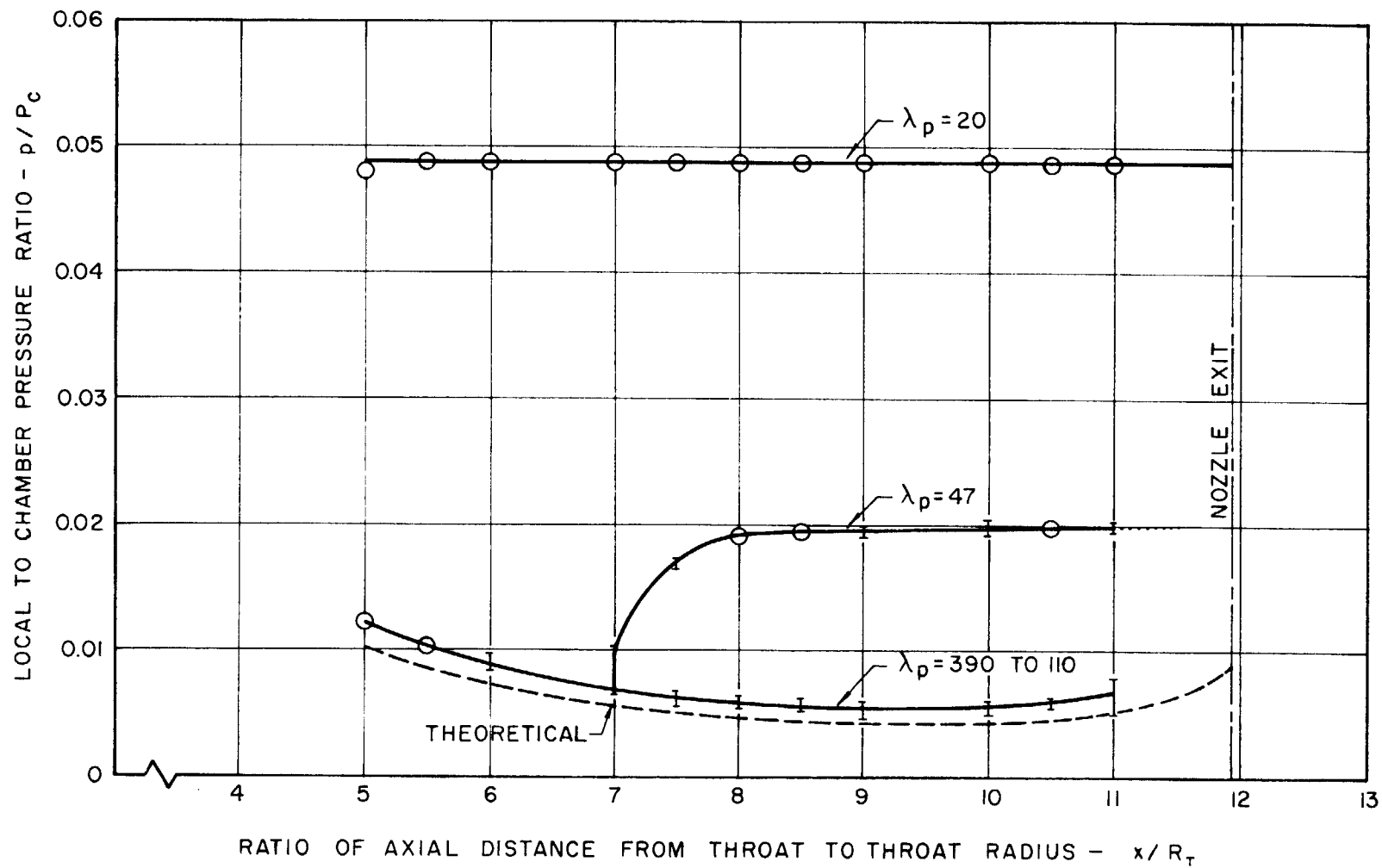
FIGURE 9

EFFECT OF TEST PRESSURE RATIO ON THE WALL PRESSURE DISTRIBUTION
WITH NO SECONDARY INJECTION IN THE APG-1 NOZZLE

EXISTING SECTION

NEW RING

EXISTING SECTION

EXISTING SECTION

OPPOSED-TANGENTIAL PORT
CONFIGURATION

MULTIRADIAL PORT
CONFIGURATION
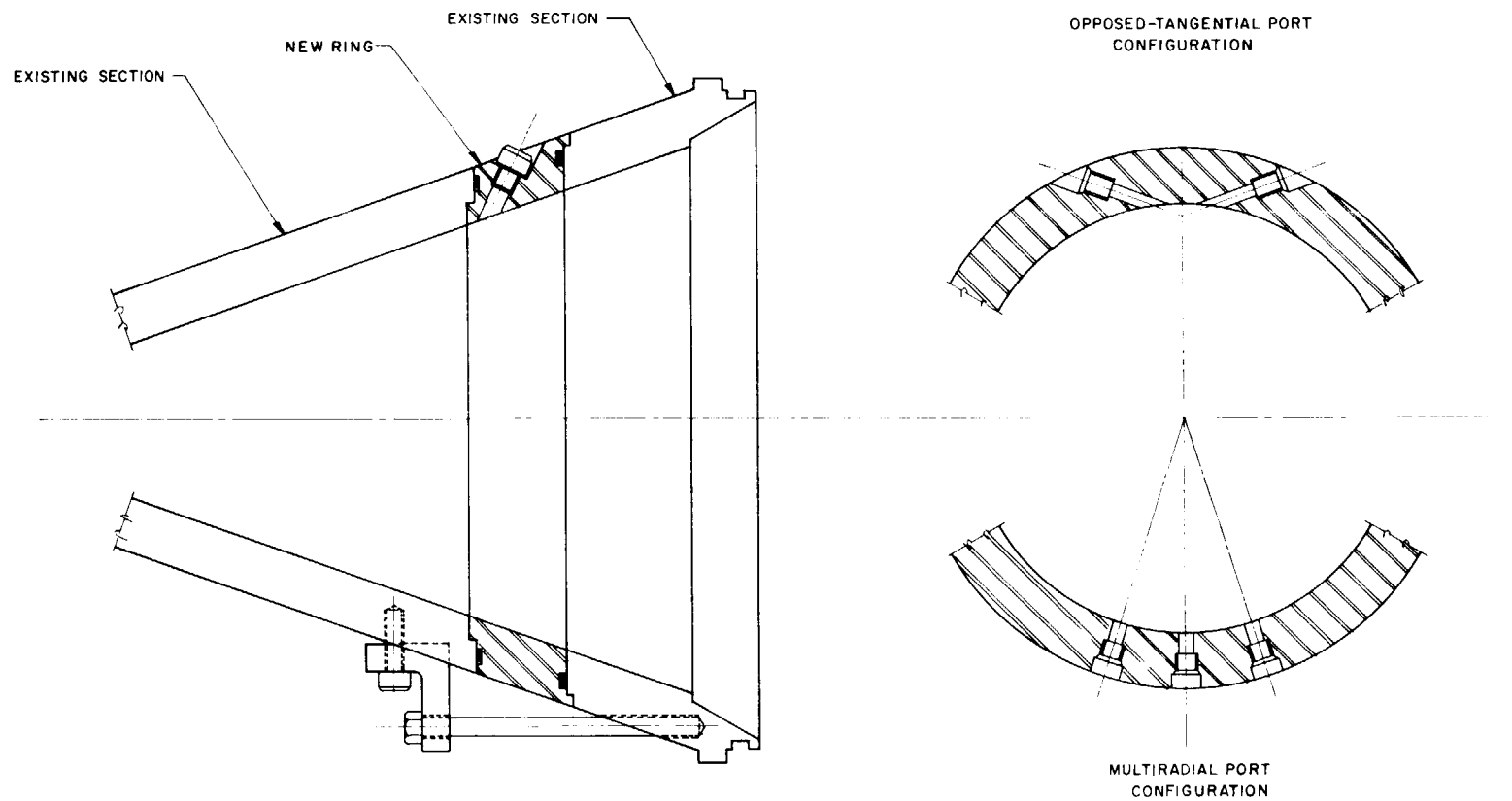
FIGURE 10

SKETCH OF CONICAL NOZZLE WITH MODIFICATION AND TYPICAL INJECTION
PORT CONFIGURATIONS

MULTIRADIAL PORT
CONFIGURATION

NEW RING

EXISTING SECTION

OPPOSED-TANGENTIAL PORT
CONFIGURATION
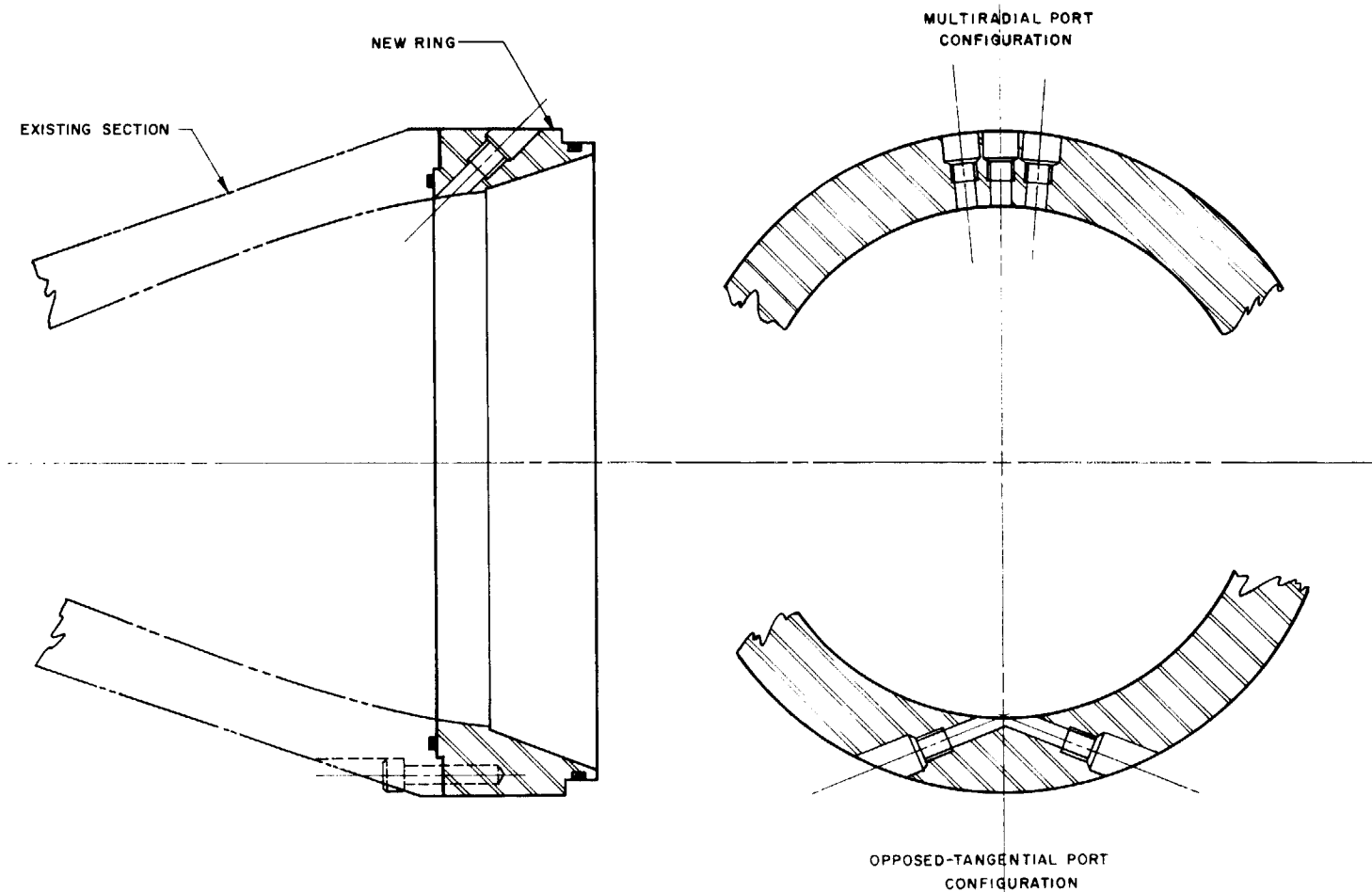
FIGURE 11

SKETCH OF APG-1 NOZZLE WITH MODIFICATION AND TYPICAL INJECTION PORT
CONFIGURATIONS
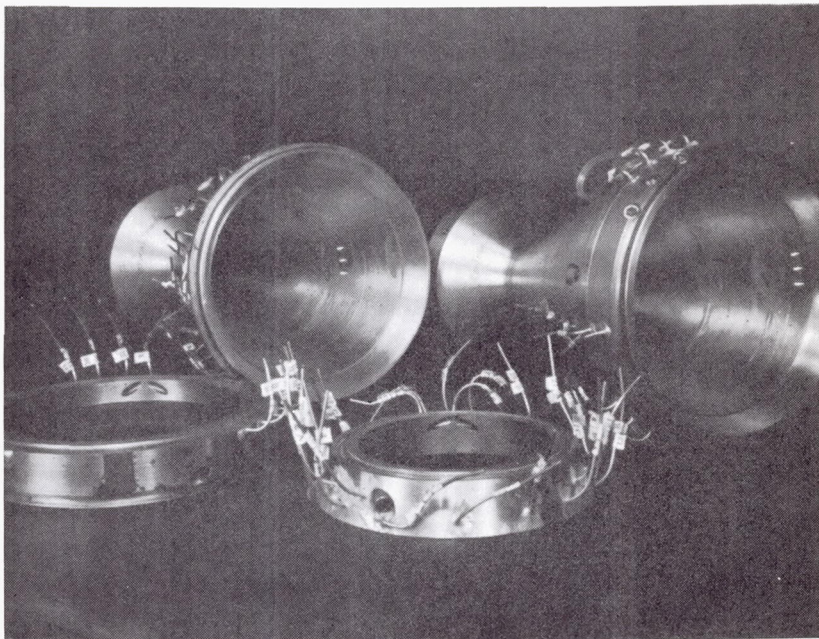
FIGURE 12

APG-1 AND CONICAL NOZZLES

45°

60°

NORMAL TO
WALL

SECTION I - I
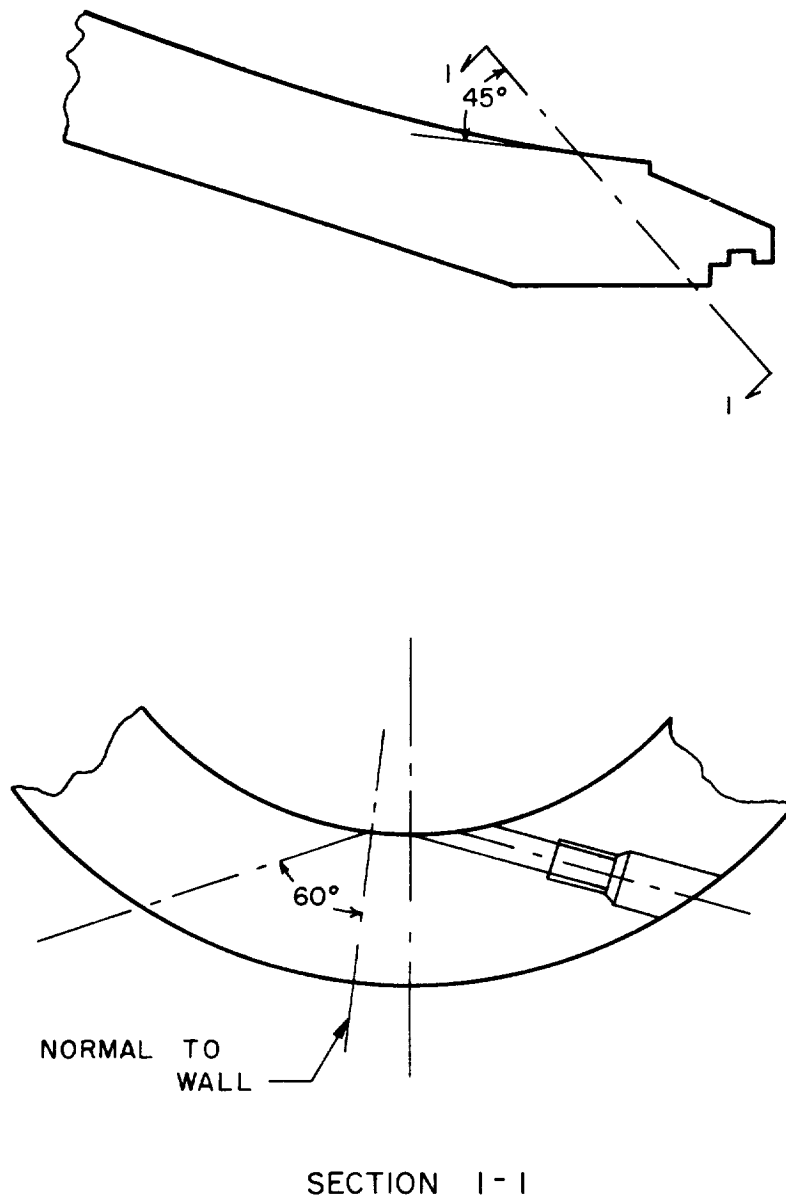
FIGURE 13

SKETCH SHOWING INJECTION PORT ORIENTATION

.676

#1 #2 #3

10°-23'

PORT A

$\theta° = 180$

.940

#1 #2 #3

14°-30'

PORT B

$\theta° = 300$

.74
26°

≈ .188

452

TYPICAL SECTION

1.316

#1 #2 #3

20°-35'

PORT C

$\theta° = 60$
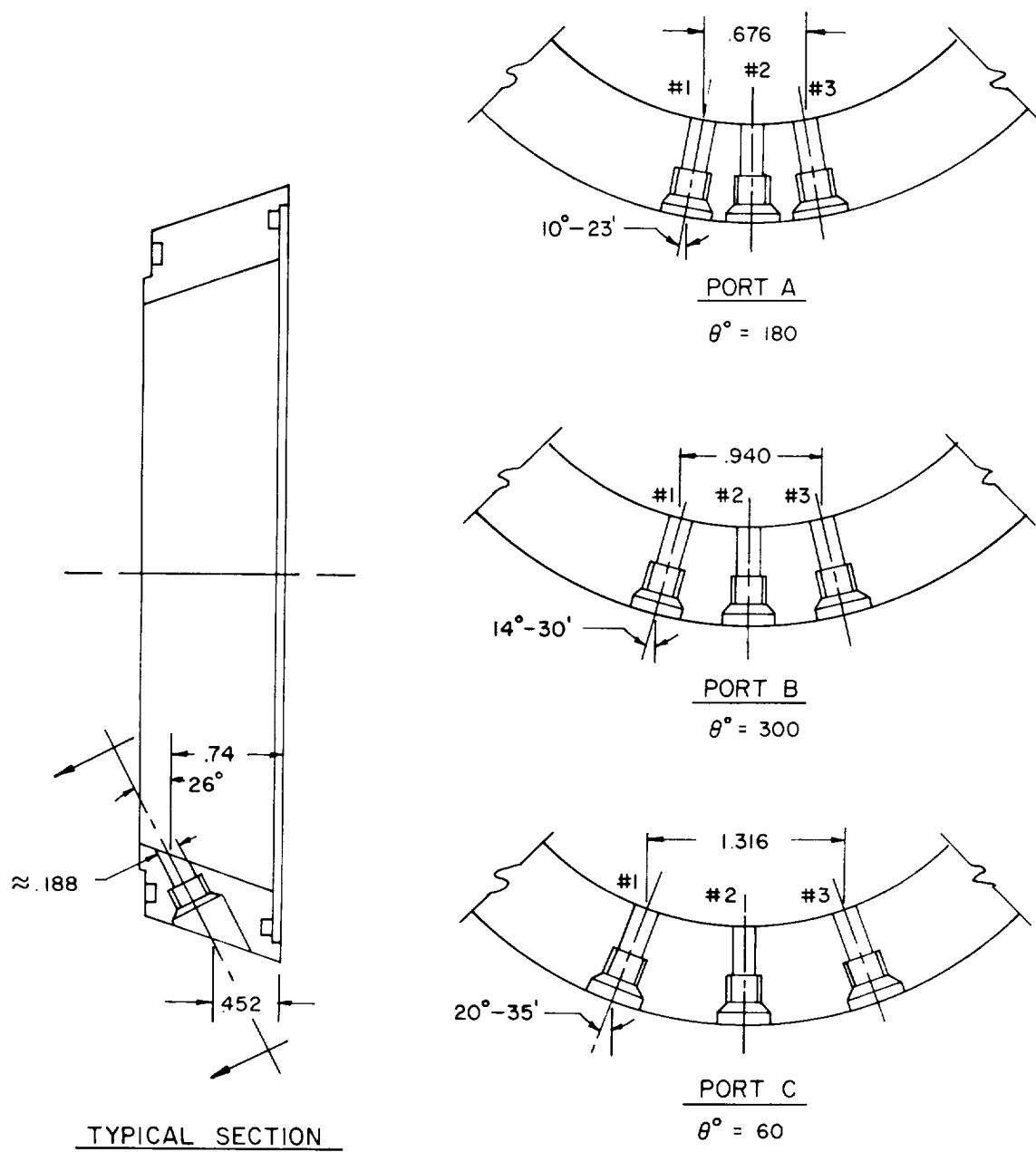
FIGURE 14

PORT ORIENTATION AND SPACING OF MULTIRADIAL PORT
CONFIGURATION FOR CONICAL NOZZLE

TYPICAL SECTION

PORT A

$\theta° = 180$

PORT B

$\theta° = 300$

PORT C

$\theta° = 60$
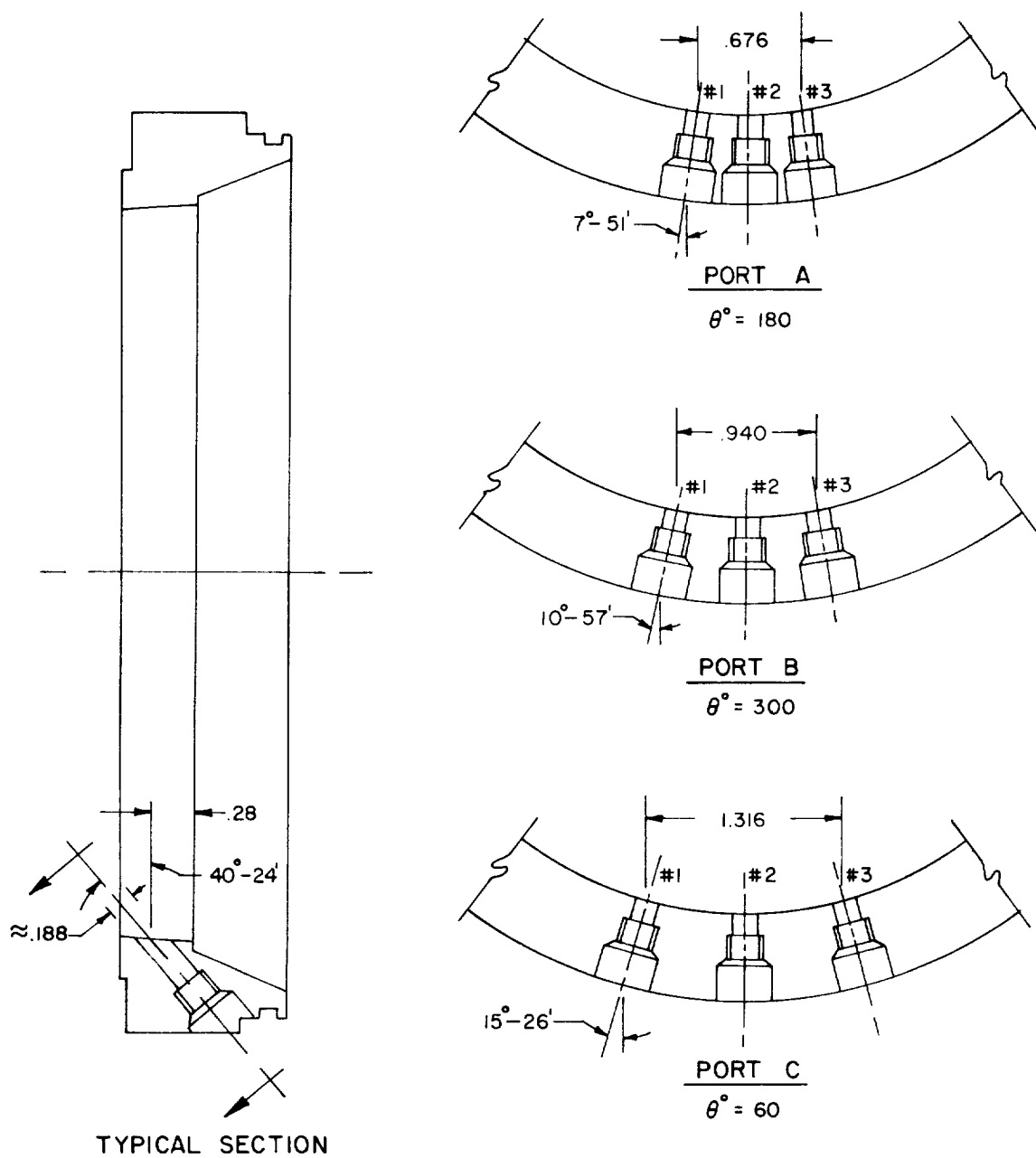
FIGURE 15

PORT ORIENTATION AND SPACING OF MULTIRADIAL PORT
CONFIGURATION FOR APG-1 NOZZLE

.395

#1 #3

66°-03'

PORT A

$\theta° = 180$

.489

#1 #3

67°-28'

PORT B

$\theta° = 300$

.602

#1 #3

69°-12'

PORT C

$\theta° = 60$

.74

26°

≈.195

TYPICAL SECTION
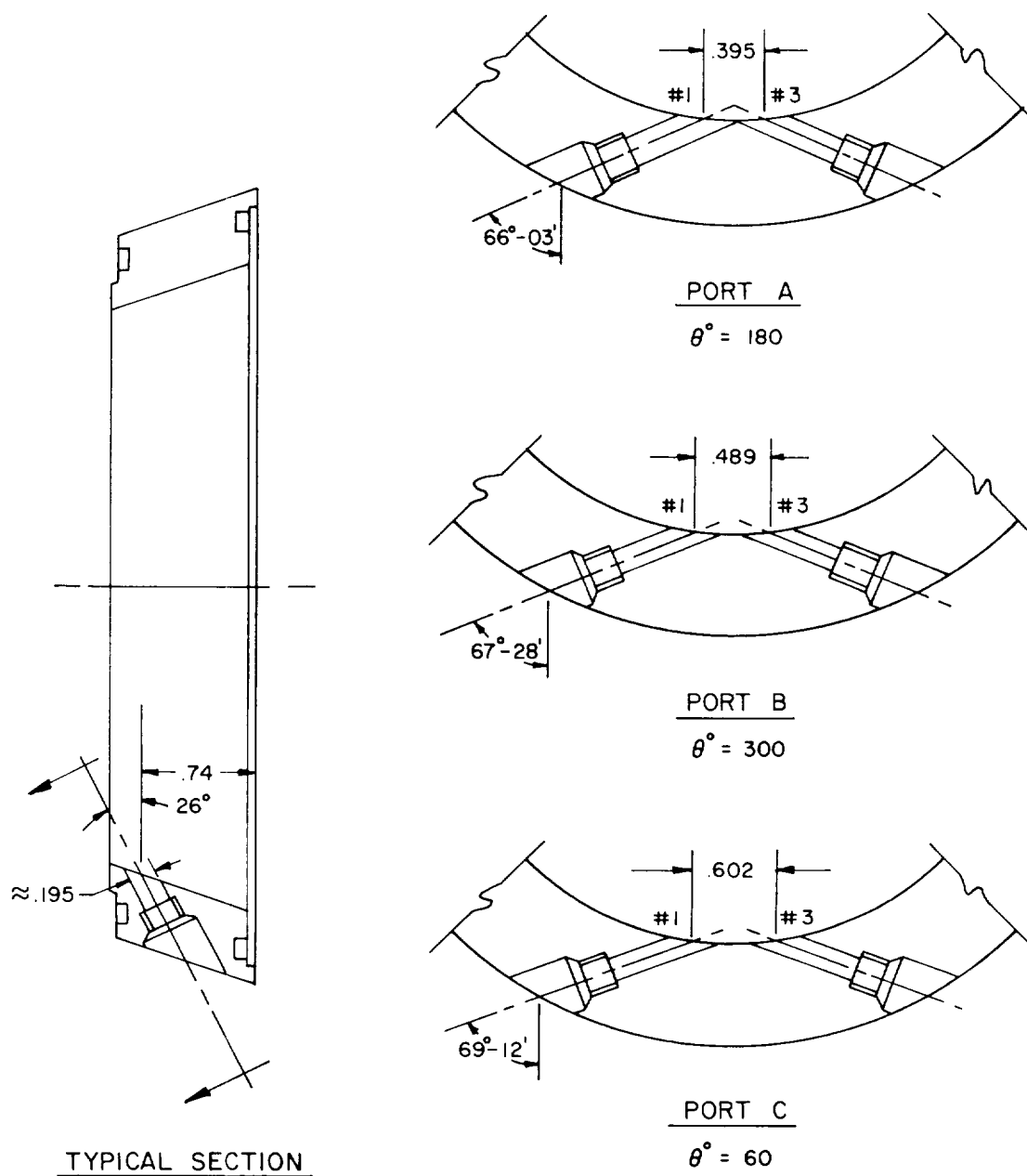
FIGURE 16

PORT ORIENTATION AND SPACING OF OPPOSED-TANGENTIAL
PORT CONFIGURATION FOR CONICAL NOZZLE

-165-
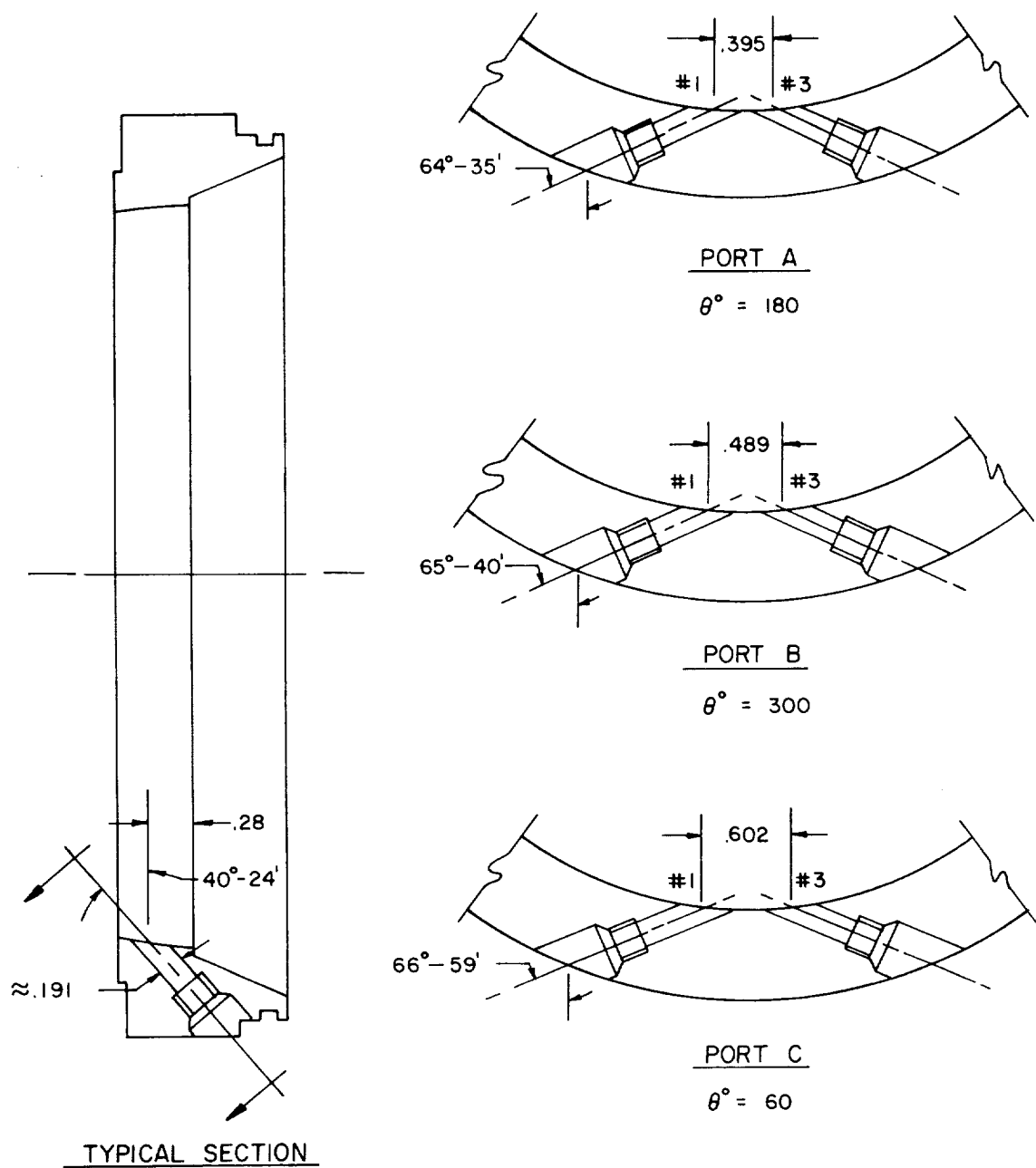
FIGURE 17

PORT ORIENTATION AND SPACING OF OPPOSED-TANGENTIAL
PORT CONFIGURATION FOR APG-1 NOZZLE

NOZZLE TEST CABIN

AIR EJECTOR

STEAM EJECTOR

PLAN   VIEW

3 COMPONENT
BALANCE SYSTEM

ELEVATION — NOZZLE TEST CABIN
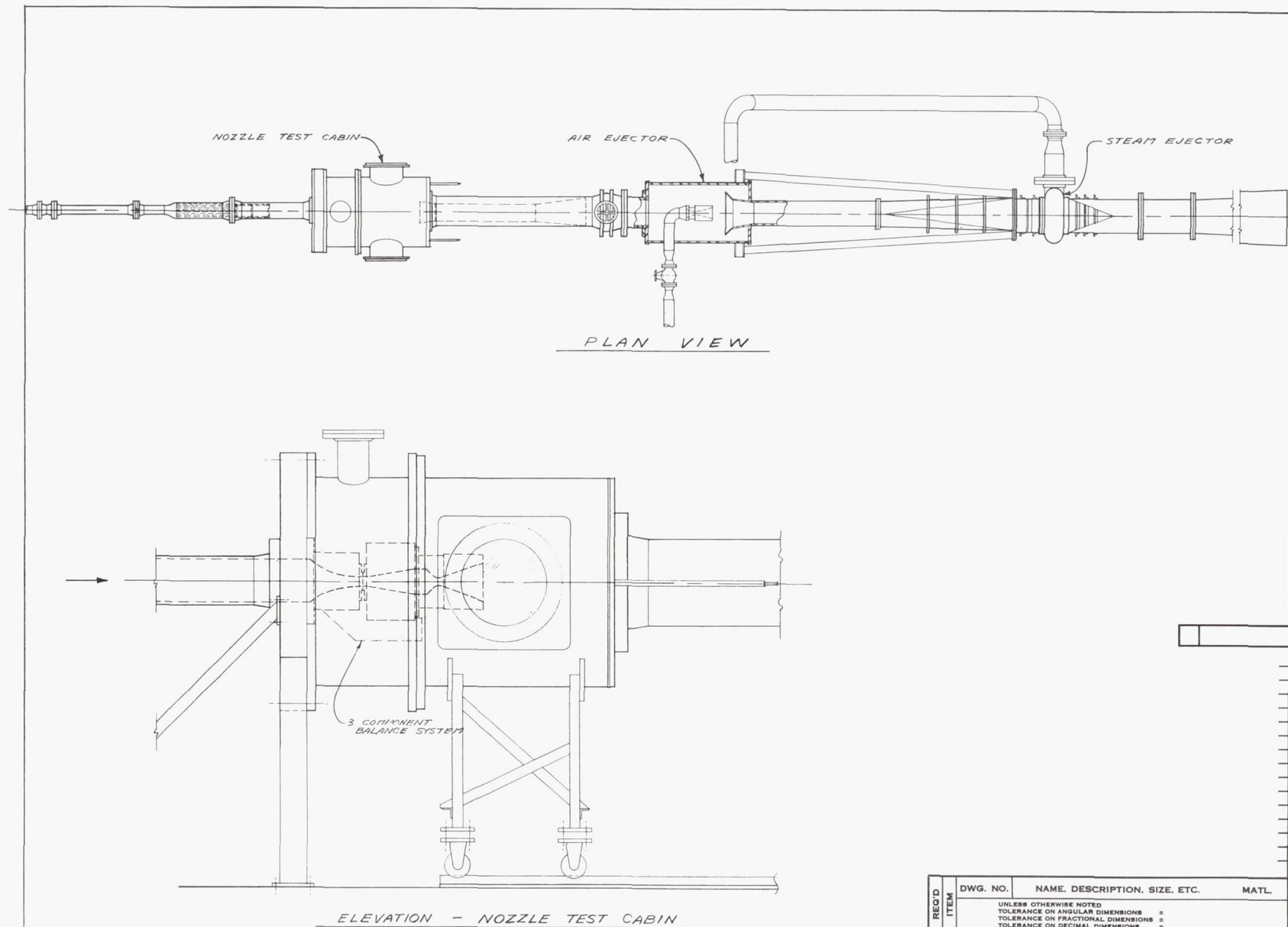
FIGURE 18

HIGH AREA RATIO NOZZLE TEST FACILITY

REQ'D	ITEM	DWG. NO.	NAME, DESCRIPTION, SIZE, ETC.		MATL.
			UNLESS OTHERWISE NOTED TOLERANCE ON ANGULAR DIMENSIONS ± TOLERANCE ON FRACTIONAL DIMENSIONS ± TOLERANCE ON DECIMAL DIMENSIONS ±		
			FluiDyne ENGINEERING CORP. 5900 OLSON MEMORIAL HIGHWAY MINNEAPOLIS 22, MINNESOTA		
	PART NO.	TITLE	HIGH PRESSURE RATIO TVC NOZZLE TEST FACILITY		
		DRWN. BY	DATE	NEXT ASS'Y	CODE
		CHK'D		JOB	
		APP'D	APP'D	SCALE DRAWING NO.	REV.
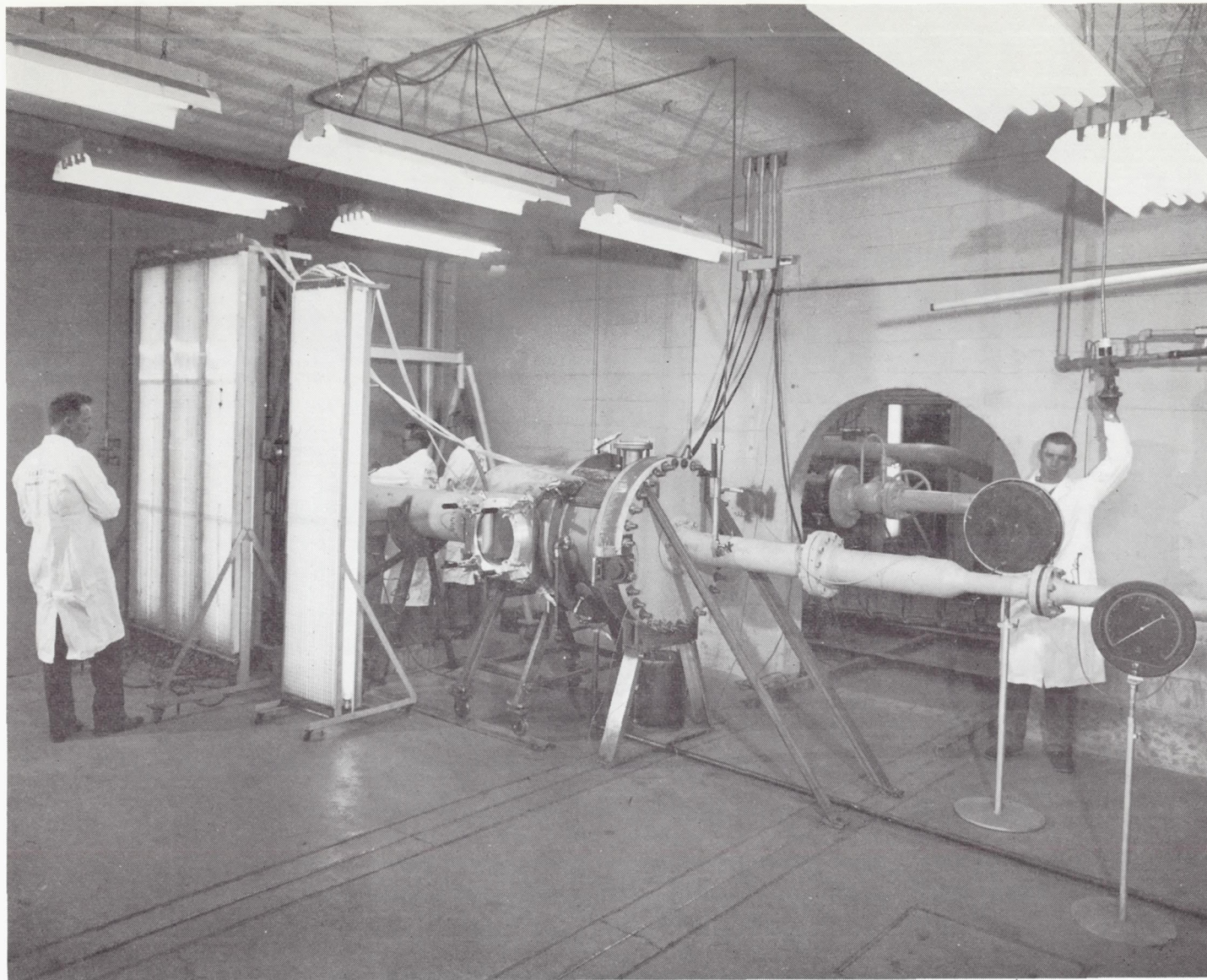
FIGURE 19

AXISYMMETRIC FREE-JET NOZZLE FACILITY

FIGURE 20

ASSEMBLY OF TEST NOZZLE

LEGEND:
x INJECTION PORT
⊘ EXISTING PRESSURE TAPS
O NEW PRESSURE TAPS
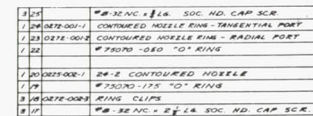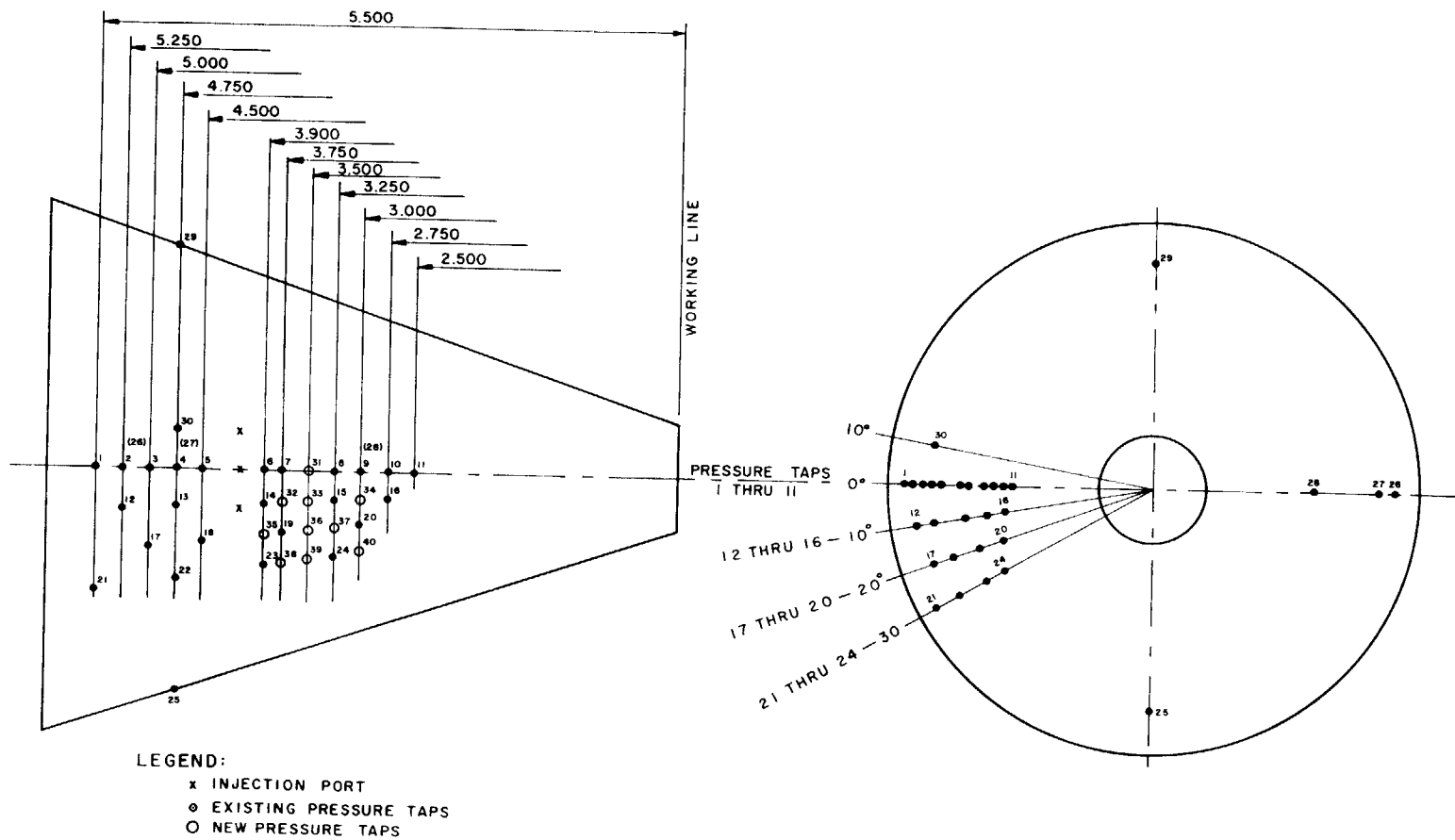
FIGURE 21

PRESSURE TAP LOCATION FOR CONICAL NOZZLE
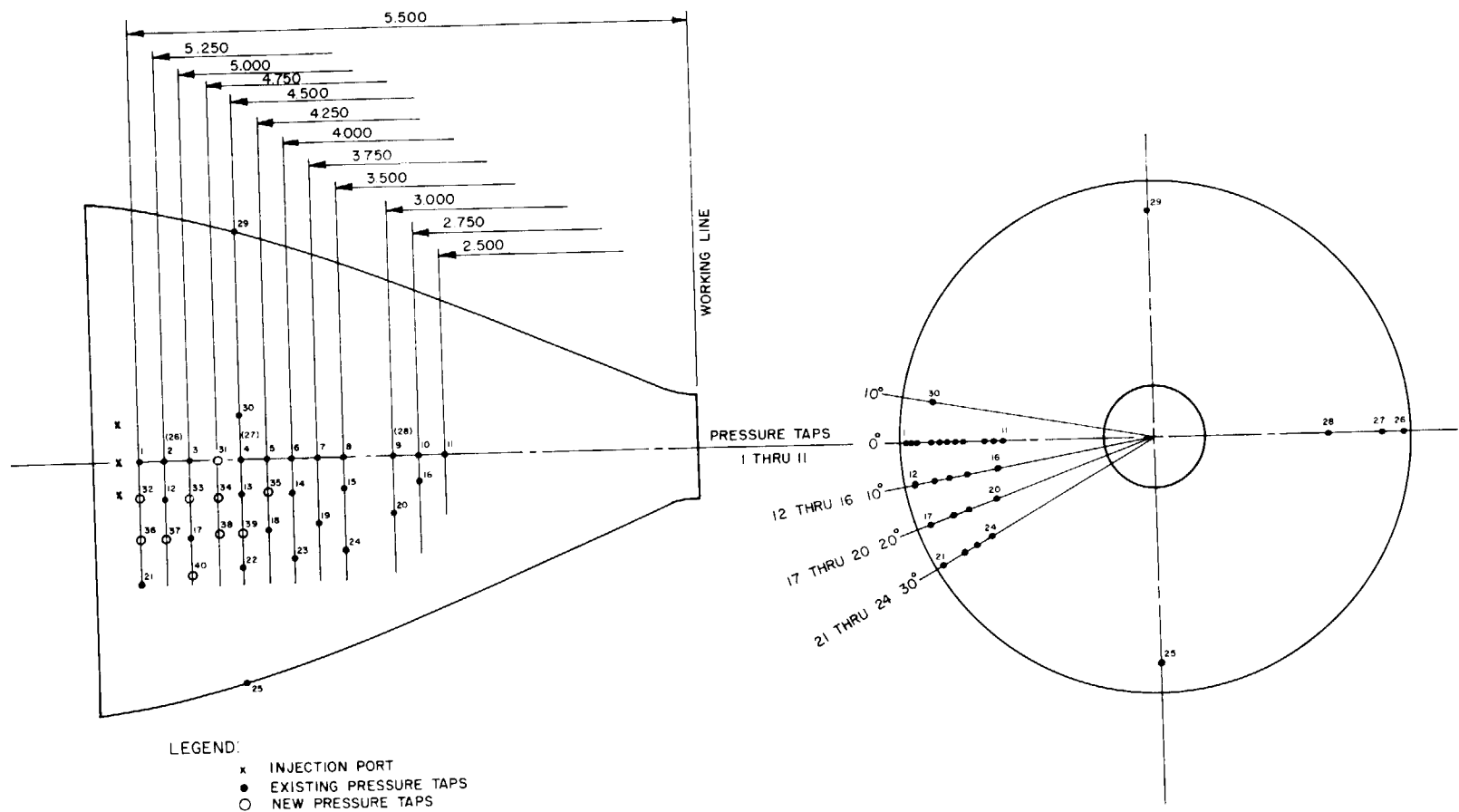
FIGURE 22

PRESSURE TAP LOCATION FOR APG-1 NOZZLE

FIGURE 23
MEASURED PRESSURE TAP LOCATIONS FROM INSPECTION IN CONICAL NOZZLE,
MULTIRADIAL PORT CONFIGURATION

TAP NO.	X	R	A	θ	TAP NO.	X	R	A	θ
1	.471	2.339	17.173	180	22A	1.215	2.082	13.640	210
2	.720	2.253	15.933	180	22B	1.210	2.084	13.640	210
3	.971	2.166	14.725	180	22C	1.213	2.083	13.640	210
4A	1.204	2.086	13.640	180	23	2.069	1.787	10.032	210
4B	1.214	2.082	13.640	180	24	2.716	1.564	7.721	210
4C	1.198	2.088	13.640	180	25A	1.211	2.083	13.640	270
5A	1.458	1.998	12.578	180	25B	1.211	2.083	13.640	270
5B	1.450	2.001	12.578	180	25C	1.210	2.084	13.640	270
5C	1.444	2.003	12.578	180	26	.722	2.252	15.933	0
6	2.068	1.788	10.032	180	27A	1.210	2.084	13.640	0
7	2.207	1.740	9.497	180	27B	1.210	2.084	13.640	0
8	2.722	1.562	7.721	180	27C	1.212	2.083	13.640	0
9	2.967	1.477	6.875	180	28	2.975	1.475	6.875	0
10	3.215	1.392	6.250	180	29A	1.213	2.083	13.640	90
11	3.470	1.304	5.400	180	29B	1.215	2.082	13.640	90
12	.722	2.252	15.933	190	29C	1.210	2.084	13.640	90
13A	1.208	2.084	13.640	190	30A	1.218	2.081	13.640	170
13B	1.212	2.083	13.640	190	30B	1.216	2.081	13.640	170
13C	1.210	2.084	13.640	190	30C	1.200	2.087	13.640	170
14	2.068	1.788	10.032	190	31	2.469	1.649	8.543	180
15	2.720	1.563	7.721	190	32	2.220	1.735	9.497	190
16	3.217	1.391	6.250	190	33	2.470	1.649	8.543	190
17	.975	2.165	14.725	200	34	2.970	1.476	6.875	190
18A	1.460	1.997	12.578	200	35	2.075	1.785	10.032	200
18B	1.455	1.999	12.578	200	36	2.471	1.649	8.543	200
18C	1.445	2.002	12.578	200	37	2.717	1.564	7.721	200
19	2.212	1.738	9.497	200	38	2.218	1.736	9.497	210
20	2.976	1.474	6.875	200	39	2.467	1.650	8.543	210
21	.472	2.338	17.173	210	40	2.967	1.477	6.875	210

FIGURE 24
MEASURED PRESSURE TAP LOCATIONS FROM INSPECTION IN CONICAL NOZZLE,
OPPOSED—TANGENTIAL PORT CONFIGURATION

TAP NO.	X	R	A	θ	TAP NO.	X	R	A	θ
1	.471	2.339	17.173	180	22A	1.210	2.083	13.644	210
2	.720	2.253	15.933	180	22B	1.208	2.084	13.644	210
3	.971	2.166	14.725	180	22C	1.209	2.084	13.644	210
4A	1.209	2.084	13.644	180	23	2.069	1.787	10.032	210
4B	1.212	2.083	13.644	180	24	2.716	1.564	7.721	210
4C	1.206	2.085	13.644	180	25A	1.210	2.083	13.644	270
5A	1.462	1.997	12.529	180	25B	1.205	2.085	13.644	270
5B	1.462	1.997	12.529	180	25C	1.203	2.086	13.644	270
5C	1.458	1.998	12.529	180	26	.722	2.252	15.933	0
6	2.068	1.788	10.032	180	27A	1.209	2.084	13.644	0
7	2.207	1.740	9.497	180	27B	1.205	2.085	13.644	0
8	2.722	1.562	7.721	180	27C	1.210	2.083	13.644	0
9	2.969	1.477	6.875	180	28	2.975	1.475	6.875	0
10	3.215	1.392	6.250	180	29A	1.209	2.084	13.644	90
11	3.470	1.304	5.400	180	29B	1.210	2.083	13.644	90
12	.722	2.252	15.933	190	29C	1.208	2.084	13.644	90
13A	1.210	2.084	13.644	190	30A	1.213	2.083	13.644	170
13B	1.213	2.083	13.644	190	30B	1.208	2.084	13.644	170
13C	1.205	2.085	13.644	190	30C	1.206	2.085	13.644	170
14	2.068	1.788	10.032	190	31	2.469	1.649	8.543	180
15	2.720	1.563	7.721	190	32	2.220	1.735	9.497	190
16	3.217	1.391	6.250	190	33	2.470	1.649	8.543	190
17	.975	2.165	14.725	200	34	2.970	1.476	6.875	190
18A	1.462	1.997	12.529	200	35	2.075	1.785	10.032	200
18B	1.460	1.997	12.529	200	36	2.471	1.649	8.543	200
18C	1.455	1.999	12.529	200	37	2.717	1.564	7.721	200
19	2.212	1.738	9.497	200	38	2.218	1.736	9.497	210
20	2.976	1.474	6.875	200	39	2.467	1.650	8.543	210
21	.472	2.338	17.173	210	40	2.967	1.477	6.875	210

9.382"
5.999"
5.141"
5.002"
3.900"
2.790"
1.000"
3.944"
.898"
1.145"
.605"
1.839"
19° Ref.
X
R
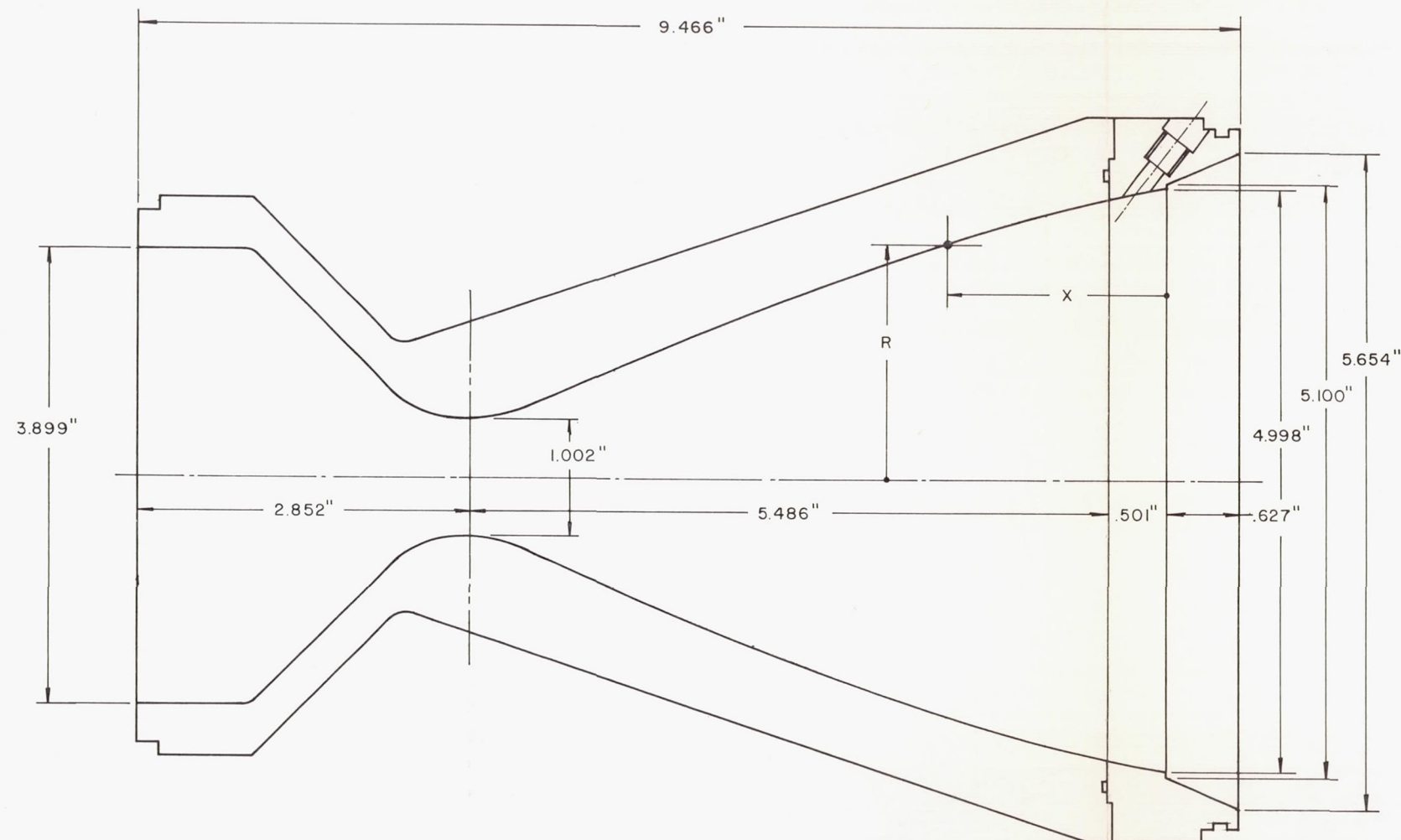
FIGURE 25
MEASURED PRESSURE TAP LOCATIONS FROM INSPECTION IN APG—I NOZZLE,
MULTIRADIAL PORT CONFIGURATION

TAP NO.	X	R	A	θ	TAP NO.	X	R	A	θ
1A	.405	2.454	18.919	180	22	1.470	2.201	15.219	210
1B	.406	2.454	18.919	180	23	1.972	2.043	13.113	210
1C	.405	2.454	18.919	180	24	2.469	1.869	10.986	210
2	.728	2.393	18.005	180	25	1.474	2.200	15.219	270
3	.965	2.337	17.143	180	26	.728	2.394	18.005	0
4	1.471	2.201	15.219	180	27	1.470	2.201	15.219	0
5	1.717	2.126	14.173	180	28	2.976	1.680	8.867	0
6	1.971	2.043	13.113	180	29	1.471	2.201	15.219	90
7	2.218	1.958	12.032	180	30	1.467	2.202	15.219	170
8	2.458	1.673	10.986	180	31	1.239	2.267	16.160	180
9	2.979	1.678	8.867	180	32A	.411	2.453	18.919	190
10	3.222	1.626	8.296	180	32B	.400	2.455	18.919	190
11	3.477	1.529	7.345	180	32C	.405	2.454	18.919	190
12	.721	2.395	18.005	190	33	.973	2.333	11.143	190
13	1.474	2.200	15.219	190	34	1.243	2.265	16.160	190
14	1.969	2.044	13.113	190	35	1.727	2.123	14.173	190
15	2.470	1.869	10.986	190	36A	.411	2.453	18.919	200
16	3.229	1.624	8.296	190	36B	.408	2.454	18.919	200
17	.979	2.333	17.143	200	36C	.411	2.453	18.919	200
18	1.722	2.124	14.173	200	37	.732	2.393	18.005	200
19	2.224	1.956	12.032	200	38	1.224	2.271	16.160	200
20	2.971	1.682	8.867	200	39	1.481	2.199	15.219	200
21A	.411	2.453	18.919	210	40	.949	2.339	17.143	210
21B	.408	2.454	18.919	210	90	-.312	Base		
21C	.411	2.453	18.919	210	91	0	Base		
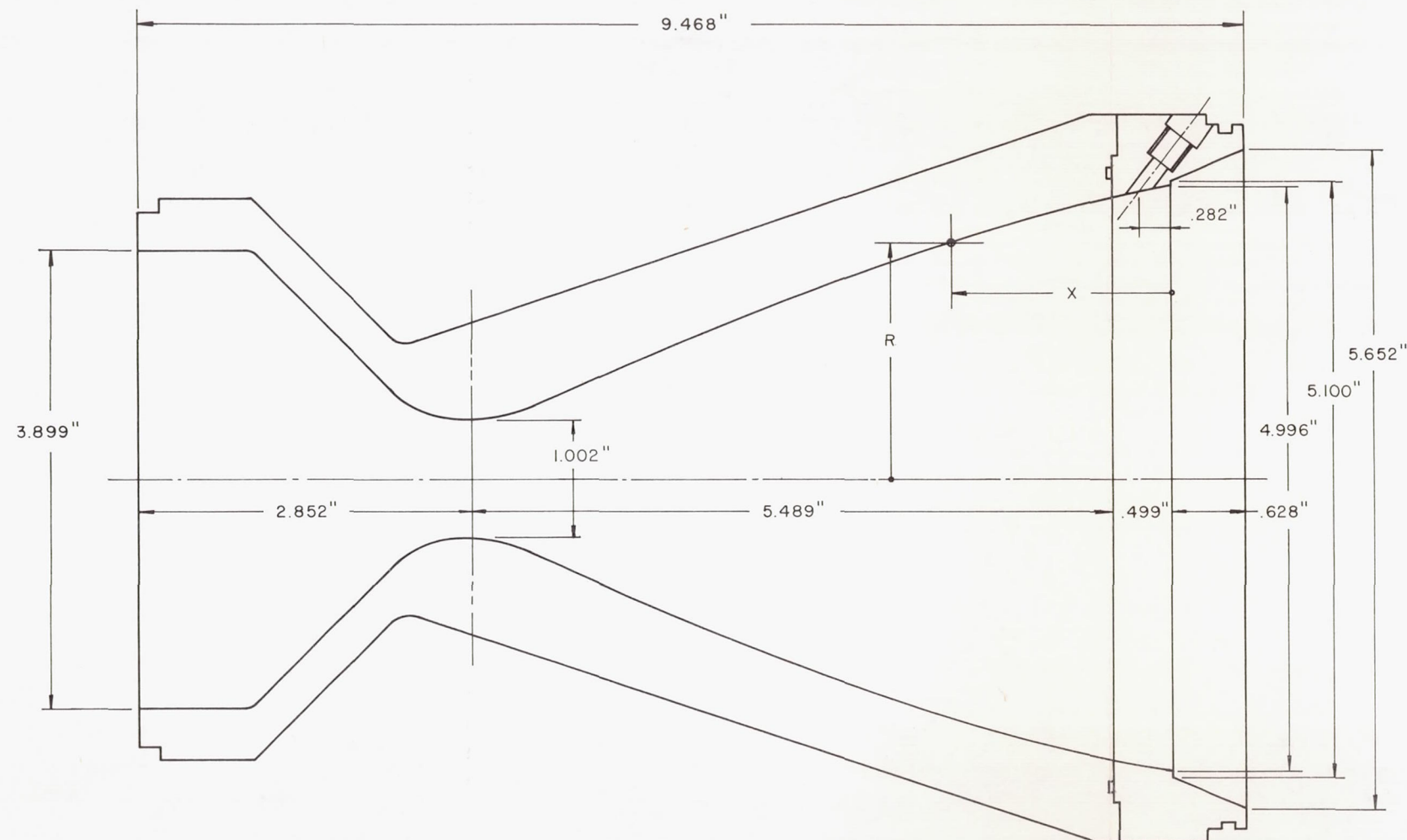
FIGURE 26
MEASURED PRESSURE TAP LOCATIONS FROM INSPECTION IN APG-I NOZZLE,
OPPOSED-TANGENTIAL PORT CONFIGURATION

TAP NO.	X	R	A	θ	TAP NO.	X	R	A	θ
1A	.415	2.452	18.886	180	22	1.470	2.201	15.219	210
1B	.419	2.451	18.886	180	23	1.972	2.043	13.113	210
1C	.414	2.452	18.886	180	24	2.469	1.869	10.986	210
2	.728	2.393	18.005	180	25	1.474	2.200	15.219	270
3	.965	2.337	17.143	180	26	.723	2.394	18.005	0
4	1.471	2.201	15.219	180	27	1.470	2.201	15.219	0
5	1.717	2.126	14.173	180	28	2.976	1.680	8.867	0
6	1.971	2.043	13.113	180	29	1.471	2.201	15.219	90
7	2.218	1.958	12.032	180	30	1.467	2.202	15.219	170
8	2.458	1.673	10.986	180	31	1.239	2.267	16.160	180
9	2.979	1.678	8.867	180	32A	.414	2.452	18.886	190
10	3.222	1.626	8.296	180	32B	.416	2.452	18.886	190
11	3.477	1.529	7.345	180	32C	.413	2.452	18.886	190
12	.721	2.395	18.005	190	33	.973	2.333	11.143	190
13	1.474	2.200	15.219	190	34	1.243	2.265	16.160	190
14	1.969	2.044	13.113	190	35	1.727	2.123	14.173	190
15	2.470	1.869	10.986	190	36A	.416	2.451	18.886	200
16	3.229	1.624	8.296	190	36B	.413	2.452	18.886	200
17	.979	2.333	17.143	200	36C	.415	2.452	18.886	200
18	1.722	2.124	14.173	200	37	.732	2.393	18.005	200
19	2.224	1.956	12.032	200	38	1.224	2.271	16.160	200
20	2.971	1.682	8.867	200	39	1.481	2.199	15.219	200
21A	.414	2.452	18.886	210	40	.949	2.339	17.143	210
21B	.417	2.451	18.886	210	90	-.320	Base		
21C	.414	2.452	18.886	210	91	0	Base		
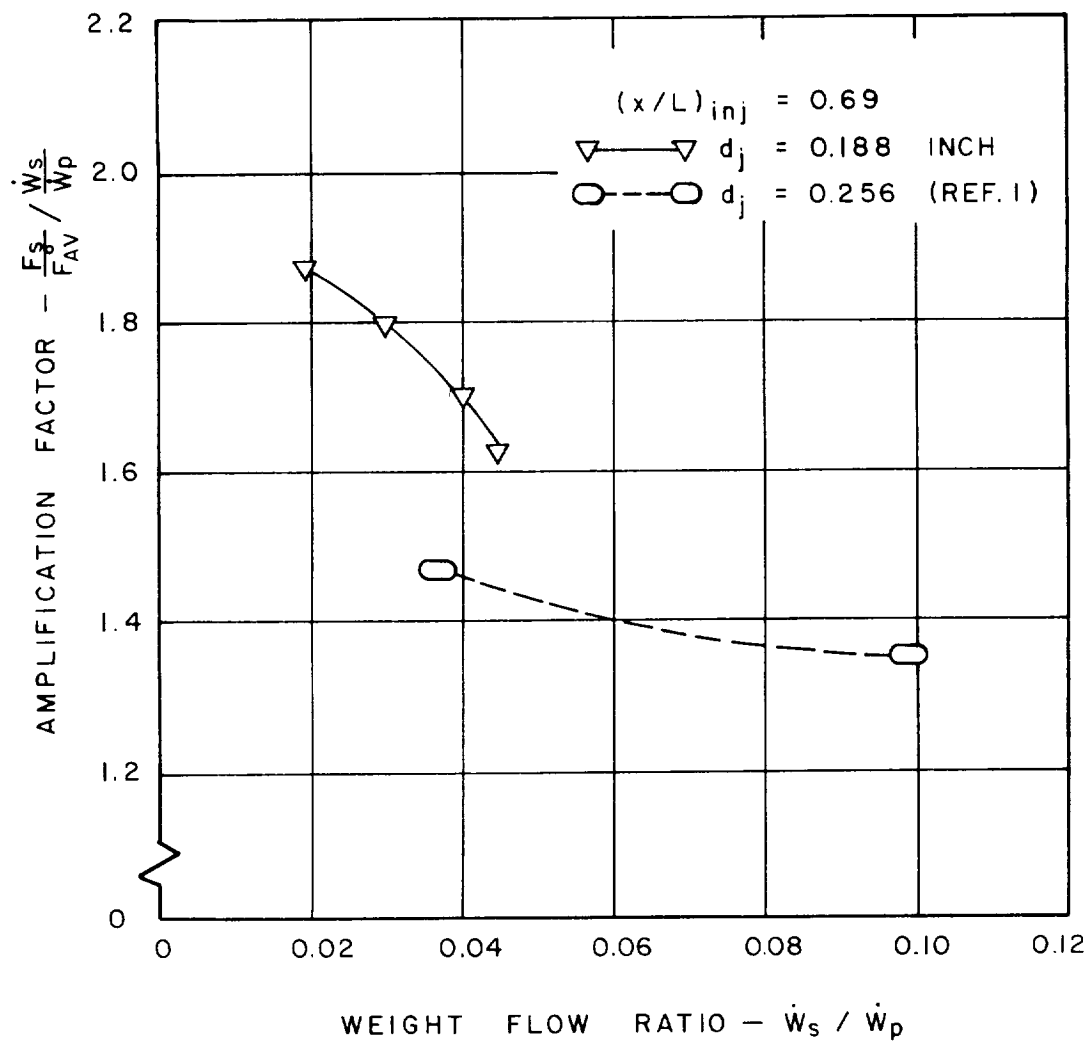
FIGURE 27

EFFECT OF INJECTION PORT DIAMETER ON THE
AMPLIFICATION FACTOR USING SINGLE PORT IN-
JECTION IN THE CONICAL NOZZLE
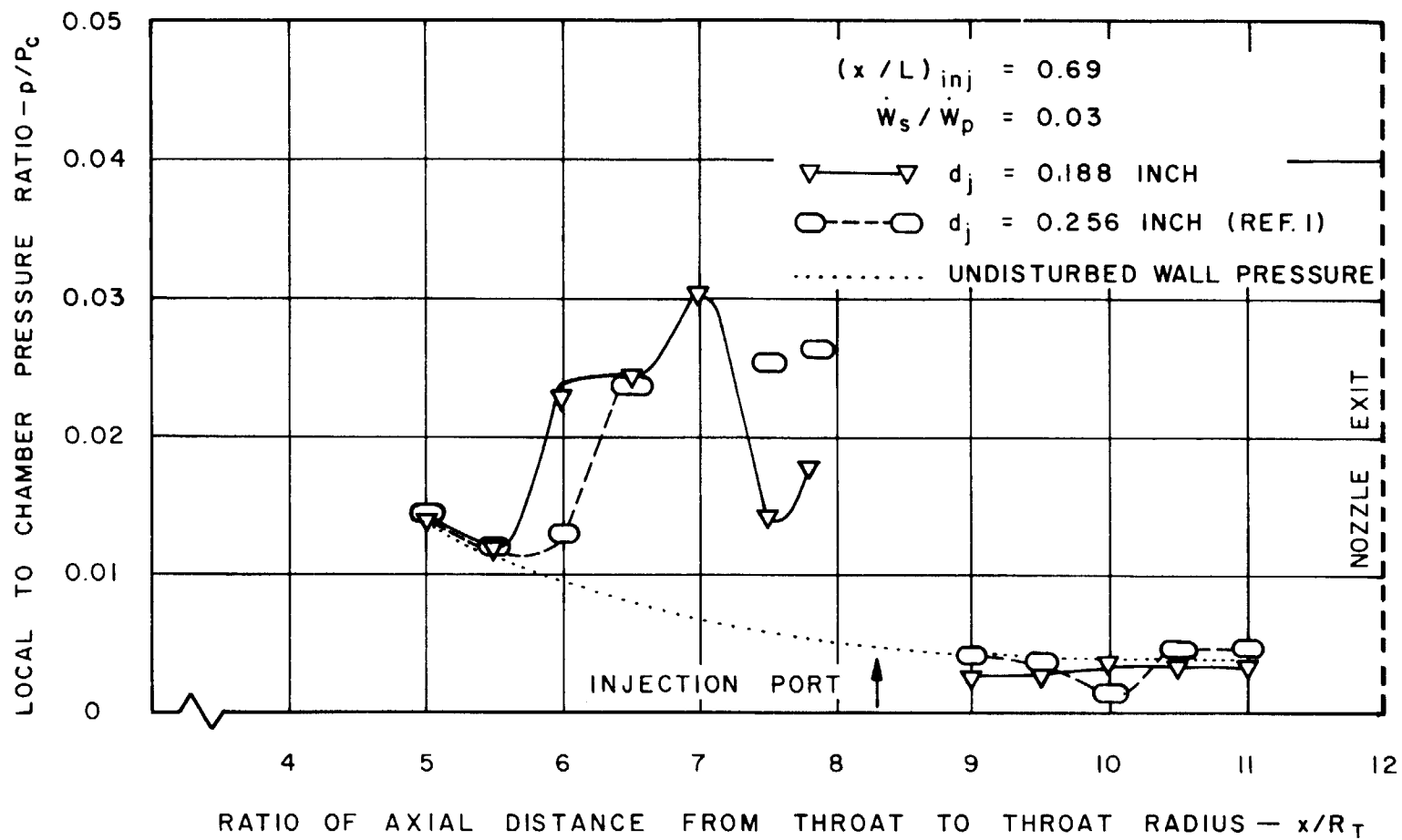
FIGURE 28

EFFECT OF INJECTION PORT DIAMETER ON THE WALL PRESSURE DISTRI-
BUTION IN MERIDIONAL PLANE IN THE CONICAL NOZZLE USING SINGLE
PORT INJECTION
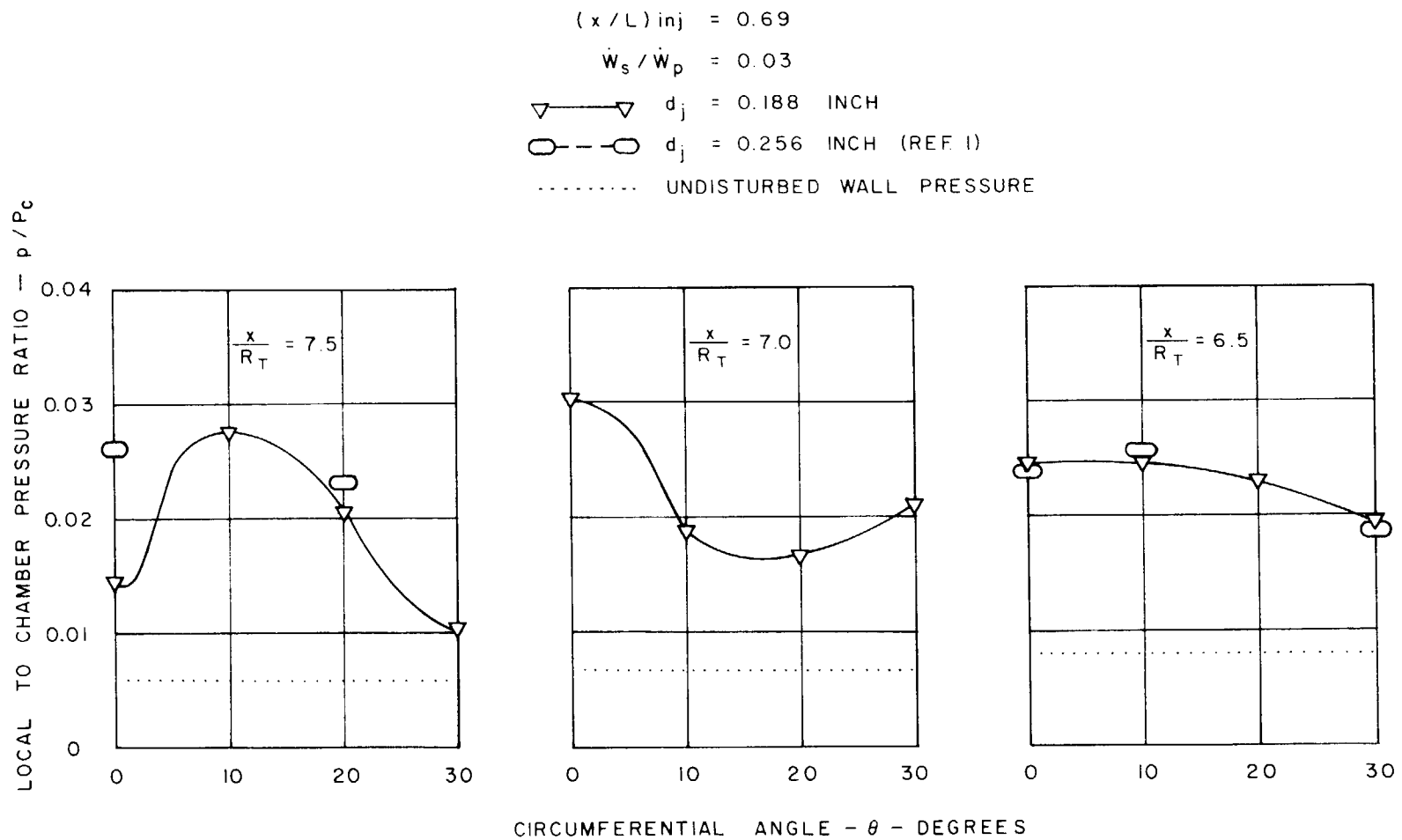
FIGURE 29

EFFECT OF INJECTION PORT DIAMETER ON THE WALL PRESSURE DISTRIBUTION
IN CIRCUMFERENTIAL PLANE IN THE CONICAL NOZZLE USING SINGLE PORT
INJECTION
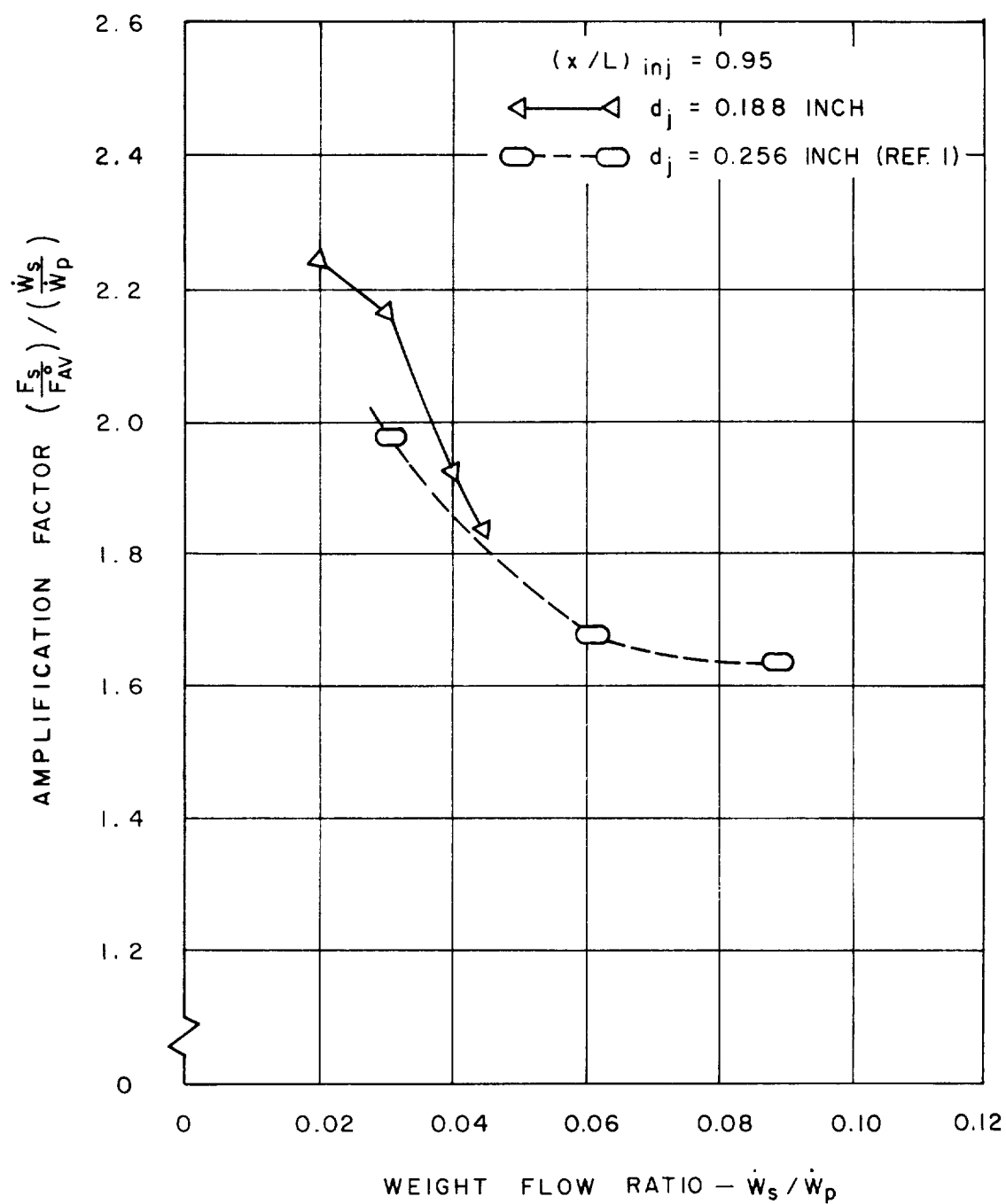
FIGURE 30

EFFECT OF INJECTION PORT DIAMETER ON THE
AMPLIFICATION FACTOR USING SINGLE PORT
INJECTION IN THE APG-1 NOZZLE
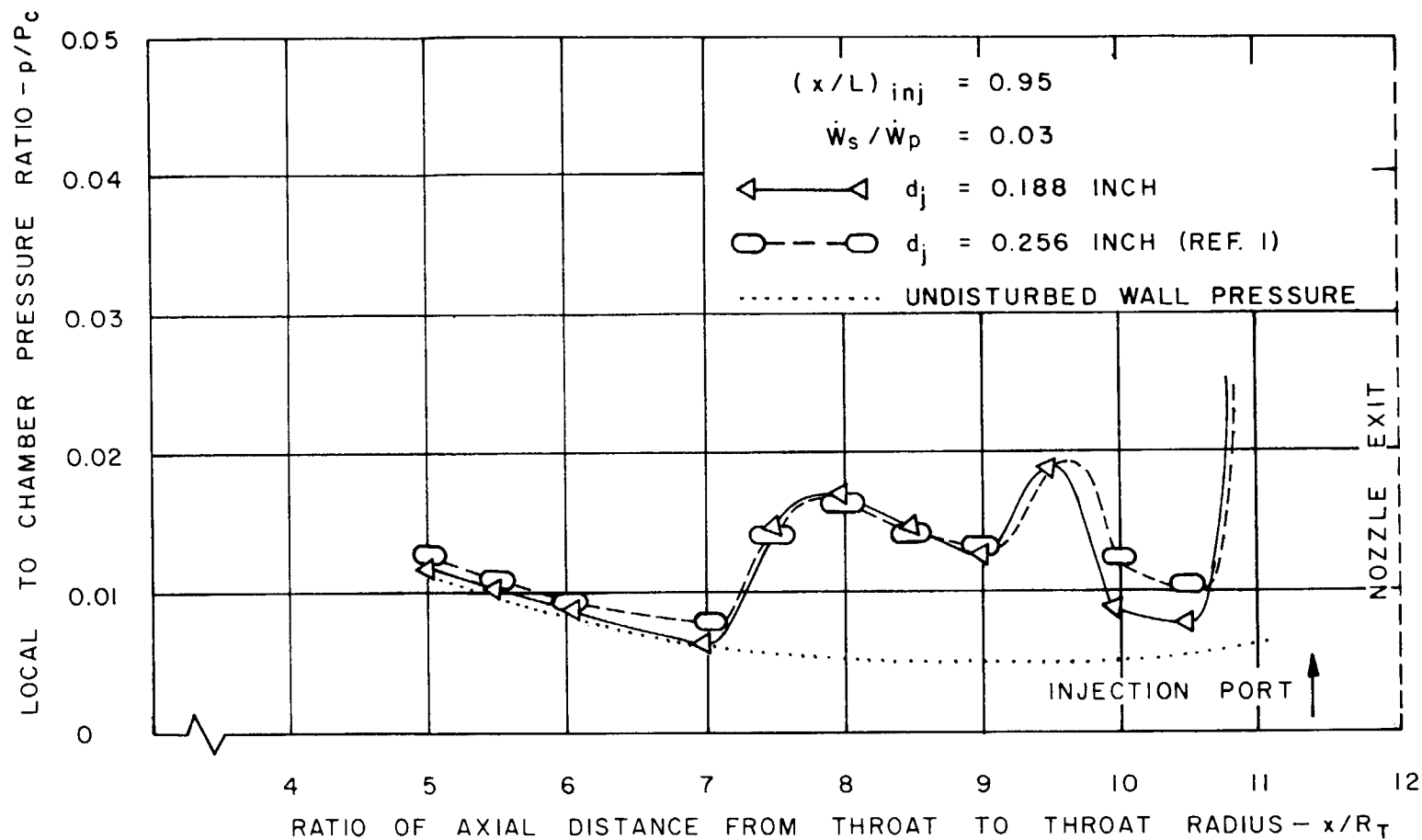
FIGURE 31

EFFECT OF INJECTION PORT DIAMETER ON THE WALL PRESSURE DISTRI-
BUTION IN MERIDIONAL PLANE IN THE APG-1 NOZZLE USING SINGLE PORT
INJECTION
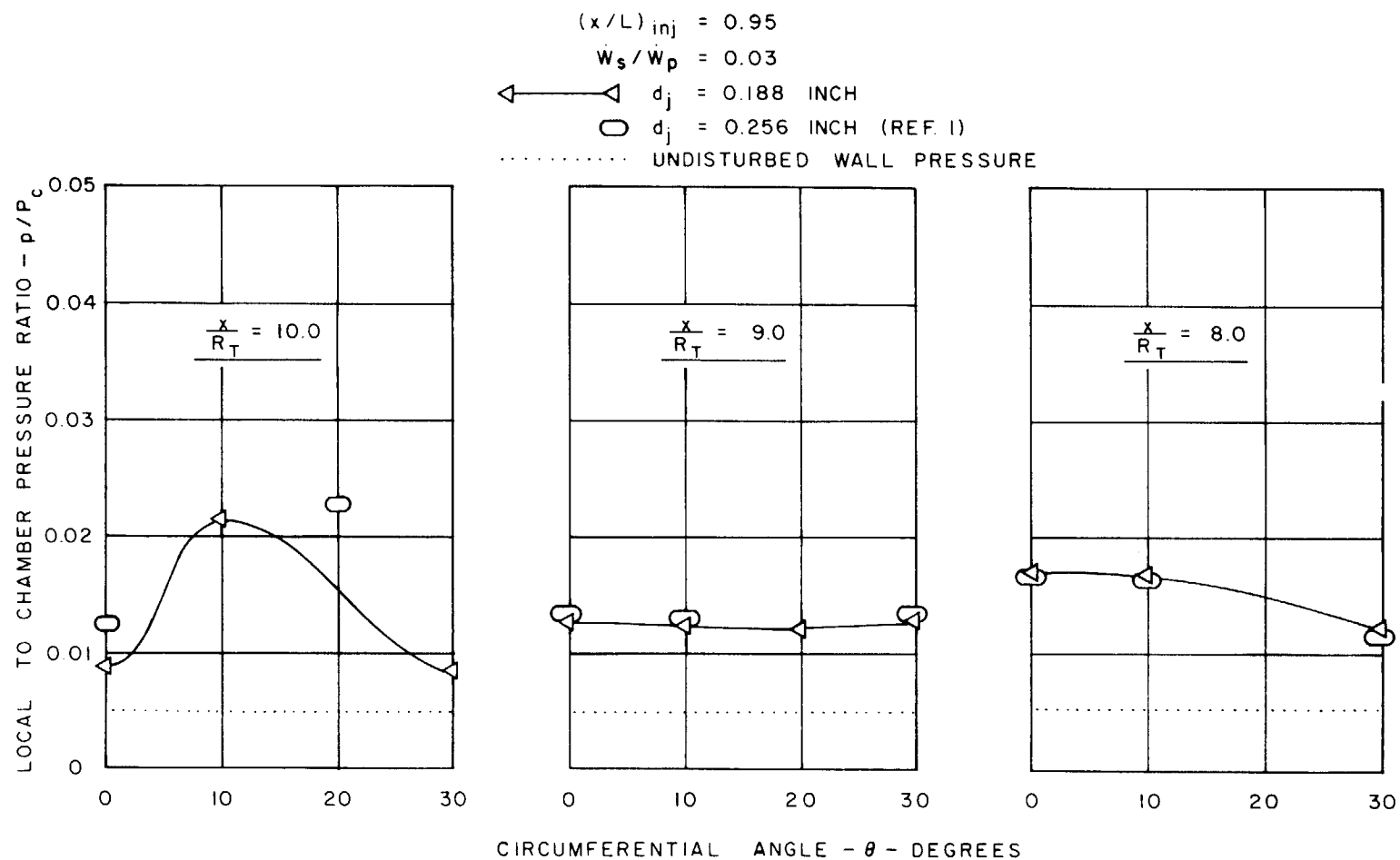
FIGURE 32

EFFECT OF INJECTION DIAMETER ON THE WALL PRESSURE DISTRIBUTION
IN CIRCUMFERENTIAL PLANE IN THE APG-1 NOZZLE USING SINGLE PORT
INJECTION
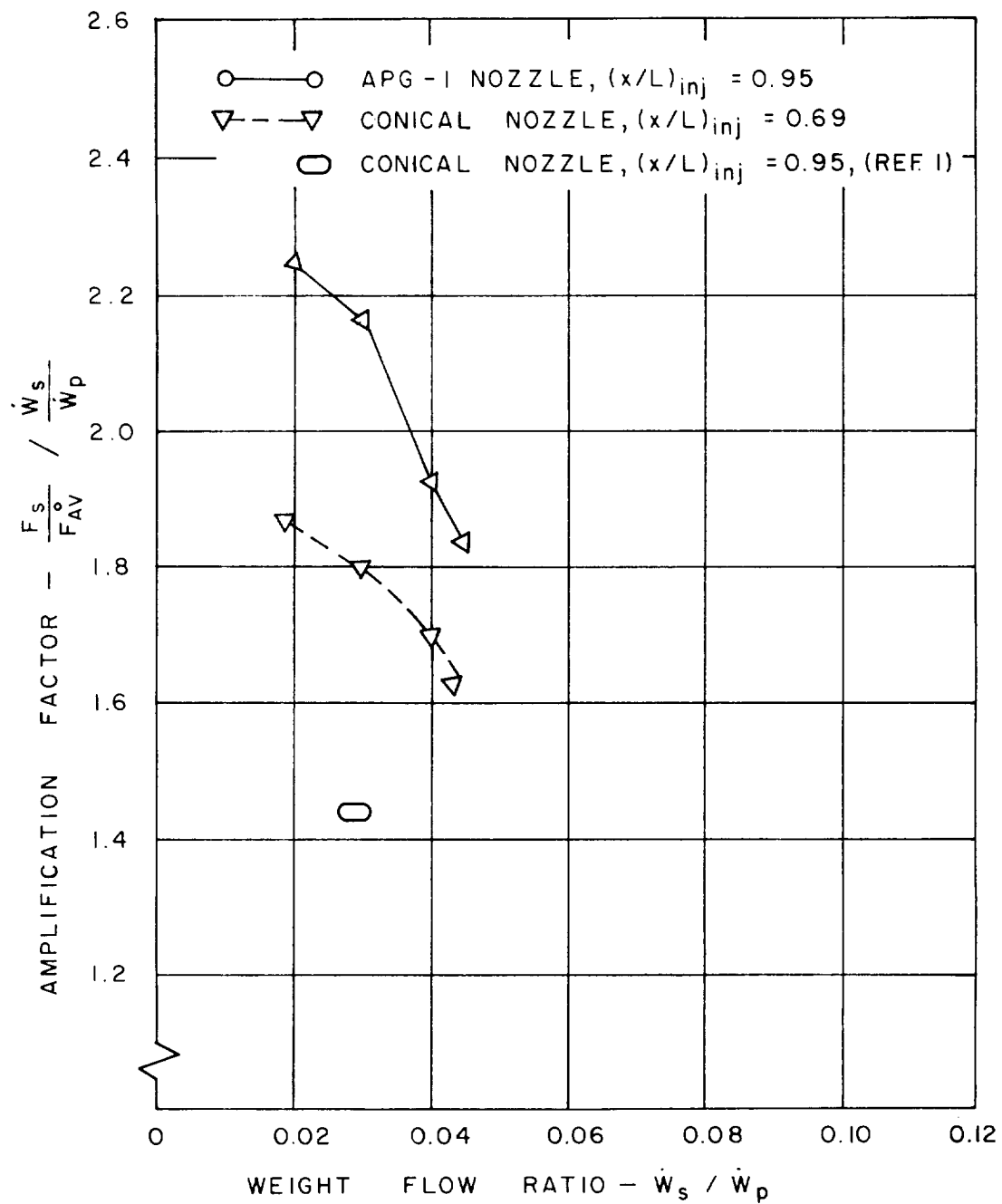
FIGURE 33

COMPARISON OF THE AMPLIFICATION FACTOR
BETWEEN THE APG-1 AND CONICAL NOZZLES USING
SINGLE PORT INJECTION

-187-
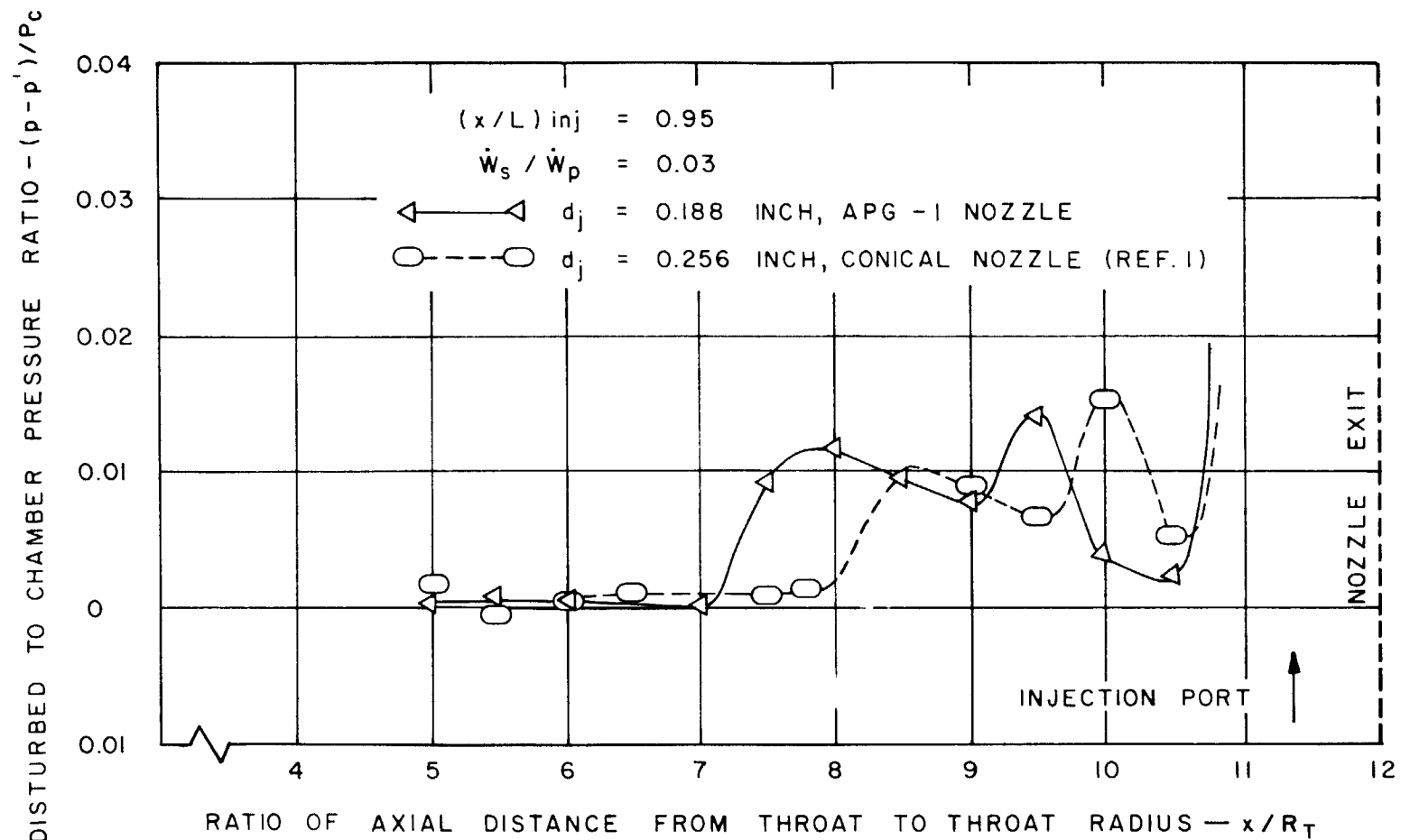
FIGURE 34

COMPARISON OF WALL PRESSURE DISTRIBUTION IN MERIDIONAL PLANE IN
THE APG-1 AND CONICAL NOZZLES USING SINGLE PORT INJECTION
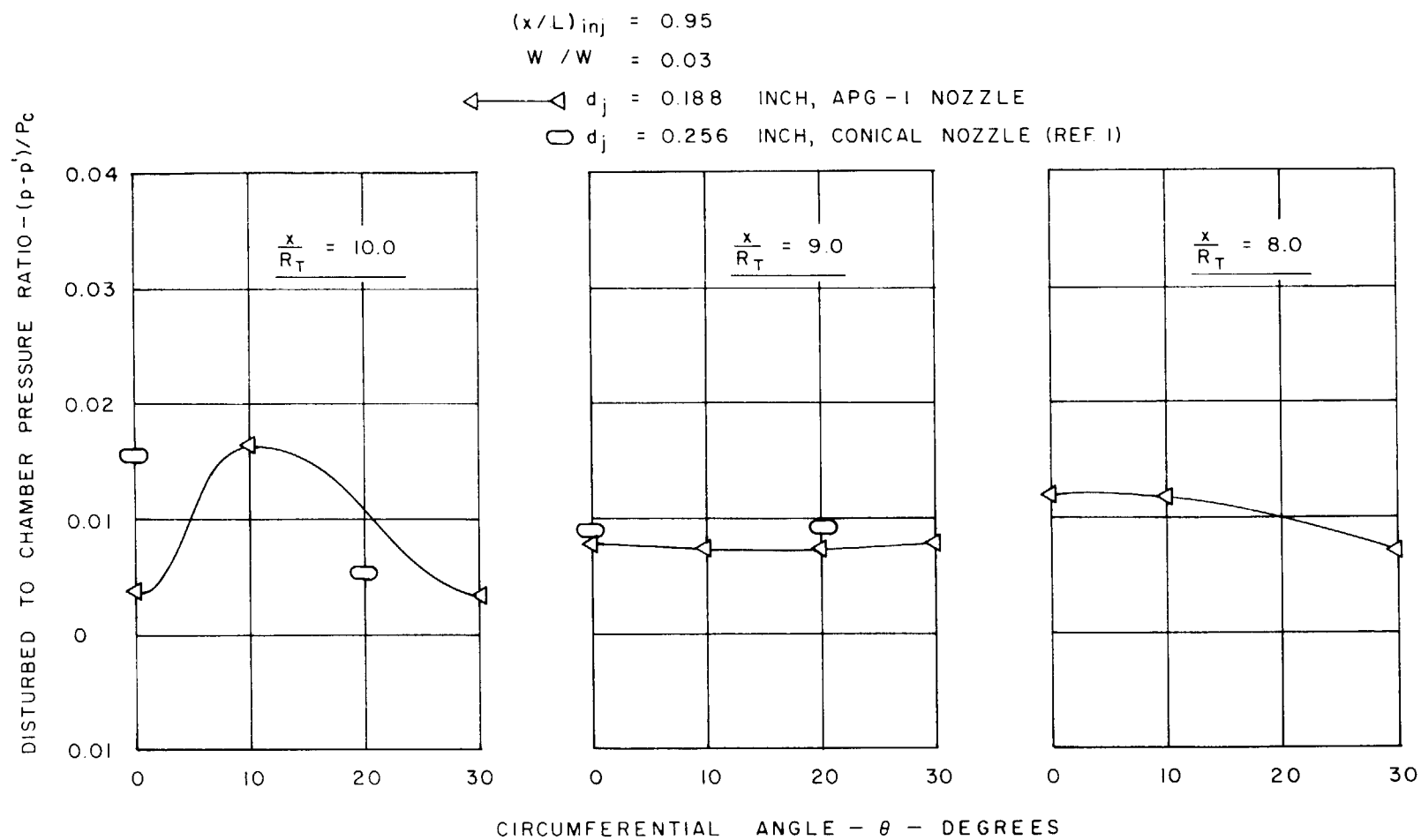
FIGURE 35

COMPARISON OF WALL PRESSURE DISTRIBUTION IN CIRCUMFERENTIAL PLANE
IN THE APG-1 AND CONICAL NOZZLES USING SINGLE PORT INJECTION
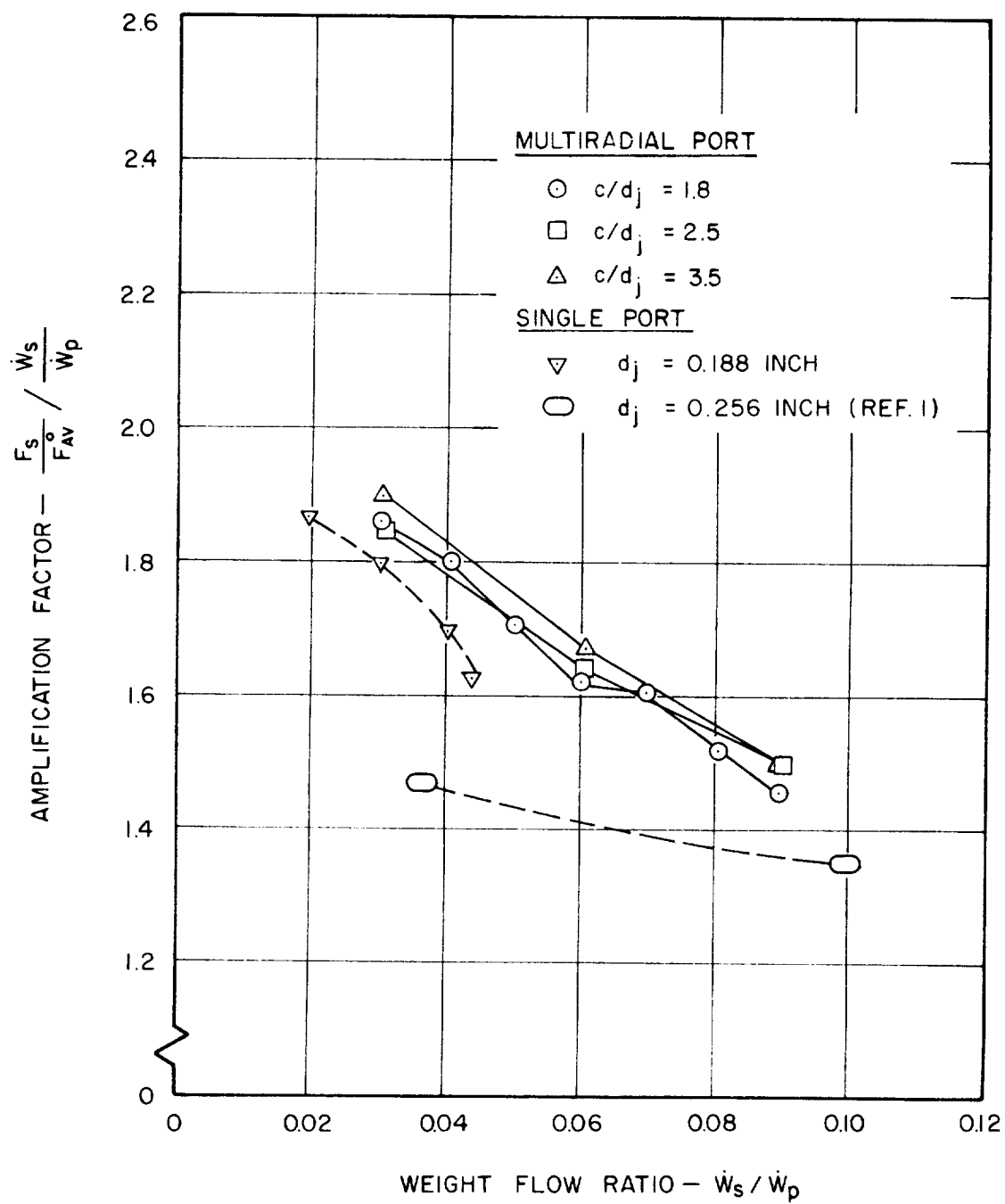
FIGURE 36

INFLUENCE OF WEIGHT FLOW RATIO ON THE AMPLI-
FICATION FACTOR USING SINGLE AND MULTIRADIAL
PORT INJECTION AT $(x/L)_{inj}$ = 0.69 IN THE CONICAL
NOZZLE
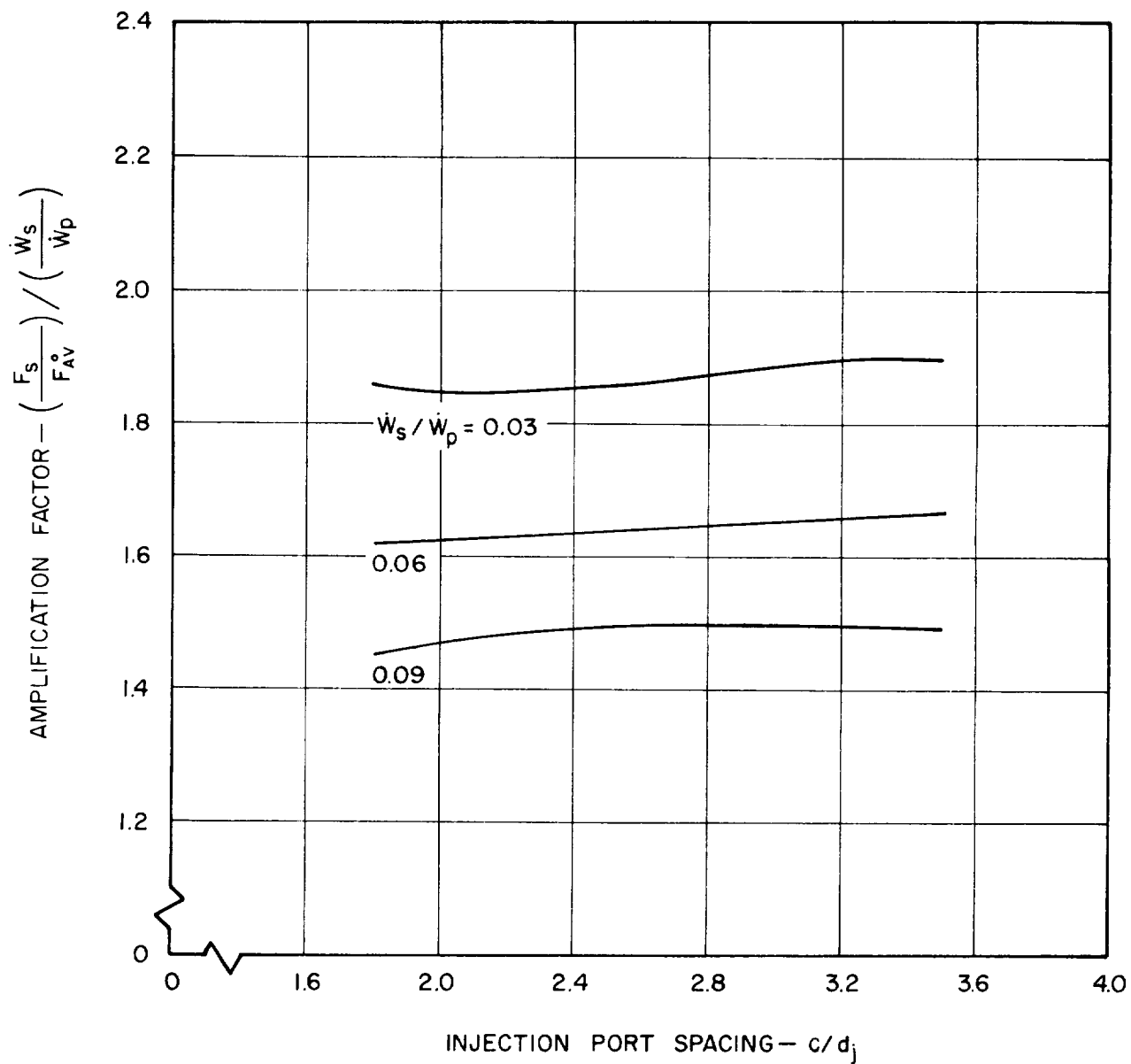
FIGURE 37

EFFECT OF INJECTION PORT SPACING ON THE
AMPLIFICATION FACTOR USING MULTIRADIAL
PORT INJECTION IN THE CONICAL NOZZLE
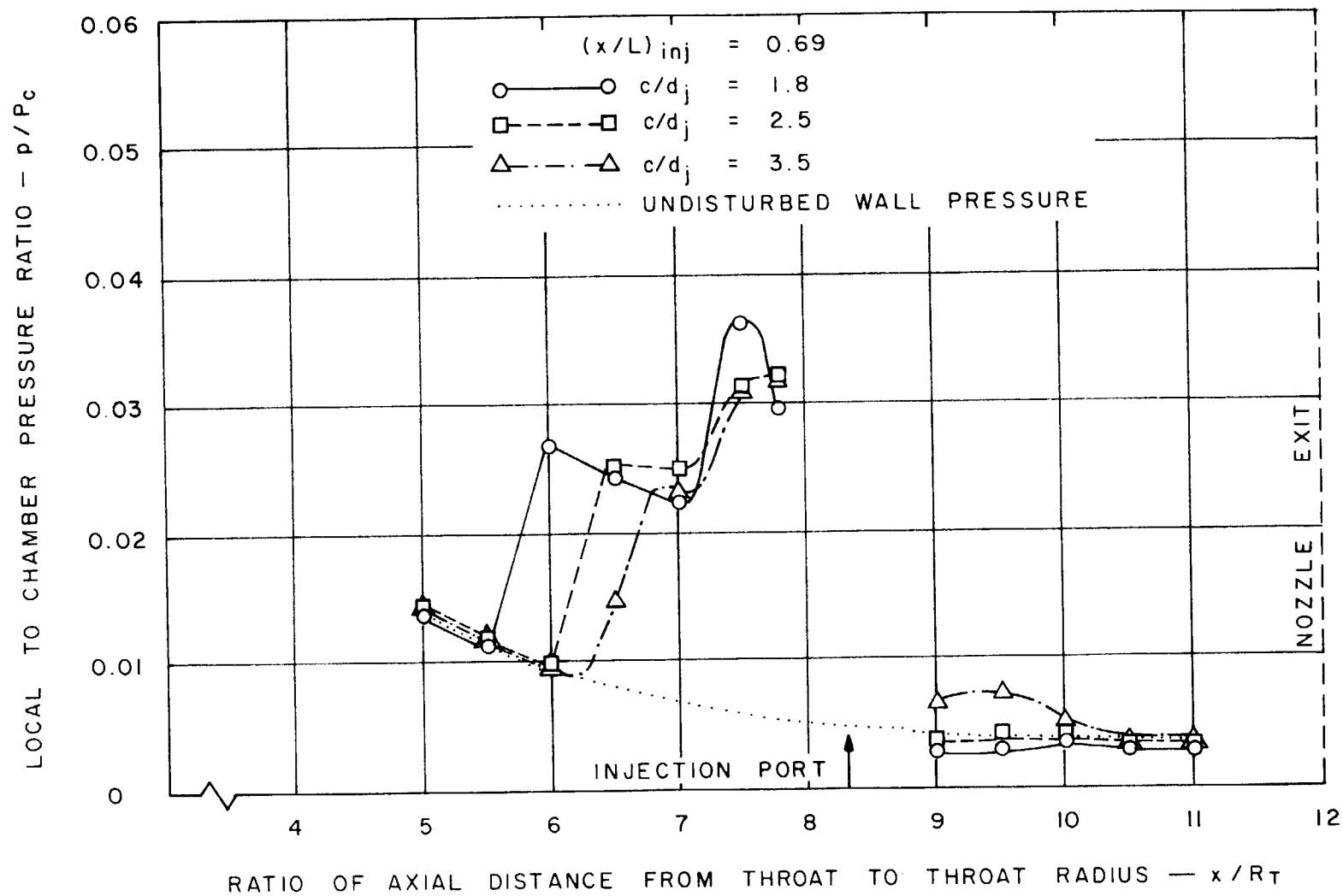
FIGURE 38

WALL PRESSURE DISTRIBUTION IN MERIDIONAL PLANE OF INJECTION IN THE
CONICAL NOZZLE USING MULTIRADIAL PORT INJECTION ($\dot{w}_s / \dot{w}_p$ = 0.03)
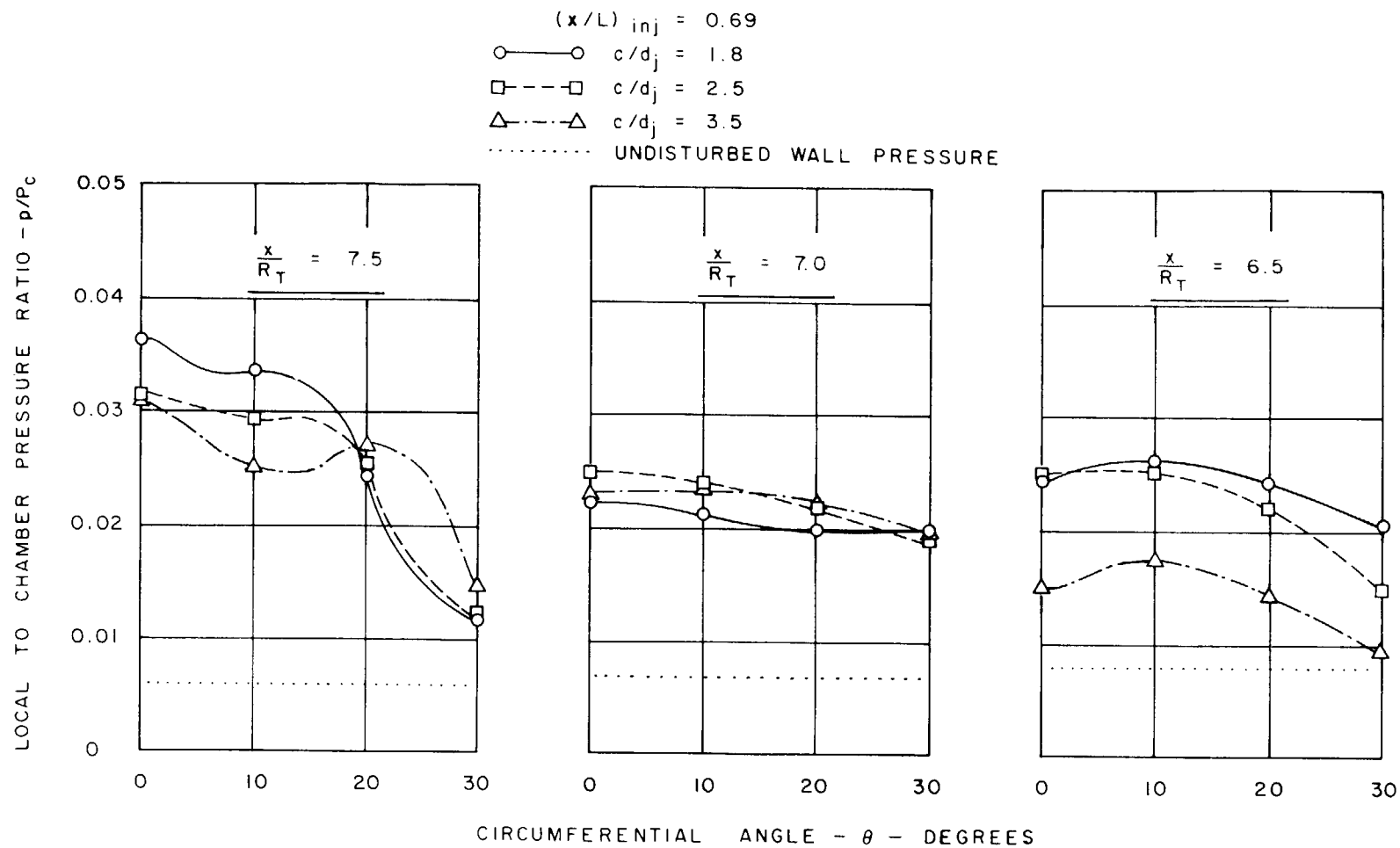
FIGURE 39

WALL PRESSURE DISTRIBUTION IN CIRCUMFERENTIAL PLANE IN THE CONICAL
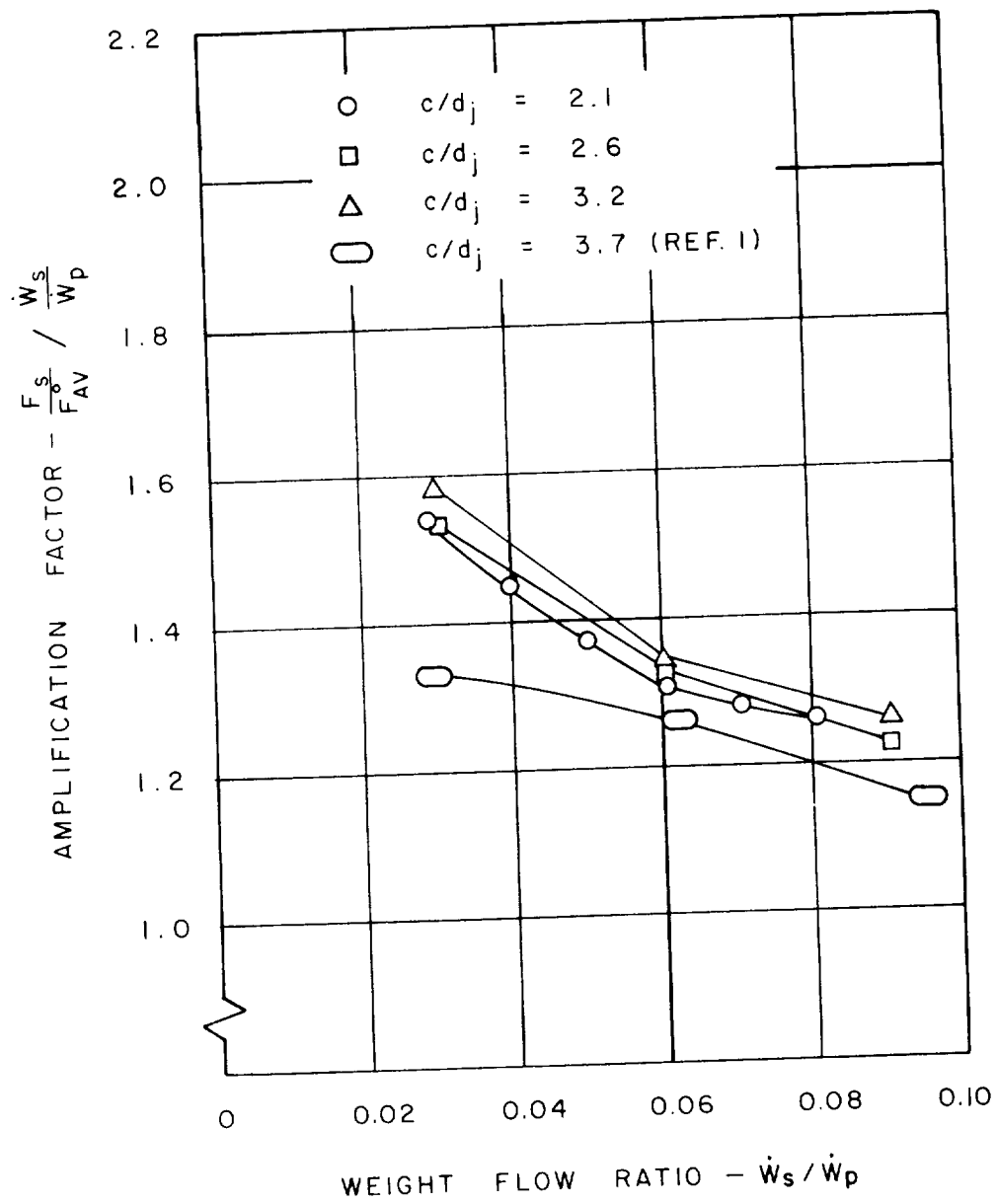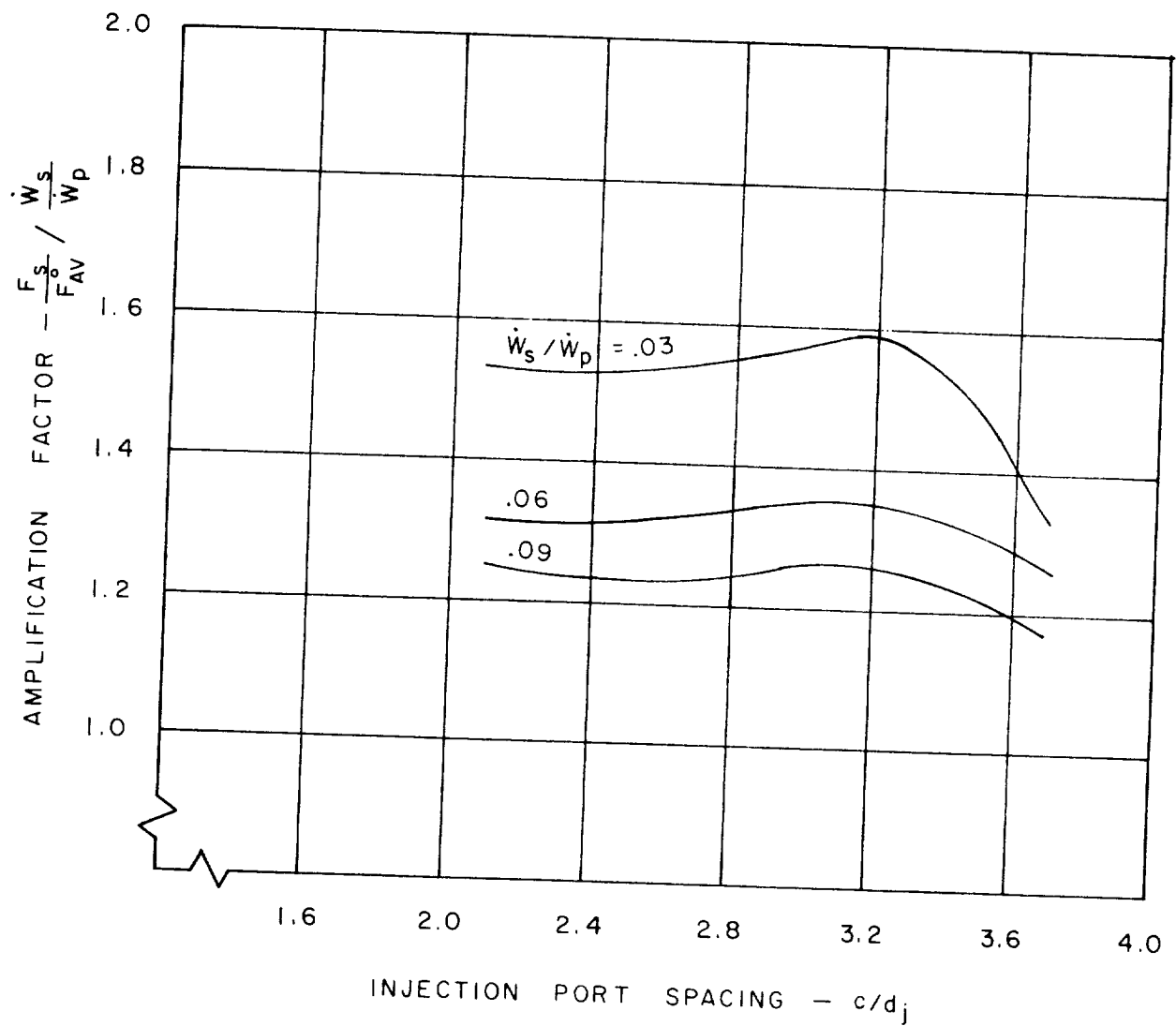NOZZLE USING MULTIRADIAL PORT INJECTION ($\dot{w}_s / \dot{w}_p$ = 0.03)
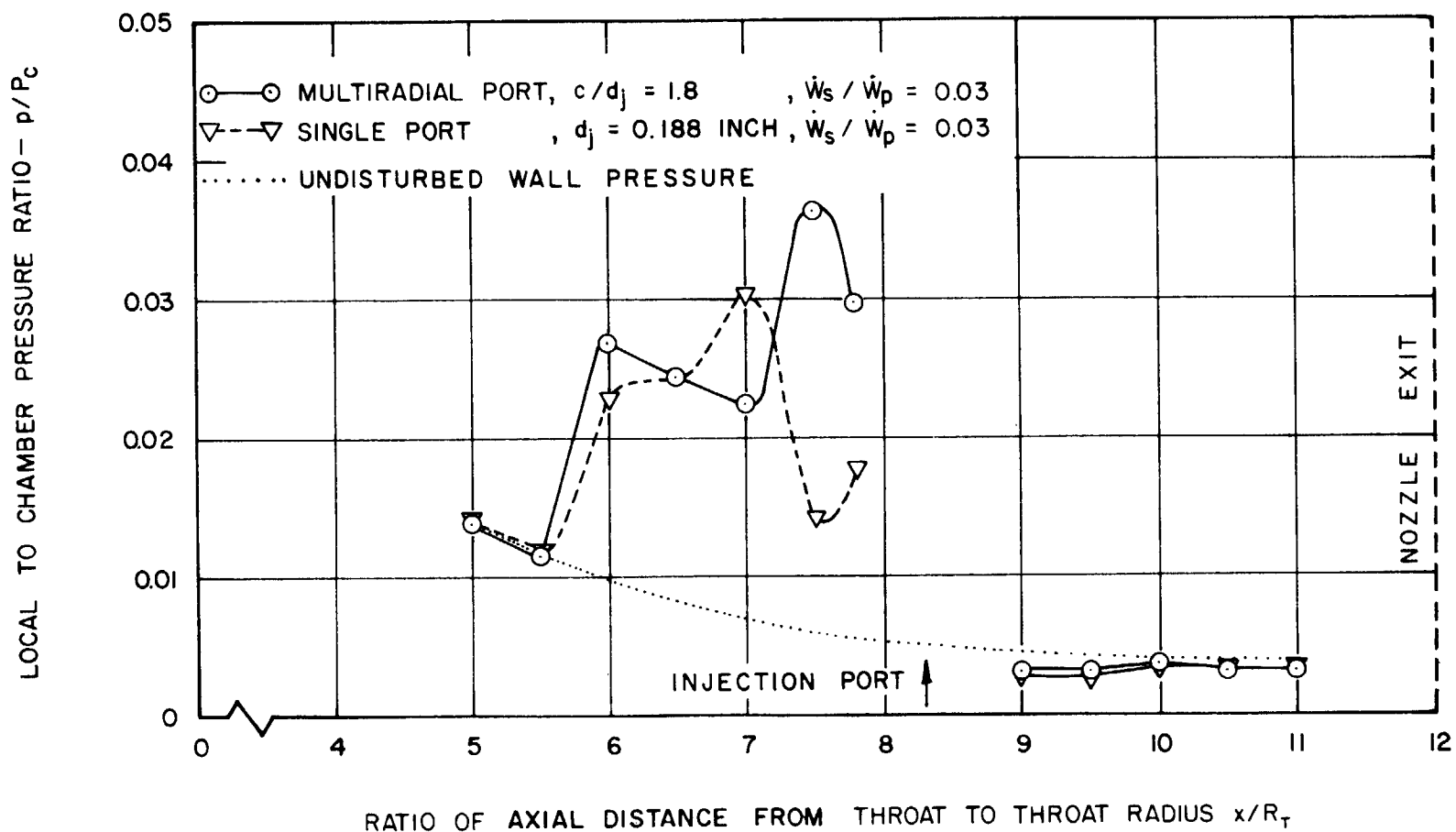
FIGURE 40

COMPARISON OF THE WALL PRESSURE DISTRIBUTION IN MERIDIONAL PLANE
IN CONICAL NOZZLE USING SINGLE AND MULTIRADIAL PORT INJECTION
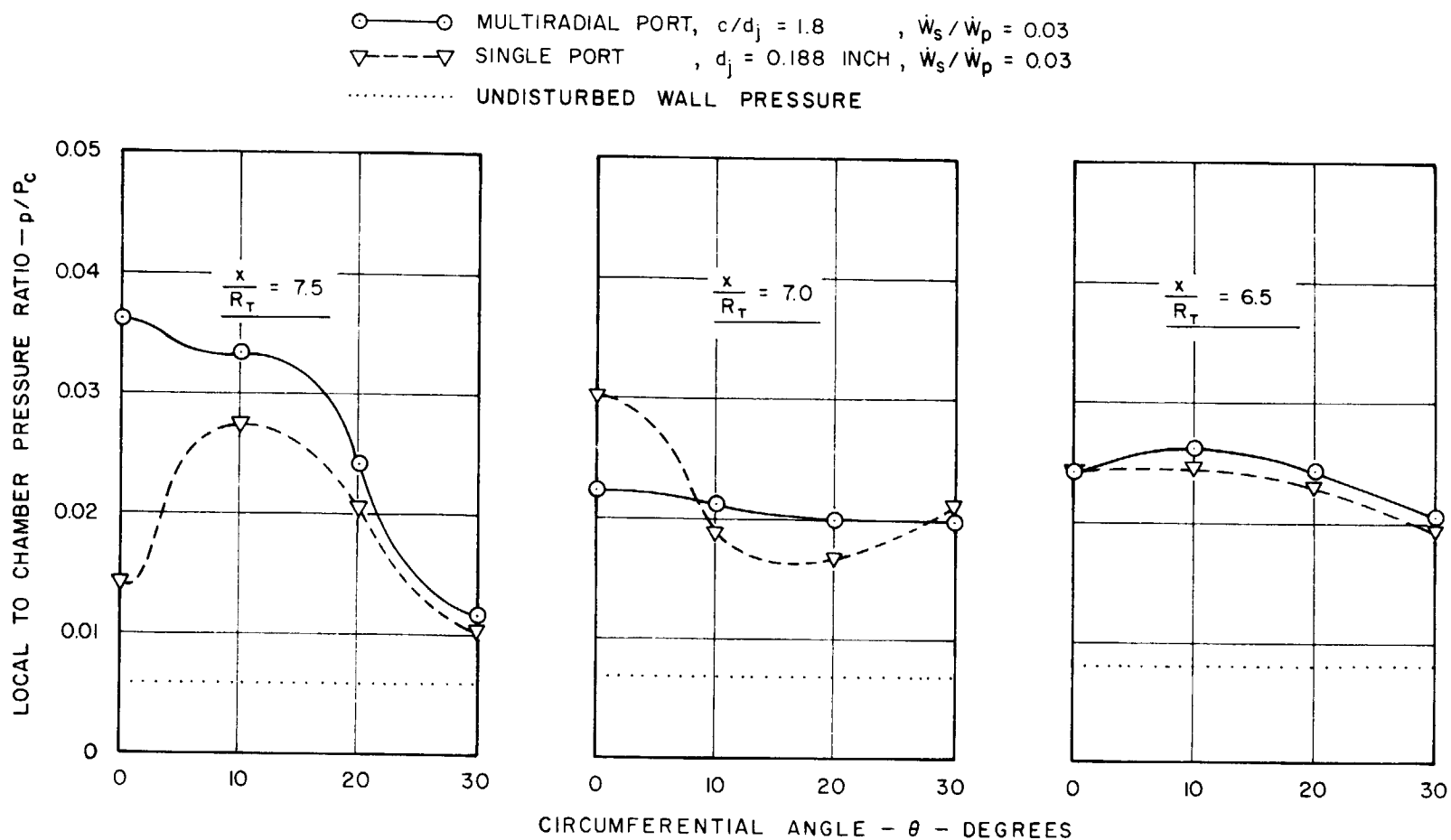
FIGURE 41

COMPARISON OF THE WALL PRESSURE DISTRIBUTION IN CIRCUMFERENTIAL PLANE
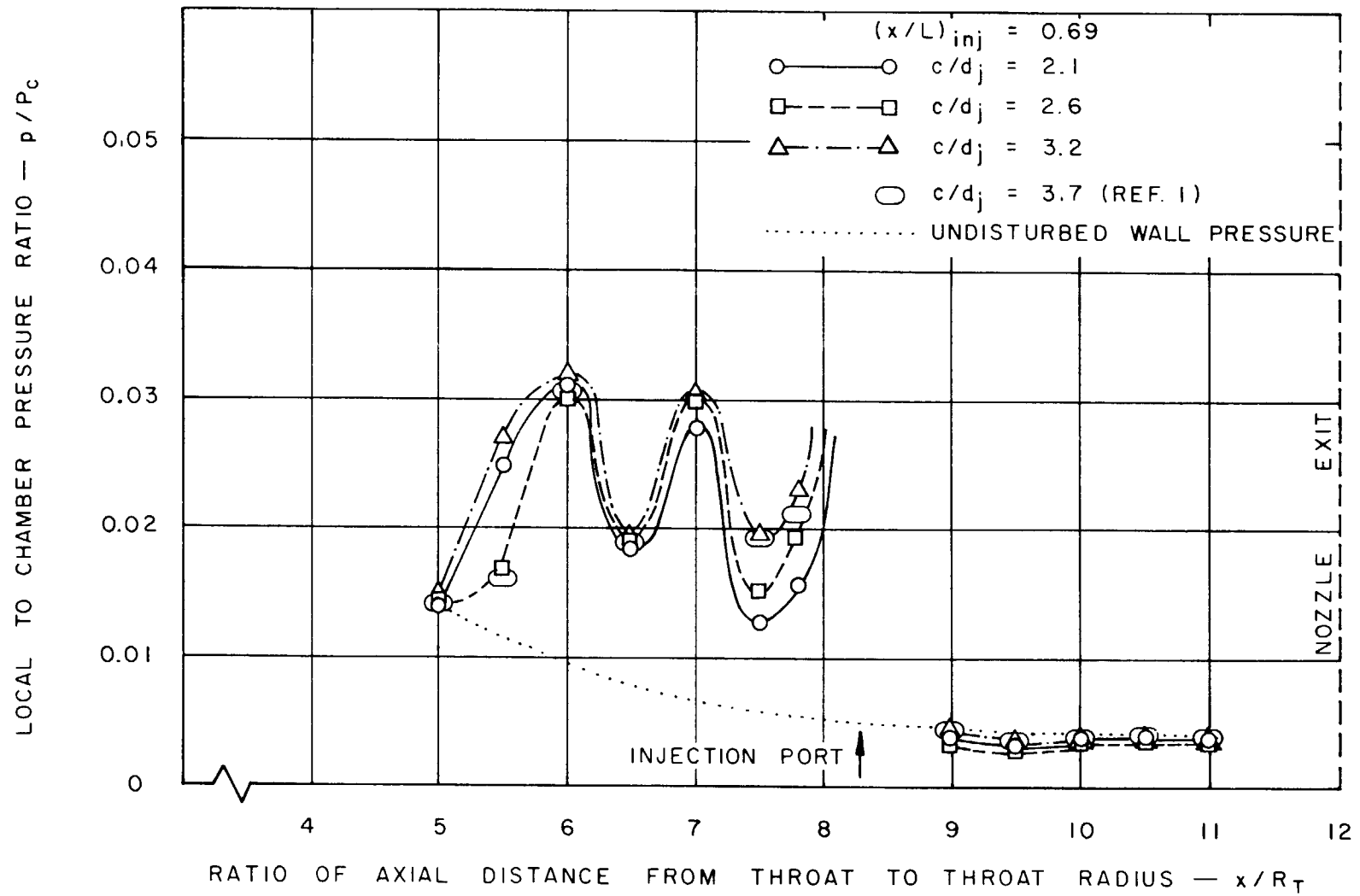IN CONICAL NOZZLE USING SINGLE AND MULTIRADIAL PORT INJECTION
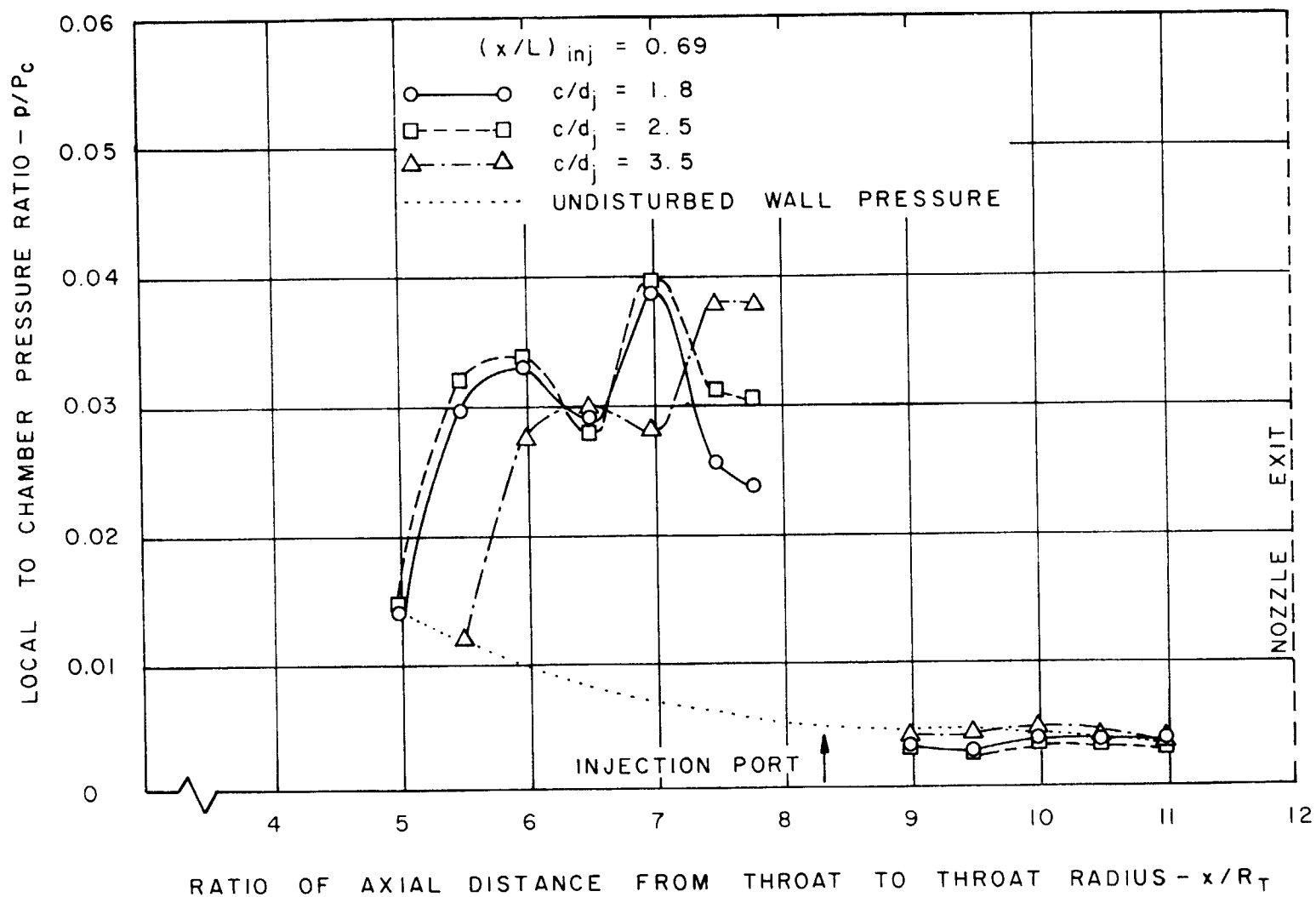
FIGURE 42

WALL PRESSURE DISTRIBUTION IN MERIDIONAL PLANE OF INJECTION IN THE
CONICAL NOZZLE USING MULTIRADIAL PORT INJECTION ($\dot{w}_s / \dot{w}_p = 0.06$)
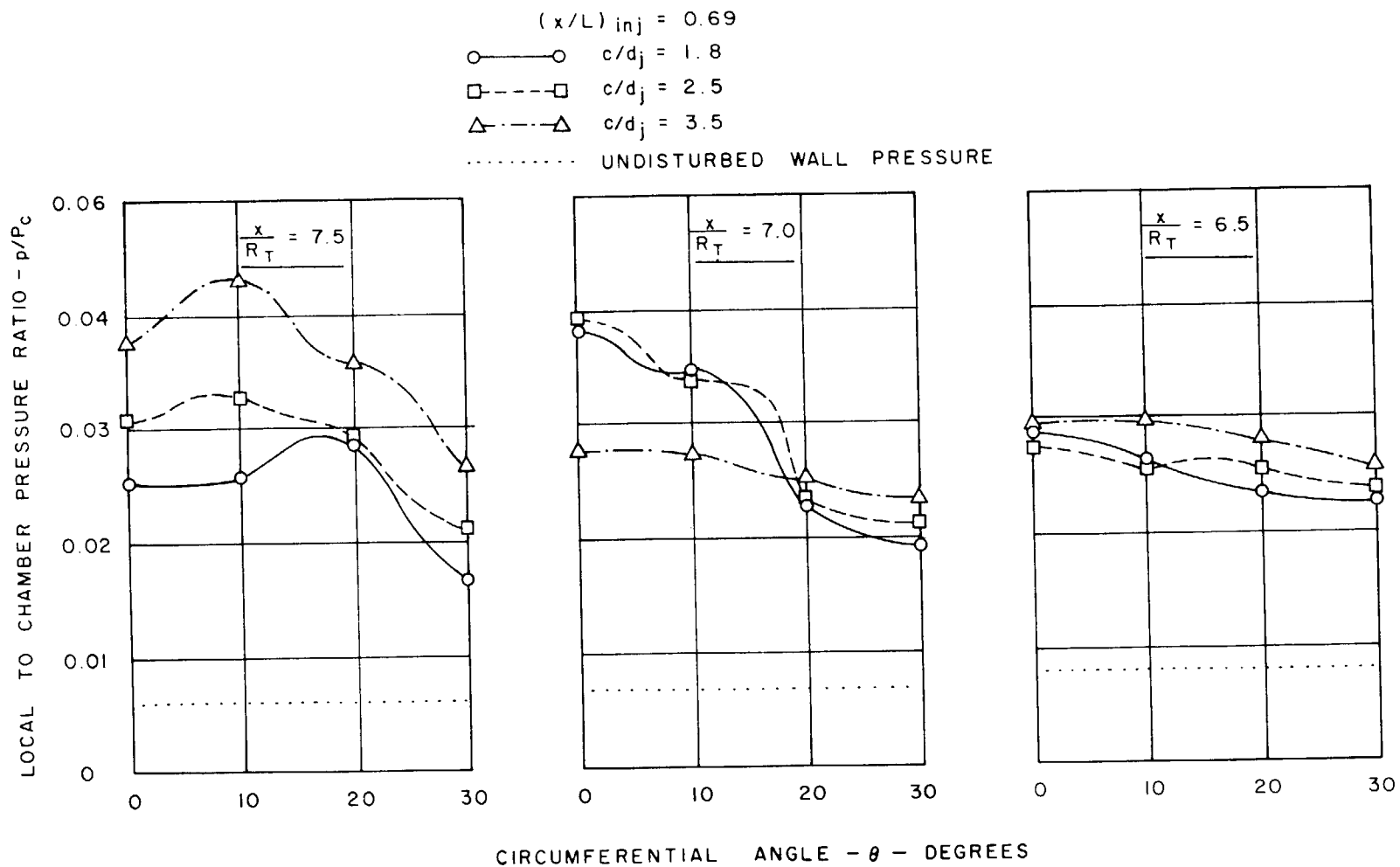
FIGURE 43

WALL PRESSURE DISTRIBUTION IN CIRCUMFERENTIAL PLANE IN THE CONICAL NOZZLE USING MULTIRADIAL PORT INJECTION ($\dot{w}_s / \dot{w}_p$ = 0.06)
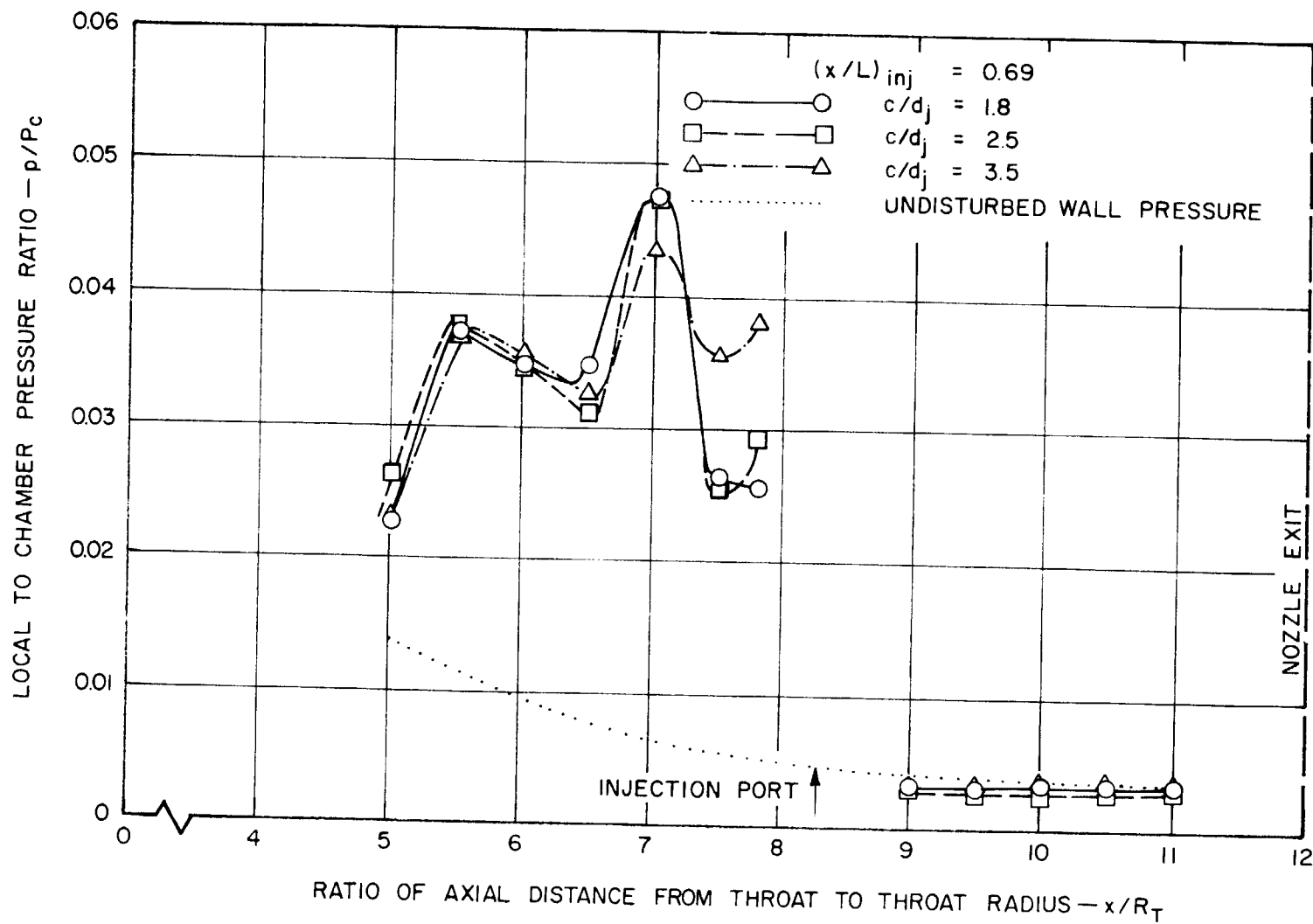
FIGURE 44

WALL PRESSURE DISTRIBUTION IN MERIDIONAL PLANE OF INJECTION IN THE
CONICAL NOZZLE USING MULTIRADIAL PORT INJECTION ($\dot{w}_s/\dot{w}_p$ = 0.09)
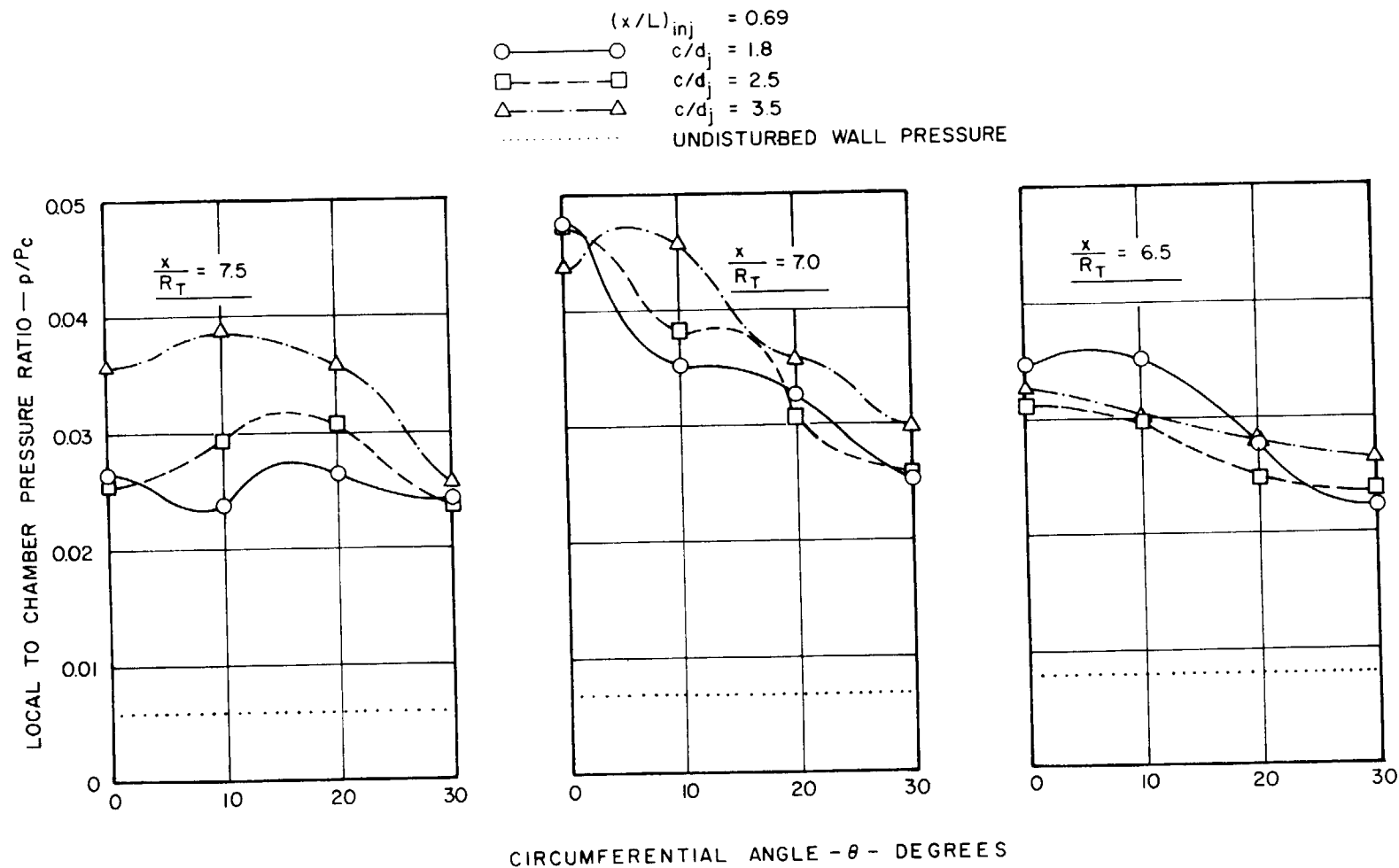
FIGURE 45
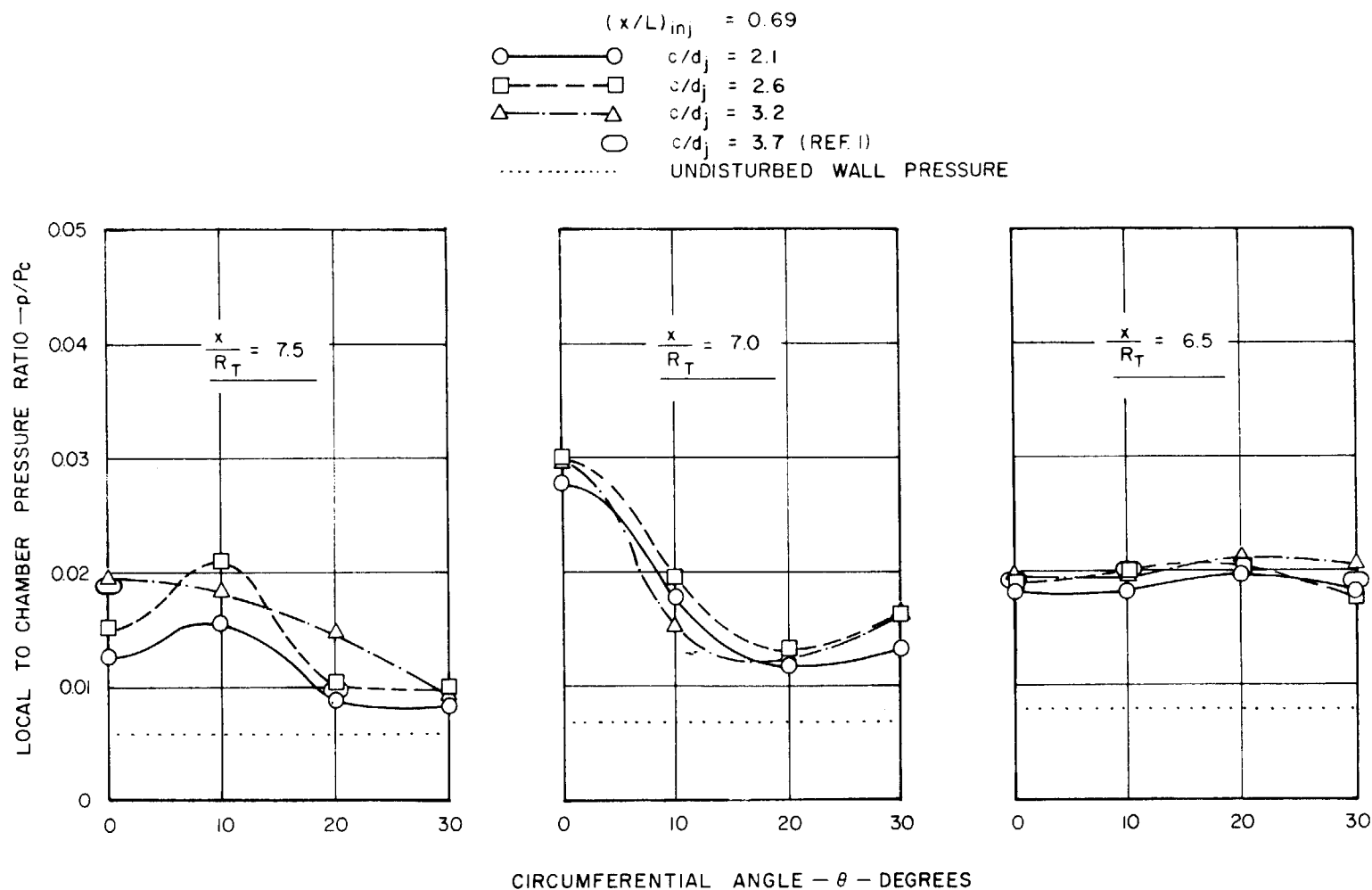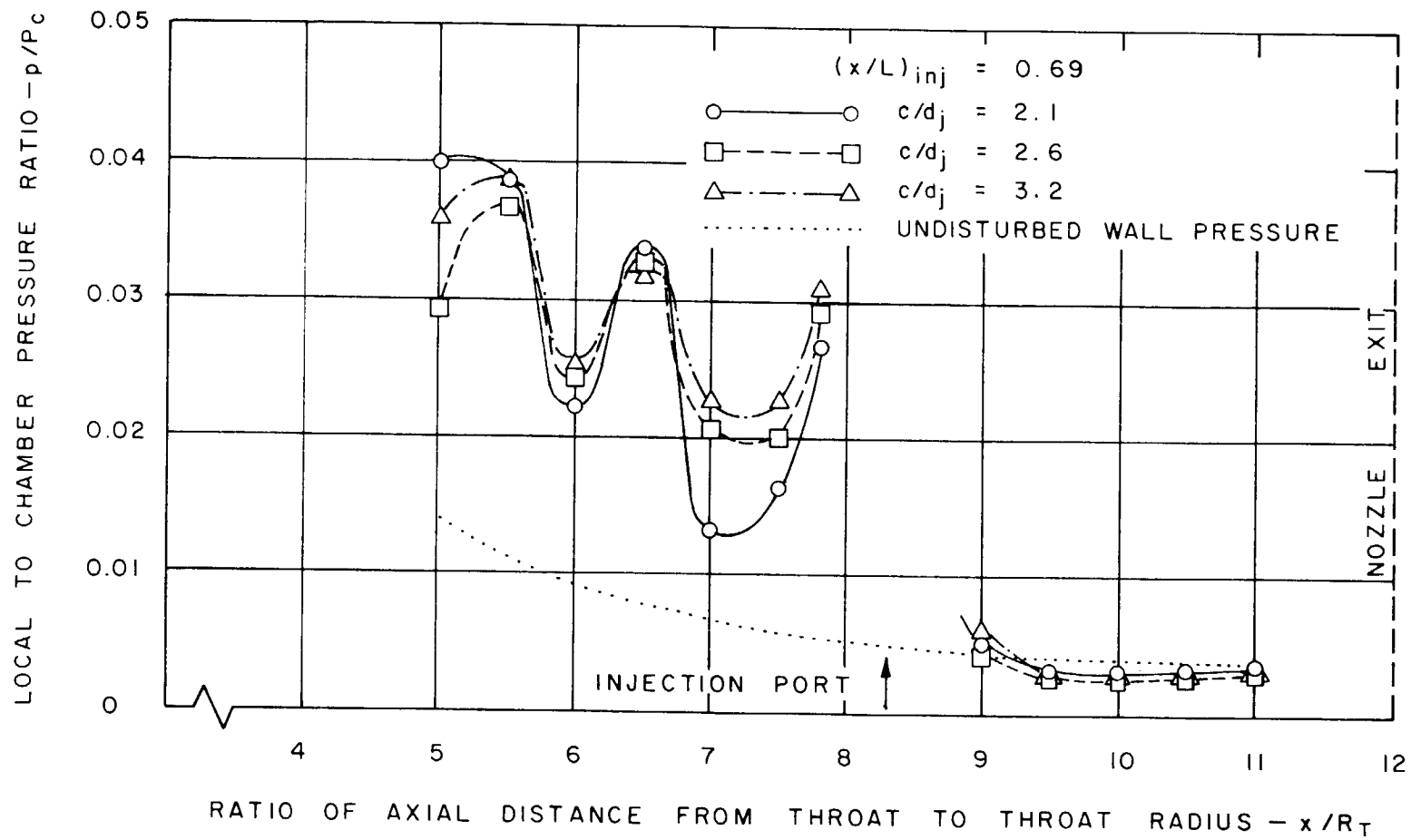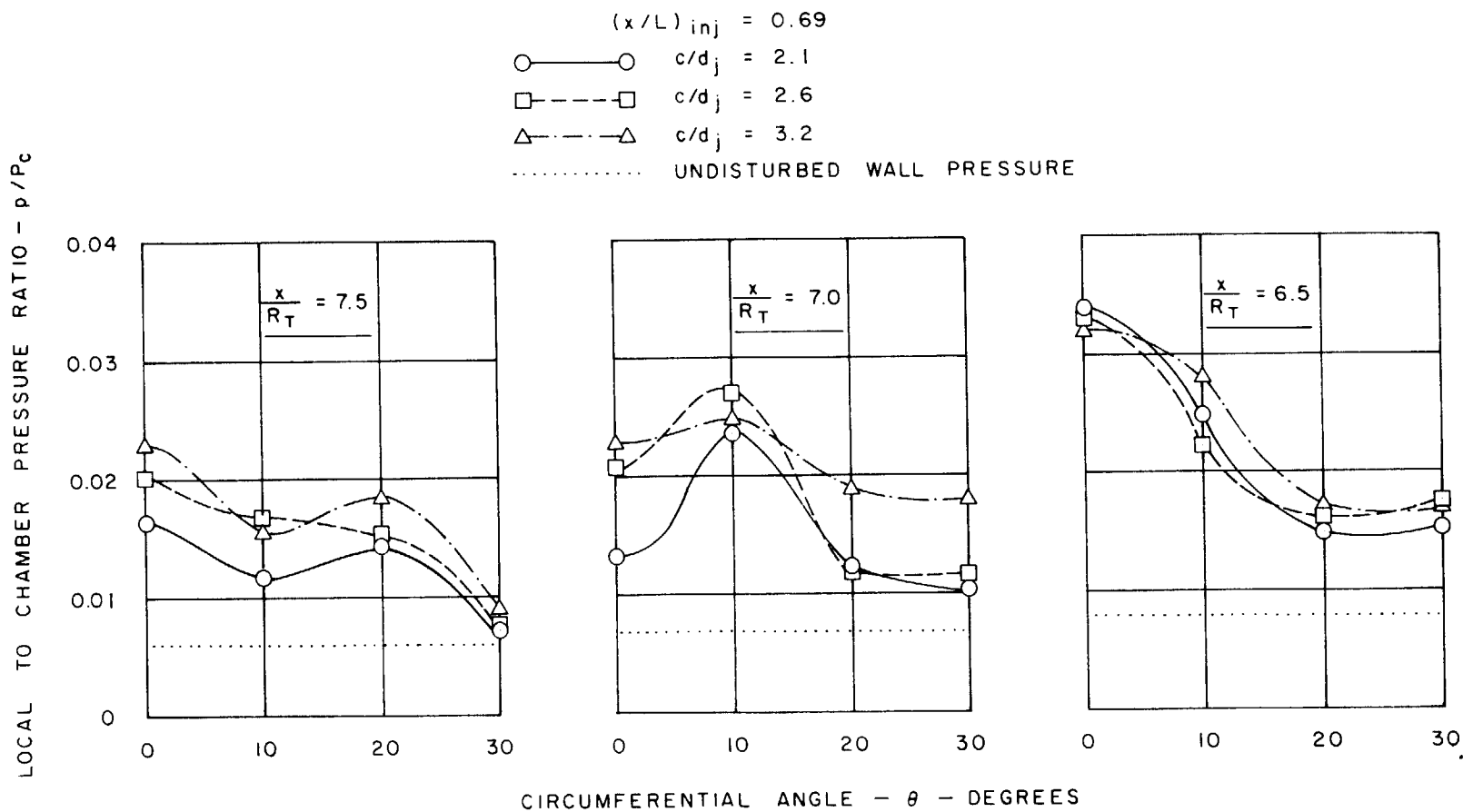
WALL PRESSURE DISTRIBUTION IN CIRCUMFERENTIAL PLANE IN THE CONICAL

NOZZLE USING MULTIRADIAL PORT INJECTION ($\dot{w}_s / \dot{w}_p = 0.09$)
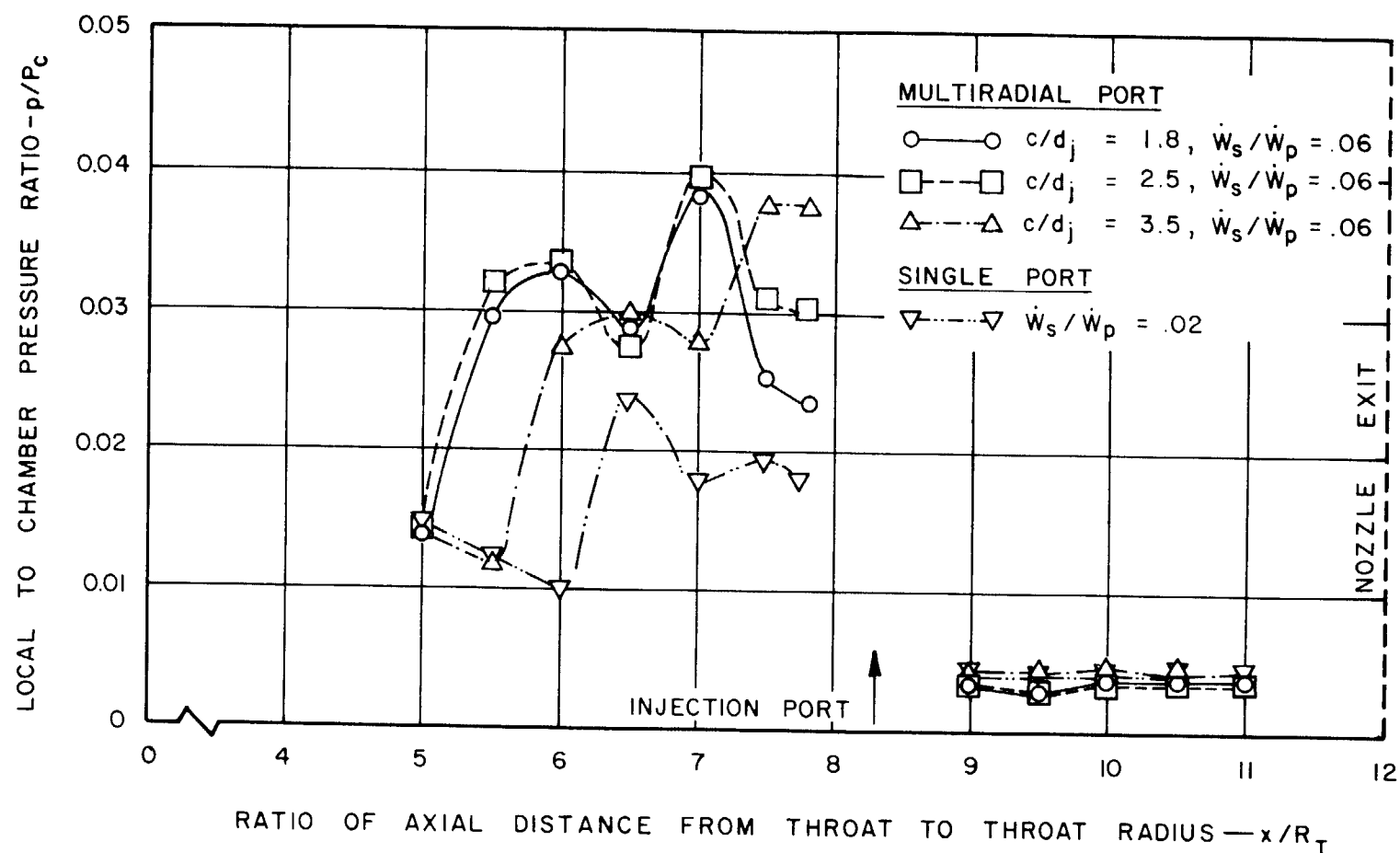
FIGURE 46

WALL PRESSURE DISTRIBUTION IN MERIDIONAL PLANE OF INJECTION IN THE
CONICAL NOZZLE USING SINGLE AND MULTIRADIAL PORT INJECTION
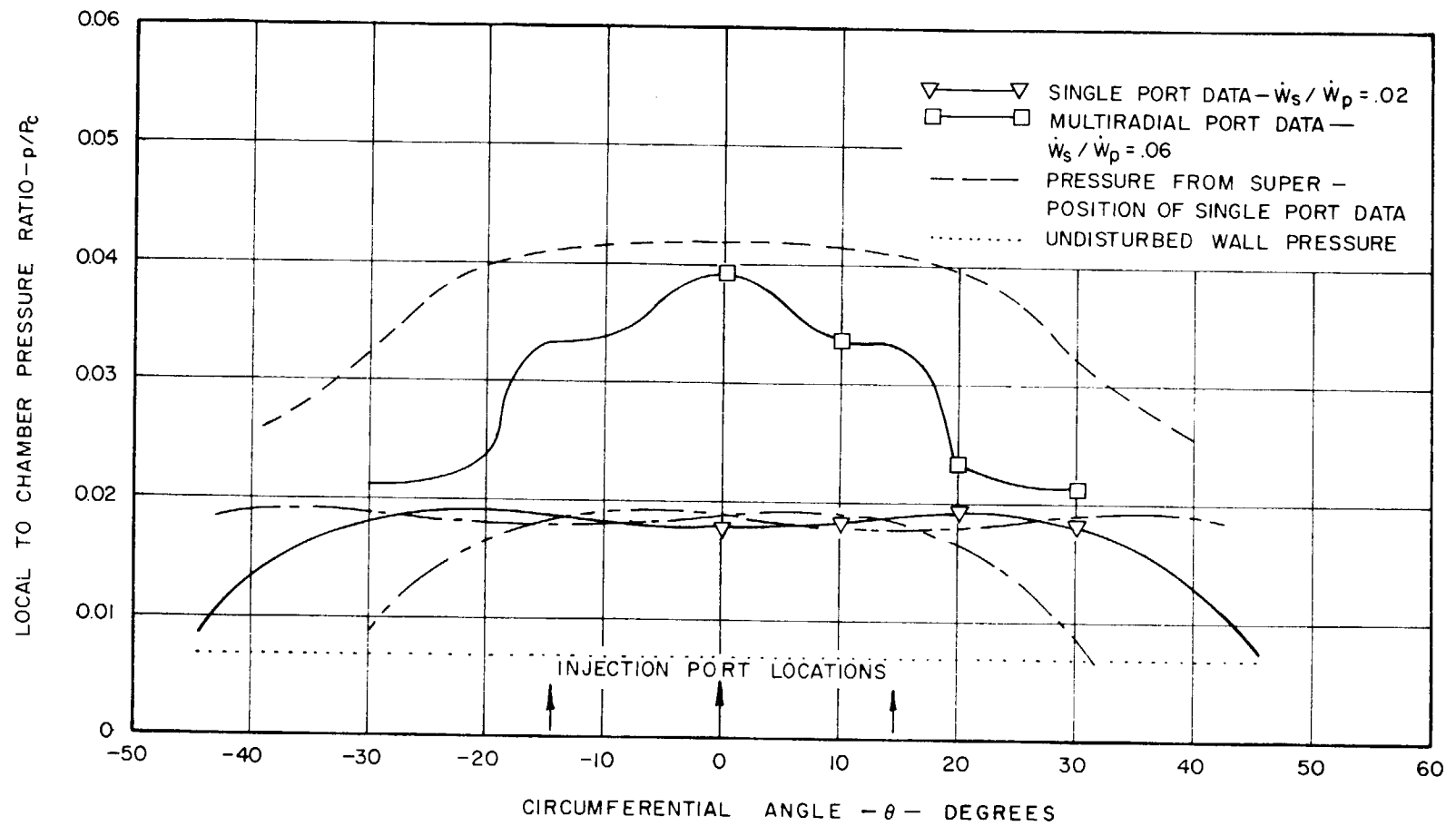
FIGURE 47

COMPARISON OF THE WALL PRESSURE IN CIRCUMFERENTIAL PLANE ($x/R_T = 7.0$) OBTAINED FROM SUPERPOSITION OF SINGLE PORT DATA WITH MULTIRADIAL PORT DATA IN THE CONICAL NOZZLE
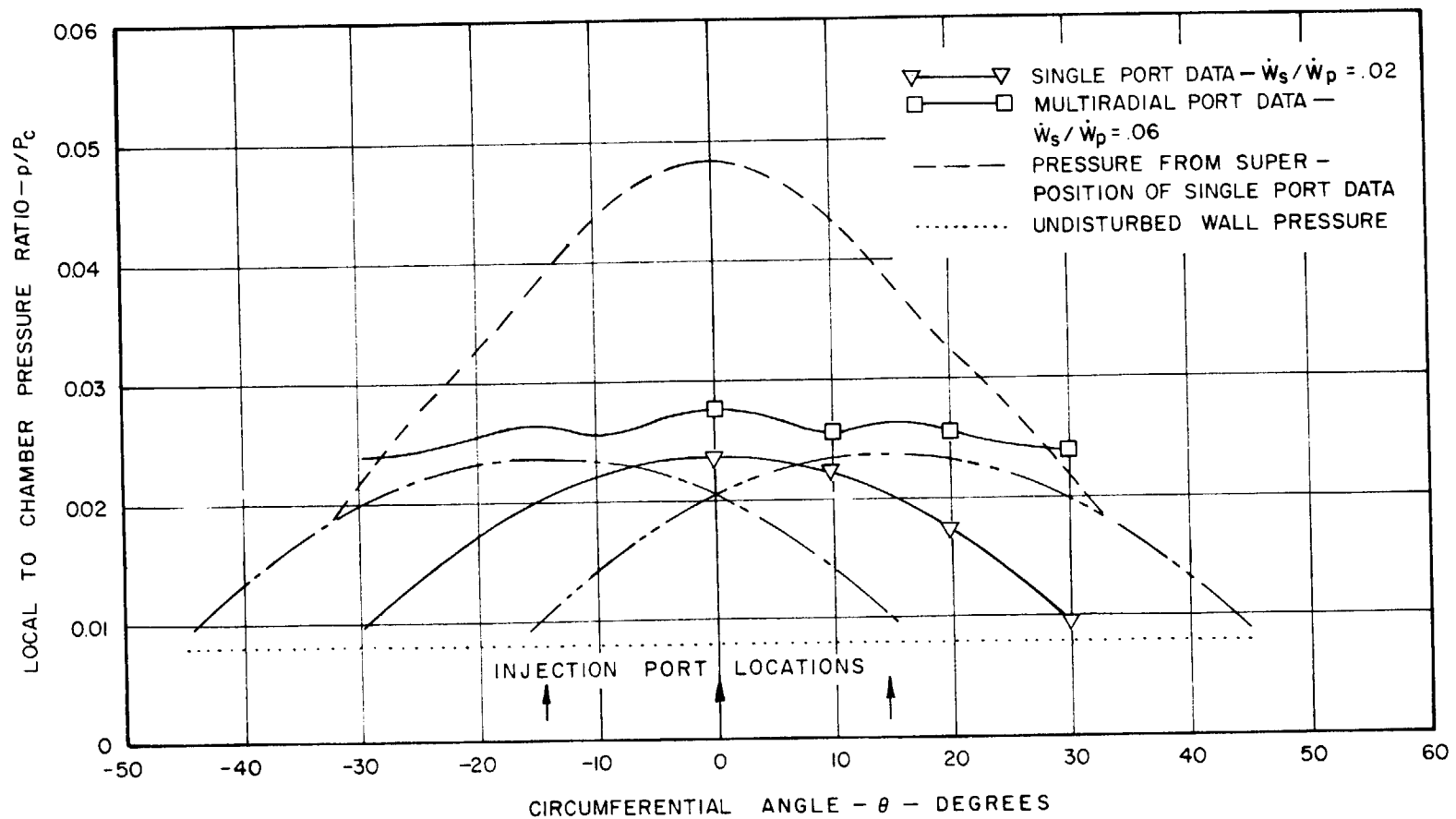
FIGURE 48

COMPARISON OF THE WALL PRESSURE IN CIRCUMFERENTIAL PLANE $(x/R_T = 6.5)$
OBTAINED FROM SUPERPOSITION OF SINGLE PORT DATA WITH MULTIRADIAL
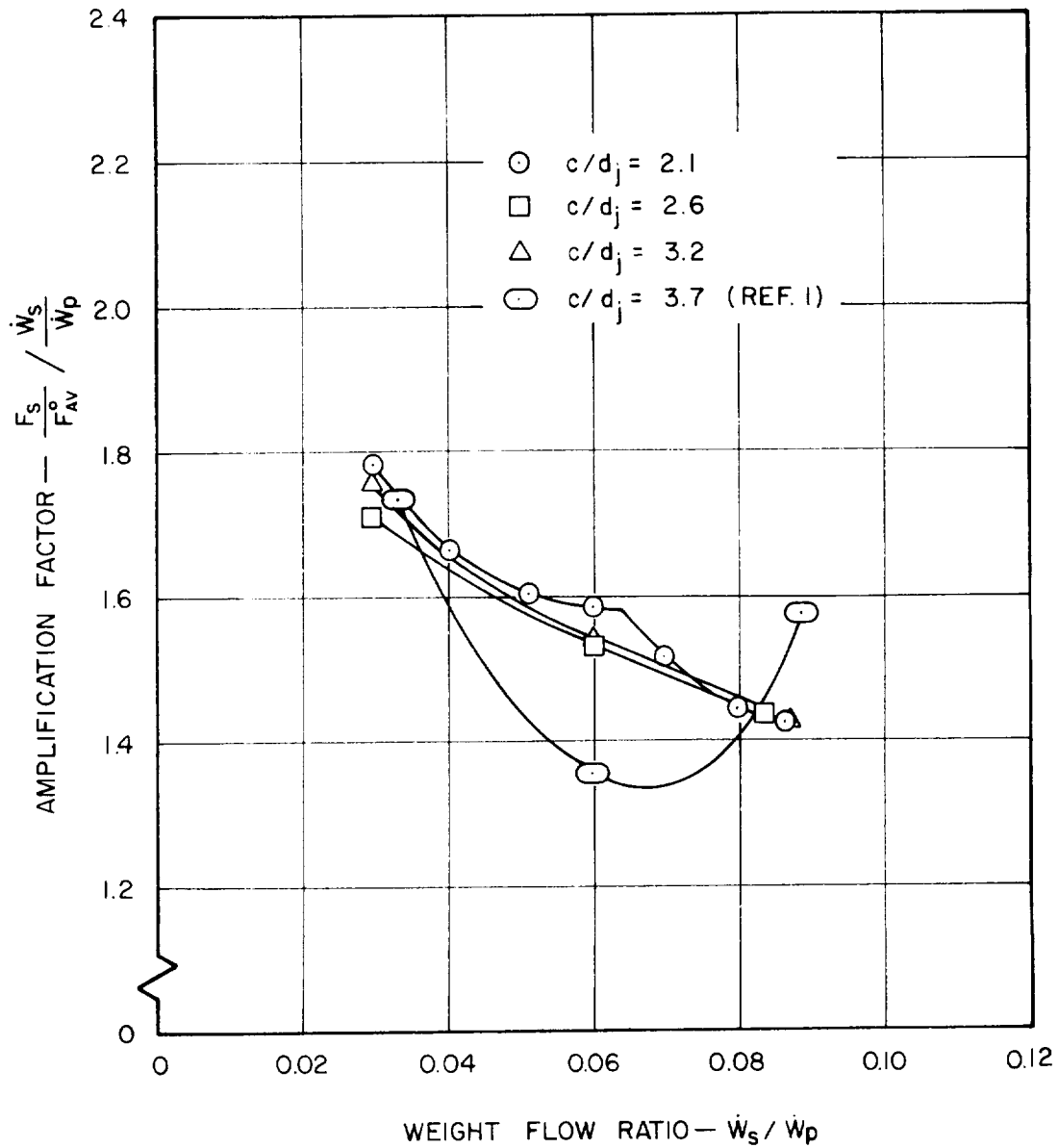PORT DATA IN THE CONICAL NOZZLE
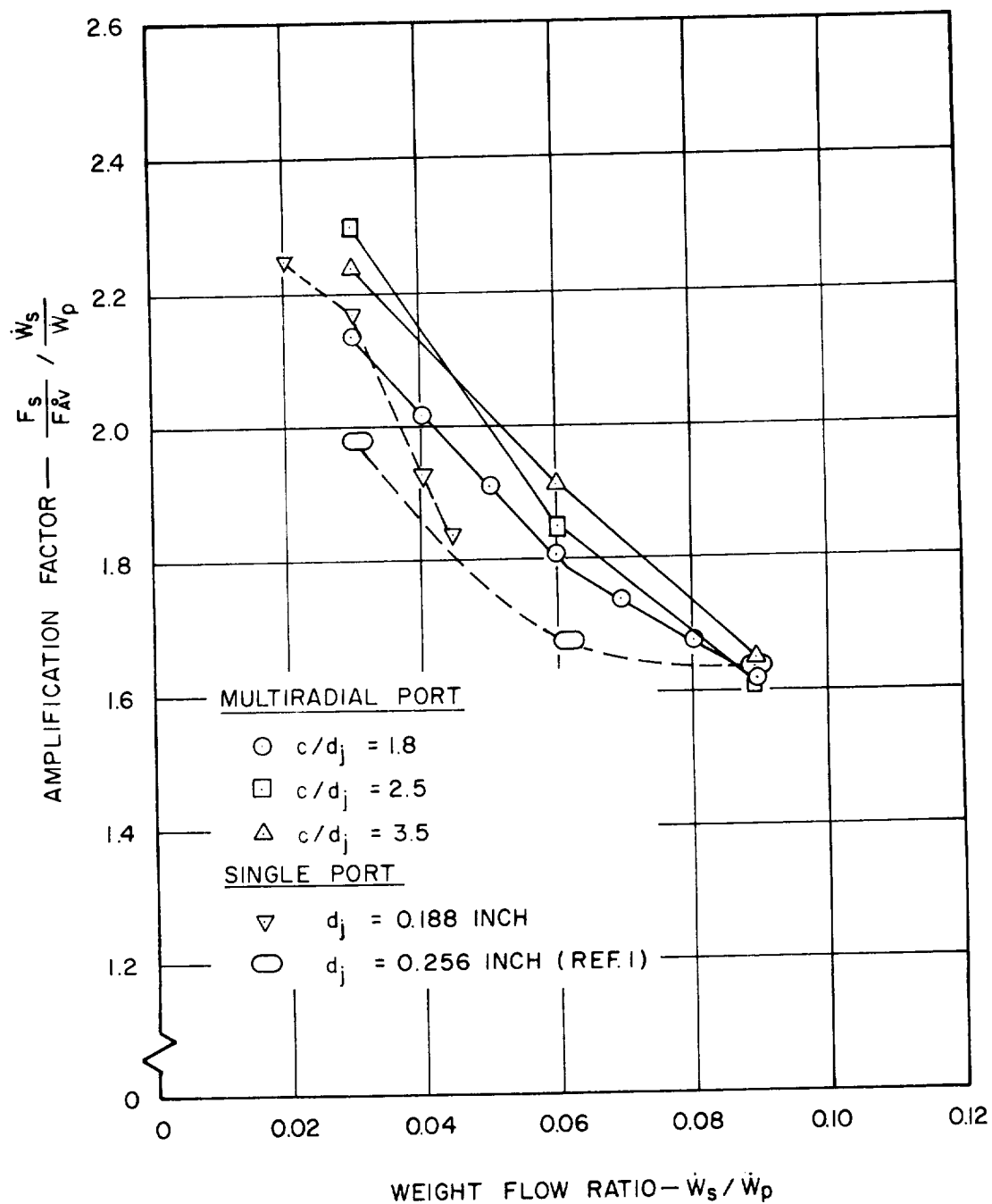
FIGURE 49

INFLUENCE OF WEIGHT FLOW RATIO ON THE
AMPLIFICATION FACTOR USING MULTIRADIAL PORT
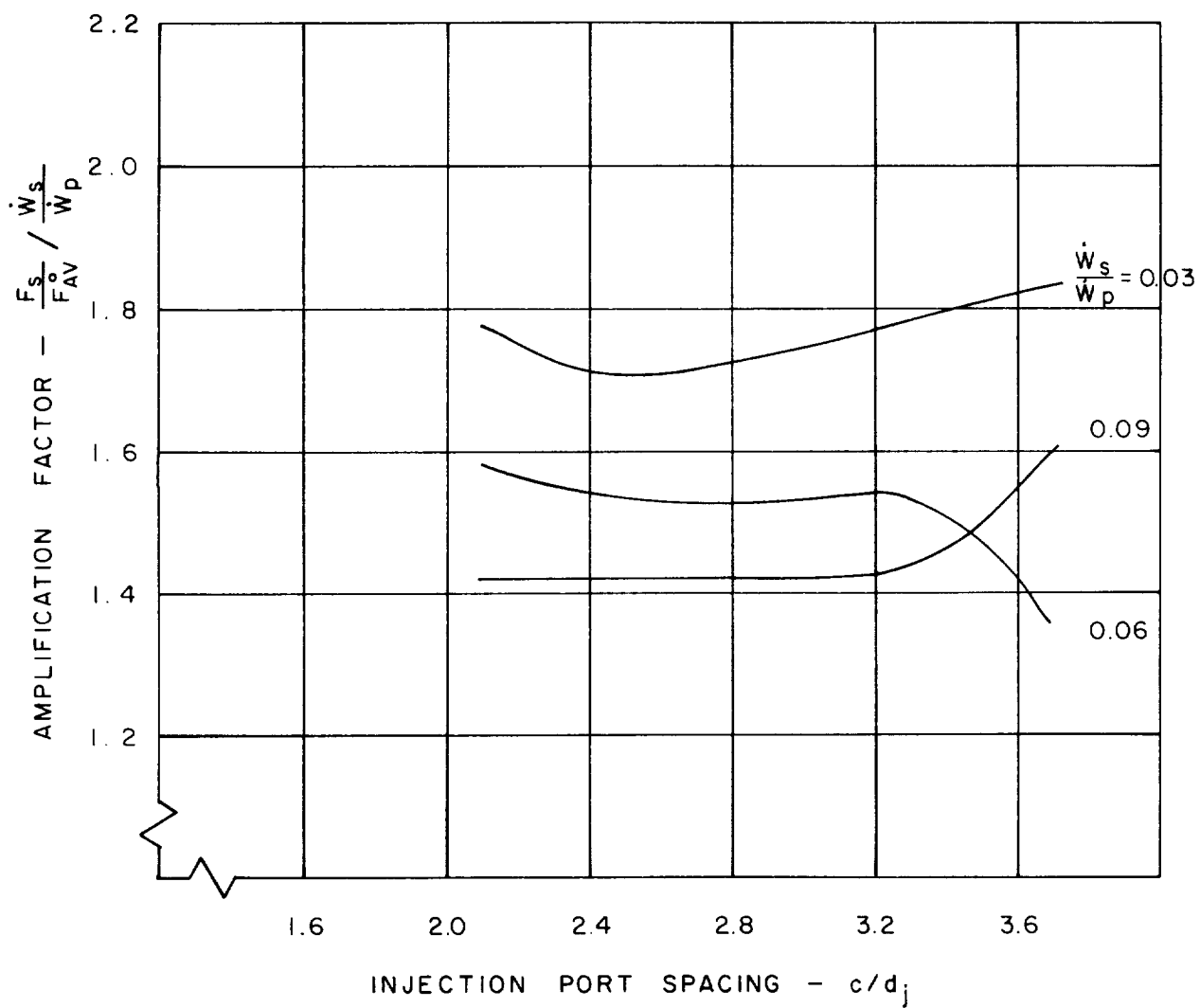INJECTION AT $(x/L)_{inj} = 0.95$ IN THE APG-1 NOZZLE
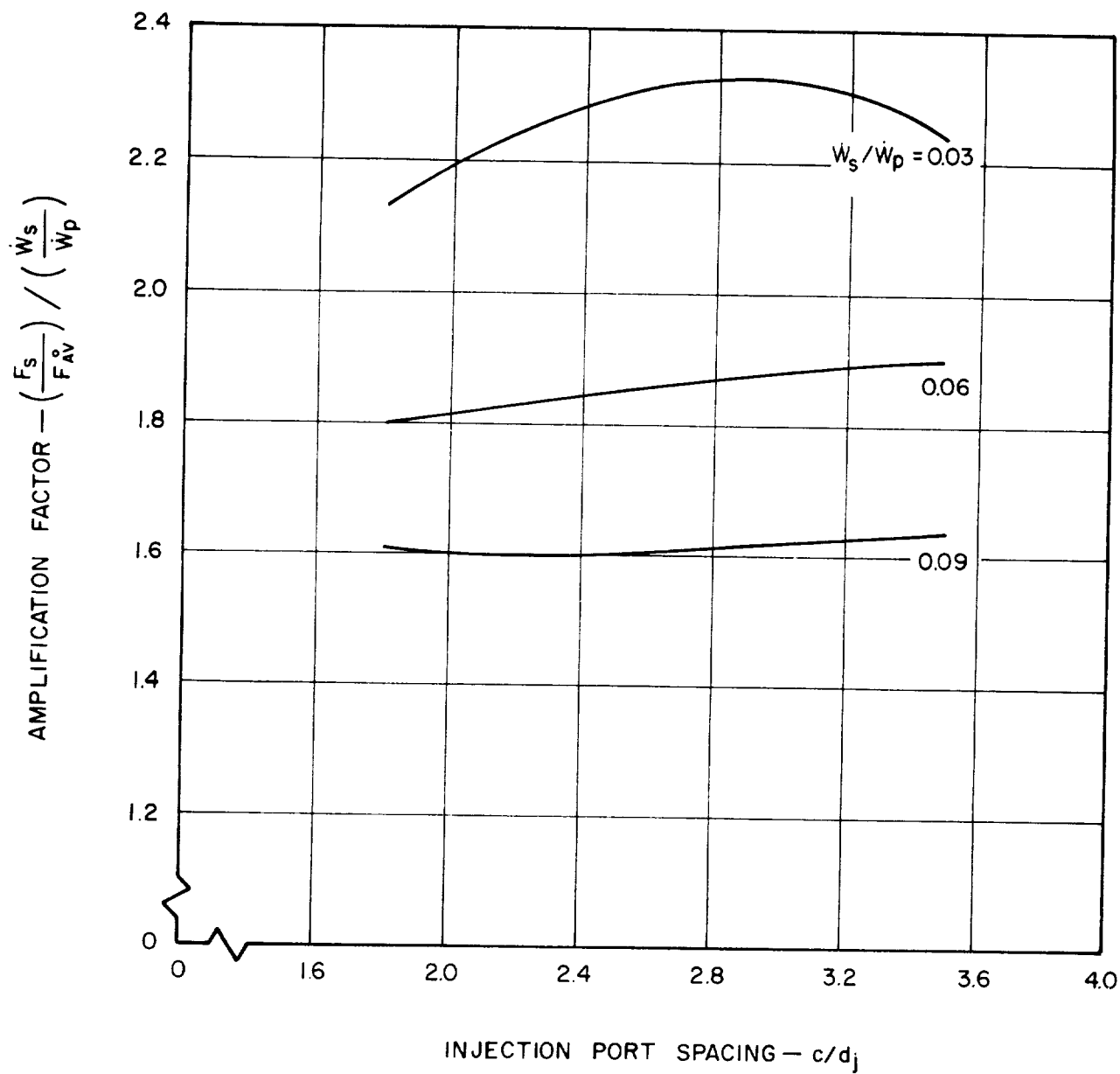
FIGURE 50

EFFECT OF INJECTION PORT SPACING ON THE AMPLIFI-
CATION FACTOR USING MULTIRADIAL PORT INJECTION AT
$(x/L)_{inj}$ = 0.95 IN THE APG-1 NOZZLE
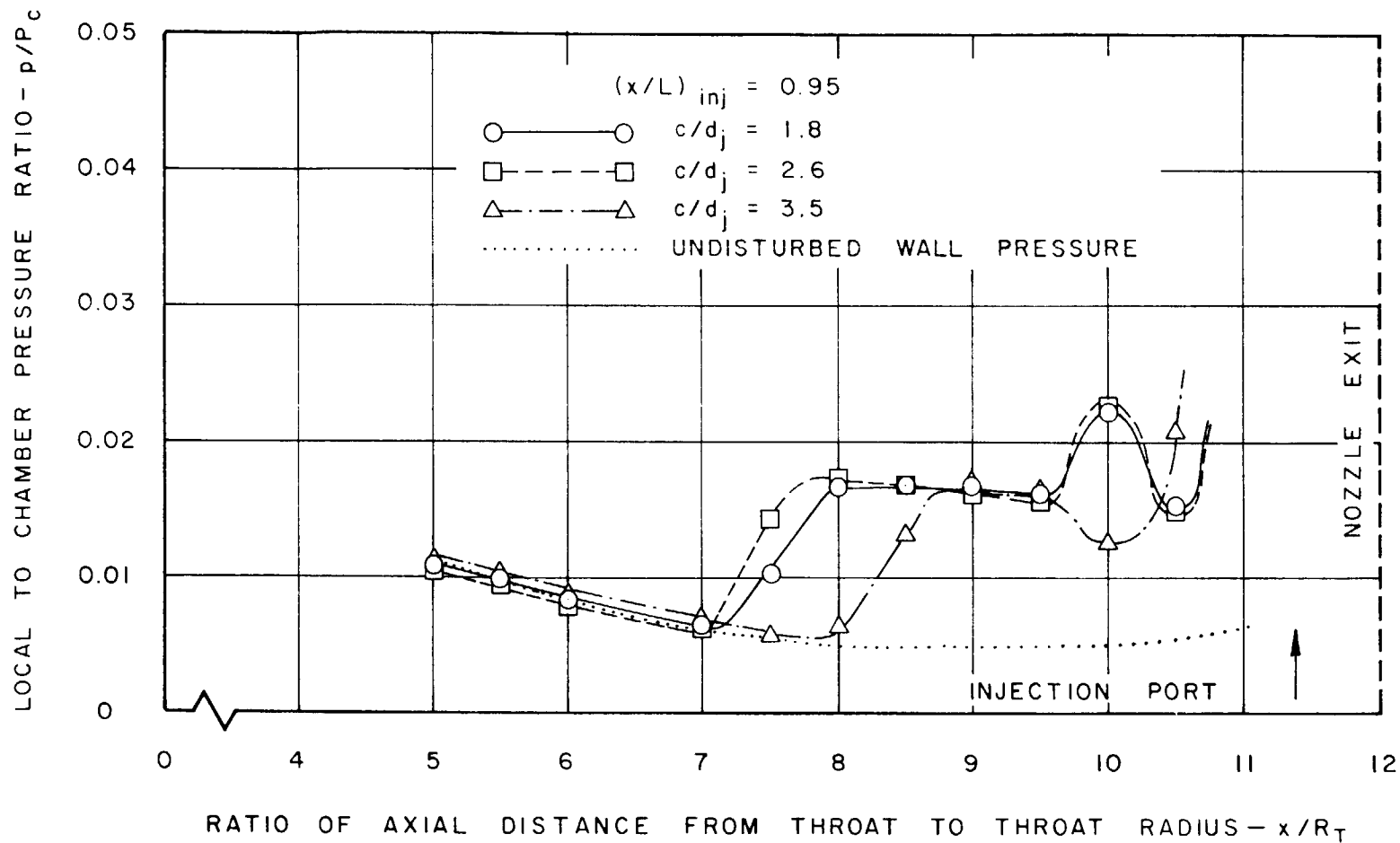
FIGURE 51

WALL PRESSURE DISTRIBUTION IN MERIDIONAL PLANE OF INJECTION IN THE APG-1 NOZZLE USING MULTIRADIAL PORT INJECTION ($\dot{w}_s/\dot{w}_p = 0.03$)
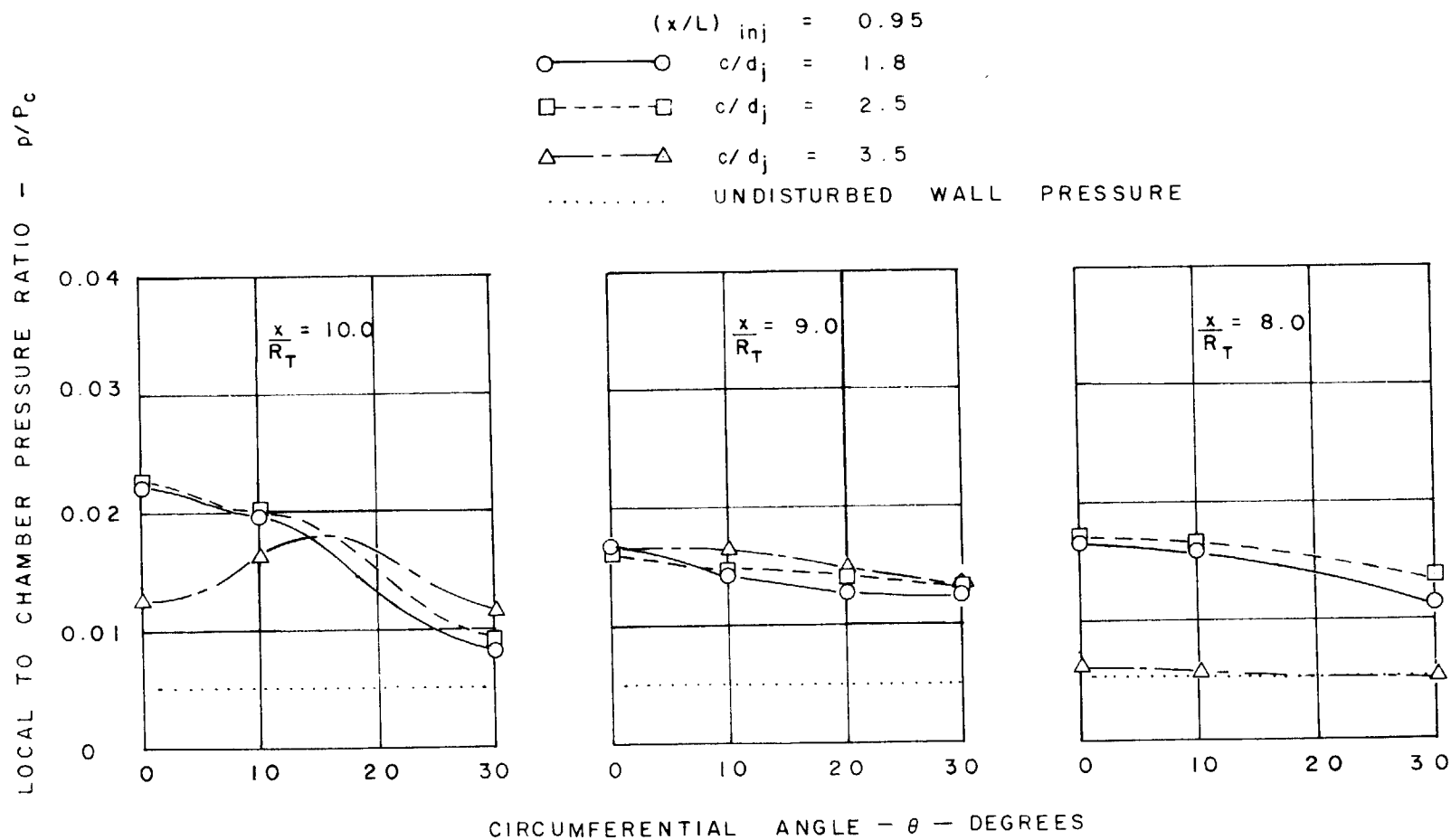
FIGURE 52

WALL PRESSURE DISTRIBUTION IN CIRCUMFERENTIAL PLANE IN THE APG-1

NOZZLE USING MULTIRADIAL PORT INJECTION ($\dot{w}_s/\dot{w}_p = 0.03$)
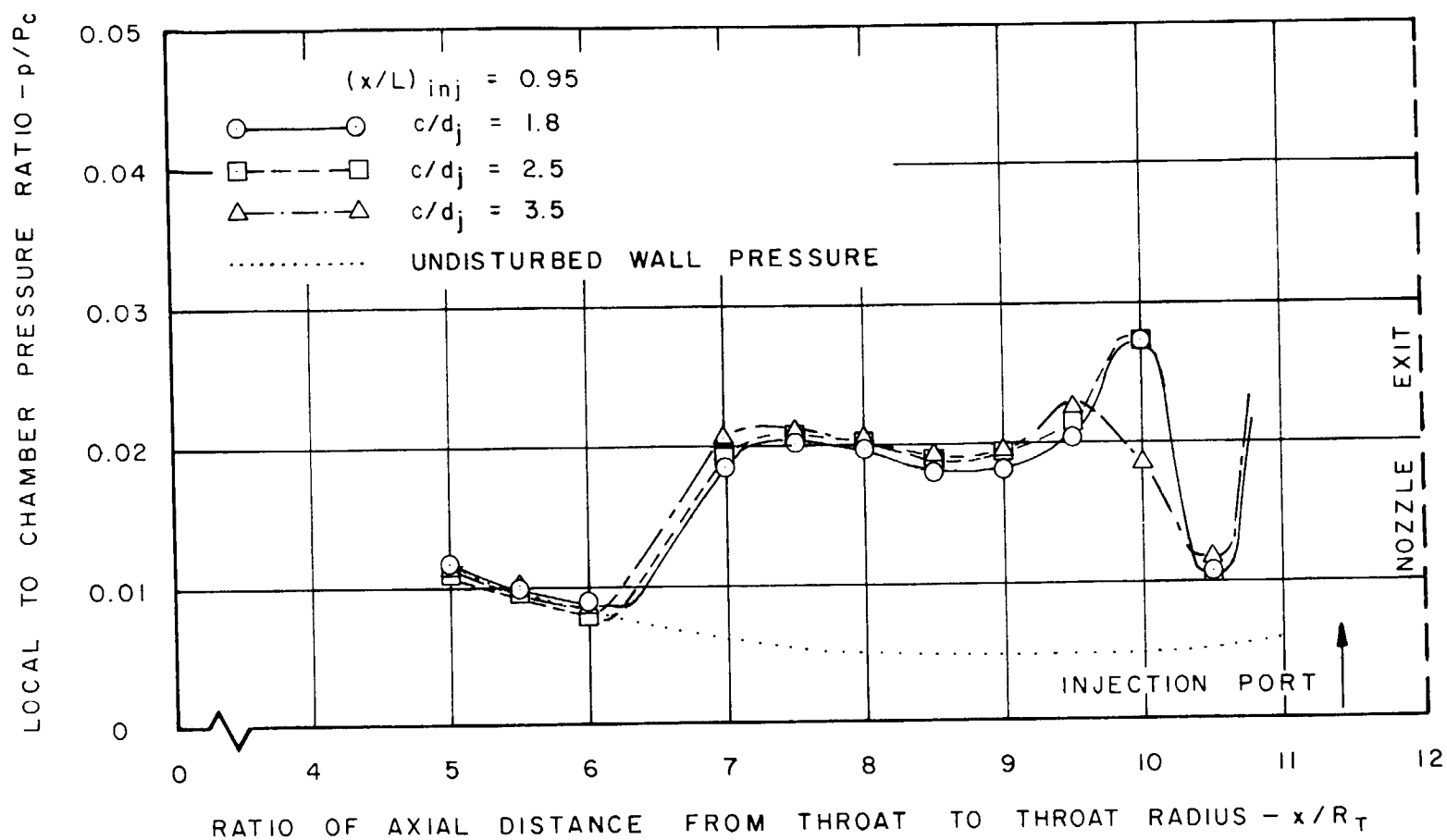
FIGURE 53

WALL PRESSURE DISTRIBUTION IN MERIDIONAL PLANE OF INJECTION IN THE
APG-1 NOZZLE USING MULTIRADIAL PORT INJECTION ($\dot{w}_s / \dot{w}_p = 0.06$)
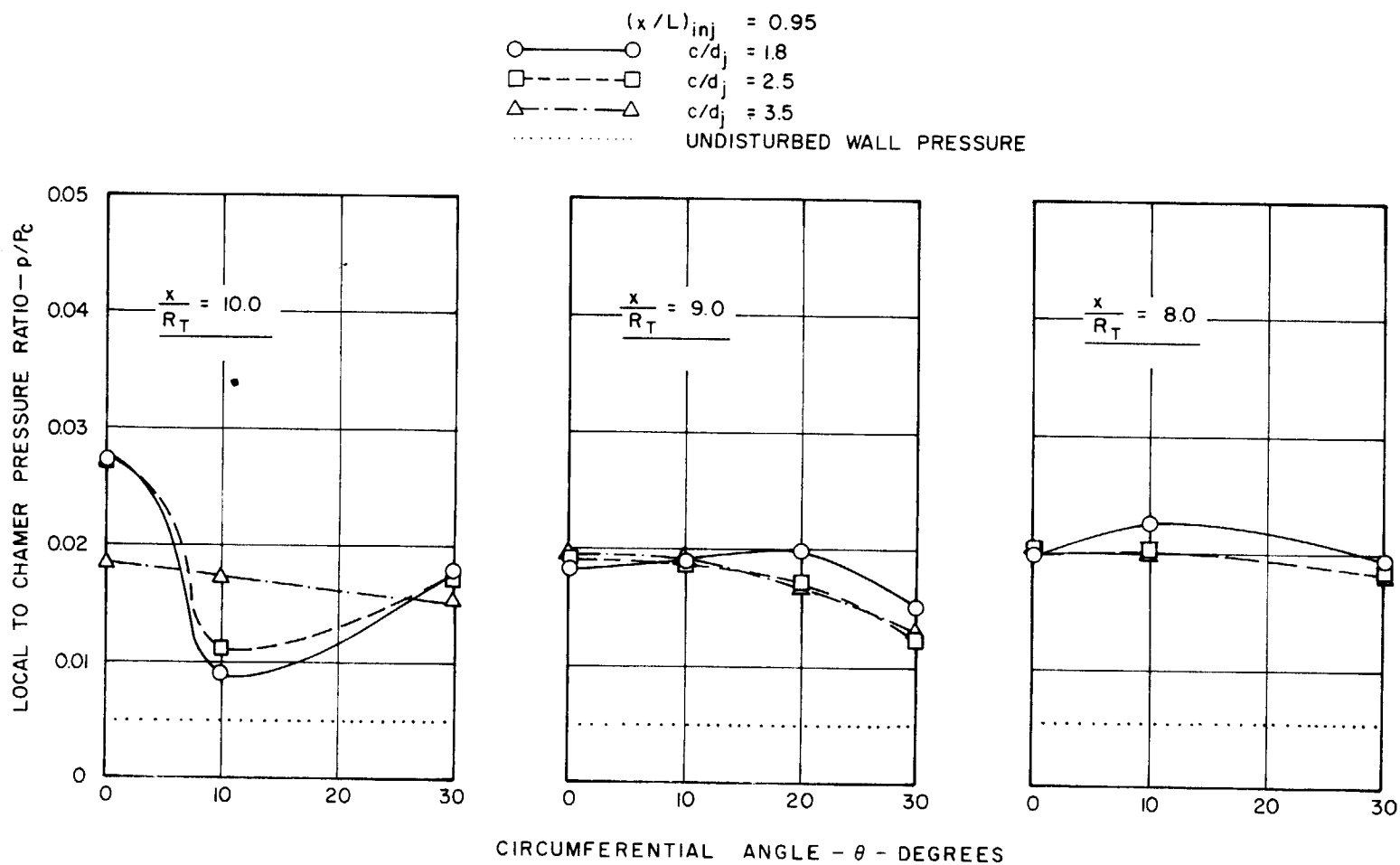
FIGURE 54

WALL PRESSURE DISTRIBUTION IN CIRCUMFERENTIAL PLANE IN THE APG-1
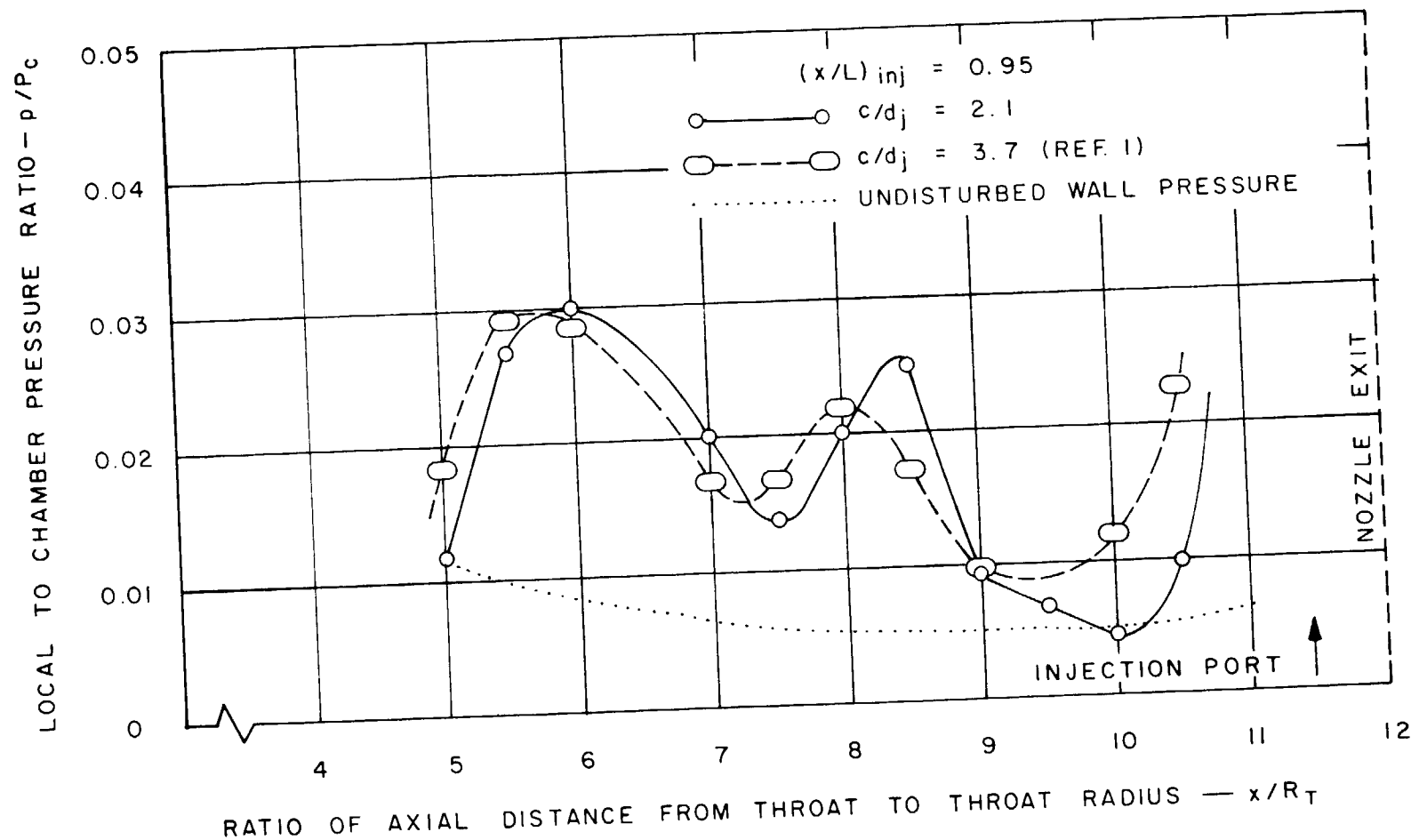NOZZLE USING MULTIRADIAL PORT INJECTION ($\dot{w}_s/\dot{w}_p$ = 0.06)
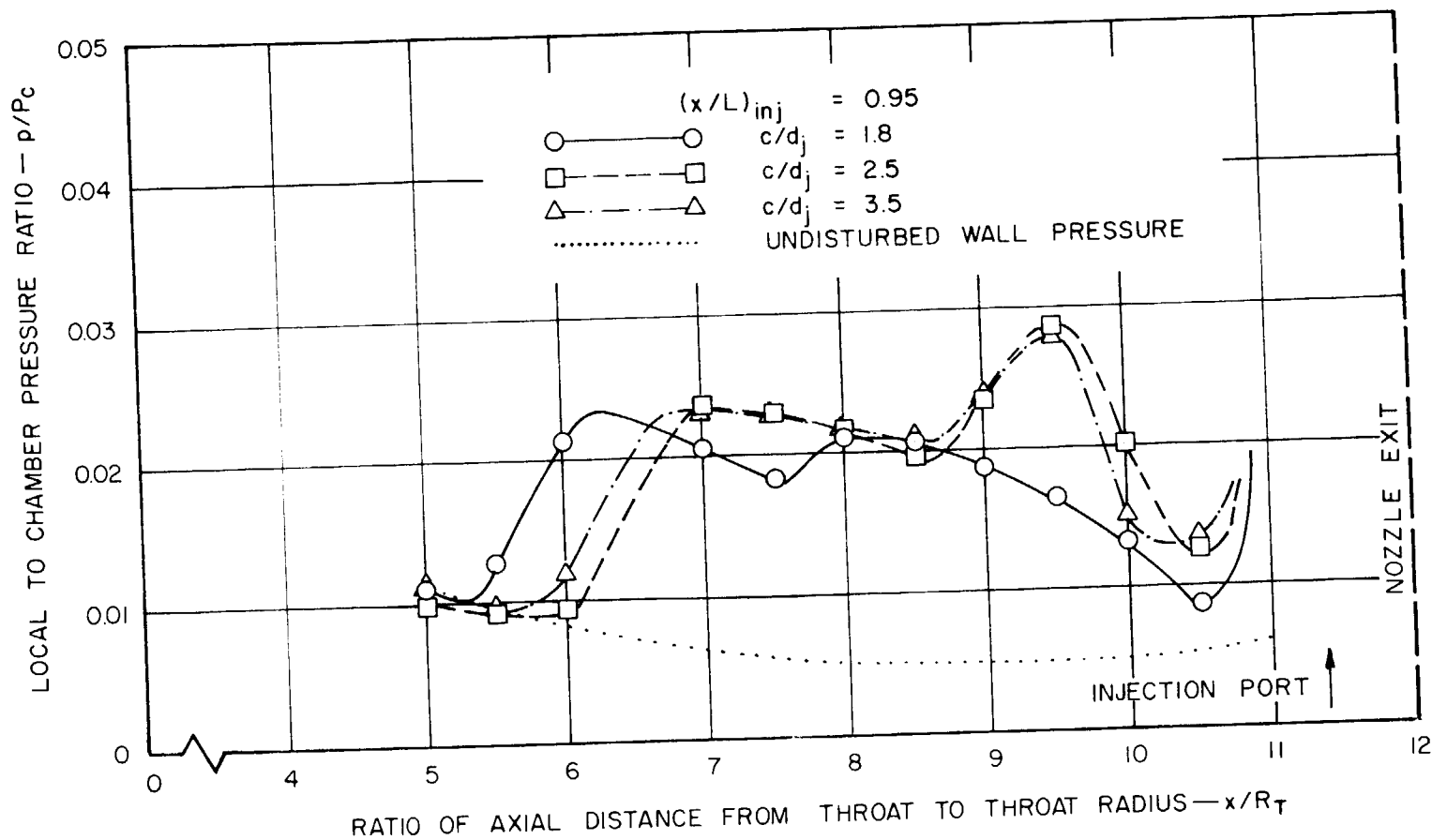
FIGURE 55

WALL PRESSURE DISTRIBUTION IN MERIDIONAL PLANE OF INJECTION IN THE APG-1 NOZZLE USING MULTIRADIAL PORT INJECTION ($\dot{w}_s/\dot{w}_p$ = 0.09)
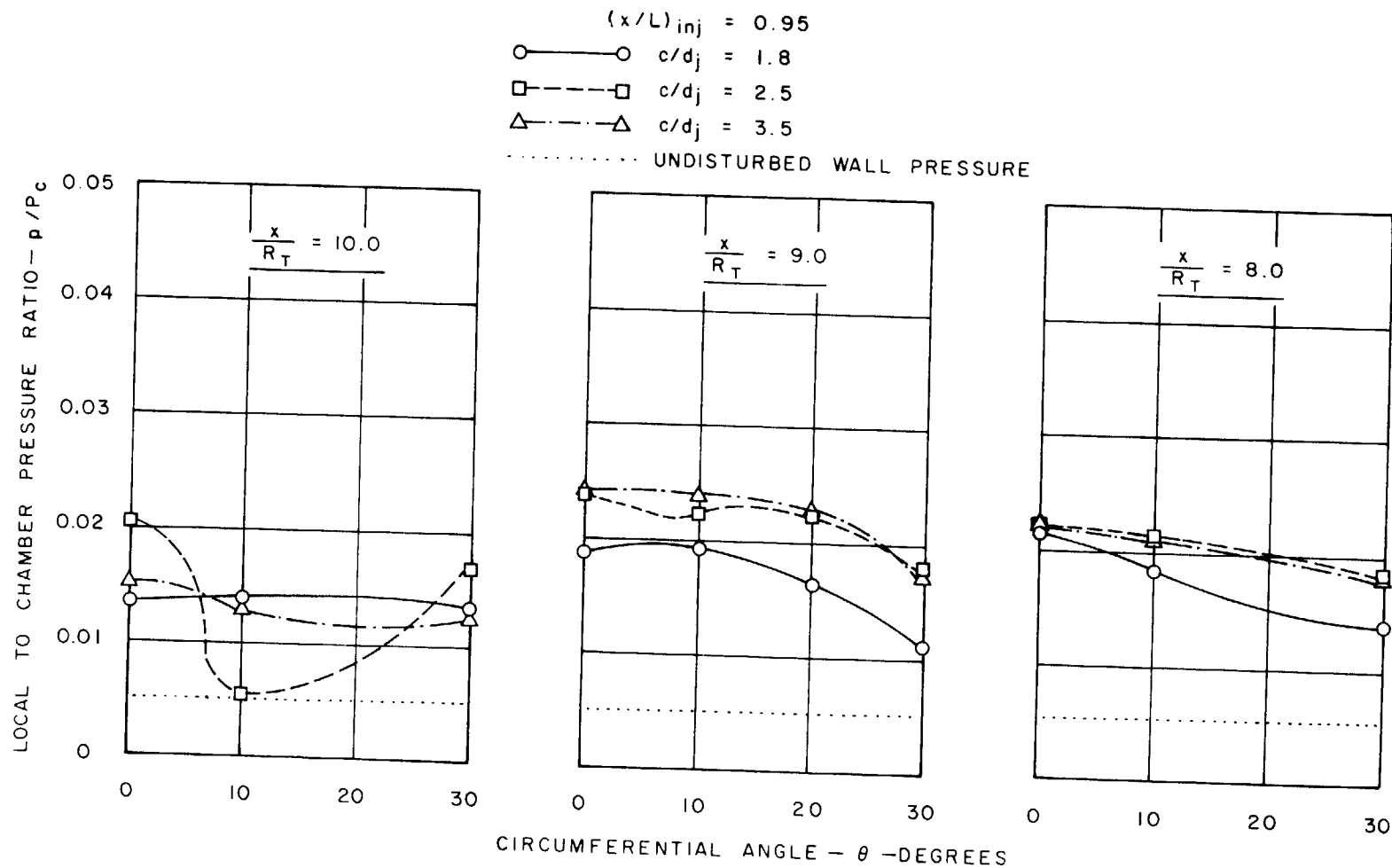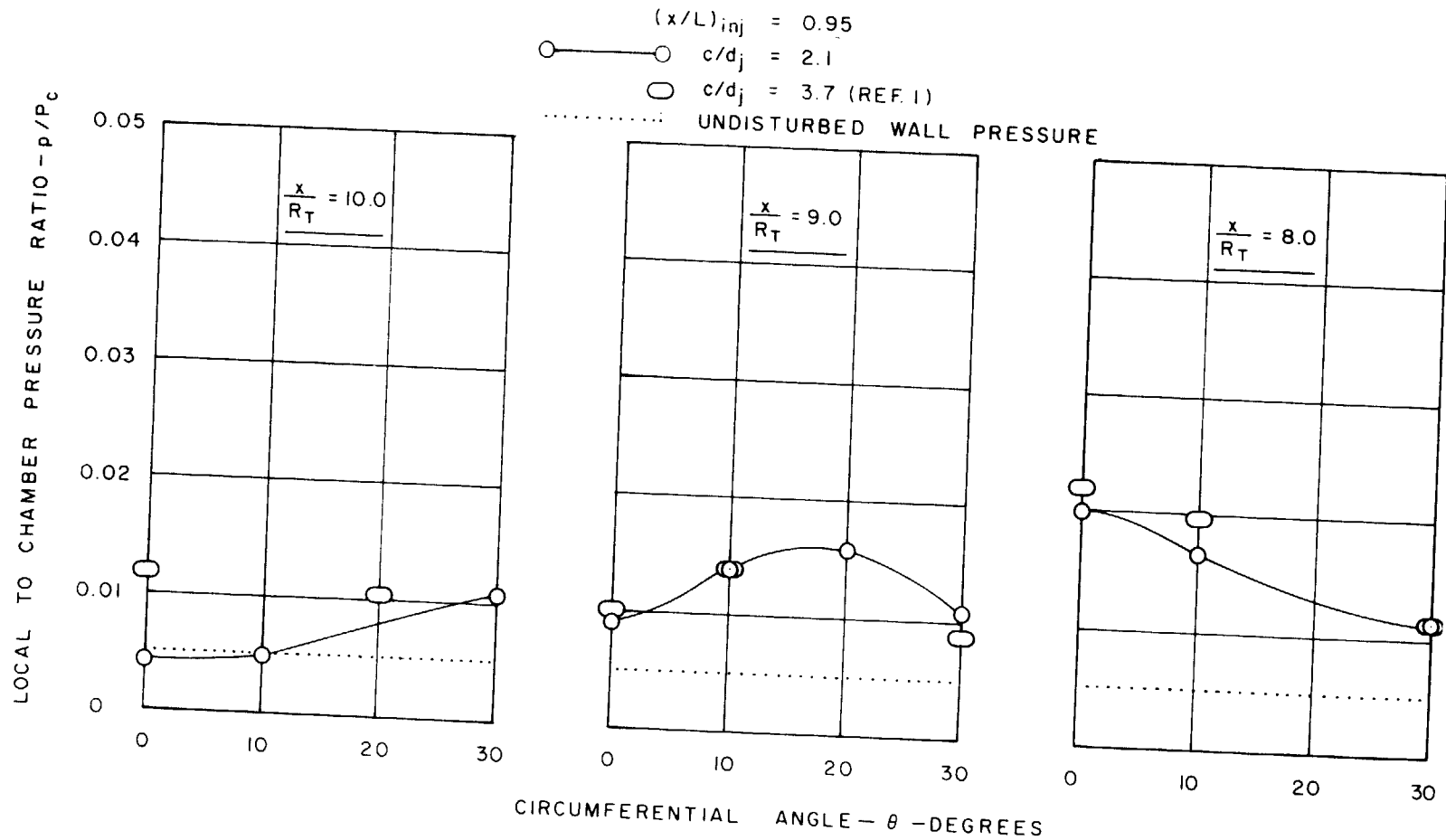
FIGURE 56

WALL PRESSURE DISTRIBUTION IN CIRCUMFERENTIAL PLANE IN THE APG-1
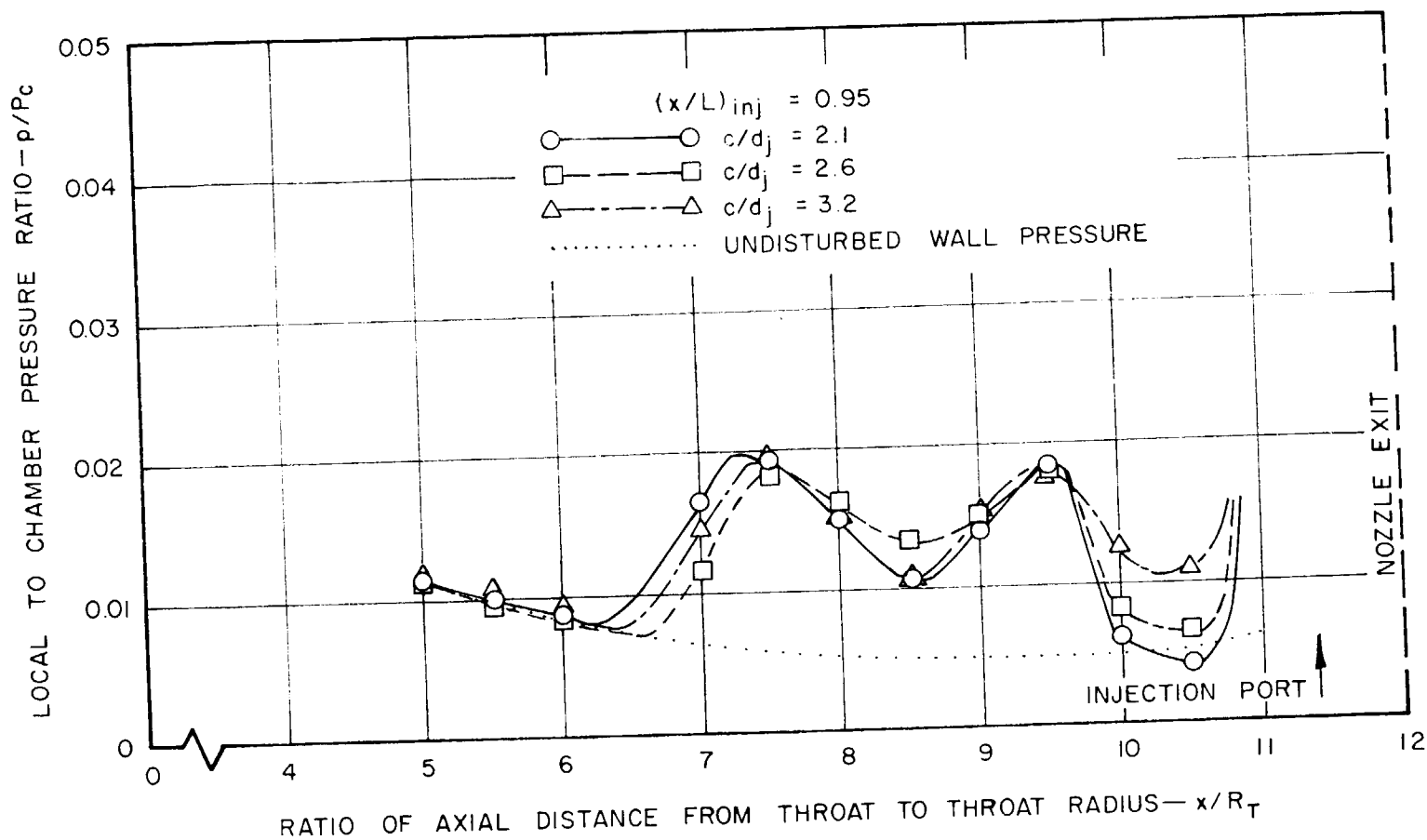NOZZLE USING MULTIRADIAL PORT INJECTION ($\dot{w}_s/\dot{w}_p$ = 0.09)
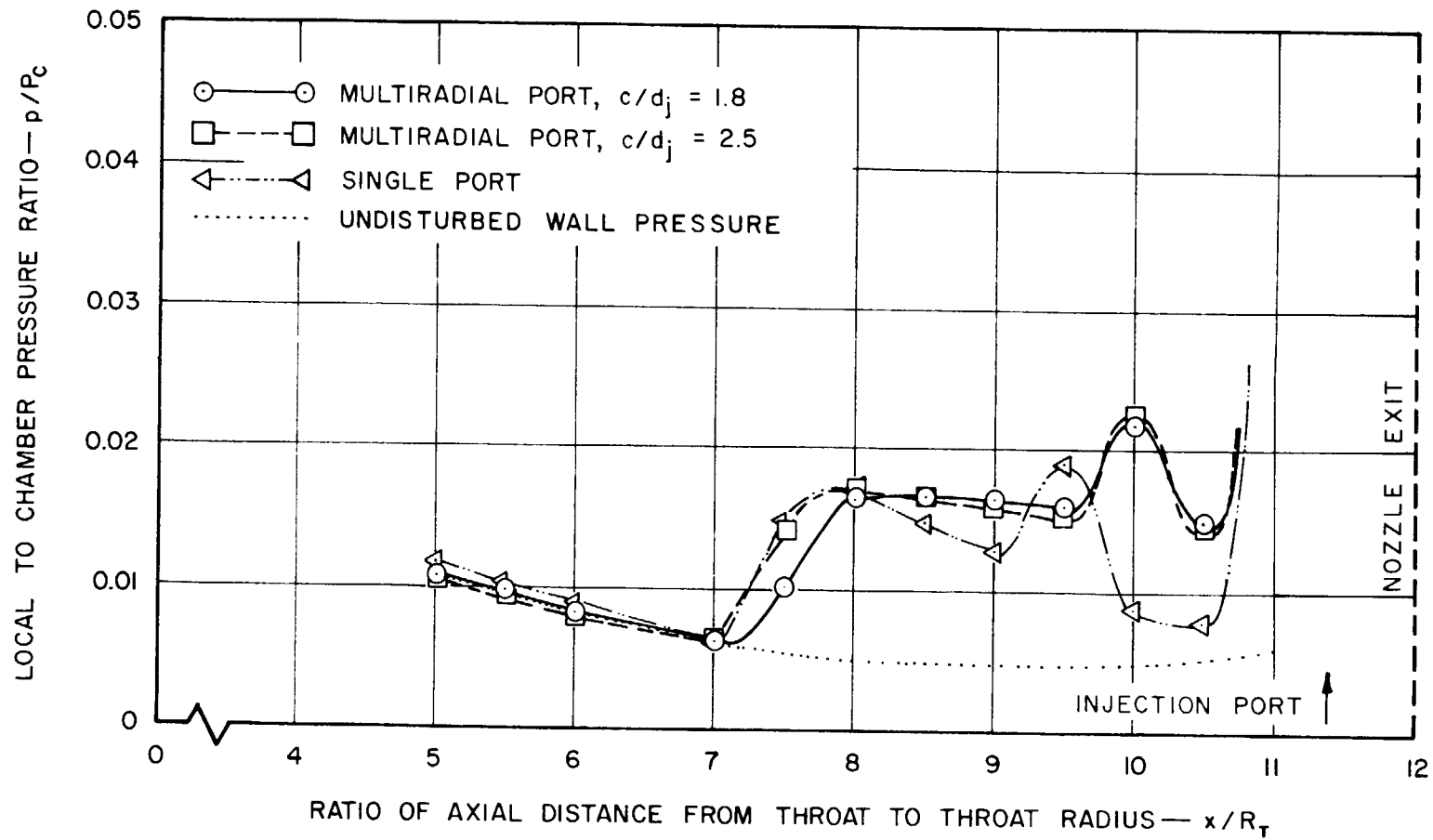
FIGURE 57

COMPARISON OF WALL PRESSURE DISTRIBUTION IN MERIDIONAL PLANE OF INJECTION IN THE APG-1 NOZZLE WITH SINGLE AND MULTIRADIAL PORT INJECTION ($\dot{w}_s/\dot{w}_p = 0.03$)
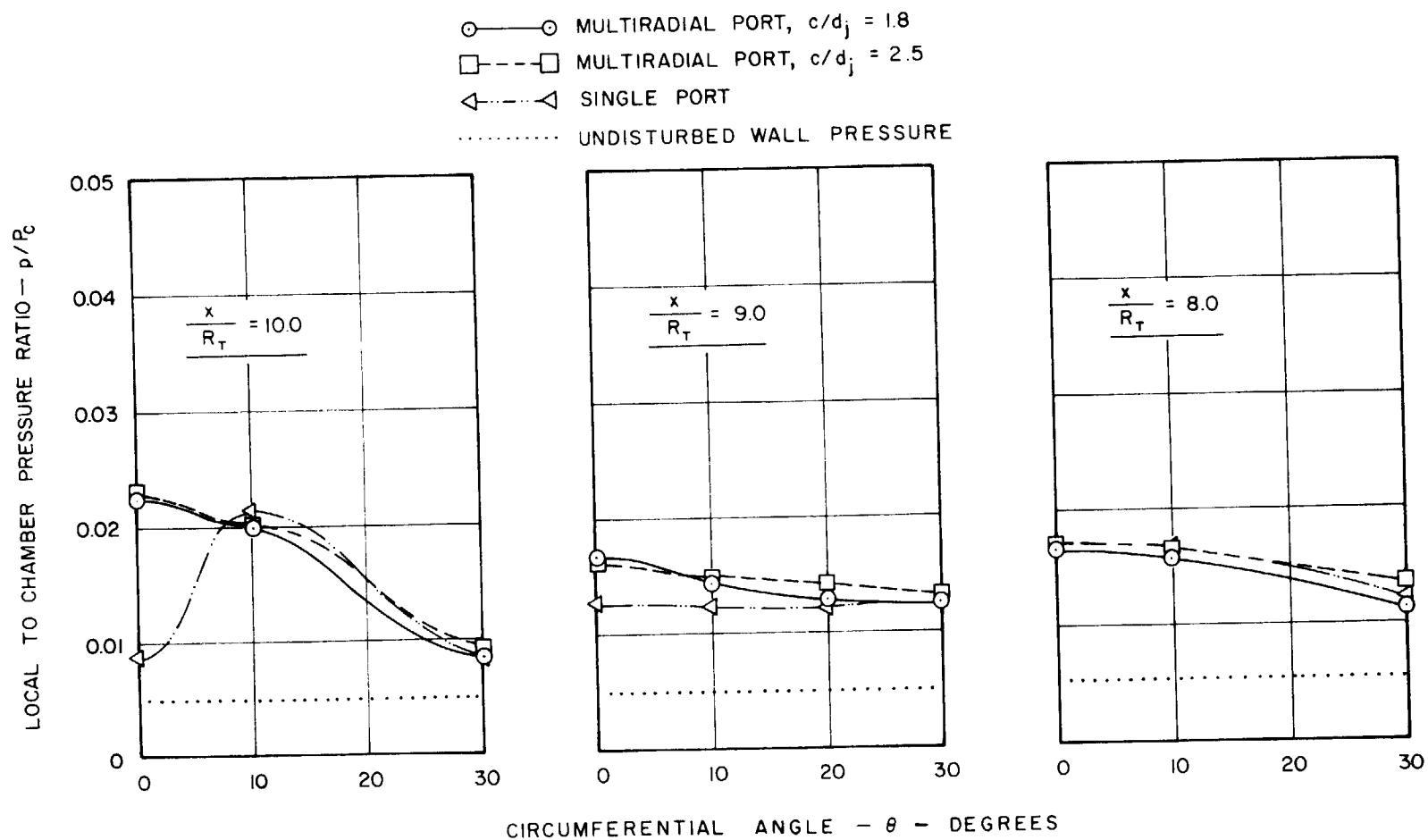
FIGURE 58

COMPARISON OF WALL PRESSURE DISTRIBUTION IN CIRCUMFERENTIAL PLANE IN THE APG-1 NOZZLE WITH SINGLE AND MULTIRADIAL PORT INJECTION $(\dot{w}_s/\dot{w}_p = 0.03)$

FIGURE 59

INFLUENCE OF WEIGHT FLOW RATIO ON
THE AMPLIFICATION FACTOR USING
OPPOSED-TANGENTIAL PORT INJECTION
AT $(x/L)_{inj} = 0.69$ IN THE CONICAL NOZZLE

FIGURE 60

EFFECT OF INJECTION PORT SPACING ON THE
AMPLIFICATION FACTOR USING OPPOSED-
TANGENTIAL PORT INJECTION AT $(x/L)_{inj}$ = 0.69
IN THE CONICAL NOZZLE

FIGURE 61

WALL PRESSURE DISTRIBUTION IN MERIDIONAL PLANE OF INJECTION IN THE CONICAL NOZZLE USING OPPOSED-TANGENTIAL PORT INJECTION $(\dot{w}_s/\dot{w}_p = 0.03)$
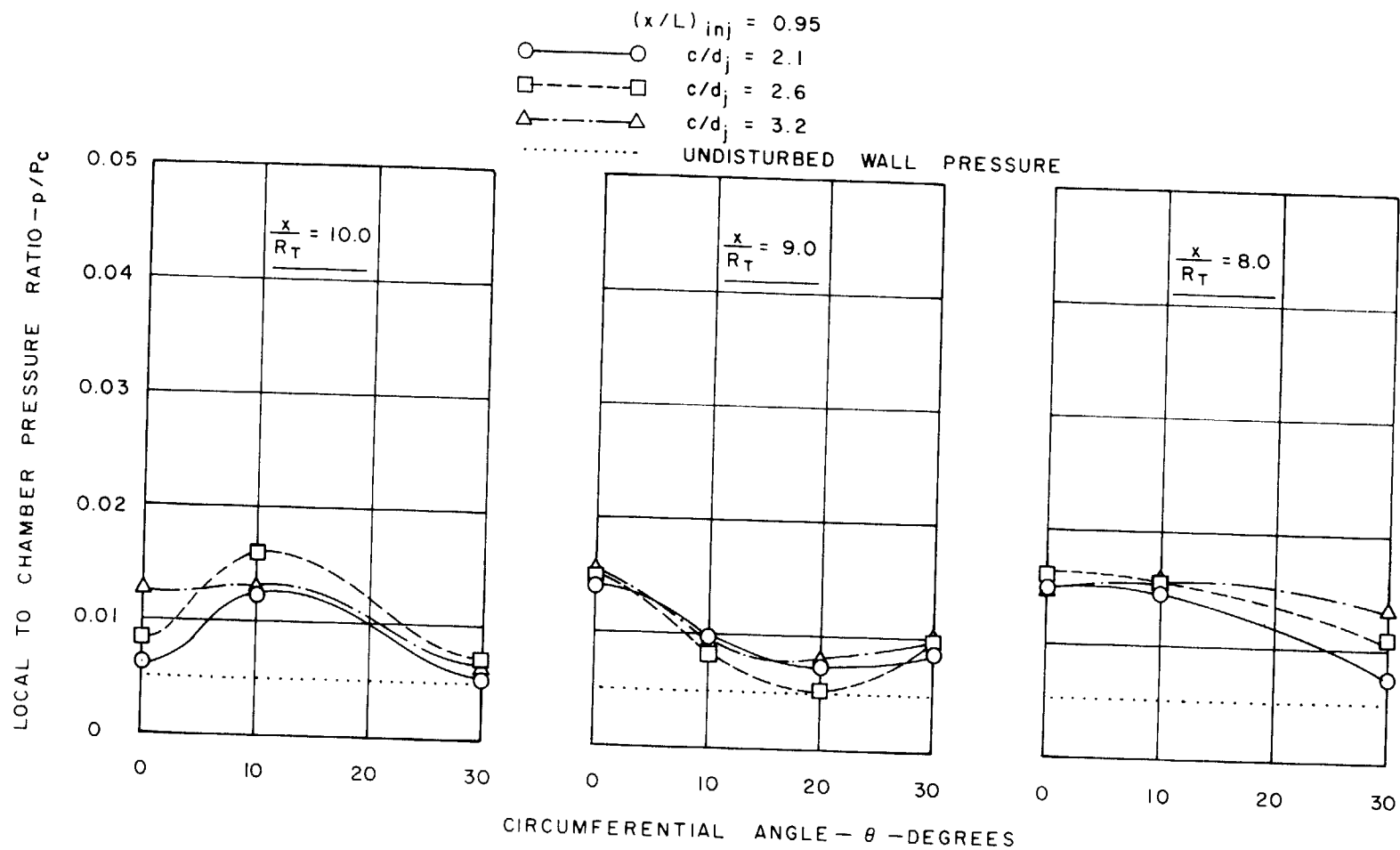
FIGURE 62

WALL PRESSURE DISTRIBUTION IN CIRCUMFERENTIAL PLANE IN THE CONICAL
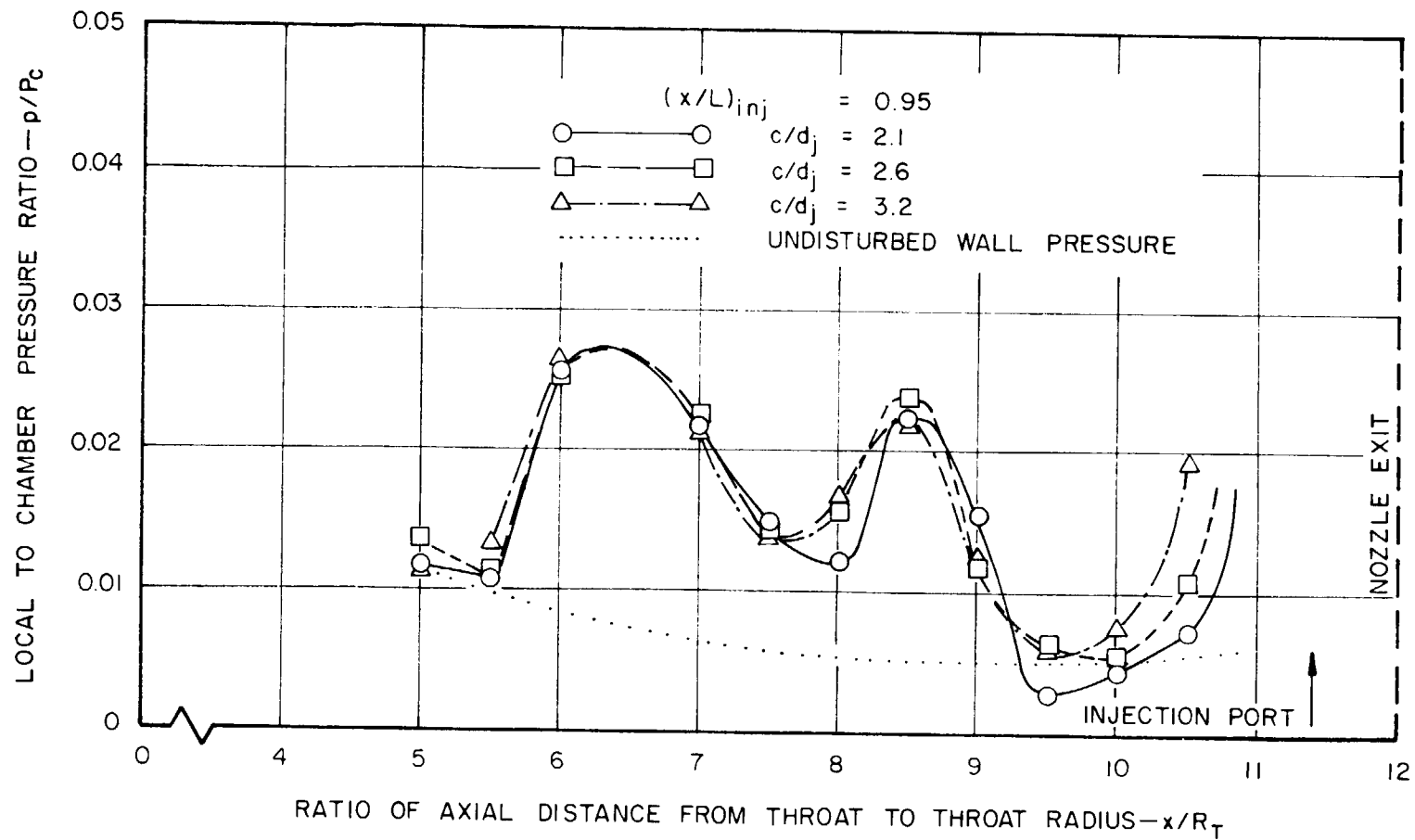NOZZLE USING OPPOSED-TANGENTIAL PORT INJECTION ($\dot{w}_s/\dot{w}_p = 0.03$)

FIGURE 63

WALL PRESSURE DISTRIBUTION IN MERIDIONAL PLANE OF INJECTION IN
THE CONICAL NOZZLE USING OPPOSED-TANGENTIAL PORT INJECTION
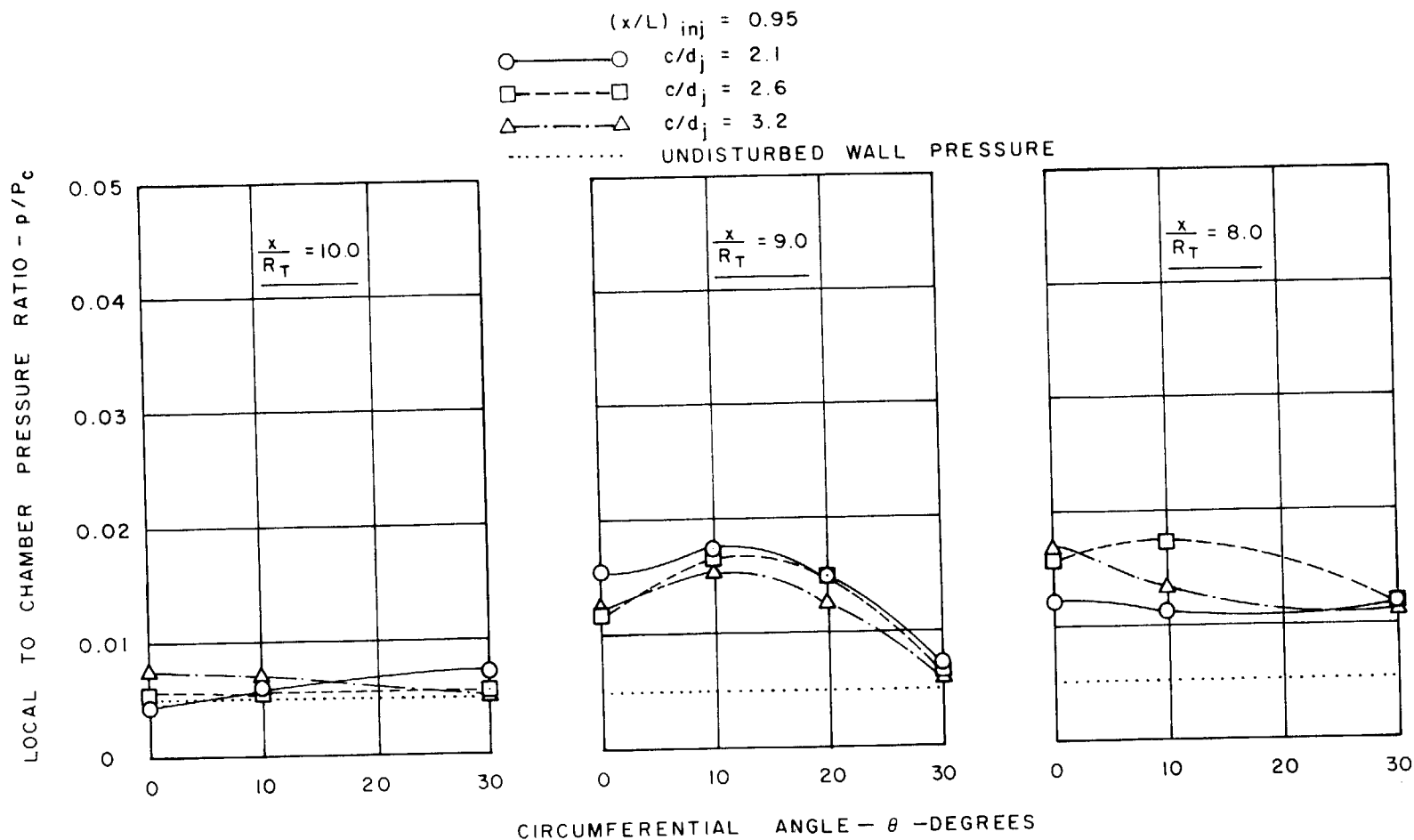($\dot{w}_s/\dot{w}_p = 0.06$)

FIGURE 64

WALL PRESSURE DISTRIBUTION IN CIRCUMFERENTIAL PLANE IN THE CONICAL NOZZLE USING OPPOSED-TANGENTIAL PORT INJECTION ($\dot{w}_s/\dot{w}_p$ = 0.06)
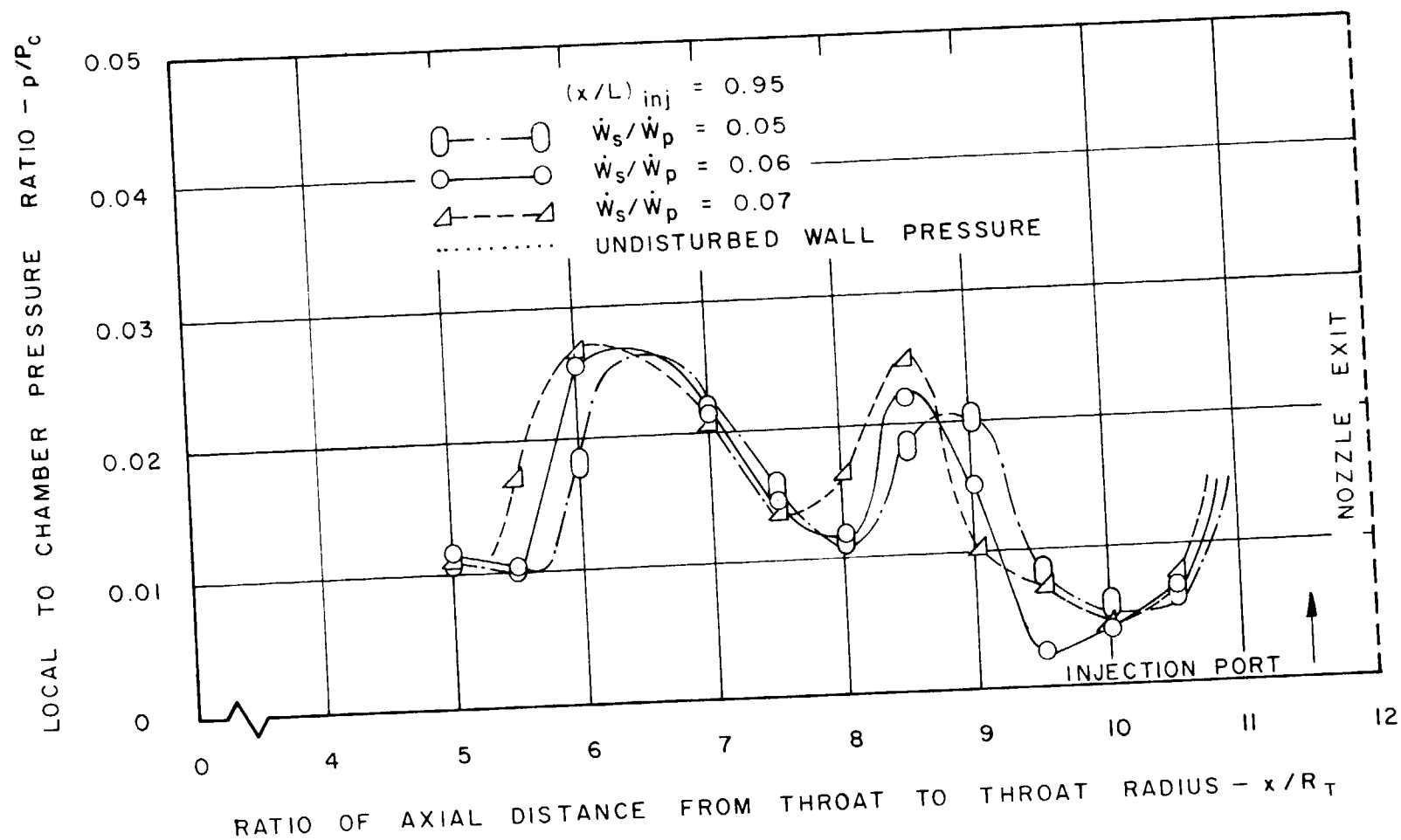
FIGURE 65

INFLUENCE OF WEIGHT FLOW RATIO ON THE AMPLI-
FICATION FACTOR USING OPPOSED-TANGENTIAL
PORT INJECTION AT $(x/L)_{inj}$ = 0.95 IN THE APG-1
NOZZLE

FIGURE 66

EFFECT OF INJECTION PORT SPACING ON THE AMPLIFI-
CATION FACTOR USING OPPOSED-TANGENTIAL PORT
INJECTION AT $(x/L)_{inj}$ = 0.95 IN THE APG-1 NOZZLE

FIGURE 67

WALL PRESSURE DISTRIBUTION IN MERIDIONAL PLANE OF INJECTION IN
THE APG-1 NOZZLE USING OPPOSED-TANGENTIAL PORT INJECTION

$(\dot{w}_s/\dot{w}_p = 0.09)$

$(x/L)_{inj}$ = 0.95

○————○ c/d_j = 2.1

○ c/d_j = 3.7 (REF. 1)

.... UNDISTURBED WALL PRESSURE

LOCAL TO CHAMBER PRESSURE RATIO - p/P_c

0.05
0.04
0.03
0.02
0.01
0

$\dfrac{x}{R_T}$ = 10.0

$\dfrac{x}{R_T}$ = 9.0

$\dfrac{x}{R_T}$ = 8.0

0   10   20   30

0   10   20   30

0   10   20   30

CIRCUMFERENTIAL ANGLE - θ - DEGREES

FIGURE 68

WALL PRESSURE DISTRIBUTION IN CIRCUMFERENTIAL PLANE IN THE APG-1 NOZZLE USING OPPOSED-TANGENTIAL PORT INJECTION ($\dot{w}_s/\dot{w}_p$ = 0.09)

LOCAL TO CHAMBER PRESSURE RATIO — p/P_c

RATIO OF AXIAL DISTANCE FROM THROAT TO THROAT RADIUS — x/R_T

$(x/L)_{inj} = 0.95$

○————○ $c/d_j = 2.1$

□————□ $c/d_j = 2.6$

△————△ $c/d_j = 3.2$

.... UNDISTURBED WALL PRESSURE

NOZZLE EXIT

INJECTION PORT

FIGURE 69

WALL PRESSURE DISTRIBUTION IN MERIDIONAL PLANE OF INJECTION IN THE APG-1 NOZZLE USING OPPOSED-TANGENTIAL PORT INJECTION

$(\dot{w}_s/\dot{w}_p = 0.03)$

FIGURE 70

WALL PRESSURE DISTRIBUTION IN CIRCUMFERENTIAL PLANE IN THE APG-1 NOZZLE USING OPPOSED-TANGENTIAL PORT INJECTION ($\dot{w}_s/\dot{w}_p = 0.03$)

FIGURE 71

WALL PRESSURE DISTRIBUTION IN MERIDIONAL PLANE OF INJECTION IN
THE APG-1 NOZZLE USING OPPOSED-TANGENTIAL PORT INJECTION
$(\dot{w}_s/\dot{w}_p = 0.06)$

FIGURE 72

WALL PRESSURE DISTRIBUTION IN CIRCUMFERENTIAL PLANE IN THE APG-1
NOZZLE USING OPPOSED-TANGENTIAL PORT INJECTION ($\dot{w}_s/\dot{w}_p = 0.06$)

FIGURE 73

WALL PRESSURE DISTRIBUTION IN MERIDIONAL PLANE OF INJECTION
IN THE APG-1 NOZZLE USING OPPOSED-TANGENTIAL PORT INJECTION
$(c/d_j = 2.1)$
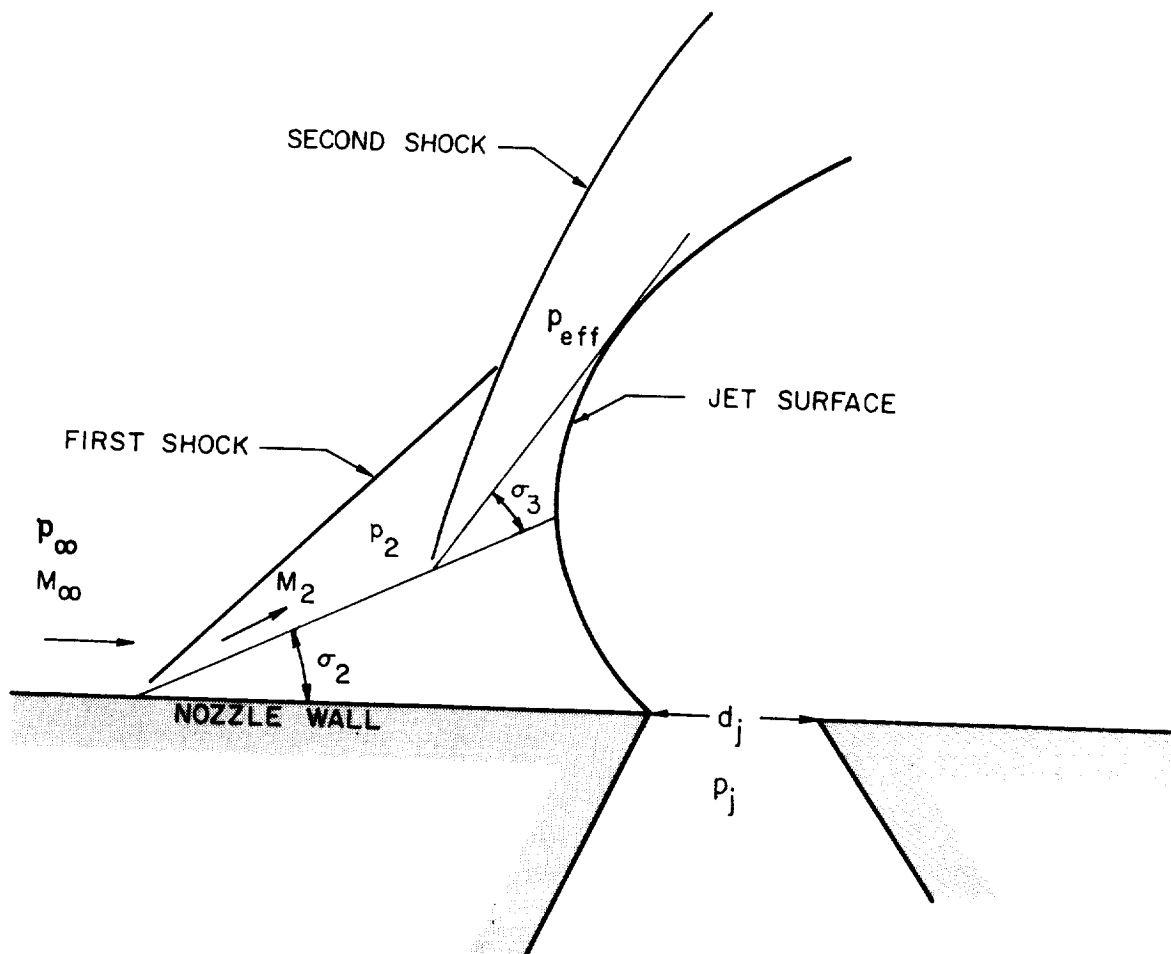
FIGURE 74

MODEL OF TWO-SHOCK SYSTEM
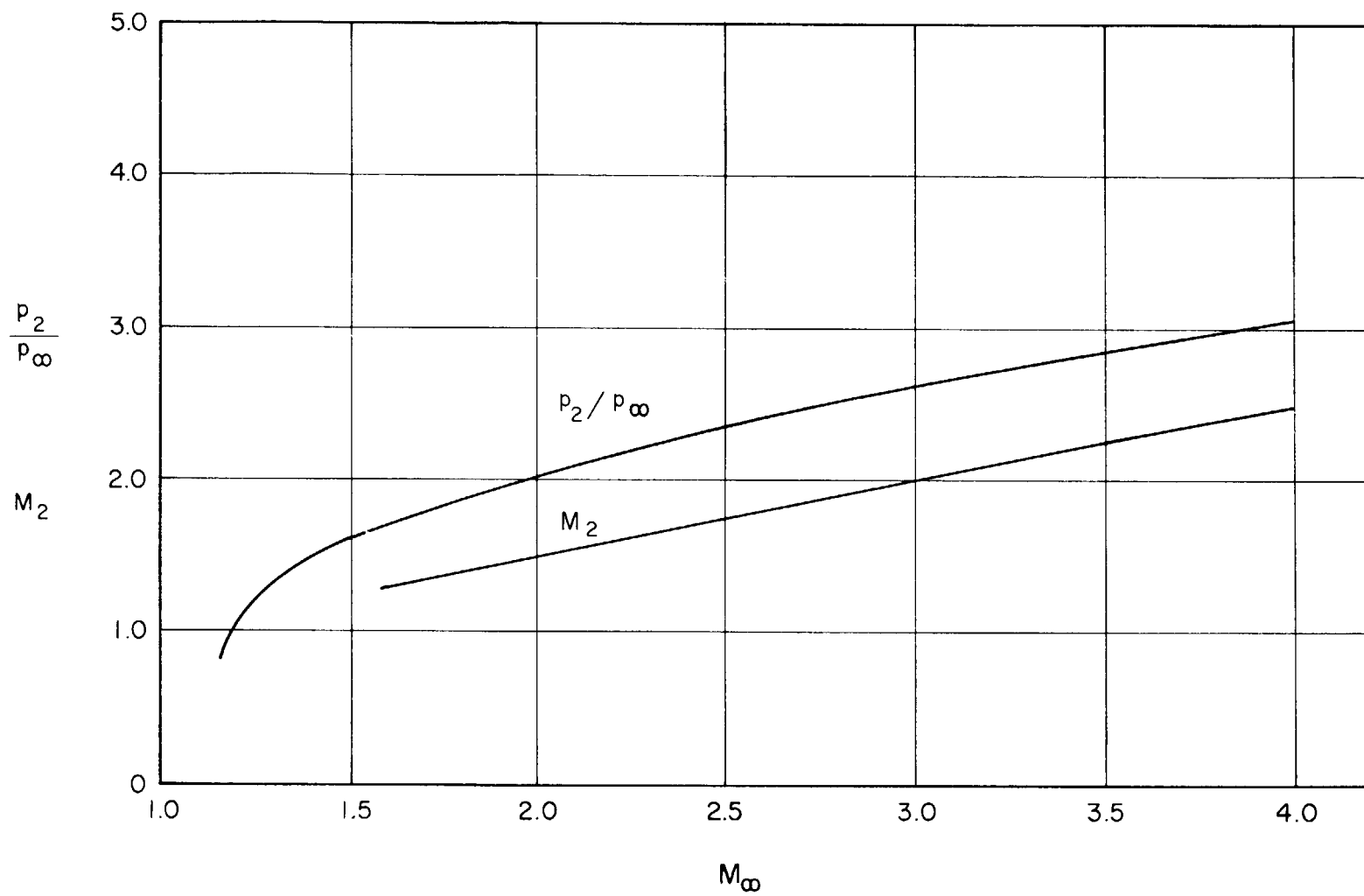
FIGURE 75

PRESSURE RATIO OF TURBULENT BOUNDARY LAYER SEPARATED BY CONICAL SHOCK, $\gamma = 1.4$
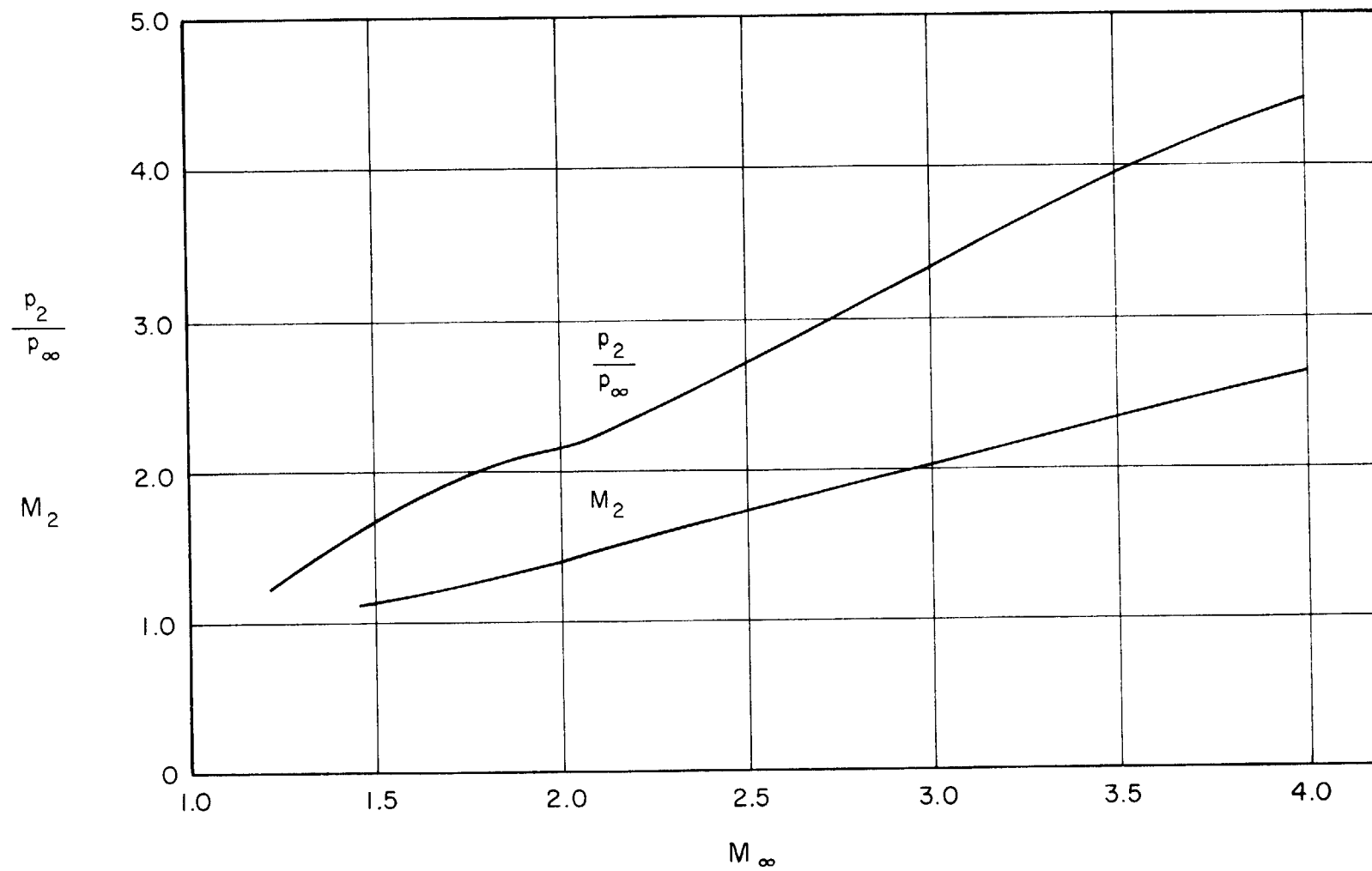
FIGURE 76

PRESSURE RATIO OF TURBULENT BOUNDARY LAYER SEPARATED BY CONICAL SHOCK, $\gamma = 1.2$
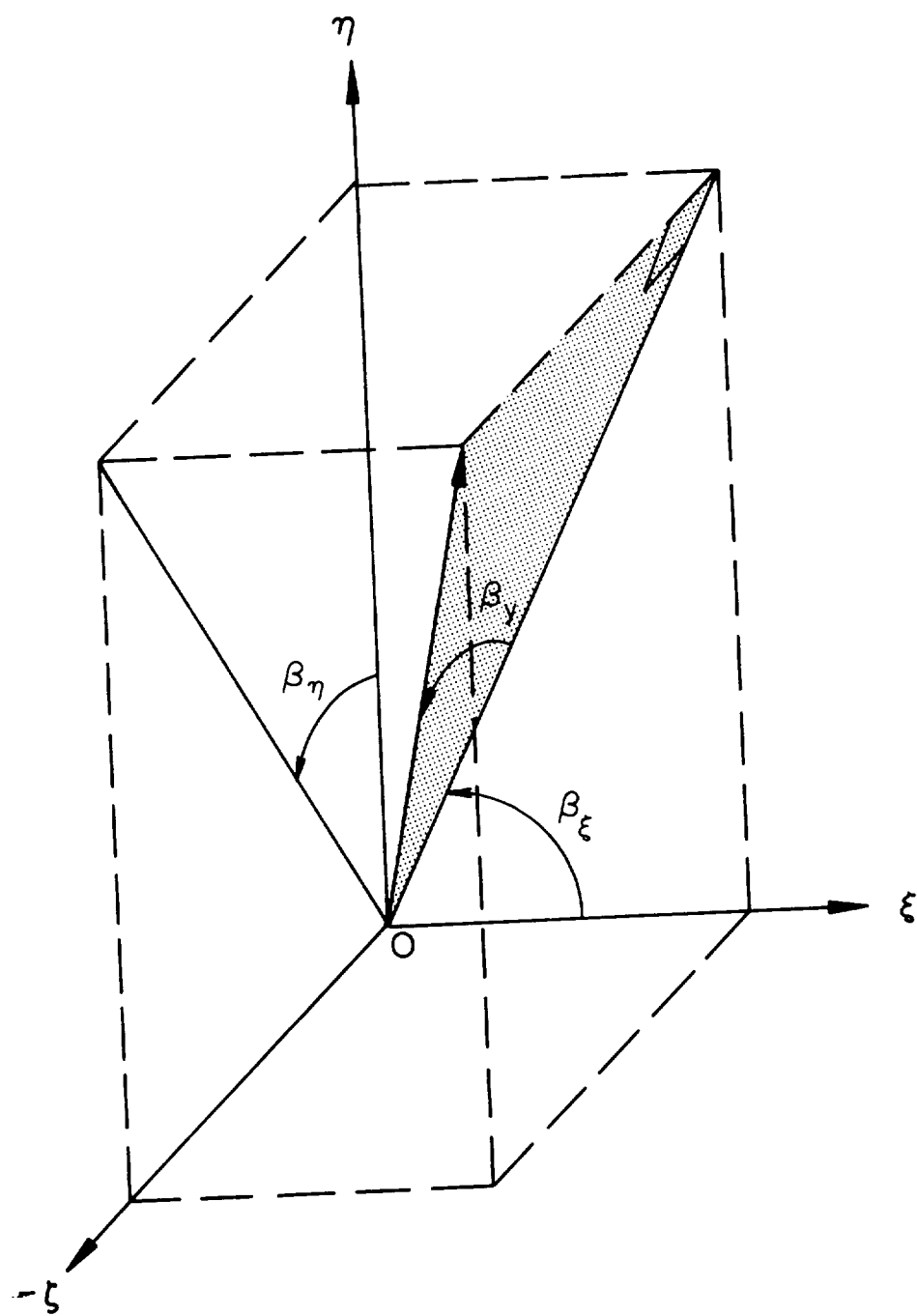
FIGURE 77

KINEMATIC RELATIONS FOR INJECTANT VELOCITY

VECTOR
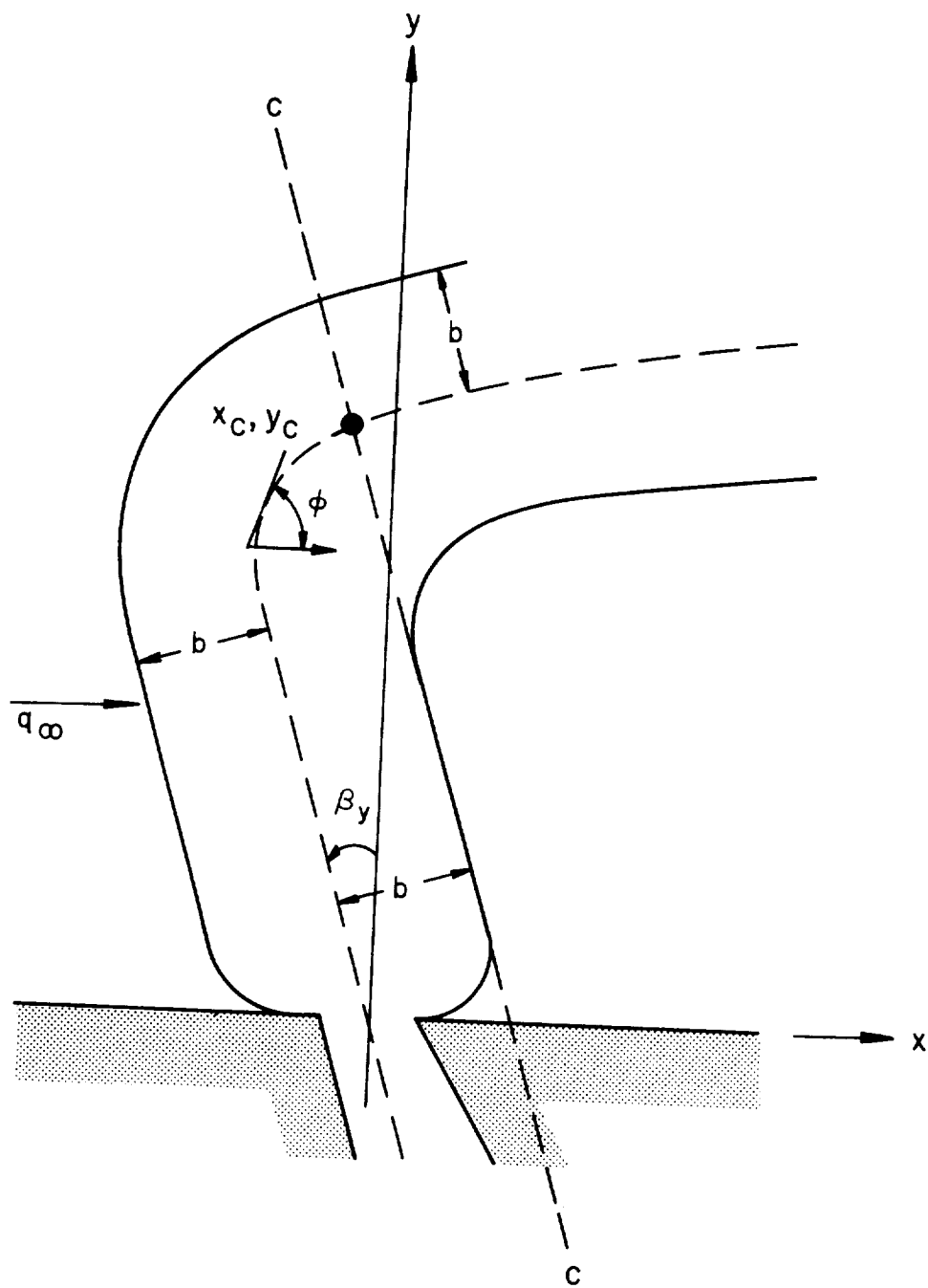
FIGURE 78

CONDITIONS FOR DETERMINATION OF PENETRATION
DEPTH
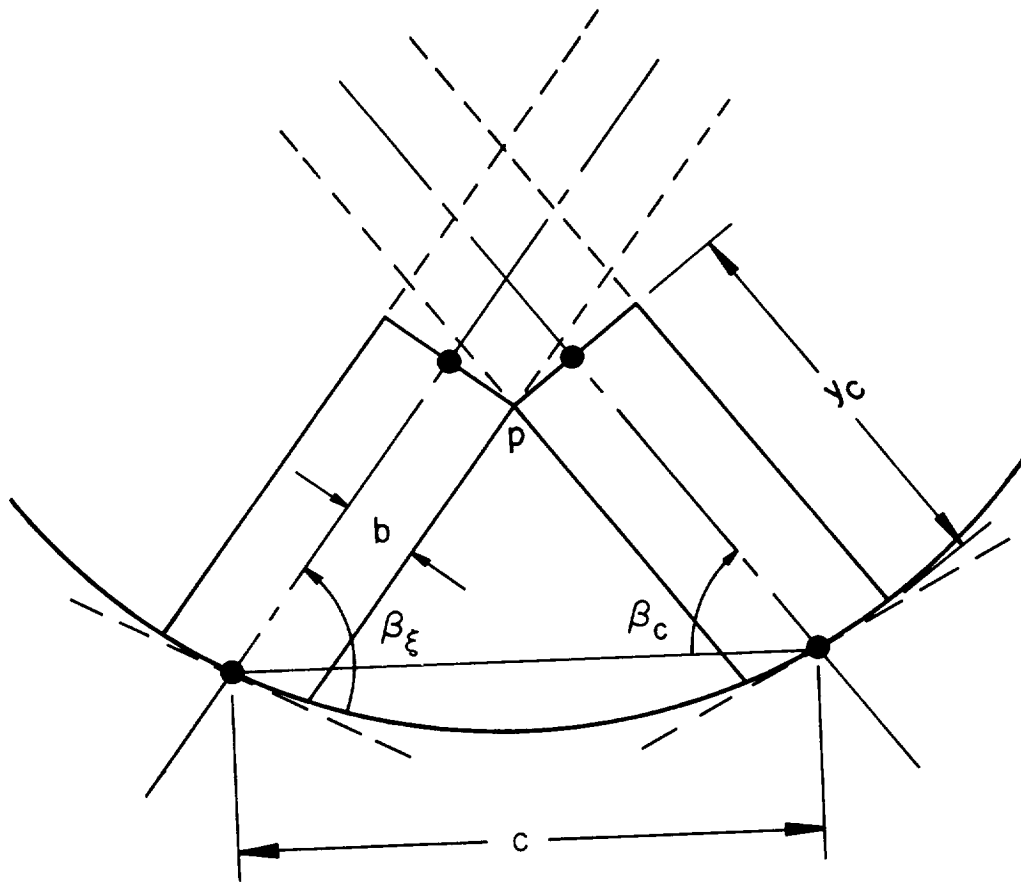
$$c_{cr} = 2y_c \; \text{Cos} \; \beta_c + 2b \; \text{Sin} \; \beta_c$$

FIGURE 79
IMPINGING JET CONFIGURATION AT MULTIPORT
INTERACTION
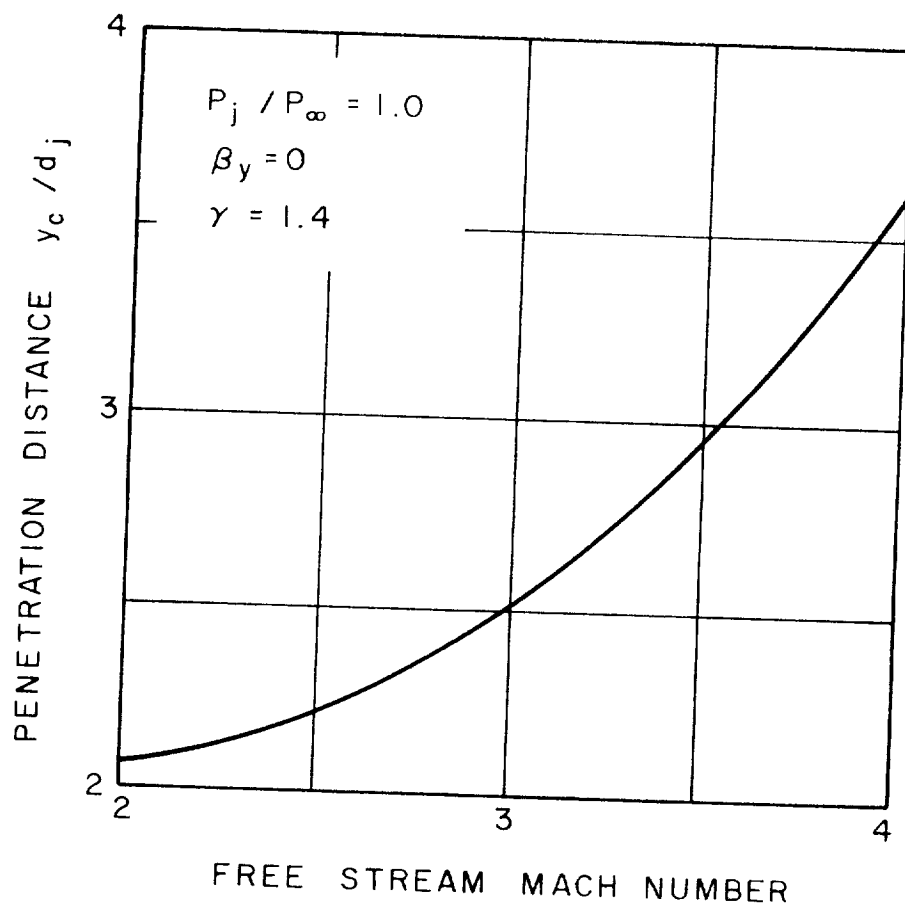
FIGURE 80

EFFECT OF FREE STREAM MACH NUMBER
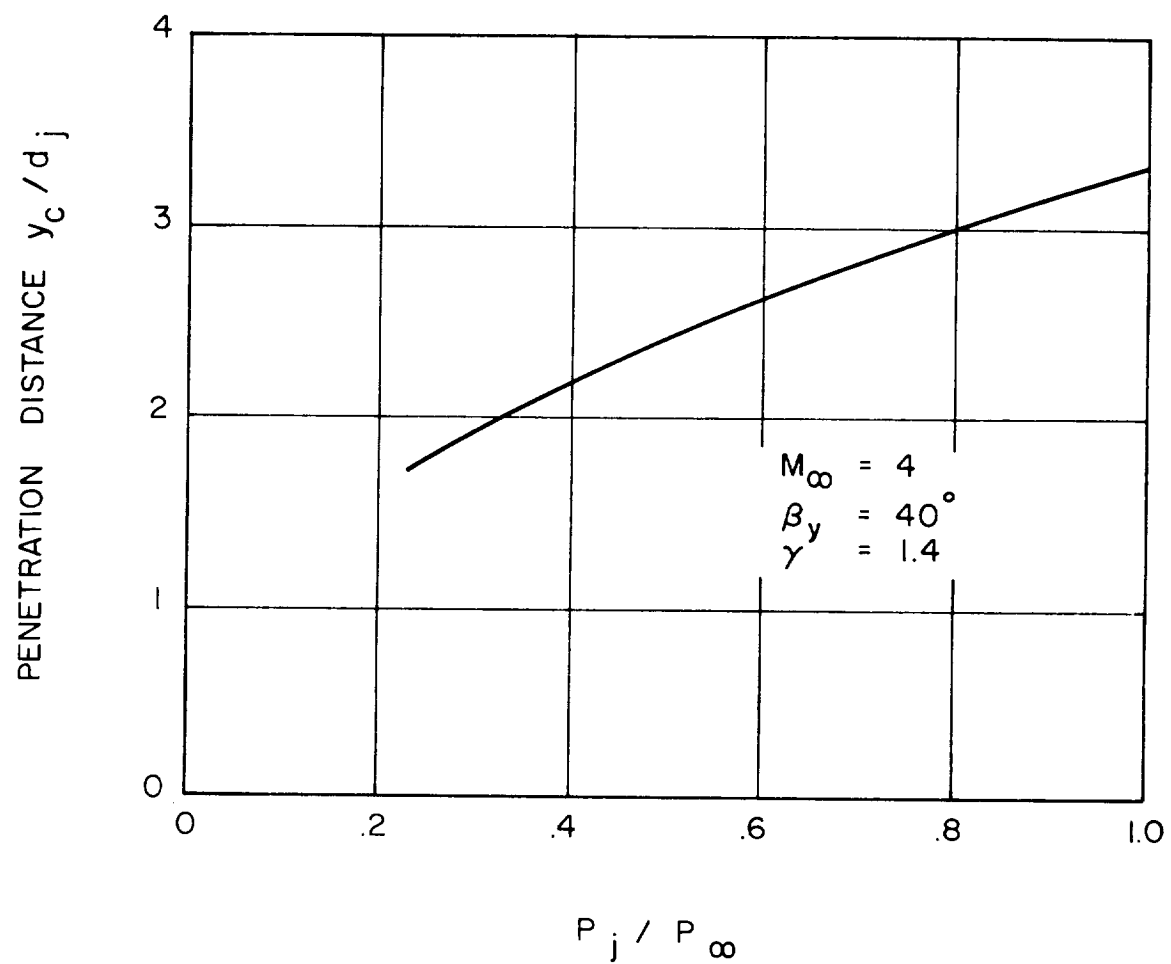ON PENETRATION DISTANCE

FIGURE 81

EFFECT OF JET-TO-PRIMARY STREAM STAGNATION
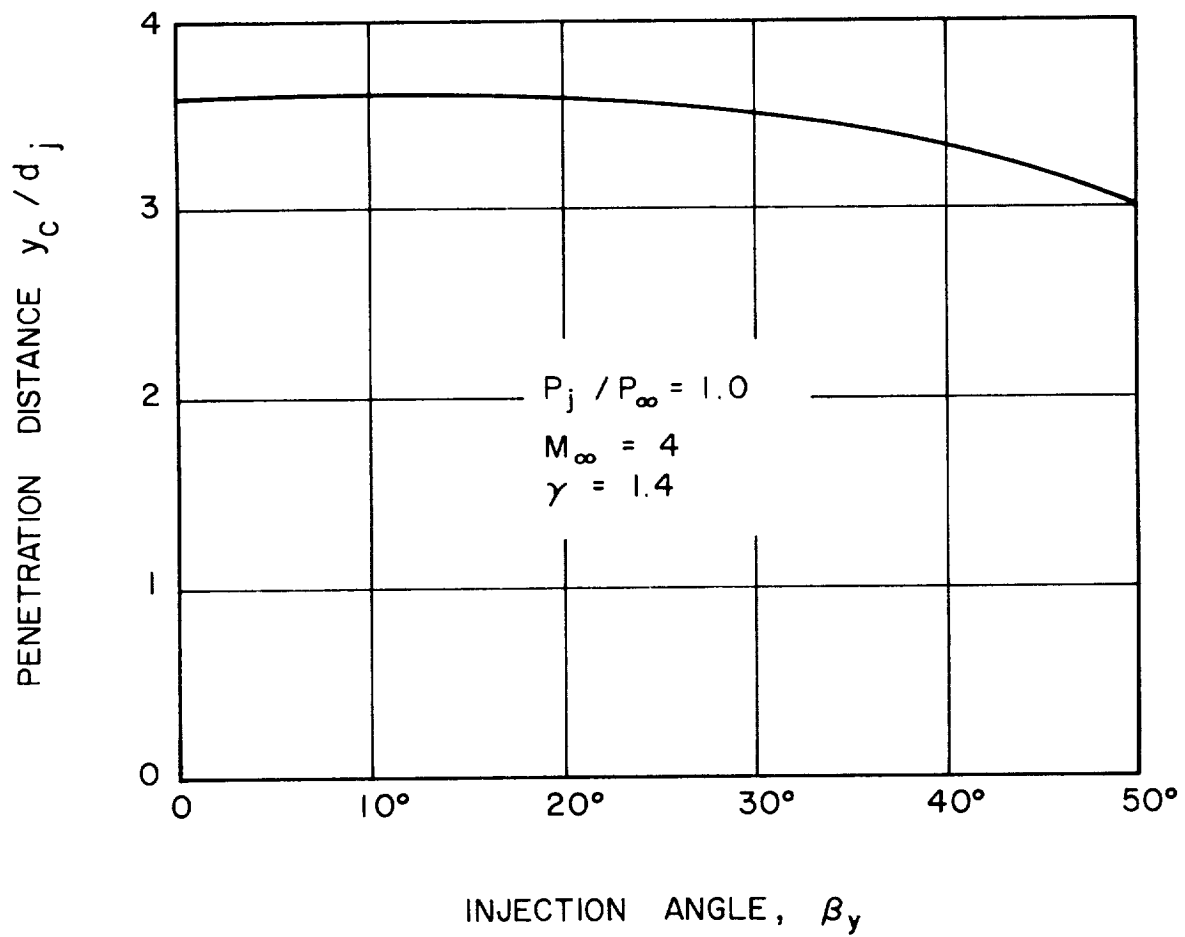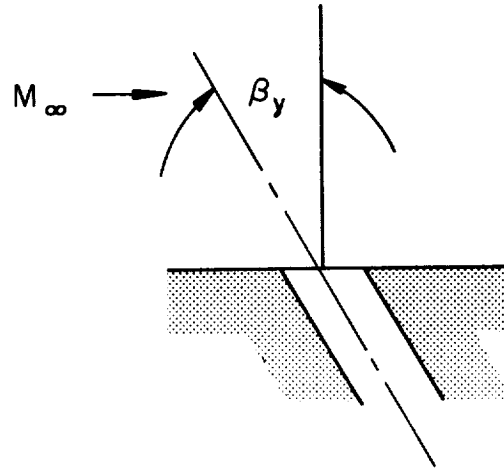PRESSURE RATIO ON PENETRATION DISTANCE

FIGURE 82

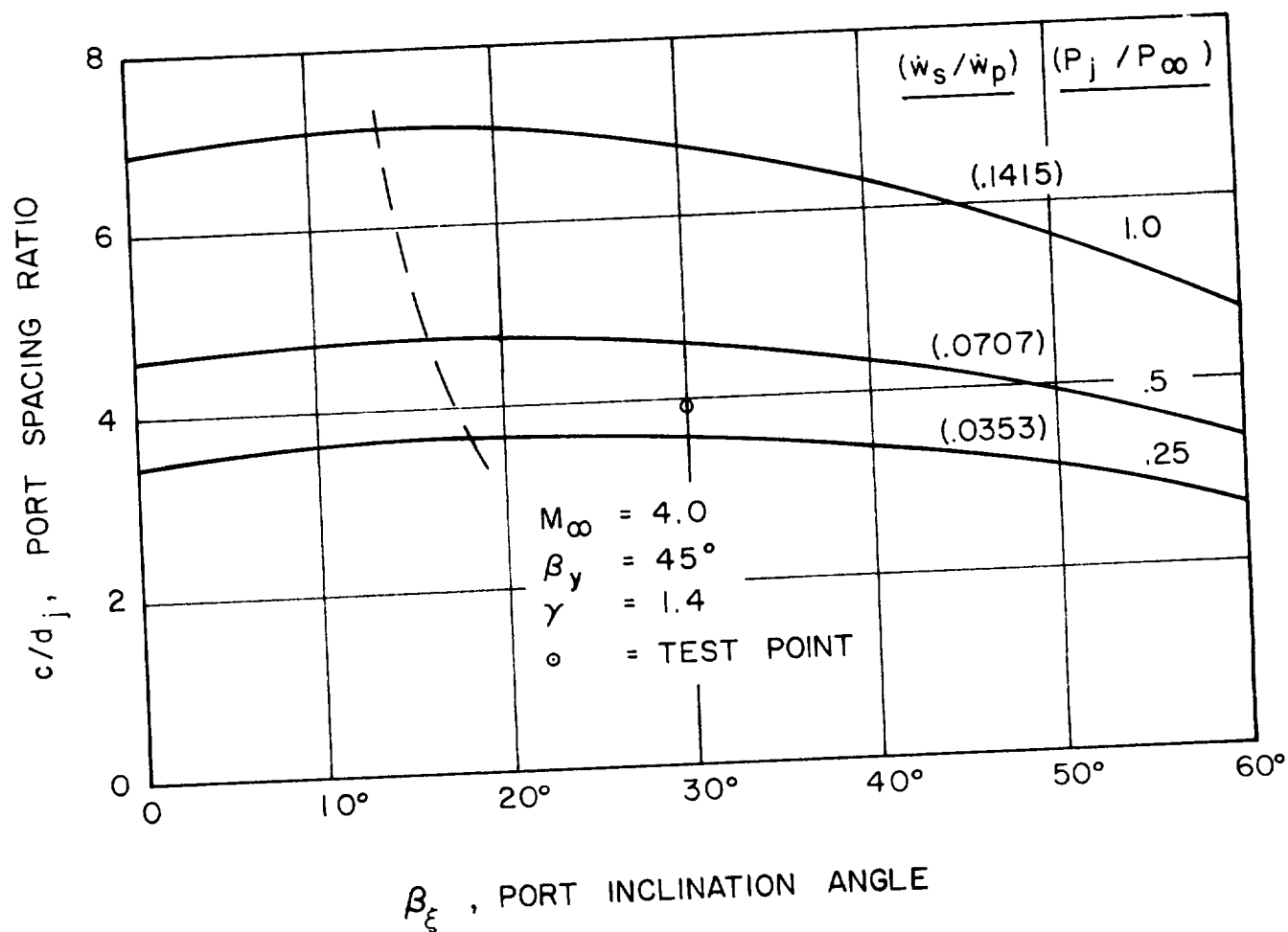EFFECT OF INJECTION ANGLE ON PENETRATION
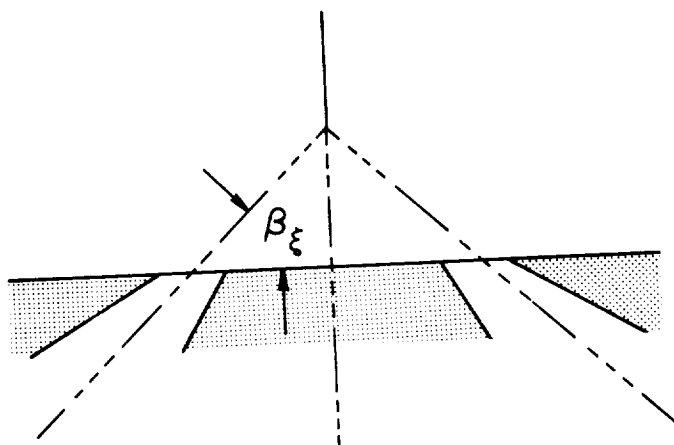DISTANCE

FIGURE 83

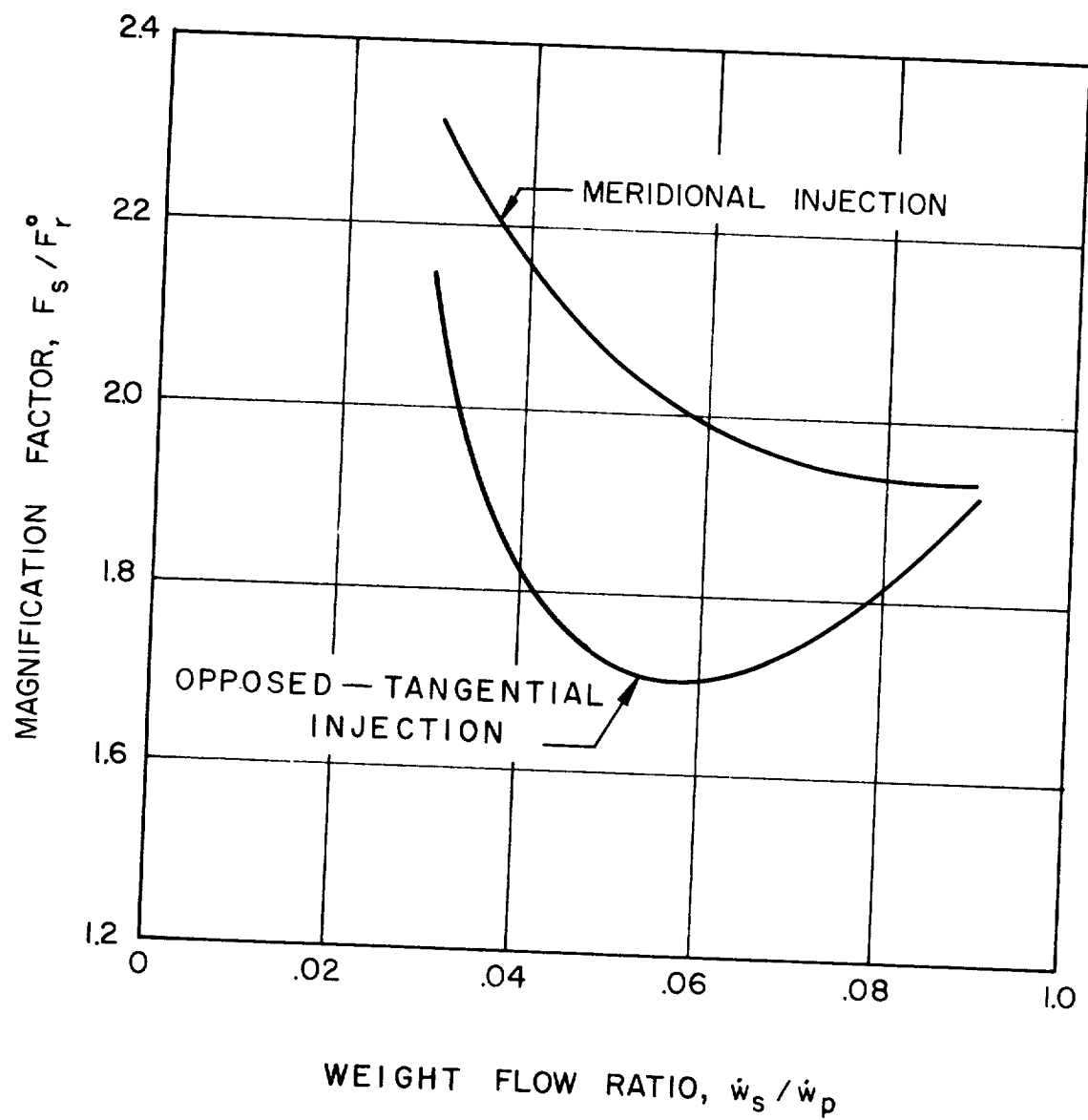EFFECT OF PORT INCLINATION ANGLE ON PORT SPACING

FIGURE 84

TEST RESULTS (FROM REFERENCE 1) SHOWING
MAGNIFICATION FACTOR FOR MERIDIONAL AND
OPPOSED-TANGENTIAL INJECTION
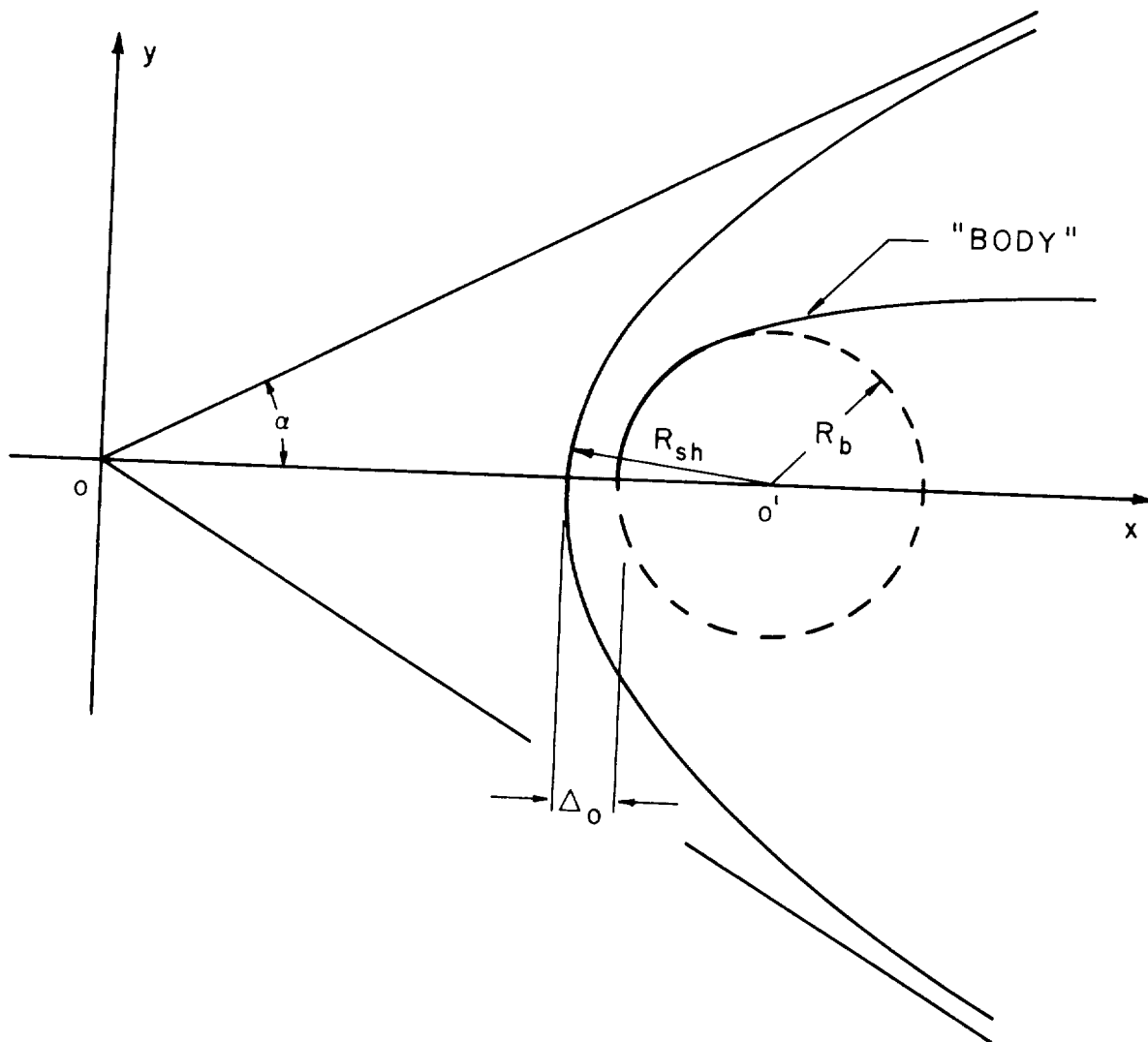
FIGURE 85

SCHEMATIC OF THE BOW SHOCK WAVE CREATED BY A
SPHERE R_b

The figure shows coordinate axes with origin o at the lower left. A straight line rises from the origin at angle $\cot^{-1}\beta_M$ above the x-axis. A curve branches from this line described by the equation:

$$y^2 = \frac{1}{\beta_M^2}x^2 - \beta_M^2 R_{sh}^2$$

A circle is centered at o' on the x-axis. The horizontal distance from the origin to the circle region is labeled $\beta_M^2 R_{sh}$, and a small distance Δ_o is indicated near the circle.
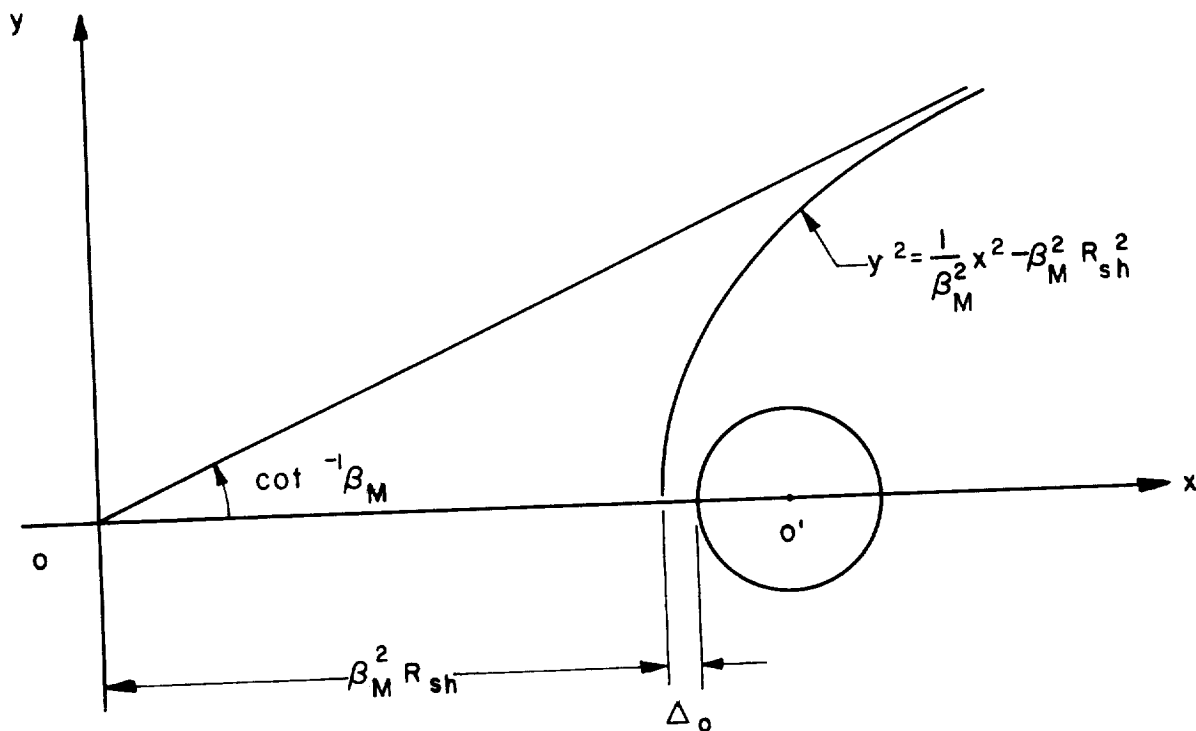
FIGURE 86

SCHEMATIC SHOWING THE POSITION AND COORDINATES OF THE BOW SHOCK WAVE

APPENDIX G

DISTRIBUTION LIST

COPIES	RECIPIENT
	NASA Western Operations Office 150 Pico Blvd. Santa Monica, California
1	Office of Technical Information
1	Contracting Officer
1	Patent Office
	NASA Headquarters Washington 25, D. C.
4	Mr. Henry Burlage, Jr. Chief, Liquid Propulsion Systems, RPL
1	Mr. A. O. Tischler Assistant Director for Propulsion, MLP
5	Mr. T. Mariani, Technical Manager Advanced Technology Office NASA Lewis Research Center 21000 Brookpark Road Cleveland 35, Ohio
2	Ames Research Center Moffett Field, California
2	Goddard Space Flight Center Greenbelt, Maryland
2	Jet Propulsion Laboratory California Institute of Technology 4800 Oak Grove Drive Pasadena, California
2	Langley Research Center Langley Field, Virginia
2	Lewis Research Center 21000 Brookpark Road Cleveland 35, Ohio
2	Marshall Space Flight Center Huntsville, Alabama

COPIES	RECIPIENT
2	Manned Spacecraft Center Houston, Texas
1	Advanced Research Projects Agency Pentagon, Room 3D154 Washington 25, D. C.
1	Aeronautical Systems Division Air Force Systems Command Wright-Patterson Air Force Base, Ohio
1	Air Force Missile Development Center Holloman Air Force Base, New Mexico
1	Air Force Missile Test Center Patrick Air Force Base, Florida
1	Air Force Systems Command, Dyna-Soar Air Force Unit Post Office Los Angeles 45, California
1	Army Ordnance Missile Command Redstone Arsenal, Alabama
1	Armed Services Technical Information Agency Arlington Hall Station Arlington 12, Virginia
1	Arnold Engineering Development Center A. E. O. R. Tullahoma, Tennessee
1	Bureau of Naval Weapons Department of the Navy Washington 25, D. C.
1	Central Intelligence Agency 2430 E Street, N. W. Washington 25, D. C.
1	Headquarters, United States Air Force Washington 25, D. C.
1	Office of Naval Research Washington 25, D. C.

COPIES	RECIPIENT
1	Picatinny Arsenal Dover, New Jersey
1	Rocket Research Laboratories Edwards Air Force Base, California
1	U.S. Naval Ordnance Test Station China Lake, California
1	U.S. Atomic Energy Commission Technical Information Services Box 62 Oak Ridge, Tennessee
1	Chemical Propellant Information Agency Johns Hopkins University Applied Physics Laboratory 8621 Georgia Avenue Silver Spring, Maryland
1	Aerojet-General Corporation P.O. Box 296 Azusa, California
1	Aerojet-General Corporation P.O. Box 1947 Sacramento 9, California
1	Aeronutronic A Division of Ford Motor Company Ford Road Newport Beach, California
1	Aerospace Corporation 2400 East El Segundo Blvd. El Segundo, California
1	Arthur D. Little, Inc. Acorn Park Cambridge 40, Massachusetts

COPIES	RECIPIENT
1	Astropower, Inc., Subsidiary of Douglas Aircraft Company, Inc. 2968 Randolph Avenue Costa Mesa, California
1	Astrosystems, Inc. 82 Naylon Avenue Livingston, New Jersey
1	Atlantic Research Corporation Edsall Road and Shirley Highway Alexandria, Virginia
1	Beech Aircraft Corporation Boulder Facility Box 631 Boulder, Colorado
1	Bell Aerosystems Company P. O. Box 1 Buffalo 5, New York
1	Bendix Systems Division Bendix Corporation Ann Arbor, Michigan
1	Boeing Company P. O. Box 3707 Seattle 24, Washington
1	Convair (Astronautics) Division of General Dynamics Corp. P. O. Box 2672 San Diego 12, California
1	Curtiss-Wright Corporation Wright Aeronautical Division Wood-Ridge, New Jersey
1	Douglas Aircraft Company, Inc. Missile and Space Systems Division 3000 Ocean Park Blvd. Santa Monica, California
1	Fairchild Stratos Corporation Aircraft Missiles Division Hagerstown, Maryland

COPIES	RECIPIENT
1	General Electric Company Missile and Space Vehicle Department Box 8555 Philadelphia, Pennsylvania
1	General Electric Company Rocket Propulsion Units Building 300 Cincinnati 15, Ohio
1	Grumman Aircraft Engineering Corp. Bethpage, Long Island, New York
1	Kidde Aero-Space Division Walter Kidde and Company, Inc. 675 Main Street Belleville 9, New Jersey
1	Lockheed Aircraft Corporation Missile and Space Division Sunnyvale, California
1	Lockheed Propulsion Company P. O. Box 111 Redlands, California
1	Marquardt Corporation 16555 Saticoy Street Box 2013 - South Annex Van Nuys, California
1	Martin Division Martin Marietta Corporation Baltimore 3, Maryland
1	Martin Denver Division Martin Marietta Corporation Denver, Colorado
1	McDonnell Aircraft Corporation P. O. Box 6101 Lambert Field, Missouri
1	North American Aviation, Inc. Space & Information Systems Division Downey, California

COPIES	RECIPIENT
1	Northrop Corporation 1001 East Broadway Hawthorne, California
1	Pratt & Whitney Aircraft Corporation Florida Research & Development Center West Palm Beach, Florida
1	Radio Corporation of America Astro-Electronics Division Defense Electronic Products Princeton, New Jersey
1	Reaction Motors Division Thiokol Chemical Corporation Denville, New Jersey
1	Republic Aviation Corporation Farmingdale Long Island, New York
1	Rocketdyne (Library Dept. 586-306) Division of North American Aviation, Inc. 6633 Canoga Avenue Canoga Park, California
1	Space General Corporation 9200 Flair Avenue El Monte, California
1	Space Technology Laboratories P.O. Box 95001 Airport Station Los Angeles 45, California
1	Stanford Research Institute 333 Ravenswood Avenue Menlo Park, California
1	TAPCO Division Thompson-Ramo-Wooldridge, Inc. 23555 Euclid Avenue Cleveland 17, Ohio
1	Thiokol Chemical Corp., Redstone Div. Huntsville, Alabama

COPIES	RECIPIENT
1	United Aircraft Corporation East Hartford Plant 400 Main Street Hartford, Connecticut
1	United Technology Corporation 587 Methilda Avenue Sunnyvale, California
1	Vought Astronautics Box 5907 Dallas 22, Texas